Electrocatalytic Detection of Pesticides with Electrodes Modified with Nanoparticles of Phthalocyanines and Multiwalled Carbon Nanotubes

A thesis submitted in fulfillment of the requirements for the degree of

DOCTOR OF PHILOSOPHY (SCIENCE)

OF

RHODES UNIVERSITY

By

Msimelelo Patrick Siswana

February 2013

Dedication

To my parents, Golden and MaKhuze Siswana, for inspiring all of us children to get an education.

To my wife and children, for all the support they have given me throughout my PhD studies.

Acknowledgements

I would like to acknowledge the following:

My first thanks is to God Almighty, for all the blessings he has granted me.

My second thanks goes to Professor Tebello Nyokong, my supervisor, for her guidance, support and infinite patience. It has been a pleasure and a blessing to have been one of her students. I am especially grateful also to Professor Kenneth Ozoemena, my co-supervisor, who provided me with invaluable advice and insight throughout my studies.

I am also greatly indebted to Mr A. Adriaan at the chemistry workshop for the construction of the pyrolytic graphite electrodes; the Electron Microscopy lab staff for the TEM and SEM images, and to Dr Edith Entunes and the S22 research group, for the extensive support, advice and training they provided me during the project.

Finally but as importantly I would like to thank Walter Sisulu University and the NRF, for the vital financial support they gave me.

Abstract

Three types of electrodes: carbon paste electrodes modified with nanoparticles of metallophthalocyanines (MPcNP-CPEs, M = Mn, Fe, Ni, Co), basal plane pyrolytic graphite electrodes modified with iron or nickel phthalocyanine nanoparticles and multiwalled carbon nanotube composites (FePcNP/MWCNT-BPPGE or NiPcNP/MWCNT-BPPGE),and basal plane pyrolytic graphite electrodes modified with multiwalled carbon nanotubes and electropolymerized metal tetra-aminophthalocyanines (*poly*-MTAPc-MWCNT-BPPGE), where M is Mn, Fe, Ni or Co, were prepared. Electrochemical characterizations showed that faster electron transfer kinetics occurred at the NiPcNP/MWCNT-BPPGE than at the FePcNP/MWCNT-BPPGE surface. SEM and electrochemical characterizations of *poly*-MTAPc-MWCNT-BPPGE showed that MTAPc had been deposited on the MWCNT-BPPGE surface, and that the *poly*-CoTAPc-MWCNT-BPPGE exhibited the fastest electron transfer kinetics of all the *poly*-MTAPc-MWCNT-BPPGEs.

Using amitrole and asulam as test analytes, electrochemical experiments showed that, amongst the CPEs, the FePcNP-CPE and NiPcNP-CPE displayed the most electrocatalytic behavior towards amitrole and asulam oxidation, respectively, and further experiments were done to obtain the electrochemical parameters associated with these electrodes and the corresponding analytes. Although, the FePcNP/MWCNT- BPPGE displayed electrocatalytic behavior towards amitrole oxidation in comparison with the bare BPPGE, it was less electrocatalytic than the FePcNP-CPE in terms of detection potential. The NiPcNP/MWCNT-BPPGE displayed the same detection potential as the NiPcNP-CPE. The *poly*-FeTAPc-MWCNT-BPPGE

exhibited the most electrocatalytic behavior towards amitrole, of all the electrodes investigated, and the *poly*-CoTAPc-MWCNT-BPPGE displayed the best electrocatalytic behavior towards asulam, amongst the *poly*-MTAPc-MWCNT-BPPGEs.

CONTENTS

LIST OF ABBREVIATIONS

BPPGE – basal plane pyrolytic graphite electrode

CME – chemically modified electrode

CPE – carbon paste electrode

CNTs – carbon nanotubes

CV – cyclic voltammetry

CPE_{dl} – constant phase element

CTACl – hexadecyltrimethyl ammonium chloride

CTAB – hexadecyltrimethyl ammonium bromide

CT – charge transfer

Ct – catalyst

CA – chronoamperometry

DMF – dimethyl formamide

DMSO – dimethyl sulphoxide

DLLME – dispersive liquid-liquid micro extraction

EC_{cat} – electrochemical reaction preceding a chemical reaction

EIS – electrochemical impedance spectroscopy

ESCA – electron spectroscopy for chemical analysis

FIA-Amp – flow injection analysis with chronoamperometry

GCE – glassy carbon electrode

HRTEM – high-resolution transmission electron microscopy

HOMO – highest occupied molecular orbital

HOPG – highly ordered pyrolytic graphite

LUMO – lowest unoccupied molecular orbital

LMCT – ligand to metal charge transfer

LLIRT – liquid-liquid interface recrystallization technique

MPc – metallophthalocyanine

MPcNPs – metallophthalocyanine nanoparticles

ME – mecarptoethanol

MEKC – micellar electrokinetic chromatograph

MLCT – metal to ligand charge transfer

MWCNTs – multiwalled carbon nanotubes

PBS – phosphate buffer solution

Pc – phthalocyanine

PG – pyrolytic graphite

SEM – scanning electron microscopy

SWCNT – single-walled carbon nanotubes

SWV – square wave voltammetry

TAPc – tetra-aminophthalocyanine

TCAPc – tetra-carboxylic acid chloride phthalocyanine

TSPc – tetra-sulfophthalocyanine

UV/Vis – ultra violet-visible spectroscopy

XRD – X-ray diffraction

XRPD – X-ray powder diffraction

XPS – X-ray photoelectron spectroscopy

LIST OF SYMBOLS

A – geometrical surface area of electrode

$\mathbf{A_{effect}}$ – effective surface area of electrode

α - electron transfer coefficient

b – Tafel slope

β - full width at half-maximum

c – concentration of solution

$\mathbf{C_0}$ – bulk concentration of analyte

$\mathbf{C_{dl}}$ – double layer capacitance

D – diffusion coefficient

δ - bending mode (Raman)

$\mathbf{E_p}$ – peak potential

F – Faraday constant

Φ - phase shift

Γ - surface coverage of electrode

I – current

$\mathbf{I_0}$ – current amplitude,

exchange current density

$\mathbf{I_P}$ – peak current

$\mathbf{I_{pa}}$ – anodic peak current

$\mathbf{I_{cat}}$ – catalytic current

$\mathbf{I_L}$ – current due to the blank/buffer solution

$\mathbf{K_{amp}}$ – amperometric selectivity coefficient

$\mathbf{k_{et}}$ – electron transfer rate constant

k – catalytic rate constant

$\boldsymbol{L_a}$ – lateral grain size

λ - wavelength

$\mathbf{N_{CNT}}$ – number of carbon nanotubes

$\boldsymbol{n}$ – number of electrons transferred

ν - scan rate,

stretching mode (Raman spectroscopy)

ω - radial frequency

Q – electric charge

$\mathbf{R_s}$ – solution resistance

$\mathbf{R_{et}}$ – electron transfer resistance

R – gas constant

R′ – pseudo-rotational librational mode

σ - standard deviation

τ - tortional mode

T′ – pseudo-translational librational mode

V – voltage

$\mathbf{V_0}$ – voltage amplitude

Z – impedance

$\mathbf{Z_w}$ – Warburg impedance

LIST OF FIGURES

LIST OF SCHEMES

LIST OF TABLES

Chapter 1

Introduction

The chapter starts with a discussion of the concept of chemical modification of electrodes. Materials that are used to chemically modify electrodes, such as nanomaterials (nanoparticles and carbon nanotubes) and phthalocyanines, are discussed. Electrocatalysis is discussed in relation to the materials used to chemically modify electrodes. An overview of the analytes to be used in this study is presented.

The electrochemical detection of organic pollutants such as alcohols, phenols, amines, carbohydrates and their derivatives is frequently limited by slow electron transfer at conventional electrodes and complicated by irreversible passivation of the electrode surface. If the electrodes are covered with molecular materials of known electrocatalytic activity, this problem may be solved. Metallophthalocyanines (MPcs) have been immobilized on different electrode surfaces to design what are called chemically modified electrodes. It has been shown that such modified electrode surfaces behave as fast electron-transfer mediators for solution species [1].

In this study, carbon-based electrodes are chemically modified with MPcs and nanomaterials, and employed in the electrochemical detection of herbicides that are environmental pollutants.

1.1 Chemically Modified Electrodes

1.1.1 Electrodes employed in this work

A chemically modified electrode (CME) is an electrode made of a conducting or semi-conducting material that is coated with a film of a chemical modifier. The distinguishing feature of a CME is that a thin film of a selected chemical is bonded to or coated on the electrode surface to endow the electrode with the chemical, electrochemical or other desirable properties of the film in a rational, chemically designed manner [2-9]. In this study, chemical modification was done on carbon-based electrodes such as carbon paste and pyrolytic graphite electrodes, hence these will be discussed.

1.1.1.1 Carbon paste electrodes

The carbon paste electrode (CPE) was introduced for the first time in 1958 [10]. Carbon paste is a mixture of ground carbon and mulling liquid. Practical considerations require that the mulling liquid should be electroinactive and pure with respect to electroactive impurities, chemically inert, have a very low solubility or be immiscible with the analyte solution, should have low volatility, and should ensure low residual currents in the investigated potential range [2,11]. Different types of mulling liquids or binders have been used for the preparation of CPE. Among these are : paraffin or Nujol®[12], silicone lubricants [13], polychlorotrifluoroethylene oils [14]. Nujol® is more commonly used.

The required properties [15] of the particulate component (graphite) of the paste are:

(i) uniform particle size distribution

(ii) high chemical purity

(iii) low adsorption capability for oxygen and electroactive impurities.

(iv) right level of porosity [16]. Materials such as carbon black, animal charcoal or similar products which are extremely porous, are not suitable for the preparation of carbon pastes.

Typically, pastes for CPEs may be prepared by thoroughly mixing Nujol® and graphite powder until the mixture is uniformly wetted [11,17]. The usual particle size of the graphite materials is about 3 μm; larger particles produce a rough texture and unfavourable mechanical and electrochemical properties [18,19]. Graphite of smaller particle size (e.g., 0.2 μm) can be suitable for the preparation of carbon paste microelectrodes [20]. The resultant paste should have a consistency similar to

that of peanut butter. After thorough mixing, the paste is packed into an inert holder such as Teflon or glass tubes. Electrical contact with the paste is maintained using a piece of conducting wire. The surface may be "polished" using weighing paper; it is important that the face of the holder is flat and smooth so as to obtain a flat, reproducible carbon paste surface.

To prevent the separation of graphite and the pasting liquid, it is important to avoid too much pressure when packing the paste into the holder. Separation of the liquid from graphite results in high resistance at the area of contact between paste and conducting wire [2,15]. CPEs have rather low background currents compared to solid graphite or noble metal electrodes, but the magnitude increases with an increasing quantity of pasting liquid, which invariably decreases the sensitivity of the electrode [17]. CPEs can be polarized within a wide potential window of -1.0 to 1.5 V vs silver/silver chloride electrode (Ag/AgCl) in acidic media and from -1.3 to 1.4 V vs Ag/AgCl in neutral media, and between -1.2 V and 1.2 V in alkaline solutions. Simply pushing a small column of electrode material out of the holder and cutting it off with a scapel or the edge of very clean paper easily regenerates the surfaces of CPEs [21].

The major setbacks of the use of CPEs in electroanalysis have to do with reproducibility, use in non-aqueous media and presence of entrapped oxygen in the paste. In voltammetric measurements, oxygen seriously interferes when employing CPEs in the negative potential range. The reproducibility of CPEs is a bit worse than that of mercury electrodes or sensors made of compact materials such as noble metals and glassy carbon. The relative standard deviation of measurements with a

CPE is about 5%. The other disadvantage of CPEs has to do with its heterogeneous nature; when applied in non-aqueous media, the electrode disintegrates due to the solubility of the binder in organic solvents [2,21].

In this work, CPEs were modified with nanosized MPcs (M= Fe, Co, Mn, and Ni) and the modified electrodes were used to detect asulam or amitrole (depending on their ability to catalyse the oxidation of these test analytes).

1.1.1.2. Pyrolytic graphite electrodes

Up to until the mid 1980s, all available materials made exclusively of sp^2 hybridized carbon, possessed the planar graphite sheet as their structural building block: a hexagonal lattice of 3 coordinate carbon atoms where the C-C bond length is around 1.42 Å. This includes a wide variety of graphite products which have been used as working electrodes, such as amorphous carbon, glassy carbon, carbon fibres, powdered graphite, pyrolytic graphite (PG) and highly ordered pyrolytic graphite (HOPG), each with different chemical and physical properties. The key structural factor that leads to an assortment of different materials is the average graphite microcrystallite size (or lateral grain size, L_a,) which is effectively the average size of the hexagonal lattices that make up the macro structure. In principle, this can range from being infinitely large, as in the case of a macrosized single crystal of graphite, to the size of a benzene molecule which is approximately 3 Å. Pyrolytic graphite is intermediate in the range, with L_a values of around 1000 Å [22]. The largest graphite monocrystals are found in HOPG which can be 1-10 μm in size [22-24]. Regions where individual graphite monocrystals meet each other (i.e, grain boundaries) are poorly defined and, when exposed, result in surface defects. In the case of pyrolytic graphite, the individual graphite crystals lie along

the same axis making it possible to obtain carbon surfaces with significantly less defects. This is especially true for HOPG where the large lateral grain size can result in a well defined surface with values of defect coverage as low as 0.2 % [25]. **Figure 1.1** shows a pyrolytic graphite surface with the graphite crystals lying along a 'basal plane' and the edges of the crystals (the surface defects) lying along an edge plane [26].

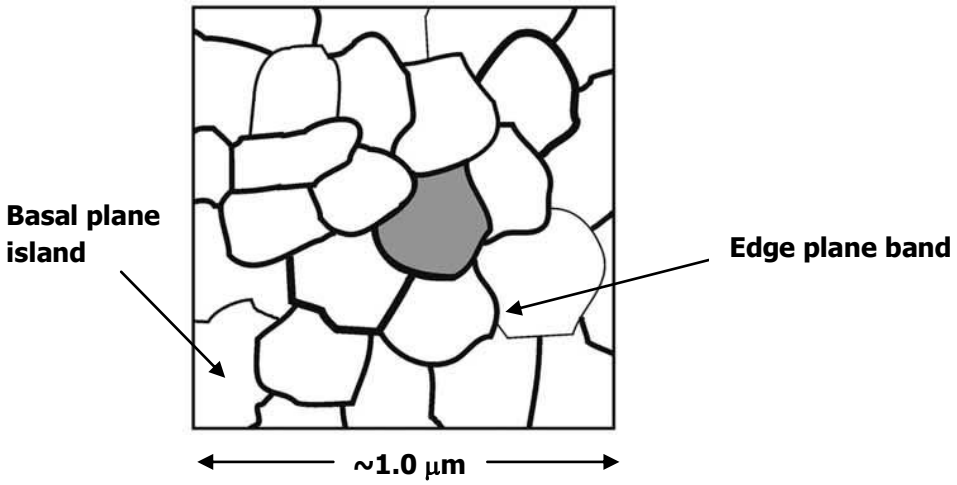

Figure 1.1: A front view of the basal and edge planes of pyrolytic graphite [26].

Edge plane and basal plane pyrolytic graphite electrodes are fabricated from slabs of HOPG. The basal plane surface of an HOPG electrode consists of layers of graphite which lie parallel to the surface and with an interlayer spacing of 3.35 Å. Surface defects occur in the form of steps exposing the edges of the graphite layers, as shown in **Figure 1.2**. The surface defects (exposed edge planes) are a very low percentage of the total surface area, as explained earlier.

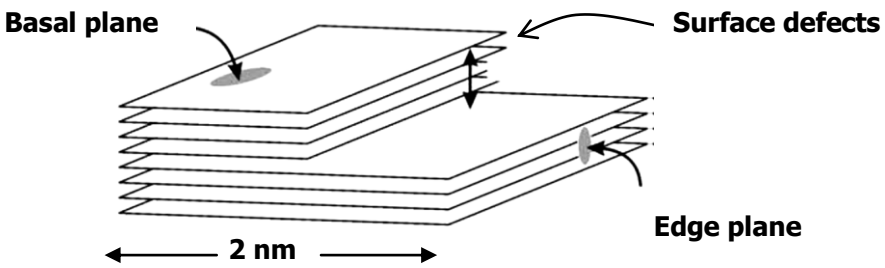

Figure 1.2: Schematic diagram of basal and edge planes of pyrolytic graphite [26].

In this work a basal plane pyrolytic graphite electrode was modified with nanoparticles of iron phthalocyanine (FePcNPs) and nickel phthalocyanine (NiPcNPs) in the presence or absence of MWCNTs, and employed in the detection of amitrole and asulam.

1.1.2 Methods for electrode modification

Various methods are used to chemically modify different types of electrodes, and the methods used in this work are discussed.

1.1.2.1 Composite

In this method, the chemical modifier is simply mixed with an electrode matrix material. The method involves the combination of the modifier with the carbon particles of carbon based electrodes [27-29] , forming the carbon paste electrode discussed above.

1.1.2.2 Electropolymerization

The use of polymer film coatings as modifying agents on electrodes is perhaps the most popular method of electrode modification for a number of reasons:

(i) it is easy to prepare multiplayer films by electropolymerization,

(ii) the thickness of the film can be controlled and reproduced,

(iii) there is no loss of the polymer on the electrode surface since the polymer films have tremendous chemical stability and can be made completely insoluble in the contacting solution phase,

(iv) other functional groups can be added as additional coats on the polymer [30].

In electropolymerization, an electrode is immersed in a concentrated solution ($\approx 10^{-3}$ M) of the desired modifier followed by repetitive voltammetric scanning within a specified potential range. The rate and extent of the polymerisation process as well as the chemical and physical properties of the resulting polymer can be carefully controlled [31-36].

1.1.2.3 Abrasive immobilization

In this method, the modifying agent is abrasively attached onto the electrode surface. The electrode is usually pyrolytic graphite. The procedure involves cleaning the electrode surface by polishing it on carborundum paper, pressing cellophane tape on the cleaned surface and then removing the cellophane tape along with several layers of graphite. This is repeated multiple times to achieve the final surface. Before modification, the electrode is rinsed with acetone to remove any adhesive. The modifying agent (in this case, the MPcNPs or carbon nanotubes) is then abrasively immobilized on the surface of the electrode [22].

1.1.3 Methods of characterizing modified electrodes

Once an electrode has been successfully modified, it is desirable to characterize such a modified surface. A number of techniques are actively in use for characterizing modified electrode surfaces. The techniques used in this work are discussed below.

1.1.3.1 Cyclic voltammetry

Electrochemical methods, particularly cyclic voltammetry, provide an effective way of determining the amount of modifier deposited on the electrode surface [37]. The amount of modifier deposited on the electrode surface (termed "surface coverage") may be obtained by cycling the electrode within an appropriate potential window in a solution that contains a supporting electrolyte, and determining the area under the oxidation or reduction wave. The area gives the charge (Q) associated with the species coated on the electrode, and from the calculated charge, the surface coverage can be determined using equation 1.1 [30,37].

$$Q = nFA\Gamma \qquad \textbf{1.1}$$

where A = effective surface area of the electrode, cm^2

Γ = surface coverage, $mol.cm^2$

n = number of electrons transferred, and F is the Faraday constant

When carbon nanotubes are employed as the modifying agents, cyclic voltammetry can be used to obtain the approximate number of nanotubes attached to the electrode surface. Firstly, the surface roughness factor for the modified electrode is determined by using the $[Fe(CN)_6]^{3-/4-}$ redox system and the Randles-Sevcik equation (equation 1.2):

$$\mathrm{I_p} = (2.69 \times 10^5)\mathrm{n}^{3/2}\mathrm{AcD}^{½}\mathrm{v}^{½} \qquad \textbf{1.2}$$

where I_p = peak current (in amperes (A)) of a reversible system at 298 K, n = number of electrons transferred, A = electrode surface area (cm^2), D = diffusion coefficient ($cm^2.s^{-1}$), c = concentration (M), and ν = scan rate ($V.s^{-1}$). The surface roughness is calculated from the ratio, I_{pa} experimental/I_{pa} theoretical. Then, the effective surface area (A_{eff} = roughness factor $\times$ calculated (geometric) area) can be calculated [38,39].

The number of carbon nanotubes on the surface is then estimated from the known dimensions of the carbon nanotubes and the calculated effective surface area [40].

1.1.3.2 Scanning electron microscopy

The kind of information that can be obtained from SEM is listed below [41]:

(i) **Topography:** the surface features of the object or "how it looks", that is, its texture.

(ii) **Morphology:** the shape of the particles making up the object.

(iii) **Crystallographic information:** how the atoms are arranged in the object.

A typical SEM picture of a copper phthalocyanine (CuPc) thin film deposited on a glass substrate using a liquid-liquid interface recrystallization technique (LLIRT) is shown in **Figure 1.3**. The micrograph revealed non-spherical domains made up from nanosized CuPc particles. Additionally, the domain showed a tendency to form chains rather than uniform growth in three dimensions. The film was shown to be non-uniform, with voids clearly visible between the grains [42].

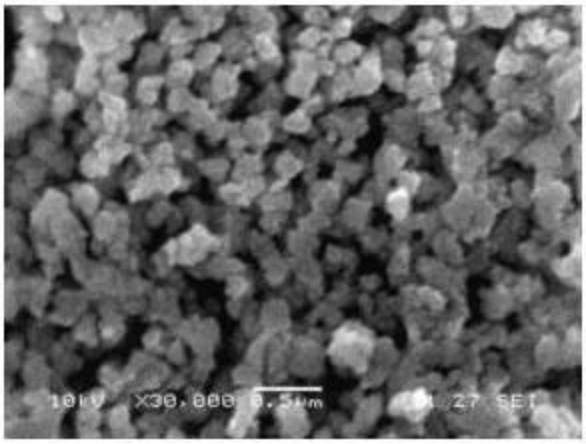

Figure 1.3: SEM micrograph of a CuPc film [42].

1.1.3.3 Transmission electron microscopy

Transmission electron microscopy (TEM), especially high-resolution transmission electron microscopy (HRTEM), is frequently used to study nanosized materials such as carbon nanotubes and other nanoparticles. The image is especially suited to study the overall shape of the nanomaterials. If the bright field images are of high magnification and high quality, the graphitic layered structure can also be visible [43].

For example, copper (II) oxide (CuO) nanoparticles were prepared by using two methods, one involving cetyl trimethyl ammonium bromide (CTAB) and the other involving sodium dodecyl sulphate (SDS). TEM (**Figure 1.4**) was used to compare the sizes of copper(II) oxide (CuO) nanoparticles produced from two syntheses [44].

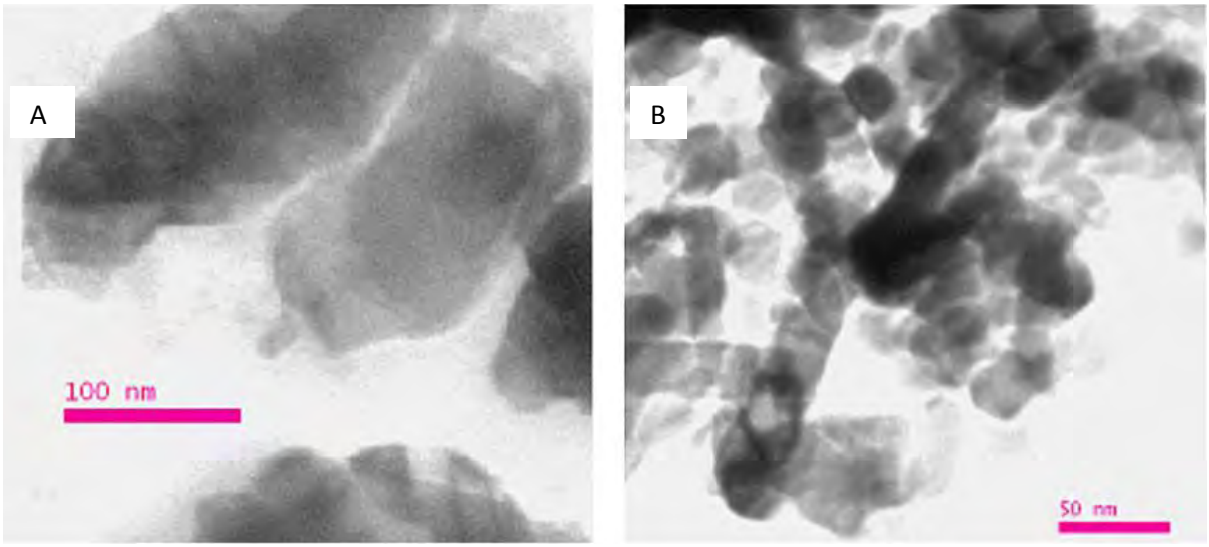

Figure 1.4: TEM images of CuO samples prepared using (A) SDS and (B) CTAB [44].

From the TEM images, the nanoparticles obtained using SDS (A) were found to have a width of ~100 nm and length of 200 nm. The nanoparticles obtained using CTAB (B) were found to have an average size of ~25 nm.

1.1.3.4 X-ray diffraction

X-ray diffraction (XRD), especially X-ray powder diffraction (XRPD), is an important technique for structure analysis because, practically, solids used in heterogeneous catalysis are almost always in powder form. The tiny particles making up the powder may be nano-sized crystallites. Characterization of both the shape and size of such nanomaterials is important in the development of these materials and as a means to control the quality of their synthesis [45].

The principle of the characterization approach used is that if crystallites are sufficiently small, the Bragg peaks in a diffraction pattern are broadened by an amount inversely proportional to the particle size. Measurement of the broadening thus gives a means of estimating the size through the well-known Debye–Scherrer [46] formula given by:

$$l = \frac{0.9\lambda}{\beta\cos\theta} \qquad \textbf{1.3}$$

where L is the apparent particle size, β is the full-width at half-maximum (FWHM) of the X-ray diffraction line in radians, λ is the wavelength used, and θ is half the scattering angle. The constant 0.9 in Equation 1.3 depends slightly on the symmetry of the crystal [47].

The nanoparticles obtained using the CTAB and SDS methods described above were characterized by employing XRD, and the spectrum obtained is shown in **Figure 1.5**

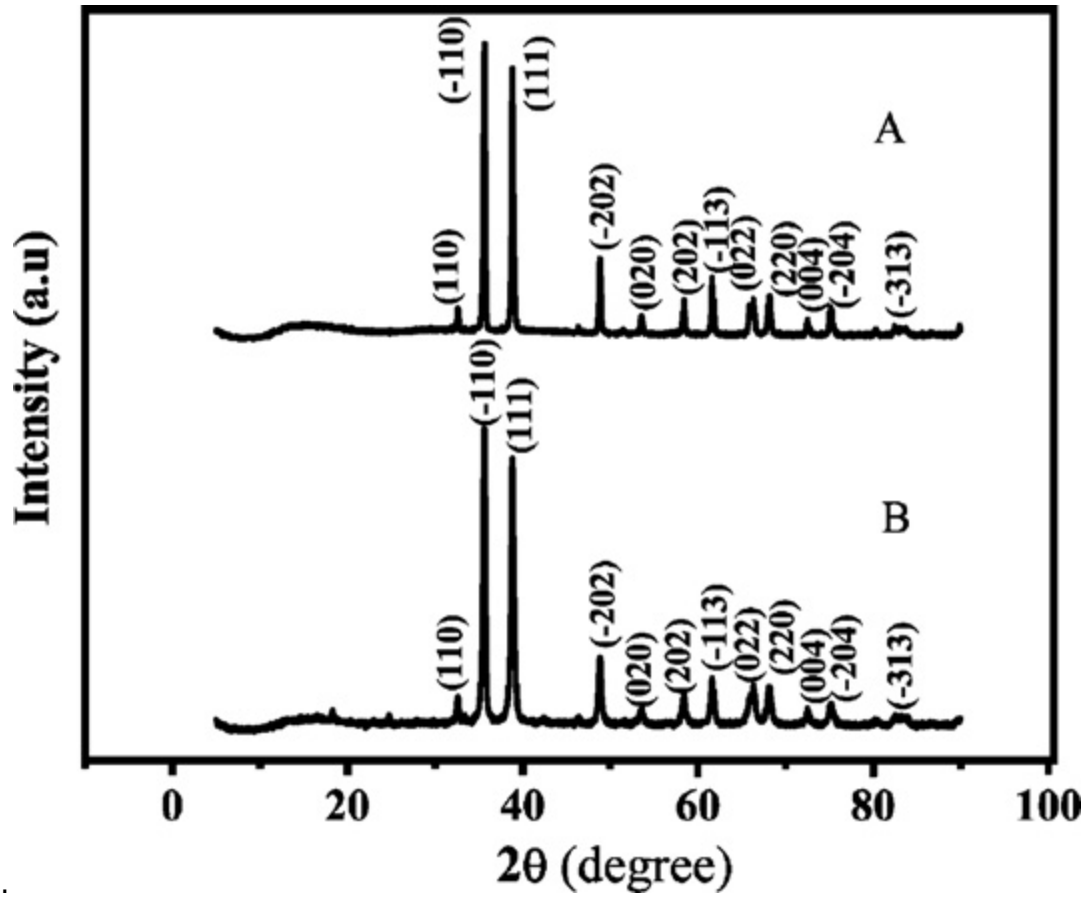

.

Figure 1.5: XRD patterns for CuO nanoparticle samples prepared using (A) SDS and (B) CTAB [44].

Using the Debye-Scherrer formula, the size of the particles synthesized using CTAB was found to be 37.2 nm, and those obtained using SDS had an average size of 110 nm.

1.1.3.5 Electrochemical impedance spectroscopy

Impedance methods are based on perturbation of the electrochemical cell with an alternating signal of small magnitude, and monitoring of the response. For example, when the applied signal is a sinusoidal perturbation of applied voltage (V(t)), expressed as:

$$V(t) = V_0 \sin\omega t \qquad \textbf{1.4}$$

the response will be a sinusoidal current response (I(t)):

$$I(t) = I_0 \sin(\omega t + \Phi) \qquad \textbf{1.5}$$

V(t) and I(t) are the voltage and current, respectively, at time *t*. V_0 and I_0 are the voltage and current amplitudes, respectively; ω is the radial frequency, and Φ is the phase shift by which the voltage lags the current [37].

The impedance, Z, is defined as : $Z = \frac{V(t)}{I(t)}$ **1.6**

Thus Z is a vector and can be represented as : $Z = Z' + jZ''$ where Z' is the real part of the impedance (Z_{re}), Z'' is the imaginary part (Z_{im}), and $j = \sqrt{-1}$. Z_{re} and Z_{im} originate mainly from the resistance and capacitance of the cell, respectively [37].

One way of modeling electrochemical processes at the electrode-solution interface involves comparison of the electrochemical process to an equivalent electrical circuit containing combinations of resistances and capacitances, for example, the Randles model [37] shown in **Figure 1.6.**

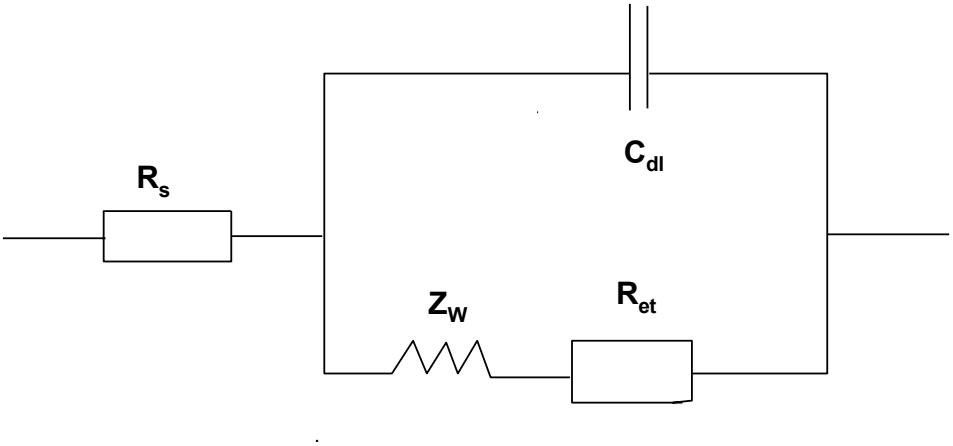

Figure 1.6: The Randles circuit model

The diagram includes the ohmic resistance of the electrolyte solution, R_s, the Warburg impedance, Z_W, resulting from the diffusion of ions from the bulk electrolyte to the electrode interface, the double layer capacitance, C_{dl}, and the electron-transfer resistance, R_{et}, that exists if an electroactive species is present in the electrolyte solution. R_s and Z_W represent bulk properties of the electrolyte solution and diffusion features of the electroactive species in solution, respectively. C_{dl} and R_{et} depend on the dielectric and insulating features of the electrode/electrolyte interface.

In the Randles circuit, it is assumed that the resistance to electron transfer and the Warburg impedance are both parallel to the interfacial capacity, C_{dl}. This parallel combination of R and C gives rise to a semicircle in the complex plane plot of -Z″ against Z′ (the Nyquist plot). The mass-transfer term (Warburg impedance), which cannot be represented by classical circuit elements, is observed as a low frequency spur with a slope of unity [48,49]. A typical shape of an impedance spectrum (presented in the form of a Nyquist plot of the imaginary part of the impedance ($-imag_i$, or -Z″) against the real part ($real_i$, or Z′)) is shown in **Figure 1.7**.

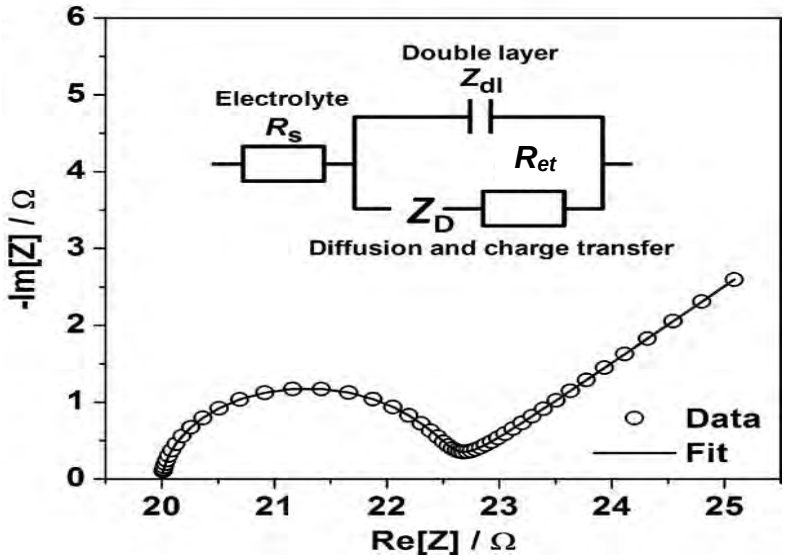

Figure 1.7: Typical shape of an impedance spectrum in the form of a Nyquist plot of Im[Z] (or -Z″) vs Re[Z] (or Z′) [49].

The semicircle portion, observed at higher frequencies, corresponds to the electron transfer-limited process, whereas the linear part is characteristic of the lower frequency range and represents the diffusion-limited electron transfer process. In the case of very fast electron-transfer processes, the impedance spectrum could include only the linear part, whereas a very slow electron-transfer step results in a big semi-circle region that is not accompanied by a straight line [50]. The semi-circle diameter equals R_{et}. The intercept of the semi-circle with the Re[Z]-axis at high frequencies ($\omega \rightarrow \infty$) is equal to R_s, the solution resistance.

The roughness of the electrode surface also has a bearing on the impedance to electron transfer at the surface. This is accounted for by the inclusion of a constant phase element (CPE_{dl}) in the Randles circuit. The impedance of the CPE_{dl} (Z_{CPE}) is defined as in equation 1.7 [51]:

$$Z_{CPE_{dl}} = (Q(j\omega)^n)^{-1} \qquad \textbf{1.7}$$

where Q is a frequency-independent constant relating to the interface. J is the √-1, ω is the radial frequency, and the exponent n arises from the slope of log Z vs log f (and has values $-1 \leq n \leq 1$). If n = 0, the CPE_{dl} behaves like a pure resistor; if n = 1, the CPE_{dl} behaves like a pure capacitor; if n = -1, the CPE_{dl} behaves like an inductor [51].

EIS can be used to characterize the deposition of self-assembled monolayers [52] or polymer films [53] on the electrode surface. For example, *poly*-manganese tetra-aminophthalocyanine (MnTAPc) and *poly*-cobalt(II) tetraaminophthalocyanine (CoTAPc) thin films were electropolymerized on bare gold and glassy carbon electrodes [54]. The electron-transfer characteristics at the surfaces of the different electrodes constructed were probed using EIS as shown in **Figure 1.8**. The GCE electrodes displayed better conductivity than the Au electrodes. The Bode plots showed that the electrode-solution interface is capacitive in nature for both GCE and Au electrodes, although it does not behave like a true capacitor ($\Phi < 90^\circ$).

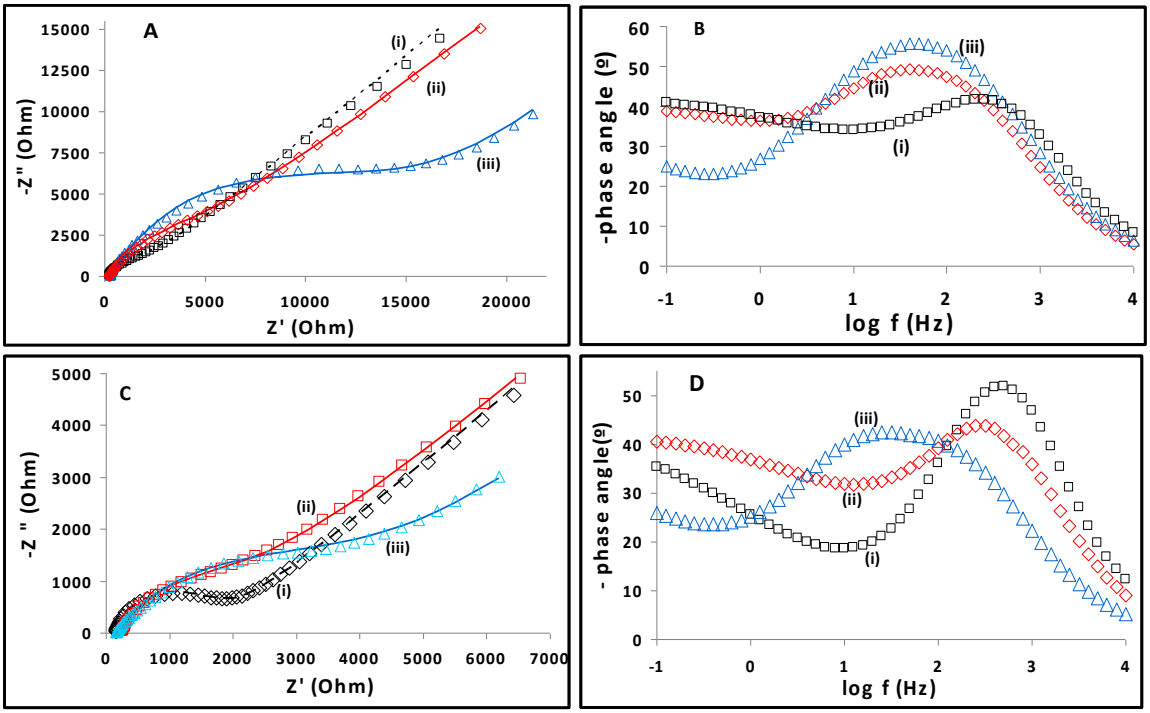

Fig. 1.8 : Nyquist (-Z″ vs Z′) and corresponding bode (-phase angle vs log f) plots (i) bare electrodes (ii) polyCoTAPc and (iii) polyMnTAPc polymer thin films on (A,B) Au and (C,D) GCE electrodes in (1:1) equimolar mixture of 1 mM $K_4[Fe(CN)_6]$ and 1 mM $K_3[Fe(CN)_6]$ solution containing 0.1 M KCl. Applied potential corresponds to $E_{1/2}$ of ferricyanide redox couple [54].

1.1.3.6 X-ray photoelectron spectroscopy

X-ray photoelectron spectroscopy (XPS) is a quantitative spectroscopic surface chemical analysis technique used to estimate the empirical formula or elemental composition, chemical state and electronic state of the elements on the surface (up to 10 nm) of a material. XPS is also known as ESCA, an abbreviation for Electron Spectroscopy for Chemical Analysis. X-ray irradiation of a material under ultra-high vacuum leads to the emission of electrons from the core orbitals. Measurement of the kinetic energy (KE) and the number of electrons escaping from the surface of the material gives the XPS spectra. From the kinetic energy, the binding energy of the electrons to the surface atoms can be calculated. The binding energy reflects

the oxidation state of the specific surface elements. The number of electrons reflects the proportion of the specific elements on the surface [55,56].

XPS can be used to probe the surface of modified electrodes to establish whether a modifying material has been successfully immobilized onto the surface of the electrode or not, and the manner of attachment of modifier to the surface. As an example, a cobalt tetra-carboxylic acid chloride phthalocyanine complex (CoTCAPc) was covalently immobilized on pre-formed mecarptoethanol (ME) self-assembled monolayer on gold (Au) electrode surface, and the resulting modified-electrode surface characterized using XPS [57]. In **Figure 1.9**, the XPS spectra confirm the presence of (i) sulfur(S) on the electrode surface and the formation of the Au-S bond, and (ii) oxygen (O) from –OH group of mercaptoethanol and from the C-O-C and C=O bonds of cobalt tetra-carboxylic acid chloride phthalocyanine.

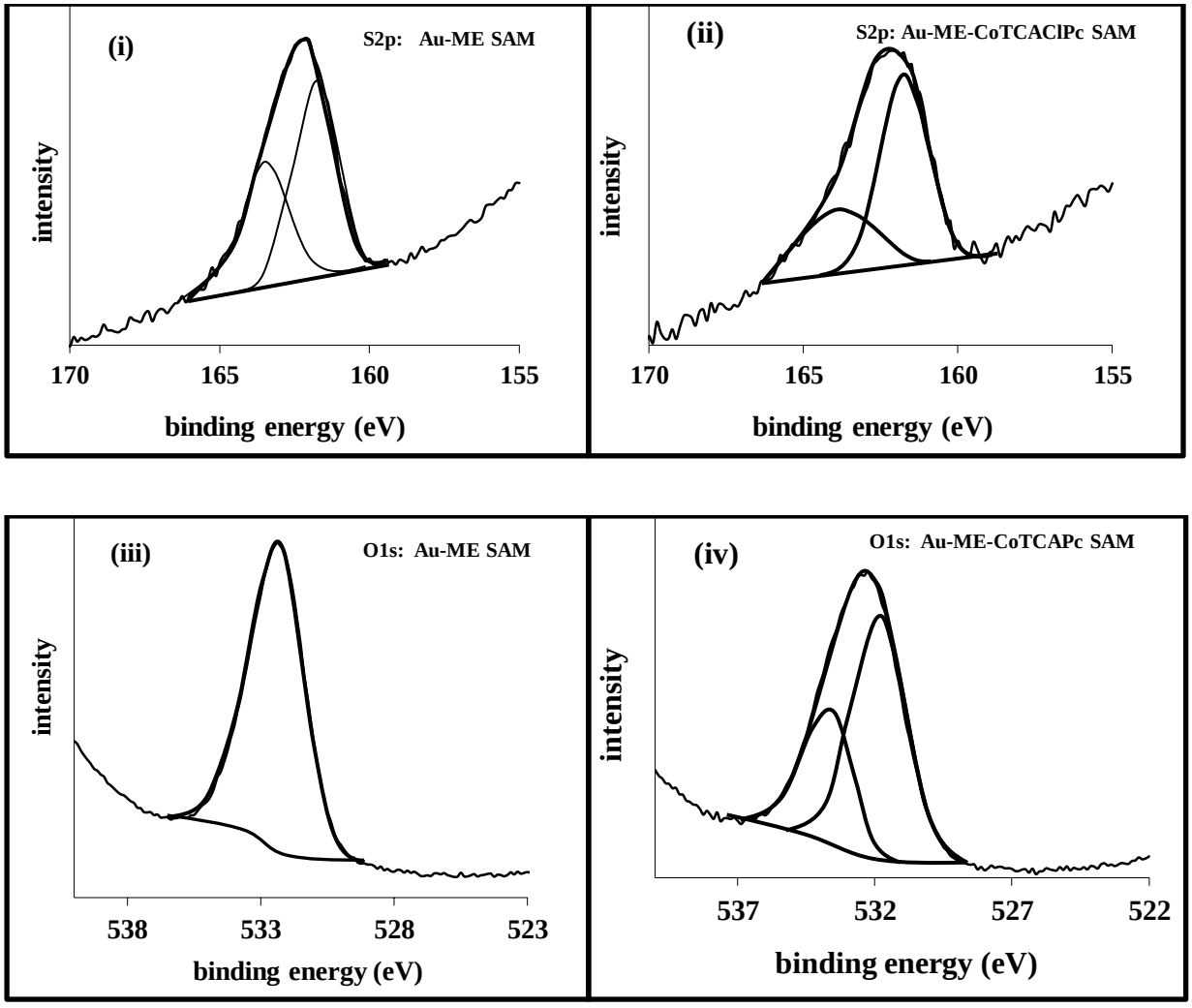

Figure 1.9: XPS spectra of sulfur for (i) Au-ME SAM and (ii) Au-ME- CoTCAPc SAM and oxygen (O1s) for (iii) Au-ME SAM and (iv) Au-ME-CoTCAPc SAM [57].

1.1.3.7 Raman Spectroscopy

The phenomenon of inelastic light scattering is known as Raman radiation and was first documented by Raman and Krishnan in 1928 [58]. When a substance is irradiated with monochromatic light, most of the scattered energy comprises radiation of the incident frequency (Rayleigh scattering). In addition, a very small quantity (0.0001%) of photons with shifted frequency is observed. The fraction of photons scattered from molecular centres with less energy than they had before the interaction is called Stokes scattering. The anti-Stokes photons have greater energy than those of the exciting radiation. Both infrared (IR) and Raman spectra are

concerned with measuring associated molecular vibration and rotational energy changes. However, the requirement for vibrational activity in Raman spectra is not a change in dipole moment, as it is in IR spectra, but a change in the polarizability of the molecule [59,60].

A given vibration then always appears in the same region, its exact position giving information about the local environment of the corresponding bonds, both in the crystalline and amorphous states [61].

A water-soluble sodium salt of cobalt tetra-sulfophthalocyanine (CoTSPc) was used to form a layer-by-layer assembly on a gold substrate pre-modified with poly(diallyldimethylammonium chloride). Raman spectroscopy was employed to confirm that CoTSPc was indeed attached to the gold surface, as shown in **Figure 1.10** [62].

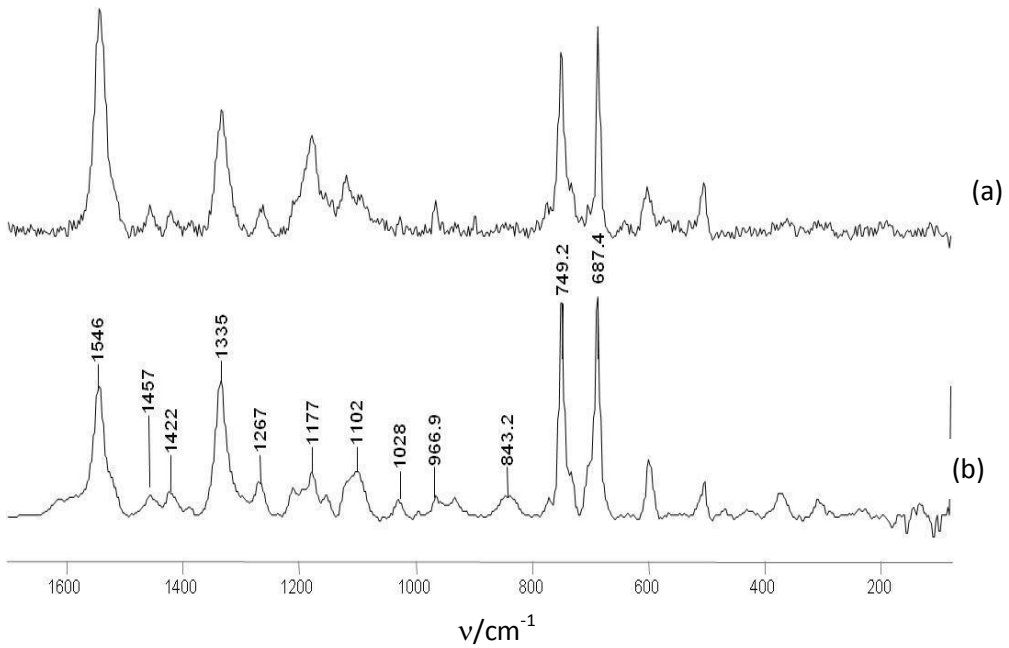

Figure 1.10: Raman spectra of CoTSPc: (a) bulk powder and (b) a monolayer film on a gold substrate [62].

A comparison of the spectrum of the monolayer film on gold with that of bulk CoTSPc powder showed that CoTSPc was attached to the surface.

1.1.4 Aim of this thesis

The aim of this work is to chemically modify carbon paste and pyrolytic graphite electrodes with nanomaterials and metallophthalocyanines, characterize these electrodes using cyclic voltammetry, scanning electron microscopy, transmission electron microscopy, X-ray diffraction, electrochemical impedance spectroscopy, X-ray photoelectron spectroscopy and Raman spectroscopy, and employ them in the electrochemical detection of selected pesticides.

1.2 General Overview of Nanomaterials Employed in this Work.

1.2.1 Carbon nanotubes

Carbon nanotubes (CNTs) were originally reported in 1976 by Orbelin and Endo [63], while two years later Wiles and Abrahamson reported "a thick matt of fine fibres and crystallites" [64]. However, the subsequent rediscovery of CNTs by Iijima in 1991 [65] has led to the current surge in interest in these materials. Since their discovery, CNTs have been used as catalysts in electrochemistry [66], diodes [67], transistors [68], and random access memory cells [69], to name but a few applications. Many other uses for these nanomaterials are still being investigated. The reason for the exploding popularity of CNTs lies in their remarkable electronic and mechanical properties combined with their chemical stability. The two principal forms of CNTs are single walled carbon nanotubes (SWCNTs) and multi walled carbon nanotubes (MWCNTs). Structurally, SWCNTs can be approximated as a "rolled-up" graphite sheet typically 1-4 nm in diameter and several microns in length [69,70], as shown in **Figure 1.11**.

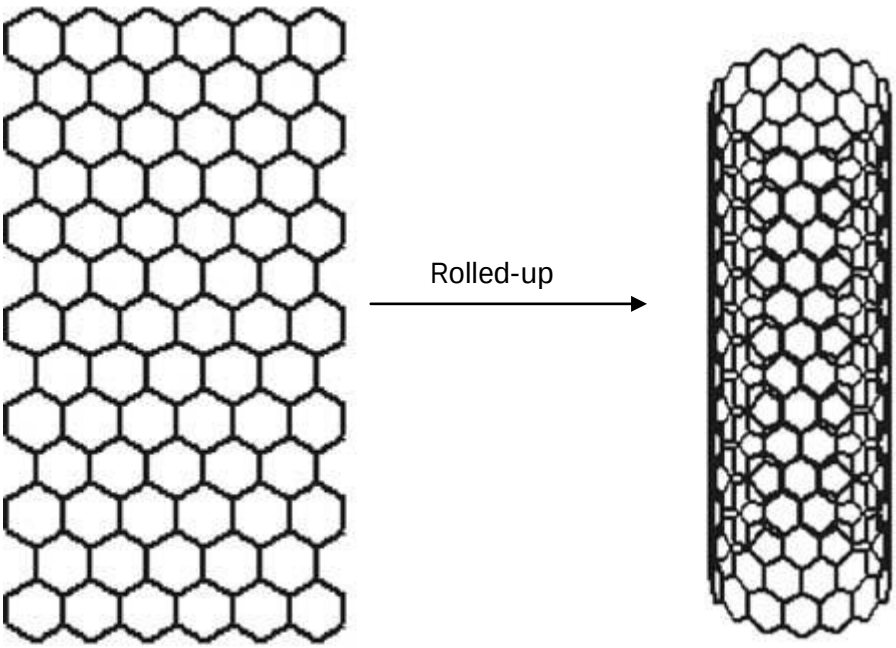

Figure 1.11: Schematic representation of a rolled-up graphite sheet [70]

Multi walled carbon nanotubes (MWCNTs) consist of several concentric tubes of graphene fitted one inside the other and are typically around 2 -25 nm in diameter (**Figure 1.12**) with a separation of about 0.36 nm between the concentric tubes [71]. It has been established that the walls of the MWCNTs are basal plane-like in behaviour, and the ends, edge plane-like.

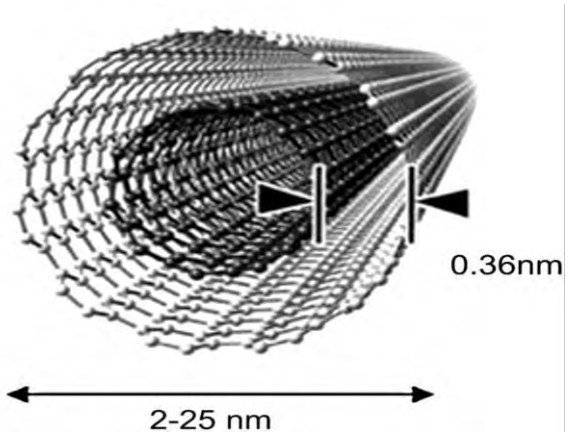

Figure 1.12: a schematic representation of MWCNTs [71].

Various morphological variations of MWCNTs are possible, depending on the conditions and the chosen method of CNT formation (**Figure 1.13**). They can be produced in "hollow-tube" form where the axis of the graphene planes is parallel to the axis of the nanotube, "herringbone" form where the graphene planes are formed at an angle to the axis of the CNT, or finally, in a "bamboo-like" form which is similar to the herringbone form except that the CNTs are periodically closed along the length of the tube into compartments rather like bamboo or a "stack of paper cups fitted one inside the other" [26,72-74].

'bamboo' MWCNTs

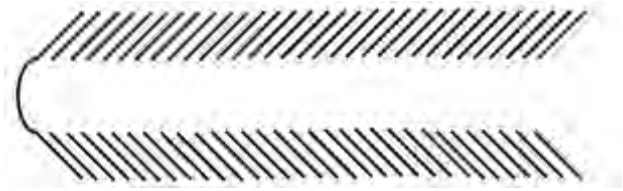

'herringbone' MWCNTs

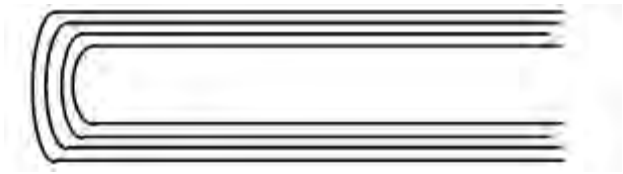

Hollow Tube MWCNTs

Figure 1.13: A schematic cross-section through the various possible morphologies of MWCNTs showing the orientation of the graphene sheets within the tube [26,72-74].

1.2.2 Nanoparticles

In this work bulky phthalocynanine (Pc) powders will be converted to nanoparticles for use in electrocatalysis. Nanoparticles are particles with a size lying in the range 1-100 nm in all three dimensions. They occupy a boundary between atoms and molecules on one side, and bulk (macroscopic) materials on the other. That is, they are much larger than atoms, molecules and ions, but much smaller than physical bodies. Nanoparticles may be individual particles or agglomerates. The location of nanoparticles between macroscopic materials and atoms is responsible for their specific character. From a chemical thermodynamics point of view, macroscopic materials (phases) are usually characterized by internal energy only, whereas only external energy is relevant to the case of atoms or simple molecules. For nanoparticles, both external energy and internal energy are of equal importance [75].

1.2.2.1 Advantages of using nanoparticles in electroanalysis

The preparation and characterization of nanoparticles has attracted a great deal of interest in the past two decades due to their ability to display optical, catalytic and structural properties that are not present in the corresponding isolated molecules and macroscopic materials [76-78]. One example is that of FeAl powder: while the conventional powder is nonmagnetic and brittle, it becomes ferromagnetic and ductile upon being made ultrafine [79]. With regards to electroanalysis, there are four main advantages to the use of a nanoparticle-modified electrode when compared to a macroelectrode [80]: high effective surface area, improved mass transport, catalysis, and control over local environment. Nanoparticle modification of inexpensive material can lead to a larger surface area-to-volume ratio than for the

expensive metal electrode, thus lowering the cost of the electrode. The large effective surface area may also result in a larger number of active sites and often a higher signal-to-noise ratio [81]. The small dimensions of nanoparticles bring about convergent rather than linear diffusion, resulting in a high rate of mass transport to the electrode surface.

The catalytic properties of some nanoparticles can cause a decrease in the overpotential needed for a reaction to become kinetically viable, producing voltammetric scans which appear to be more reversible than that displayed by the same material in a macroelectrode form. It has been shown [82] that modification of an electrode with gold nanoparticles results in a separation of the dopamine and ascorbic acid oxidation peaks, a phenomenon that is not observed when a bulk gold electrode is employed. To explain this observation, it has been suggested that modification with gold nanoparticles increases the catalytic behaviour of the electrode towards the dopamine oxidation reaction, which causes separation of the dopamine and ascorbic acid oxidation peaks.

The catalytic effects of some nanoparticles have been shown to be closely connected to the structure of their local microenvironment. It has been found [83] that addition of albumin to a preparation of gold nanoparticles led to a better dispersion of the nanoparticles in a carbon paste electrode, which increased the sensitivity of the electrode to hydroquinone and dopamine because electron transfer was better promoted.

1.2.2.2 Synthesis of Pc nanoparticles

Some of the methods used in the preparation of metallophthalocyanine nanoparticles (nanoMPcs) are discussed below. Such particles are used in this work. Only the first method was employed in this work although two methods are described.

(i) The reprecipitation method

In the reprecipitation method, a surfactant is added to a solvent in which the solubility of the Pc is poor. An acid solution of the Pc is then added to the solvent with vigorous stirring at low temperatures to produce the nanoparticles. For example, nanoparticles of oxovanadium phthalocyanine (VOPc) were prepared by dispersing a concentrated sulphuric acid solution of VOPc in water containing hexadecyltrimethyl ammonium bromide ($C_{16}H_{33}N(CH_3)_3Br$) under vigorous stirring at 0-5°C [84-88]. A colloidal solution of VOPc nanoparticles was obtained and washed to neutral with water. By changing the surfactant and the concentration of VOPc in concentrated sulphuric acid, VOPc nanoparticles with different particle sizes were prepared. This method was employed in this work for the production of FePc, CoPc, MnPc, and NiPc nanoparticles (FePcNPs, CoPcNPs, MnPcNPs, and NiPcNPs).

(ii) The laser ablation method

In this method, the Pc is suspended in a solvent in which it does not dissolve, and exposed to a laser beam. For example, when VOPc crystalline powders were suspended in water by sonication, an opaque mixture was observed. When the mixture was exposed to laser pulses, the solution became blue and transparent. It was then confirmed by UV-spectroscopy that the blue solution is a colloidal solution of VOPc nanoparticles [89].

The laser ablation method realizes the production of ultra-pure nanoparticles without any toxic substances, which allows for the functionalization of the nanoparticle surface. A recent refinement of the method involves the use of ultra-short femtosecond (fs) pulsed laser radiation [90]. Such ablation allows for a much better control of the size and dispersion of nanoparticles produced in water by changing the radiation intensity [91]. **Table 1.1** contains a list of Pcs which have been produced in nanosized form, and the analytes electrocatalysed [84-88, 92,93].

As the table shows, very little electroanalysis work has been done with nanoMPcs on their own, and the listed nanoMPcs have not been used in the analysis of pesticides. Secondly, a combination of MPc nanoparticles and carbon nanotubes has been used only once in electrocatalysis [94], and the method was not used in the analysis of pesticides.

Table 1.1: List of MPcNP complexes and their uses in electrocatalysis. The electrodes employed are also included.

nanoMPc catalyst	**Electrode material**	**Use in electrocatalysis**	**Reference**
VOPc	No electroanalysis, nanoparticles are characterized		84
ZnPc and NiPc	Carbon paste electrode	To monitor hydrogen evolution	85
CoPc	Glassy carbon electrode	Ascorbic acid detection	86
CoPc	Pyrolytic graphite electrode (modified with the nanoCoPc and glucose oxidase	Glucose biosensor development	87
CoPc	Glassy carbon electrode (modified with nanoCoPc and graphene)	Electrochemical reduction of tert-butyl hydroperoxide	88
CuPc	No electroanalysis, nanoCuPc dispersed in thin polystyrene films.		92
CuPc	No electroanalysis, CuPc nanoparticles are characterized		93

1.2.3 Aim of this thesis

Very little work has been done on the modification of carbon electrodes with MPcNPs, therefore one of the aims of this thesis is to use MPcNPs as modifiers in carbon paste electrodes. Also, not much has been done on the modification with a combination of MPcNPs and carbon nanotubes, therefore in this work a combination

of MPcNPs and multiwalled carbon nanotubes will be used to modify a pyrolytic graphite electrode.

1.3 General Properties of Metallophthalocyanines (MPcs)

Metallophthalocyanines (MPcs) were discovered by accident in 1928 during the course of industrial production of phthalimide at the Grangemouth plant of Scottish Dyes Ltd, which later became of Imperial Chemical Industries [95,96]. MPcs are planar, 18 π-electron macrocyclic aromatic compounds consisting of four isoindole subunits linked together by aza nitrogen atoms [97] (see **Scheme 1.1**).

A wide range of metals and metalloids, ranging from the groups I and II to the lanthanides and actinides [98-102], can be introduced to the central cavity of the phthalocyanine (Pc).

1.3.1 Synthesis of metallophthalocyanines

There are a number of different routes [103,104] for the preparation of metallophthalocyanine complexes (**Scheme 1.1**). The commonly used routes are:

(i) The reaction a mixture of metal salt (or metal), phthalic anhydride and urea in a refluxing solvent in the presence of a catalyst (route 1). This route requires inexpensive starting materials, thus making it the preferred route for large-scale production of MPc complexes [95].

(ii) The phthalonitrile route (route 2), on the other hand, is expensive but gives high purity products. Thus, the phthalonitrile route is used in the synthesis of MPcs used for technology applications where high quality and high purity, rather than cost, are the major considerations.

(iii) Metallophthalocyanines can also be synthesized by the reaction of, o-cyanobenzamide (route 3) with metal salts in high boiling solvents [105].

(iv) The other synthesis route for MPcs is that of the reaction of diiminoisoindoline with metal salt, urea, catalyst and solvent (route 4). There are other methods which will not be discussed here.

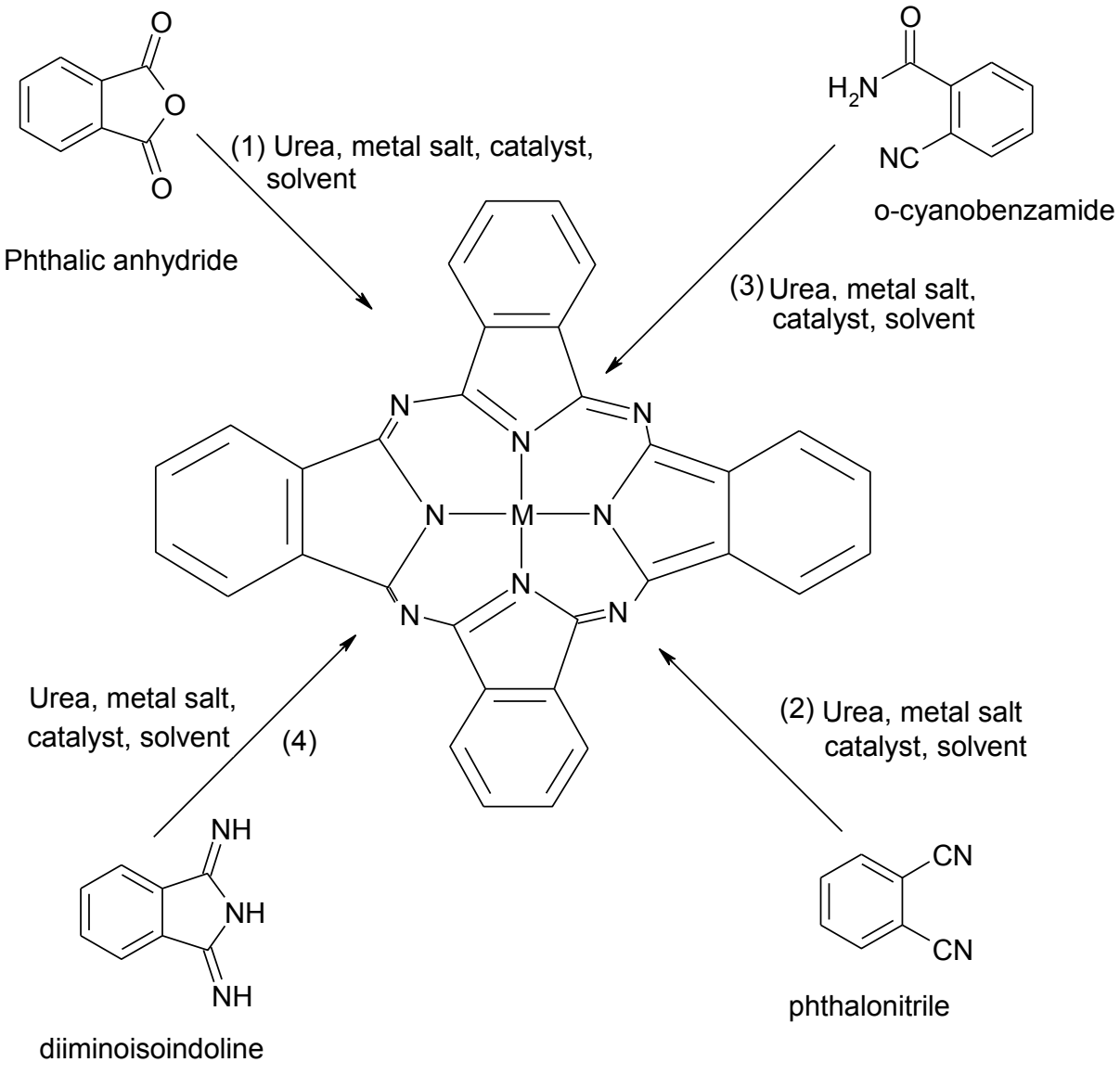

Scheme 1.1: Synthesis of MPc using different precursors as starting materials

MPc complexes may also be synthesized through the use of micro-wave irradiation [106,107]. The microwave method is fast and eliminates the use of solvents. Due

to strong intermolecular cohesion, most unsubstituted MPcs are non-melting, insoluble solids. However, the introduction of substituents on the Pc rings dramatically changes their basic properties, such as electrochemistry and solubility [108-113]. A substituted MPc complex is obtained by cyclotetramerization of the appropriate substituted phthalonitrile derivative, thereby making it possible to introduce up to four substituents into each of the four benzo subunits. For example, the soluble, peripherically octasubstituted MPc ($MPcR_8$, where R = substituent) complexes are normally synthesized from the disubstituted phthalonitrile (**Scheme 1.2**) and the metal salt [111,114].

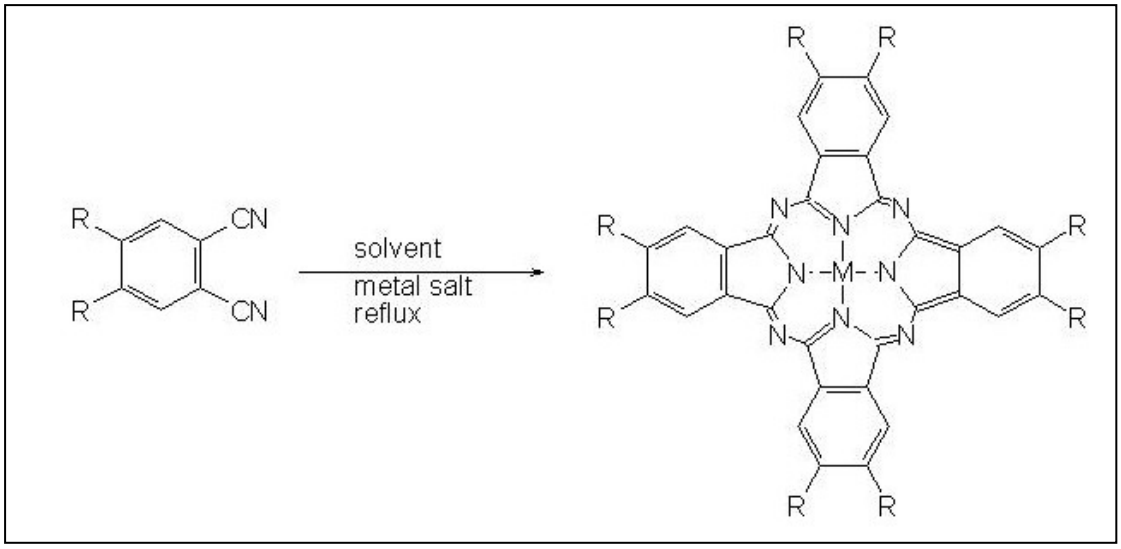

Scheme 1.2: Synthetic route for peripherically octasubstituted MPcs from substituted phthalonitrile.

Water-soluble MPc complexes are obtained by the introduction of sulphonic, carboxylic, or phosphoric acid groups on the annellated benzene rings [115]. Axial ligand substituents can be introduced onto an appropriate central cation (e.g. SiPc) held within the central cavity of the MPc [116,117].

1.3.2 Electronic absorption spectrum of MPcs.

Metallophthallocyanine complexes show a number of strong characteristic absorptions in the visible and ultraviolet regions. **Figure 1.14** shows the ultraviolet/visible (UV/Vis) absorption spectrum of a typical metallophthalocyanine.

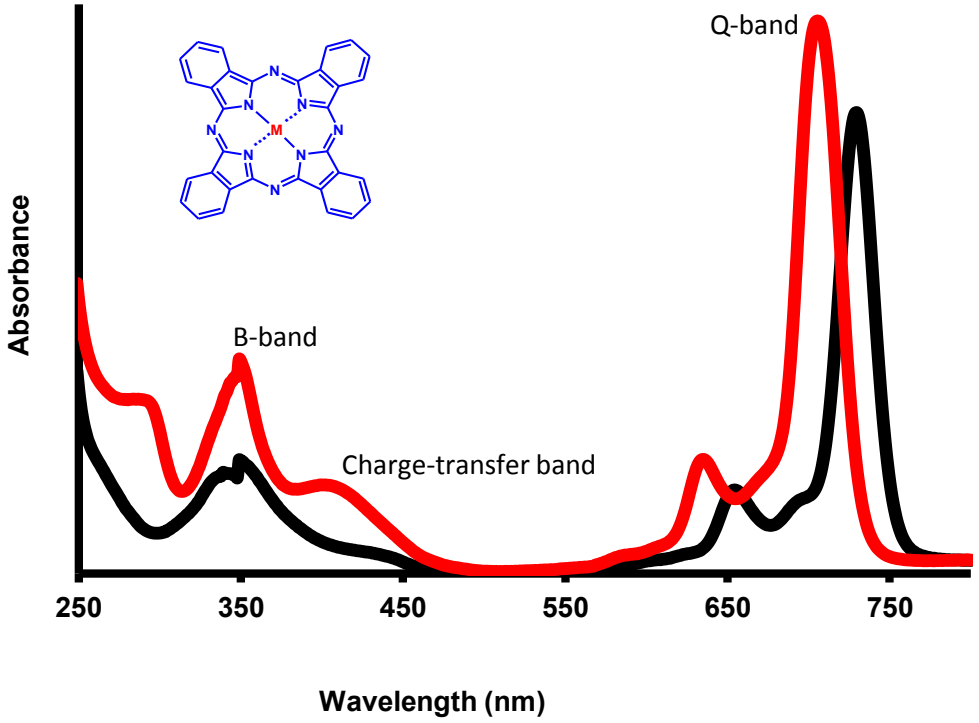

Figure 1.14: Typical UV/Vis spectrum of a MPc

This spectrum is characterized by distinct bands which arise primarily from the π to π* transitions within the delocalized phthalocyanine ring system. The isolated band in the far-red end of the visible region, which appears around 670-800 nm region is known as the Q band. The less intense band in the blue end of the UV region (near 300 – 370 nm) is called the B (or Soret) band, which is a result of a superimposition of two bands, B1 and B2 [118-120]. The origin of these first two π-π* transitions is depicted in **Figure 1.15.**

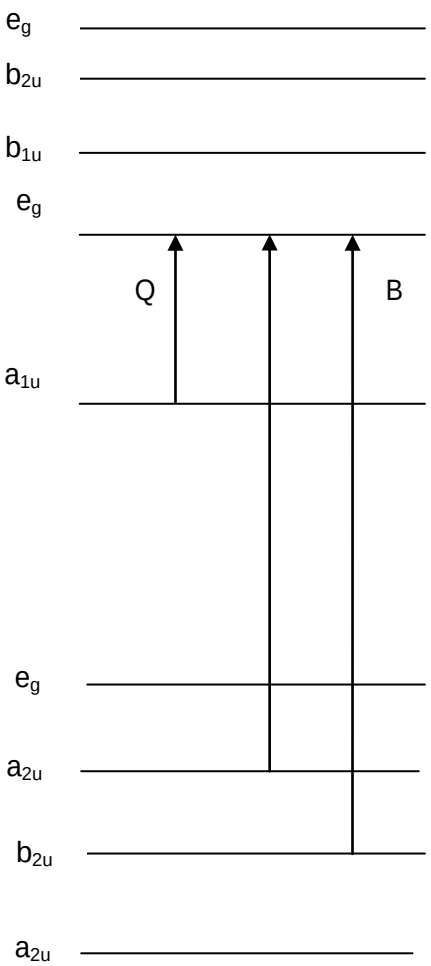

Figure 1.15: The origin of the Q and B absorption bands of phthalocyanines.

According to Gouteman's four orbital model [121], the spectra of MPc complexes are due to transition of electrons from the highest occupied molecular orbital (HOMO) of π nature to the lowest unoccupied molecular orbital (LUMO) of π^* nature. The Q and B bands arise from electronic transitions from the HOMO $a_{1u}(\pi)$ (Q band), and $a_{2u}(\pi)$ and b_{2u} (B band) to the LUMO, e_g orbital [120], Figure 1.15.

Additional absorptions that are seen in the spectra of MPc complexes have been assigned to charge transfer (CT) transitions. With the exception of d^0 or d^{10} metals, CT transitions, either metal to ligand (MLCT) or ligand to metal (LMCT), can be

expected to occur as weak bands between the Q and B bands, normally in the 400-500 nm region [120,122,123,]. As an illustration, **Figure 1.16** shows the possible symmetry allowed transitions for a low spin d^6 metal complex [120].

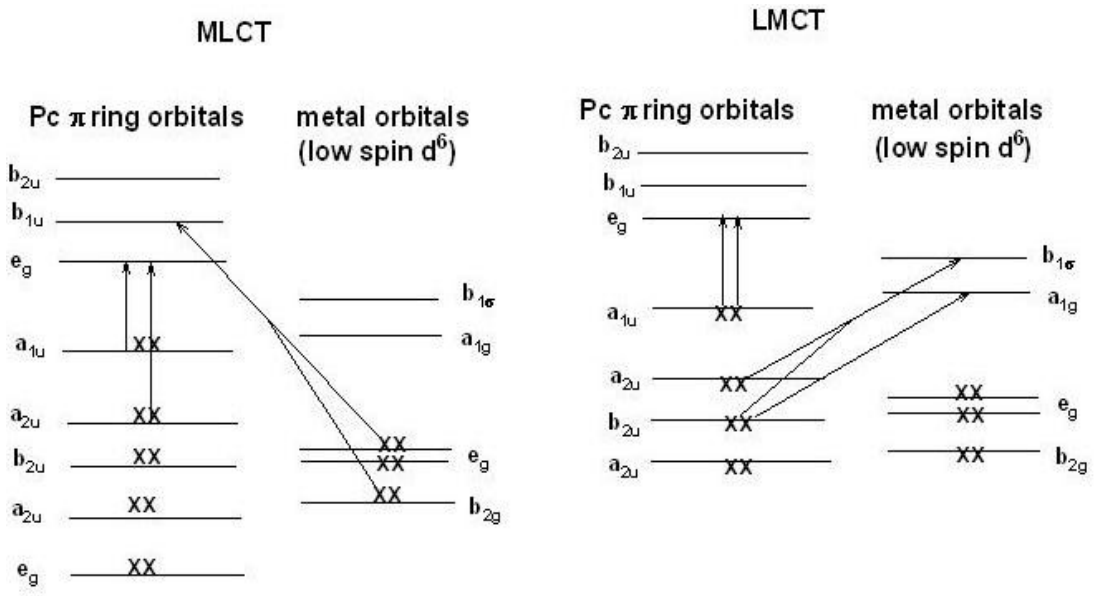

Figure 1.16: Charge transfer transitions between the metal and the Pc ring

A nomenclature proposed by Platt and his co-workers [124] is generally used to describe the bands in the UV/Vis region of MPc spectra. Additional bands (N, L and C) have been identified in the UV region of the absorption spectra of MPcs, in transparent solvents such as dichloromethane.

MPcs form aggregated species in solution. There are three major ways [120] by which MPcs may form dimeric (or polymeric) species:

(i) direct linkage or bridge between two or more Pc rings whose rings are close enough in space to allow intermolecular association [125].

(ii) covalent bonding involving the metal as μ-oxo links, especially for Fe and Si containing Pcs [126].

(iii) sandwich-type complex formation, whereby two Pc rings share one central metal [127-129].

Aggregation results in spectral effects such as broadening of bands, blue or red shifting of the Q band and the splitting of the Q band.

1.3.3 Electrochemical behaviour of metallophthalocyanines

The MPc ring carries two negative charges in its common oxidation state, designated as Pc^{-2} [130]. Reduction and oxidation reactions can occur at either the Pc ring or central metal or both. Oxidation at the Pc ring in MPc^{-2} occurs by successive loss of one or two electrons from the HOMO resulting in the formation of the $[MPc^{-1}]^{+\cdot}$ and $[MPc^{0}]^{2+\cdot}$ cation radicals, respectively. The formation of $[MPc^{-1}]^{+\cdot}$ creates a hole in the $a_{1u}(\pi)$ level, thus permitting an allowed transition from the low-lying $e_g(\pi)$ level. The presence of $[MPc^{-1}]^{+\cdot}$ is normally characterized by a loss of intensity in the Q band, formation of weak bands in the 700 – 825 nm region, and a broad band near 500 nm. The band around 700 nm is usually associated with the dimerization of the radical species [131-136]. Reduction of the Pc ring occurs by the successive gain of one to four electrons by the LUMO of the MPc complex, resulting in the formation of MPc^{-3}, MPc^{-4}, MPc^{-5} and MPc^{-6} species [120, 137-147]. **Figure 1.17** shows the energy level diagram for one-electron ring reduced or ring oxidized MPc complex.

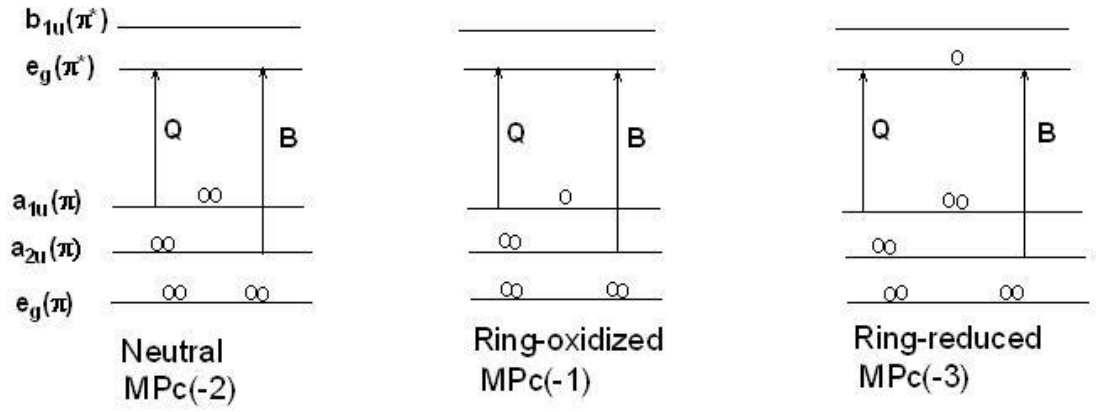

Figure 1.17: A simplified energy level diagram of ring-oxidized and ring-reduced metallophthalocyanine species

Cyclic voltammetry provides a rapid assessment of the electrochemical properties of MPc species, such as establishing whether the electron transfer process is electrochemically reversible or not, and whether there are coupled chemical reactions involved. On a broader scale, ring reduction processes are often electrochemically reversible, while ring oxidation processes, especially those associated with MPc(0)/MPc(-1), are often irreversible.

The central metal ion of the MPc may or may not undergo redox processes, depending on its position on the Periodic Table. Transition metal MPcs whose metal ions have no accessible d-orbital levels lying in the HOMO-LUMO gap (e.g. ZnPc) and main group MPcs (e.g. MgPc) are redox inactive with respect to their metal centers [148-151]. For these complexes, all redox processes occur exclusively on the Pc ring. For main group MPcs, the first ring oxidation is separated from the first ring reduction by approximately 1.6 V. This potential difference corresponds to the magnitude of the difference between the HOMO and the LUMO [120,148].

On the other hand, redox active transition metal MPcs (e.g. FePc, CoPc and MnPc complexes) have the d-orbitals of the central metal lying within the HOMO-LUMO

gap. The redox properties for these species occur both on the Pc ring and on the central metal depending on factors within the environment of the MPc such as the nature of the axial ligand, solvent, electrolyte and ring substituents [119,122,152-154]. Metal oxidation or reduction is characterized by a shift in the Q band without much reduction in intensity [155].

1.4 Electrocatalysis

1.4.1 Using cyclic voltammetry.

Electrocatalysis using cyclic voltammetry is characterized by an enhancement of either the cathodic or anodic currents, or an absence of a reverse peak, and/or a shift in redox potentials to lower values [2]. Hypothetical cyclic voltammogramms showing the electrocatalytic behaviour of a catalyst (Ct) towards the oxidation of an analyte (A) are shown in **Figure 1.18**.

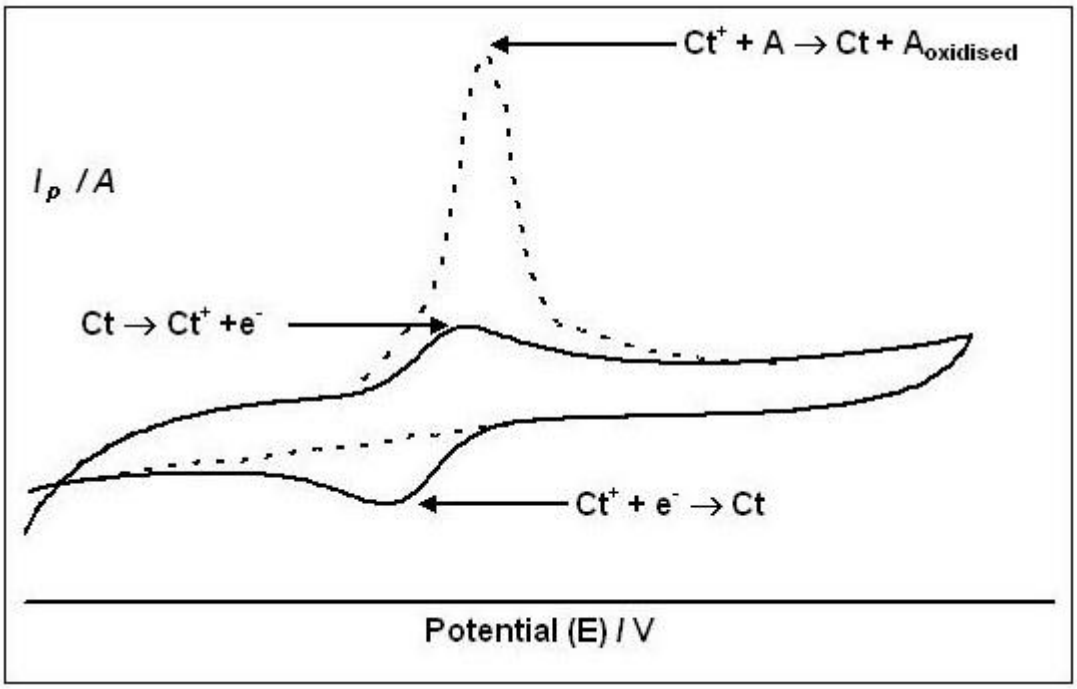

Figure 1.18: Cyclic voltammogram showing electrocatalytic behaviour.

1.4.2 Using chronoamperometry

In chronoamperometry, a potential step is applied, and the current response and its variation with time registered. A potential step is a change in potential from a value where there is no electrode reaction to a value where all the electroactive species that reach the electrode surface react. The solution is not stirred, and the potential step usually crosses the formal potential of the analyte. This gives rise to a diffusion-limited current whose value varies with time. The Cottrell equation (equation 1.8) relates the diffusion-limited current to the time, t, elapsed.

$$I(t) = \frac{nFAD^{\frac{1}{2}}c}{(\pi t)^{\frac{1}{2}}} \qquad \textbf{1.8}$$

where n = number of electrons transferred, F = Faraday constant, D = diffusion coefficient, A = geometrical area of the electrode, c = concentration of solution, and t = time interval. The current decreases with $t^{1/2}$, and a Cottrell plot of I(t) against t results in a graph with the shape shown in **Figure 1.19** [4].

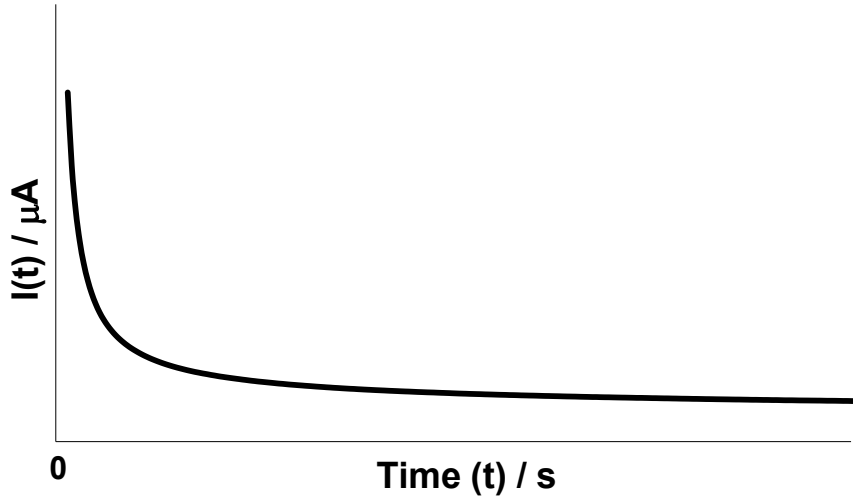

Figure 1.19: Variation of current with time according to the Cottrell equation.

When the potential is stepped to a potential that either oxidizes or reduces the analyte, a current begins to flow at the electrode. This current is quite large at first, but it rapidly decays as the analyte near the electrode surface is consumed, and a transient signal is observed. Chronoamperometry can be used to evaluate the catalytic rate constant (k) for an electrocatalysed oxidation or reduction of an analyte in solution. Equation 1.9 [156]:

$$\frac{I_{cat}}{I_L} = \pi^{1/2}(kC_0t)^{1/2} \qquad \textbf{1.9},$$

where I_{cat} and I_L are the currents of the catalyst-modified working electrode in the presence and absence of the analyte, respectively, C_0 is the bulk concentration of the analyte, and t represents the time interval where I_{cat} is dominated by the rate of oxidation or reduction of the analyte [156], can be used to determine the catalytic rate constant (k). This is done by plotting I_{cat}/I_L against $t^{1/2}$ and evaluating k from the slope of the straight line obtained.

1.4.3 Using electrochemical impedance spectroscopy

The rate of electron transfer at the electrode surface is expected to increase when a catalyst is attached to the bare surface. That is, the electron-transfer resistance (R_{et}) at the electrode surface should decrease when a catalyst is used as the modifier. The semi-circle diameter (= R_{et}) in the Nyquist plot discussed earlier is expected to be smaller when an electrode is modified with a catalyst than when it is bare. Therefore, a comparison of the semi-circles obtained from the bare and modified electrodes determines whether the modifier is a catalyst or not. Depending on the efficiency of the catalyst, R_{et} can be so low (that is, the rate of electron transfer so high) that it is insignificant when compared to Z_W, the Warburg

impedance due to diffusion of the ions of the redox probe through the solution. In that case, the Nyquist plot obtained is a 45° straight line through the origin, as explained earlier [50].

1.4.4 Use of MPcs in electrocatalysis

Metallophthalocyanines have the ability to gain or loose many electrons and still retain their molecular structure and stability [157] due to their dual donor π-acceptor function. This property accounts for their ability to exhibit electrocatalytic activity towards various technologically important redox reactions ranging from use in organic synthesis, removal of waste from water, to detection of low concentrations of compounds [158,159]. The electrocatalytic activity is believed to be mediated by the metal and/or the ring [33,115,157,160,161] because electrocatalytic activities are generally observed at potentials close to those of the metal and/or the ring [161,162]. The catalytic activity of the MPc complex largely depends on the particular central metal and the total oxidation state of the complex as well as the presence of substituents on the MPc backbone [115].

The established mechanism [33,157,163-165] of electrocatalysis by MPcs is believed to be a two-step process initiated by the electrochemical oxidation of the central metal or the ring, followed by the transfer of electrons from the species being oxidized to the metal or the ring, regenerating the initial catalyst. Equations 1.10 and 1.11 show that the mechanism for metal-based electrocatalytic oxidation of an analyte:

$$M^{II}Pc^{-2} \rightarrow M^{III}Pc^{-2} + e^{-} \qquad \textbf{1.10}$$

$$M^{III}Pc^{-2} + A \rightarrow M^{II}Pc^{-2} + A_{ox} \qquad \textbf{1.11}$$

where A is the analyte of interest and A_{ox} is the oxidation product of A. Similarly, equations 1.12 to 1.14 describe the mechanism for a ring-mediated electrocatalysis [163].

$$MPc^{-2} \rightarrow [MPc^{-1}]^{+} + e^{-} \quad \textbf{1.12}$$

$$2[MPc^{-1}]^{+} \rightarrow ([MPc^{-1}]^{+})_2 \quad \textbf{1.13}$$

$$([MPc^{-1}]^{+})_2 + 2A \rightarrow 2MPc^{-2} + 2A_{ox} \quad \textbf{1.14}$$

In this work MPcs (in bulky and nanosized form) have been combined with multiwalled carbon nanotubes and employed in electroanalysis. **Table 1.2** lists MPc's that have been used in combination with carbon nanotubes (single-walled and multi-walled), and the analytes involved [166-205]. The electrodes used are also included.

From **Table 1.2** it is clear that combinations of MPcs and SWCNT (composite or linked) have been employed extensively in electrocatalytic determination of analytes of interest, including pesticides and herbicides, although nanosized MPcs and SWCNT have been used only once before [187]. It is also clear from the table that a combination of MWCNT and MPcs (bulky) has rarely been used for pesticide electroanalysis, with carbaryl [195] being the only pesticide analysed. Again, a combination of nanosized MPcs and MWCNTs has been employed only once before [193], but not for pesticide determination. It is also clear that even though the analysis of amitrole has been reported on SWCNTs/Pc conjugates, there have been no reports on asulam. There have also been no reports on the analysis of amitrole and asulam on MWCNTs/Pc conjugates.

Table 1.2: List of MPc-CNT complexes and the analytes whose oxidation or reduction they catalyse.

MPc + CNT[a]	**Electrode**	**Analyte**	**Reference**
CoTCPc-SWCNT	GCE	Diuron	166
TaPc-SWCNT	Gold disk electrode	Bisphenol A	167
CoMCPc-SWCNT	GCE	**Amitrole** and diuron	168
CoPc-SWCNT and NiTSPc-SWCNT	GCE	2-mercaptoethanol, nitric oxide	169
NiTAPc-SWCNT	GCE	2-mercaptoethanol	170
CoTAPc-SWCNT	GCE	2-mercaptoethanol	171
PdPc-SWCNT		4-nitrophenol	172
CoTOBPc-SWCNT	GCE	**Amitrole**	173
CoPc-SWCNT	GCE	Hydrazine	174
CoTAPc-SWCNT and Mn(OH)TAPc-SWCNT	Screen-printed gold electrode	H_2O_2	175
PbPc-SWCNT		NH_3 gas	176

FePc-SWCNT	Gold electrode		177
FeOHETPc-SWCNT-Cys	Gold electrode	Thiocyanate	178
CoTAPc-SWCNT-AET	Gold electrode	Dopamine	179
CoTAPc-SWCNT-Cys	Gold electrode	Epinephrine	180
CoMAPc-SWCNT	GCE	**Amitrole**	181
FeTAPc-SWCNT	GCE	**Amitrole** and diuron	182
CoPc-SWCNT	Screen-printed electrode	Thiocholine	183
CoTAPc-SWCNT	Basal plane pyrolytic graphite (BPPGE)	DMAET (dimethylaminoethanol) and DEAET (diethylaminoethanol)	184
CoTCPc-EA-SWCNT	GCE	**Amitrole**	185
CoOBCPPc-SWCNT	GCE	NADH	186
nanoFePc-SWCNT	Au electrode	H_2O_2	187
CoTAPc-MWCNT	GCE	H_2O_2	188

CoPc-MWCNT	GCE	Bisphenol A	189
CoPc-MWCNT	GCE	Ascorbic acid	190
CoPc-MWCNT	CPE	Epinephrin	191
PbPc-MWCNT	Gold electrode	NH_3 gas	42
nanoFeTSPc-MWCNT	GCE	Dopamine	192
CoPc-MWCNT, CuPc-MWCNT	Thin film (no electrode)	H_2O_2	193
CoPc/MWCNT	GCE	Carbaryl	194
CoPc/MWCNT	GCE	Oxygen reduction reaction	195
FePc/ Amino-MWCNT	GCE	Oxygen reduction reaction	196
CoPc/MWCNT	MWCNT/CoPc paste	Guanine (nucleic acid base)	197
CoPc/ MWCNT/PAMAN	GCE	DNA biosensor	198
FeOBSPc/MWCNT and CoOBSPc-MWCNT	EPPGE	Oxygen reduction reaction	199
CoPc/ MWCNT	GCE	Phenolic compounds after benzene oxidation	200
FePc/MWCNT/PEDOT	GCE	Nitrite	201

FePc/MWCNT	GCE	Dopamine (in the presence of serotonin)	202
CoTtBPc/MWCNT	GCE	Oxygen reduction	203
Nafion/GOD/poly-NiTSPc/MWCNT	GCE	Glucose biosensor	204
PtFeOCPc-MWCNT	EPPGE	Oxygen reduction reaction	205

[a] CoTCPc=Co(II)tetracarboxy phthalocyanine, TaPc=Tantalum phthalocyanine, CoMCPc=Co(II)-tris(benzyl-mercapto)-mono(carboxy phenoxy)-phthalocyanine, CoTOBPc=2,(3)-tetra-(4-oxo-benzamide) phthalocyaninato Cobalt(II), FeOHETPc=octa(hydroxyethylthio) pthalocyaninato iron(II), AET=aminoethanethiol, FeTSPc=iron tetrasulphophthalocyanine, CoMAPc=Cobalt(II)-tris(benzyl-mercapto)-monoaminophthalocyanine, PAMAN=poly(amido amine), OBSPc=octabutylsuphonyl phthalocyanine, PEDOT=poly(3,4-ethylenedioxytheophene), CoTtBPc=cobalt(II)tetra-tert-butylphthalocyanine, GOD=glucose oxidase

1.4.5 Aims of this work

One of the aims of this work is to modify electrodes with a combination of metallophthalocyanines (in their normal bulky, powdered form or nanosized) and multiwalled carbon nanotubes, and employ such modified electrodes in the electrocatalytic determination of pesticides. The use of metallophthalocyanine nanoparticles and multiwalled carbon nanotubes as electrocatalysts in pesticide analysis is rare, and this study aims to contribute to the body of work in this field.

1.5 Overview of Analytes Used in this Work.

1.5.1 Amitrole

Amitrole (3-amino-1,2,4-triazole, also known as aminotriazole) **(Figure 1.20)** is a non-selective herbicide that is widely used as an industrial herbicide to control weeds along road and railway tracks and also in agriculture, in mixed formulations with other chemical agents [206]. Its low volatility and excellent solubility in water make it a potential contaminant to ground and drinking water [207,208]. The scarcity of data on amitrole in environmental water is explained by the difficult determination of this compound at trace levels in water, because there is no efficient procedure that allows its extraction from aqueous samples.

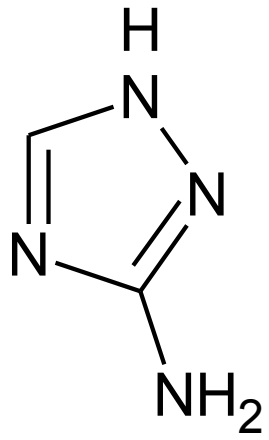

Figure 1.20: Structure of amitrole

Amitrole causes alveolar damage due to inhalation [209], and is a carcinogernic agent in animals [210]. The Environmental Protection Agency (EPA) of the United States of America cancelled the use of this herbicide for food crops in 1971 [211].

Different high performance liquid chromatography (HPLC) methods have been described in the literature [212, 213] to determine amitrole derivatives. Due to the

high polarity of this compound, its determination by reversed-phase HPLC with the usual aqueous phases is not possible, since the resolution between the amitrole and solvent peaks is poor [214]. Determination of amitrole by gas chromatography is also difficult, owing to its high polarity and low volatility. Since amitrole is ionized at low pH, ion-exchangers can be used for its extraction from water. However, the presence of inorganic cations causes a rapid solution of amitrole in drinking water, even after the standard chemical pretreatment to remove these cations before the extraction [215-217]. The presence of amitrole in plants can also be detected by using fluorescence techniques [218]. Paper chromatography and thin layer chromatography (TLC) have also been used for a quantitative estimation of amitrole [219]. The major draw-back of all these methods is that preliminary extraction and concentration from the aqueous medium is necessary before trace amounts of amitrole can be quantitatively determined.

Previously, amitrole has been determined by electrochemical detection after chromatographic separation [213]. In this method, a gold disk electrode was used as the working electrode, and the oxidation potential for amitrole was 0.225 V. Direct electrochemical detection of amitrole using electrodes modified with MPcs alone or in combination with carbon nanotubes is a recent, attractive development (see [168,173,181,182,185] in **Table 1.2**). Surprisingly, detection of amitrole with electrodes modified with MPc complexes alone is very rare, although these complexes are known for their electrocatalysing ability. Also, modification of electrodes with a combination of MPcs and MWCNTs has not been attempted before for the purpose of amitrole detection.

1.5.2 Asulam

Asulam (methyl-4-aminophenyl-sulphonylcarbamate) **(Figure 1.21)** is a herbicide used in weed control. It is soluble in water and it can easily migrate from the soil to crops and enter the food chain. Depending on rainfall conditions and soil properties, the herbicide can reach ground waters where, due to the absence of microbial activity, degradation processes are very slow and accumulation phenomena can easily lead to toxic levels [220].

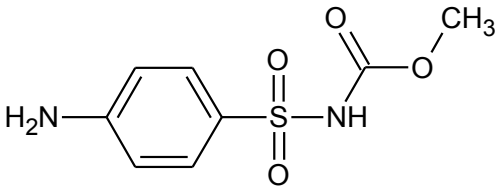

Figure 1.21: Structure of asulam

A recently developed method for the detection of asulam involves the incorporation of dispersive liquid-liquid micro extraction (DLLME) into a micellar electrokinetic chromatograph (MEKC) coupled to a mass spectrometer, and the limit of detection obtained was 1.4 ng/L [221]. Chicharro at al [222] employed the same method, without DLLME, but using a glassy carbon electrode modified with MWCNTs for electrochemical detection. A flow-multicommutation method for the photo-chemiluminometric determination of the herbicide has also been employed [223], and a stopped-flow method based on asulam's inhibiting effect on the horse radish peroxidase-luminol-hydrogen peroxide chemiluminescence reaction [224] has been developed. Other chromatographic and electrophoretic methods that have been used in the past include capillary isotachophoresis [225], electrokinetic capillary chromatography with simultaneous UV and electrochemical detection (in tap water) [226], thin-layer chromatography (TLC) (in soil) [227], HPLC-UV absorption (in

water) [228], HPLC-fluorescence detection in combination with pre-column derivatization with fluorescamine [229], and gas chromatography-mass spectrometry (in water) [230].

Only a few methods involving electrochemical detection have been mentioned in the literature [223,226,231,232], and of these, only one [231], is a strictly electrochemical method that is not combined with other methods. **Table 1.3** shows a list of the electrochemical methods used for asulam detection and the conditions under which they have been used.

Table 1.3: Different electrochemical methods to detect asulam.

Electrode	**Electrolyte**	**Potential/ V**	**Detection Limit**	**Linear range**	**References**
MWCNT-glassy carbon electrode	0.05 M phosphate buffer at pH 7	1.0	----------	----------	223
Glassy carbon electrode attached to a capillary electrophoresis instrument	0.02 M boric acid at pH 8.20 + 0.025 M SDS	0.90	1.7 μM	1.0 – 25.0 $mg.L^{-1}$	226
Glassy carbon electrode	0.3 M Britton-Robinson buffer at pH 1.9	1.20	7.1 μM	1.0 – 9.0 × 10^{-5} M	231
Reticulated vitrous carbon electrode within a liquid chromatography system	Solution of 0.01 M Na_2HPO_4, 0.015 M KH_2PO_4, 0.10 M $NaOOCCH_3$ at pH 7.0 + methanol (1:1)	1.25	----------	----------	232

1.5.3 Aims of this work

Very little work has been done on the electrochemical detection of asulam, and the measuring potentials in the published work are very high. This may result in fouling of the electrode surface. Metallophthalocyanines (bulky or nanosized) have not been used before in the detection of asulam. Although a combination of MPcs with multiwalled carbon nanotubes has been employed before in electrochemical analyses, its use in pesticide analysis is very rare, and in fact, such a combination has not been reported for the detection of asulam. Amitrole (or any other pesticide) has not been determined with nanosized MPcs alone as electrocatalyst, and a combination of nanosized MPcs and multiwalled carbon nanotubes for pesticide analysis has also not been reported.

In this work, as opposed to SWCNTs which have been reported, metallophthalocyanine nanoparticles and multiwalled carbon nanotubes are employed for the first time in the electrochemical detection of asulam and amitrole.

1.6 Summary of Aims

In summary, the aims of this thesis are as follows:

- the chemical modification of carbon paste electrodes with nanoparticles of metallophthalocyanines and the use of the modified electrodes in the detection of amitrole and asulam.
- modification of pyrolytic graphite electrodes with metallophthalocyanine nanoparticles and multi-walled carbon nanotubes, and the use of such electrodes in the detection of amitrole and asulam.

- characterization of the different chemical modifiers and modified electrodes using different methods, to confirm the formation of modifiers and their attachment to the electrode surface.

Chapter 2

Experimental

In this chapter the different experimental methods followed, and materials and equipment used, are presented.

2.1 Materials

Amitrole, asulam, graphite powder (1-2 μm, synthetic), mineral oil (nujol), iron phthalocyanine (FePc), cobalt phthalocyanine (CoPc), manganese phthalocyanine (MnPc), nickel phthalocyanine (NiPc), multi walled carbon nanotubes (length: 5-20μm, diameter: 15 ± 5 nm), potassium chloride, potassium ferricyanide, potassium ferrocyanide, dimethyl sulphoxide (DMSO) and dimethyl formamide (DMF) were obtained from Sigma-Aldrich, SAARCHEM, Fluka or Merck, and were of analytical grade. The DMSO and DMF were dried before use. Iron(II) tetra-aminophthalocyanine (FeTAPc), Co(II)tetra-aminophthalocyanine (CoTAPc), manganese tetra-aminophthalocyanine (MnTAPc) and nickel tetra-aminophthalocyanine (NiTAPc) were prepared by following established procedures [233-235]. Basal plane pyrolytic graphite was obtained from Le Carbone (Sussex, UK), Norton carborundum paper (1200 c) was obtained from Saint Gorbain Abrasives (pty) Ltd, Isando, South Africa. Hexadecyltrimethyl ammonium chloride (CTACl), tetrabutylammonium tetrafluoro borate ($TBABF_4$), disodium hydrogen orthophosphate, sodium dihydrogen orthophosphate, dipotassium hydrogen orthophosphate, potassium dihydrogen orthophosphate, phosphoric acid and sodium hydroxide were of analytical grade and were used as received without further purification. Ultrapure water of resistivity 18.2 W was obtained from a Milli-Q Water System (Millipore Corp., Bedford, MA, USA).

2.2 General Equipment

(1) Electrochemical impedance spectroscopy (EIS) measurements, were performed with an Autolab Potentiostat PGSTAT 30 (Eco Chemie, Utrecht,

The Netherlands) driven by a General Purpose Electrochemical Systems data processing software (GPES, software version 4.9)

(2) X-ray photoelectron spectra (XPS) were recorded with a Physical Electronics model 5400 spectrometer system equipped with an Mg/Al dual source and a small area analyzer with a photon stimulated desorption (PSD) detector. An achromatic Mg K X-ray (1,253.6 eV) source was operated at 300 W. Indium oxide was used as the substrate.

(3) Scanning electron microscopic (SEM) images of the bulk and nano-scaled MPcs were obtained using a JEOL JSM 840 scanning electron microscope at 5 kV accelerating voltage. Solid powder samples were sputtered on a piece of carbon tape which was placed on an aluminium stub sample holder.

(4) Transmission electron microscope (TEM) pictures were obtained using a JEOL JEM 1210 transmission electron microscope at 100 kV accelerating voltage. Sample suspensions were prepared in ultra-pure Milli-Q water or DMF with ultra-sonication for 1 hour.

(5) Shimadzu UV - 2550 spectrophotometer was used to collect UV-Vis spectral data.

(6) X-ray powder diffraction (XRD) patterns were recorded on a Bruker D8 Discover, equipped with a PSD LynxEye detector, using Cu-K_α radiation (λ = 1.5405 Å, nickel filter). Samples were placed on a zero background (511) silicon wafer embedded in a generic sample holder and data recorded within the range $2\theta = 5^o$ to 100^o, scanning at 1^o min^{-1} with a filter time-constant of 2.0 s per step at room temperature. A slit width of 6.0 mm was used in the

measurements. X-ray diffraction data were fitted using Eva (evaluation curve fitting) software, while analysis of data was done using International Center Diffraction Data (ICDD) database.

(7) A Bruker Vertex 70 - Ram II spectrometer (equipped with a 1064 nm Nd:YAG laser and a liquid nitrogen cooled germanium detector) was used to collect the Raman data. The spectral data for the MPcs and the MPcNPs/MWCNT (composite) were obtained in their solid powder forms (using KBr for dilution).

2.3 Activation of graphite

Activation of the graphite leads to generation of carboxylic and/or hydroxyl functionalities at the graphitic carbon surface [15]. Thus, the fragments become markedly hydrophilic and repel hydrophobic molecules of the binder used to make the graphite paste. The activation method used in this work involved washing the graphite with acetone, then with a 1:3 mixture of HCl and HNO_3, and finally with pure distilled water. The graphite sediment was then dried in an oven for 4 h at 400 °C.

2.4 Synthesis of nanoparticles of metallophthalocyanines

The MPc nanoparticles (MPcNPs) were synthesized as described previously for CoPcNPs [85,86,236] with a slight modification. Briefly, 0.15 g MPc was dissolved in 5 ml of 98% concentrated sulphuric acid. The solution was then added drop-by drop into a vigorously stirred 300 mL aqueous solution containing 0.45 g hexadecyltrimethyl ammonium-chloride (CTACl). The resulting solution was centrifugally separated. The obtained sediment was washed repeatedly with water until neutral. It was then vacuum-dried to obtain the MPcNP powder.

2.5 Purification of MWCNTs

The MWCNTs were purified as described previously [237]. Briefly, 1 g of MWCNTs was added to 140 ml of 2.6 M HNO_3, and the mixture was refluxed for 45 h to expel spheroidal fullerenes, amorphous carbon and other unwanted species from the carbon nanotubes. The carbon nanotube sediment, now consisting of purified 'endless' carbon nanotubes, was separated from solution and washed with distilled water. The carbon nanotubes were then cut into smaller pieces by sonication in a 3:1 mixture of H_2SO_4 and HNO_3 for 24 h. To ensure that the carbon nanotubes were chemically clean and molecularly perfect, the sediment of cut carbon nanotube pieces was first washed with distilled water, then the ends of the carbon nanotubes were subjected to further etching by stirring in a 4:1 H_2SO_4/H_2O_2 mixture for 30 min at 70 °C. The carbon nanotubes were then washed again with distilled water. Due to exposure to strong acids in the purication steps outlined above, the carbon nanotube ends are terminated with carboxylic acid groups. The purified MWCNT paste was then air-dried for 48 h.

2.6 Preparation and Modification of Electrodes

2.6.1 Carbon paste electrodes (CPEs)

Mineral oil, activated graphite powder and MPcNPs (M=Fe, Co, Mn, Ni) were mixed in the ratio of 20:77:3 ratio (w/w) thoroughly, to obtain the MPcNP-modified graphite paste. The graphite paste containing MPcNPs was packed firmly into the cavity (d = 3 mm) of a plastic pipette tip. Electrical contact was established with a copper wire. The resulting electrode was denoted as MPcNP-CPE. The electrodes modified with the bulk MPc (MPc-CPE) and carbon paste alone (CPE) were prepared in a similar way. The surface of each electrode was wetted with distilled deionised

water and polished with alumina paper (polishing strips 30144-001, Orion) before use.

2.6.2 Basal plane pyrolytic graphite electrodes (BPPGE)

The BPPGE disk (d =5 mm in Teflon) was fabricated in-house by Rhodes University Chemistry Machinery Workshop. Electrical contact with the disk was obtained via an inserted copper wire held in place with conducting silver varnish L 100 (Kemo® Electronic, Germany). A BPPGE was prepared for use or for further modification by renewing the electrode surface with cellotape [23,238]. This procedure involves polishing an old BPPGE surface on carborundum paper, pressing cellotape on the cleaned BPPGE surface and then removing the tape, along with several layers of graphite. Before use, the electrode was then rinsed in acetone to remove any adhesive. To prepare a carbon nanotube modified BPPGE (MWCNT–BPPGE), carbon nanotubes were abrasively immobilized onto the BPPGE by gently rubbing the electrode on a fine quality filter paper containing the carbon nanotubes [239]. To prepare a BPPGE modified with a MPcNP/MWCNT nanocomposite (M=Ni or Fe), the nanocomposite was first prepared as follows: The MPcNPs were physically attached to the MWCNTs, through a π-π interaction, by mixing 1 mg of MWCNTs with 5 mg of MPcNPs in 10 ml of water, then stirring for 2 h, forming a MPcNP/MWCNT nanocomposite [240]. The MPcNP/MWCNT nanocomposite was separated from solution by filtration and air-dried for 48 h to form a powder. The nanocomposite was then attached to the BPPGE surface in a manner similar to the attachment of the MWCNTs above, to form an MPcNP/MWCNT-BPPGE. A MPcNP-BPPGE was also prepared by attaching MPcNPs to the BPPGE in a similar manner.

A MWCNT-BPPGE was also modified with bulk metal tetra-aminophthalocyanines (MTAPc, M = Co, Fe, Mn, and Ni). To prepare a BPPGE or MWCNT–BPPGE modified with MTAPc, the electropolymerization method [4] was used. Briefly, the BPPGE or MWCNT–BPPGE was immersed in a solution of 1×10^{-3} M MTAPc in dry dimethylsulphoxide (DMSO) containing 1×10^{-2} M tetrabutylammonium tetrafluoroborate ($TBABF_4$) as the supporting electrolyte. The solution was then scanned between pre-determined potential intervals for the different MTAPcs, to effect the electropolymerization. To condition the MTAPc-modified MWCNT–BPPGE (*poly*-MTAPc–MWCNT–BPPGE) or *poly*-MTAPc–BPPGE for use in electrocatalytic studies, the electrode was then immersed in a 0.1M phosphate buffer solution of either pH 4.0 or pH 7.0, and scanned between −1.0 and 1.0V (versus Ag|AgCl) for 50 cycles to obtain a stable cyclic voltammogram.

2.7 Electrochemical Methods

All electrochemical experiments, including cyclic voltammetry (CV), square wave voltammetry (SWV), chronoamperometry (CA), and electrochemical impedance spectroscopy (EIS) measurements were carried out using the Autolab system mentioned earlier. The parameters for the SWV were: step potential 5mV; amplitude 20 mV at a frequency of 25 Hz. EIS measurements were performed between 1.0 Hz and 10 kHz using a 10 mV rms sinusoidal modulation. Chronoamperograms were obtained at an applied voltage of 0.42 V (versus Ag|AgCl for amitrole analyses and 0.65 V (versus Ag|AgCl) for asulam analyses. A conventional three-electrode system was used. The working electrodes used are listed in **Table 2.1**.

Table 2.1: Working electrodes used in electrochemistry experiments

Electrode	**Modifier**	**Method of modification**	**Electrode designation**
CPE	Bulk CoPc, FePc, MnPc, NiPc and the corresponding nanoparticles (CoPcNP, FePcNP, MnPcNP, NiPcNP)	Paste	MPc-CPE or MPcNP-CPE (M = Co, Fe, Mn, Ni)
BPPGE	MWCNT MWCNT/MPcNP (M = Ni or Fe)	Abrasive	MWCNT-BPPGE MWCNT/MPcNP-BPPGE
BPPGE	MWCNT/MTAPc (M = Co, Fe, Mn, Ni)	Polymerization	*poly*-MTAPc-MWCNT-BPPGE or *poly*-MTAPc-BPPGE

A Ag|AgCl wire or Ag|AgCl (3 M KCl) was used as reference electrode and platinum wire was used as the counter electrode. The potential response of Ag|AgCl wire pseudo-reference electrode in aqueous conditions was less than the normal Ag|AgCl (3M KCl) and SCE by 0.15±0.003 V and ~0.01 V, respectively.

Results and Discussion

Publications

Chapter 3

Characterization of MPc nanoparticles (MPcNPs), MPcNP/MWCNT Composites and modified Electrodes.

Chapter 4

Electrochemical analyses with carbon paste electrodes modified with nanoparticles of MPcs.

Chapter 5

Electrochemical analyses with basal plane pyrolytic graphite electrode modified with MWCNT/NiPcNP and MWCNT/FePcNP nanocomposites.

Chapter 6

Electrochemical analyses with basal plane pyrolytic graphite electrode modified with MWCNTs and electropolymerized metal tetra-amino phthalocyanines (MTAPcs).

Publications

The results discussed in the following chapters have been presented in the articles listed below, that have been published in peer-reviewed journals. These articles have not been referenced in this thesis:

1. Electrocatalytic behaviour of carbon paste electrode modified with iron(II) phthalocyanine (FePc) nanoparticles towards the detection of amitrole.

   Msimelelo Siswana, Kenneth I. Ozoemena, Tebello Nyokong, Talanta, 2006, 69, 1136.

2. Electrocatalysis of asulam on cobalt phthalocyanine modified multi-walled carbon nanotubes immobilized on a basal plane pyrolytic graphite electrode.

   Msimelelo Siswana, Kenneth I. Ozoemena, Tebello Nyokong, Electrochimica Acta, 2006, 52, 114.

3. Electrocatalytic Detection of Amitrole on a multi-walled carbon nanotube – Iron(II)tetra-aminophthalocyanine platform.

   Msimelelo Siswana, Kenneth I. Ozoemena, Tebello Nyokong, Sensors, 2008, 8, 5096.

4. Nanostructured nickel (II) phthalocyanine—MWCNTs as viable nanocomposite platform for electrocatalytic detection of asulam pesticide at neutral pH conditions.

   Msimelelo Siswana, Kenneth I. Oezomena, Tebello Nyokong,

   J Solid State Electrochem, 2010, 14, 1351.

Chapter 3

Characterization of MPc Nanoparticles (MPcNPs), MPcNP/MWCNT Composites and Modified Electrodes.

In this chapter, the techniques employed in the characterization of MPcNPs, MPcNP/MWCNT composites and modified electrodes are presented.

3.1 Characterization of MPcNPs

In this work, nanoparticles of MPcs (M = Mn, Fe, Ni and Co) were employed in the chemical modification of carbon paste and BPPG electrodes. The MPcNPs were characterized using transmission electron microscopy (TEM), X-ray diffraction (XRD) and UV/Vis spectroscopy. The characterization of NiPcNPs is presented as an example.

3.1.1 Transmission electron microscopy

Figure 3.1 shows TEM micrographs of NiPcNPs. The average diameter of the nanoparticles (calculated from measured diameters of the particles) is about 23.6 nm.

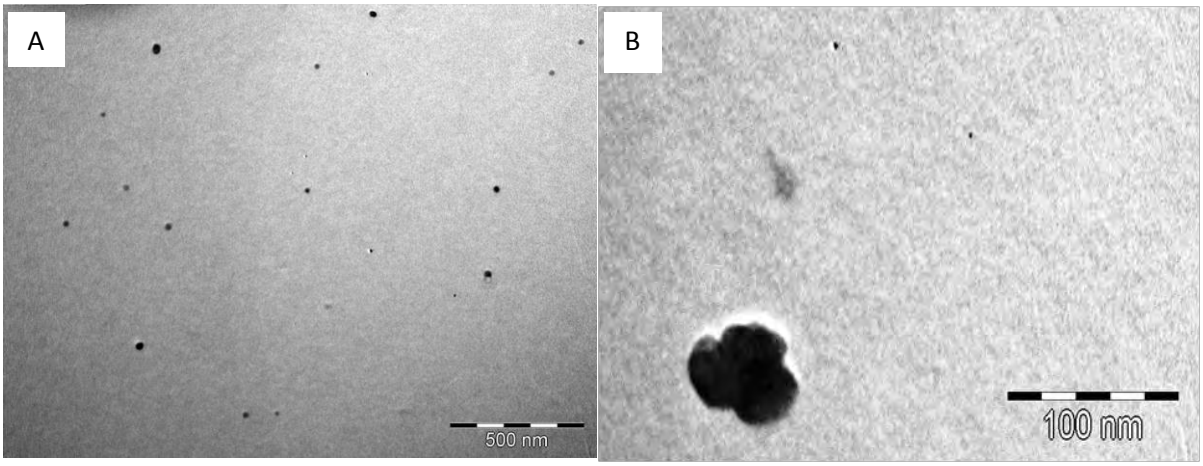

Figure 3.1: TEM images of NiPcNPs. The image in B is a close-up picture of one grain of the NiPcNPs shown in A.

The image in Figure 3.1B shows that 1 grain of nanoparticles may actually be a cluster of several nanoparticles (3 in this case). The average diameter of the NiPcNPs may therefore be less than the one calculated above.

3.1.2 X-ray diffraction (XRD)

X-ray diffraction patterns of bulk NiPc powder and NiPcNPs are shown in **Figure 3.2**. The XRD patterns of both NiPc and NiPcNPs show diffraction peaks at about the same 2θ positions, indicating that they are in the same crystal form. The width of the peak is inversely proportional to the thickness of the crystal (or grain size) [241]. Therefore, the XRD pattern of NiPcNPs is expected to exhibit broader diffraction peaks than those displayed in the NiPc pattern. This is indeed the case, as can be observed from **Figure 3.2**. The widths of the double peaks of the bulk NiPc have widened to such an extent that they overlap to form almost a single broad NiPcNP peak at each 2θ position.

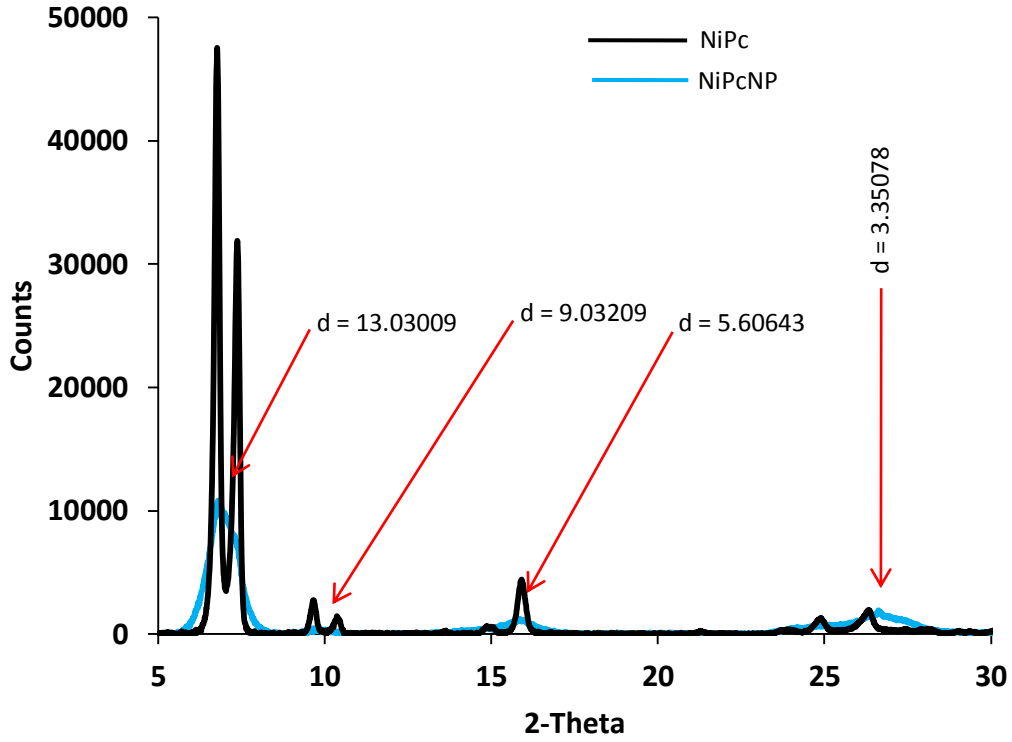

Figure 3.2: X-ray diffraction patterns of NiPc and NiPcNP powders. The red arrows point to the NiPcNP peaks, and the corresponding d-values are displayed.

The relationship between peak width and grain size is given by the Scherrer equation [46]. Using this equation, the average grain size of the NiPcNPs was found to be 7.67 nm. This grain size is much smaller than the one obtained using TEM because the grains obtained from the TEM sample preparation method may consist of more than one particle, as has been explained earlier.

3.1.3 UV/Vis spectrum of NiPcNPs

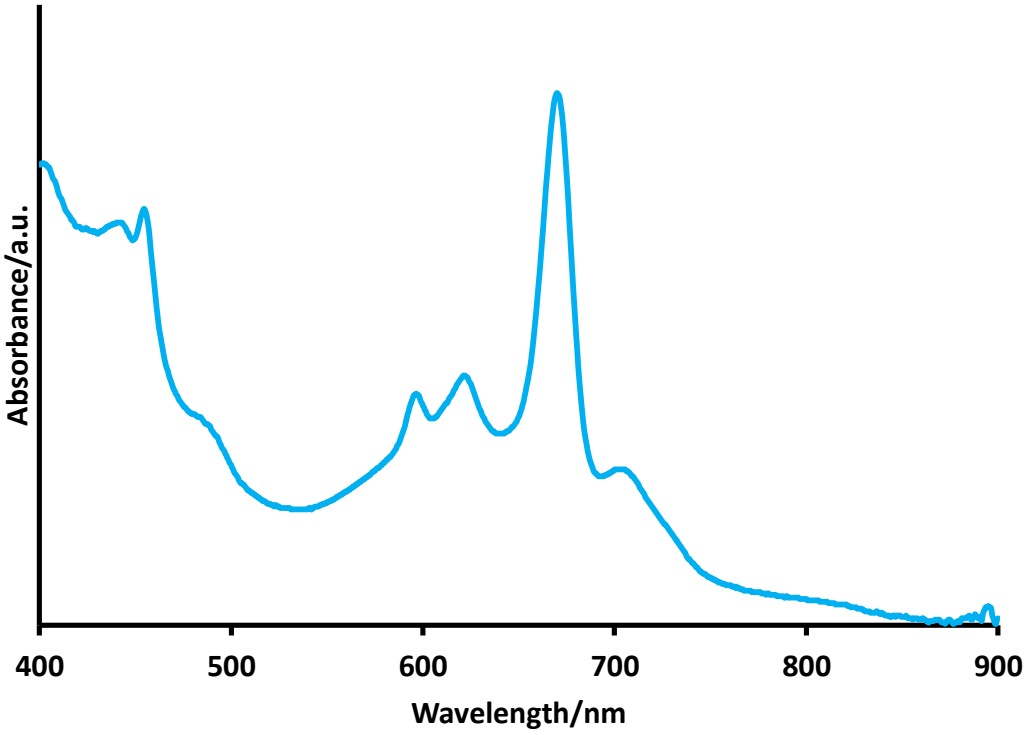

Figure 3.3: UV/Vis spectrum of NiPcNPs dissolved in DMF.

The UV/Vis spectrum of NiPcNPs, dissolved in DMF, is shown in **Figure 3.3**. Narrow peaks are displayed in the spectrum of NiPcNPs. This is typical of the spectrum of nanoparticles [242]. The Q band at 670 nm is split, probably due to aggregation of the nanoparticles.

3.2 Characterization of MWCNTs and MWCNT/MPcNP Composites.

Only NiPcNP/MWCNTs and FePcNP/MWCNTs were employed in electrocatalysis, and the characterization of NiPcNP/MWCNTs is outlined below as an example, together with that of the MWCNTs.

3.2.1 Transmission electron microscopy

TEM images of MWCNTs and NiPcNP/MWCNTs composites are shown in **Figure 3.4.** In both images, the results of the cutting action of the MWCNT purification process which causes defects and shorter CNTs, are displayed.

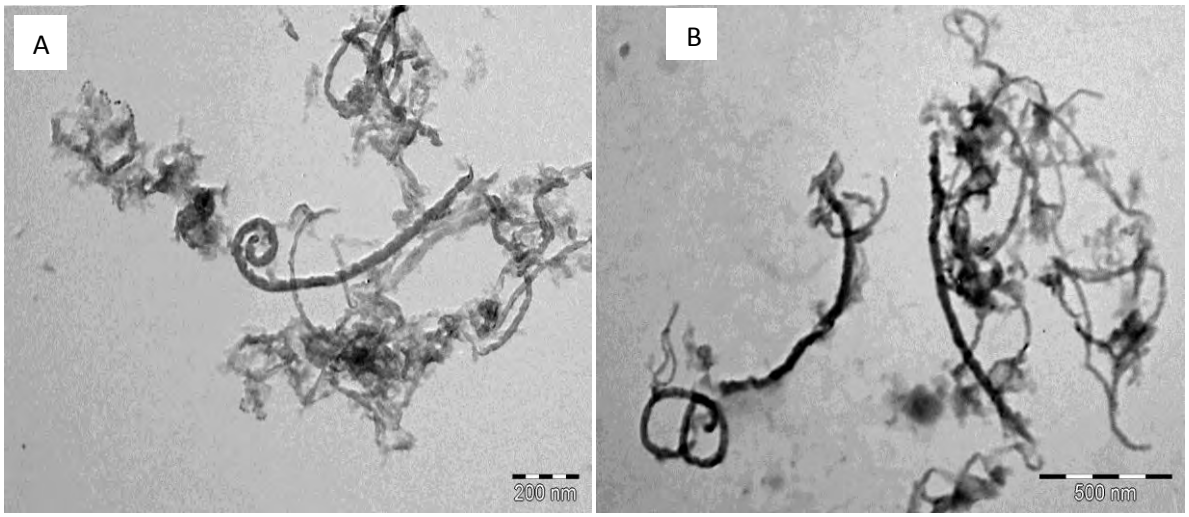

Figure 3.4: TEM images of MWCNTs (A) and NiPcNP/MWCNTs composite (B).

NiPcNPs which appear as dark spots on the walls of the MWCNTs can be seen in Figure 3.4B.

3.2.2 Raman spectroscopy

Raman spectra of NiPcNPs, NiPcNP/MWCNT composite, and MWCNTs are shown in **Figure 3.5**. Three prominent peaks can be clearly seen in the MWCNTs and NiPcNP/MWCNTs spectra. The peak located at about 1292 cm^{-1} corresponds to the disorder-induced phonon mode (D mode) due to the finite size and the presence of defects and disorders in the sp^2-hybridized carbon of MWCNTs [243]. The peak located at about 1600 cm^{-1} is due to the tangential vibration of the carbon atoms in

the MWCNTs which gives rise to the Raman-allowed phonon mode, E_{2g} (G mode). The G mode is associated with the longitudinal (LO) mode [244]. The intensity ratio between the D and G modes provides information about the degree of disorder in the MWCNTs, hence it is used to quantify defects [245]. From the spectra of the MWCNTs, the intensity of the D-band is higher than that of the G-band, and the ratio I_D/I_G was found to be ~ 1.71. This ratio is large, and this points to a large number of defects in the MWCNTs. This is not surprising, as the acid treatment of the MWCNTs causes defects, especially at the ends of the cut MWCNTs [246]. From the spectra of NiPcNP/MWCNTs, the ratio I_D/I_G was found to be ~ 1.75. This ratio is almost equal to that of the MWCNTs, which indicates that physically mixing NiPcNPs and MWCNTs does not disturb the structure of the CNTs (no additional defects on the MWCNTs). The other prominent peak which is present in all the spectra is located at about 1062 cm^{-1}. This peak corresponds to the Raman active B_{2g} mode of NiPc [247]. A small amount of NiPcNPs may be present in the MWCNTs as a consequence of the manufacturing process [248].

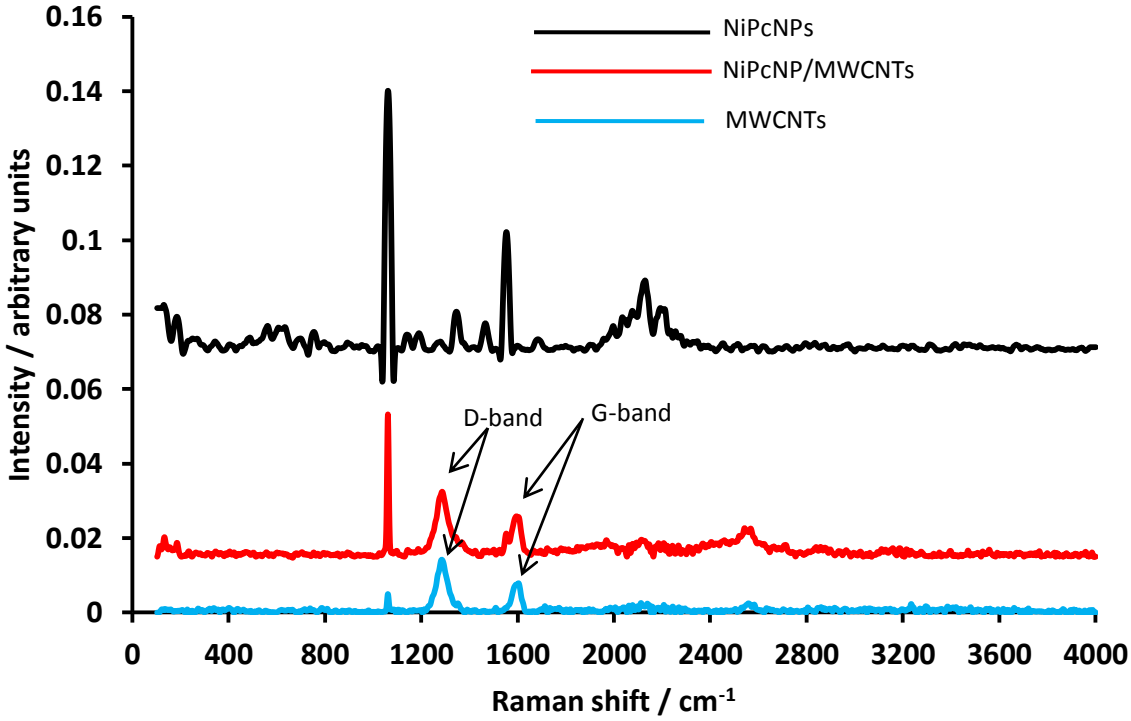

Figure 3.5: Raman spectra of NiPcNPs, NiPcNP/MWCNTs, and MWCNTs.

3.2.3 UV/Vis spectroscopy

The UV/Vis spectra of NiPcNP/MWCNT nanocomposite and NiPcNPs are shown in **Figure 3.6** as an example.

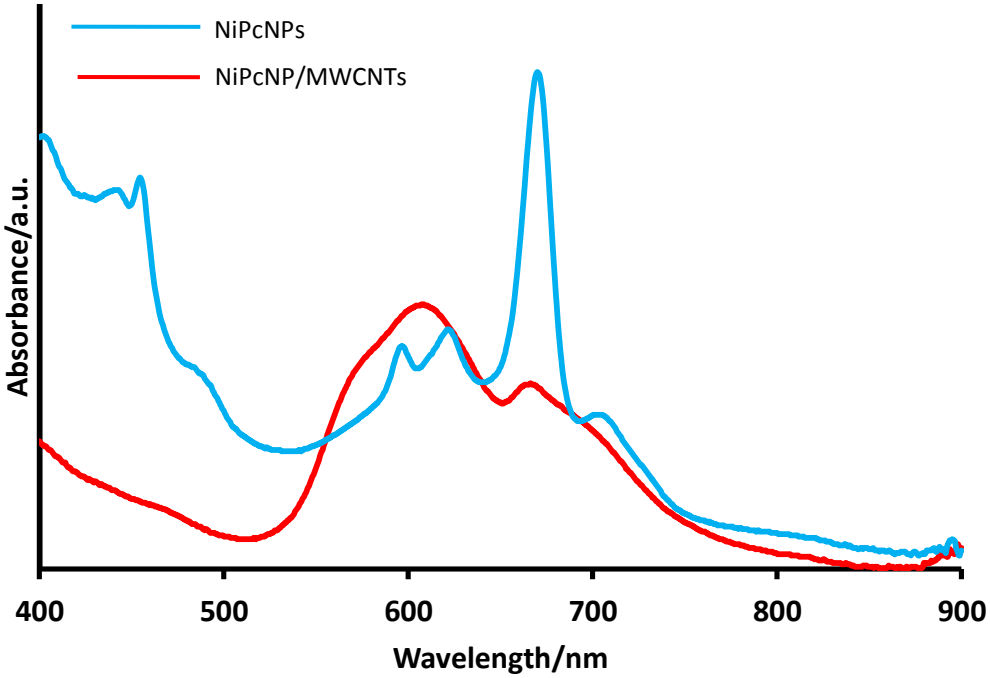

Figure 3.6: UV/Vis spectra of NiPcNP/MWCNTs and NiPcNPs

The NiPcNP/MWCNT spectrum shows extensive aggregation of the NiPcNPs within the composite, as evidenced by the blue-shifted band near 610 nm. Aggregation in Pcs is due to coplanar association of the rings. In the presence of MWCNTs, the blue-shift may also be due to attachment of the NiPcNPs to the MWCNTs.

3.2.4 XPS of MWCNT/MPcNP composites

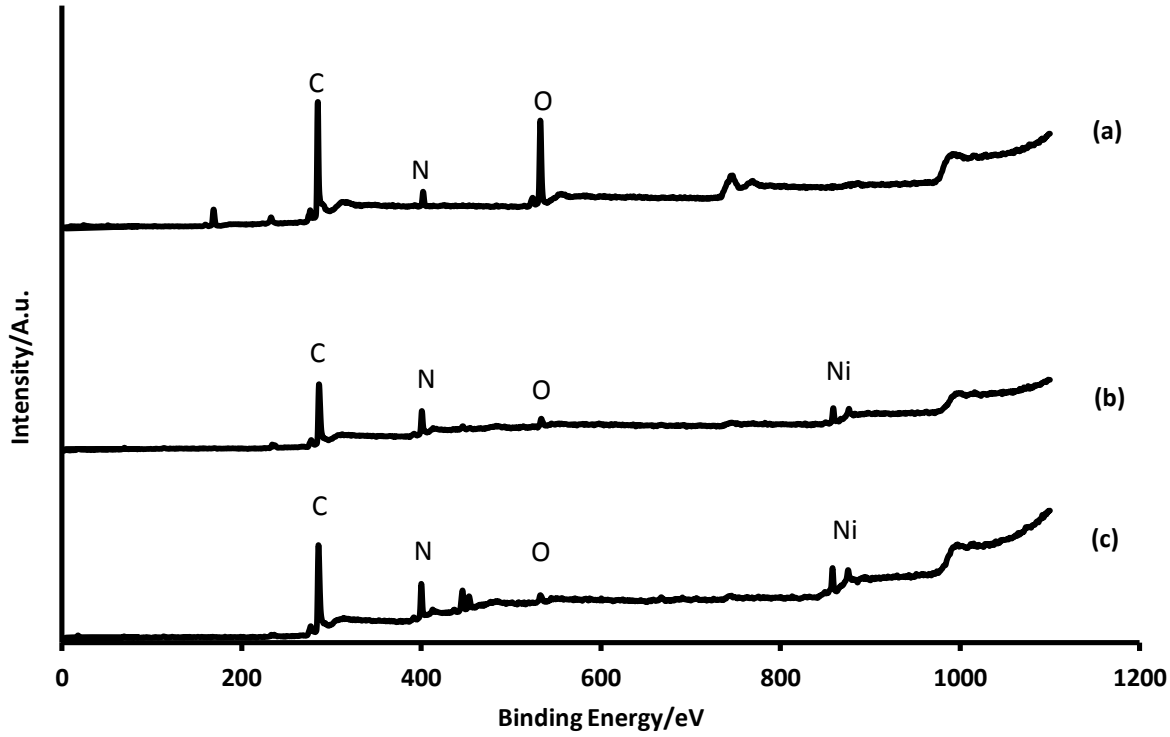

Figure 3.7: X-ray photoelectron spectra of the MWCNTs (a), NiPcNPs (b) and NiPcNP/MWCNTs (c).

In the photoelectron spectrum of the MWCNTs the C 1s peak is located at 284.4 eV, attributed to the C–C bonds of the MWCNTs. The other dominant peak is the O 1s peak at 532.3 eV, which is due to the O–H bond within the carboxyl group of the acidified MWCNTs. The small N 1s peak at about 400 eV (for MWCNT) may be due to nitrogen located either within the phthalocyanine complex from which most of the MWCNTs are reported to be synthesized [248] or in the traces of nitric acid remaining within the MWCNTs after the purification process. The XPS spectrum of NiPcNPs shows a C 1s peak at 286 V. This peak is due to the C–C bonds of the NiPcNPs. An N 1s peak due to the C–N bonds of the NiPcNPs also appears at 400 eV. The small O 1s peak at 532 eV is probably due to the oxygen in the indium

oxide substrate [249]. The Ni $2p_{3/2}$ peak appears at 857.5 eV, and the Ni $2p_{½}$ peak appears at 874.5 eV for NiPcNPs as well as for NiPcNP/MWCNTs. The XPS spectrum of the NiPcNP/MWCNTs shows a C 1s peak at 285.05 eV. This peak is due to the C–C bonds of the MWCNTs and the NiPcNPs. An N 1s peak due to the C–N bonds of the NiPcNPs also appears at 399.7 eV. The double peak appearing at ~445 eV is due to the indium oxide substrate (as has been reported before [249, 250]) on which the NiPcNP/MWCNTs composite is placed for analyses purposes. This peak is not clear in the MWCNT and NiPcNP spectra due to the different amounts of the samples. This means that the powder forms either islands or a very thin layer on the surface, thus exposing the indium oxide surface to analysis as well [250]. The small O 1s peak at 532 eV is probably due to the oxygen in the indium oxide substrate [249].

3.3 Electropolymerization of MTAPcs.

The number of MWCNTs attached to the BPPGE surface by abrasive mobilization was estimated using a procedure similar to literature report [38]. The surface roughness factor for the MWCNT-BPPGE was determined by cyclic voltammetry in an equimolar (1:1), 1.0 mM solution of $K_3[Fe(CN)_6]$ and $K_4[Fe(CN)_6]$ containing 0.05 M KCl as the redox probe, and applying the Randles-Sevcik equation (equation 1.2)[37]:

$$I_{pa} = (2.69 \times 10^5) n^{2/3} A D^{1/2} \nu^{1/2} C_0 \qquad \textbf{3.1}$$

where D and C_0 are the diffusion coefficient and bulk concentration of the redox probe, respectively. From the cyclic voltammogram obtained, the experimental anodic peak current (I_{pa} experimental) was found to be ~3.52×10^{-5} A. From the D -value for $K_3[Fe(CN)_6]$ = 7.6×10^{-6} cm^2 s^{-1} [251], n = 1, ν = 0.06 V/s and

$A \cong 0.196$ cm^2, the roughness factor was estimated to be 0.96. The effective area, A_{eff}, was then calculated and found to be ~0.192 cm^2.

The lengths of the carbon nanotubes range between 5 and 20 μm, and the diameter is 15 ± 5 nm (suppliers' values). From these dimensions, the average area of each nanotube (A_{CNT}) was estimated assuming a cylindrical shape for the nanotubes (and that the nanotubes are attached parallel to the surface of the electrode). The number of nanotubes (N_{CNT}) attached to the BPPGE surface was obtained using equation 3.2:

$$N_{CNT} = A_{eff}/A_{CNT} \qquad \textbf{3.2}$$

N_{CNT} was estimated to range between 10^7 and 10^8

The MTAPc complexes were electropolymerized from a DMSO solution containing 0.1 M $TBABF_4$ onto the MWCNT-BPPGE by repetitive cyclic voltammetry at 0.05 V s^{-1} (15 times with CoTAPc, FeTAPc, and MnTAPc, and 20 times with NiTAPc). This repetitive scanning resulted in a gradual increase in the amplitude of the cyclic voltammetric peaks, and it was terminated when the amplitude of the peaks stopped increasing. The halt in further increase of peak amplitudes is the result of increased electrical resistance and the resistance to mass transport through the polymer film as the film thickness increases [252]. Also, the potential windows for the polymerizations were chosen depending on which ones resulted in clearly increasing peak amplitudes. **Figure 3.8** shows the growth of the voltammetry peaks during cycling with the MWCNT-BPPGE as the working electrode. With MnTAPc and FeTAPc, scanning was done between -0.5 and +1.2 V (**Figures 3.8A** and **3.8B**),

and between -0.2 and +1.0 V with NiTAPc (**Figure 3.8C**) and CoTAPc (**Figure 3.8D**). The formation of new peaks such as peaks **II** and **III** in **Figure 3.8A**, and peak **II** in **Figure 3.8B-D** during the attachment process confirmed that electropolymerization was taking place.

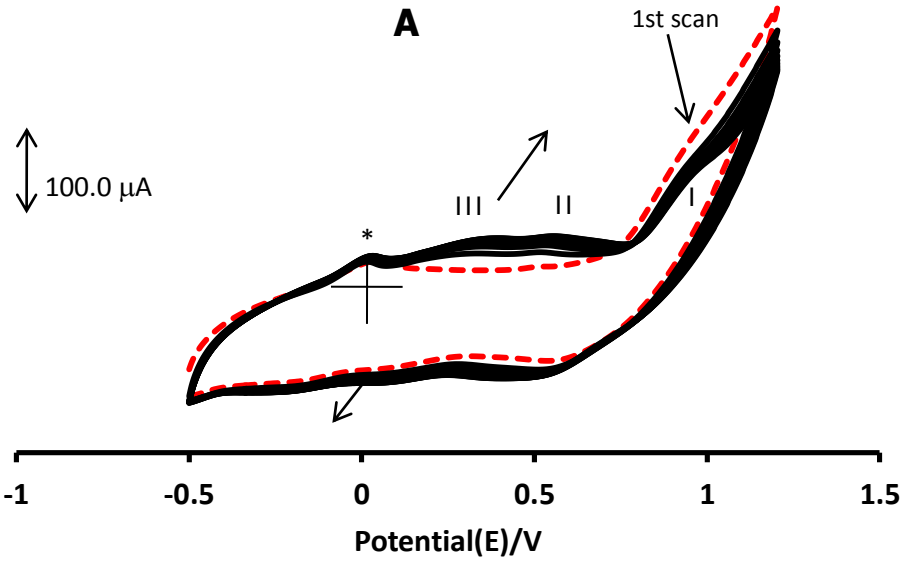
A
1st scan
100.0 μA
III
II
I
*
-1
-0.5
0
0.5
1
1.5
Potential(E)/V

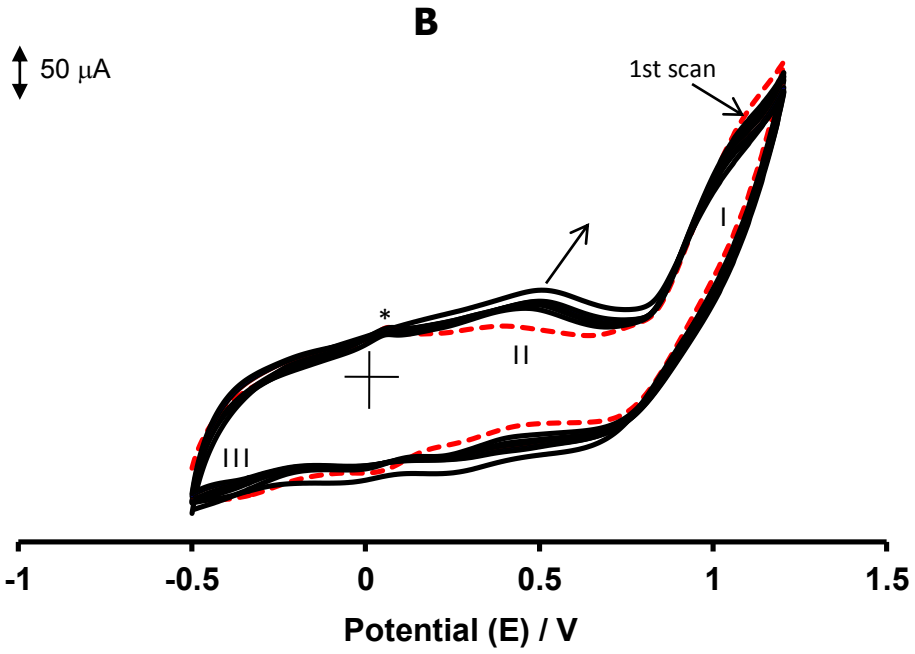
B
50 μA
1st scan
I
*
II
III
-1
-0.5
0
0.5
1
1.5
Potential (E) / V

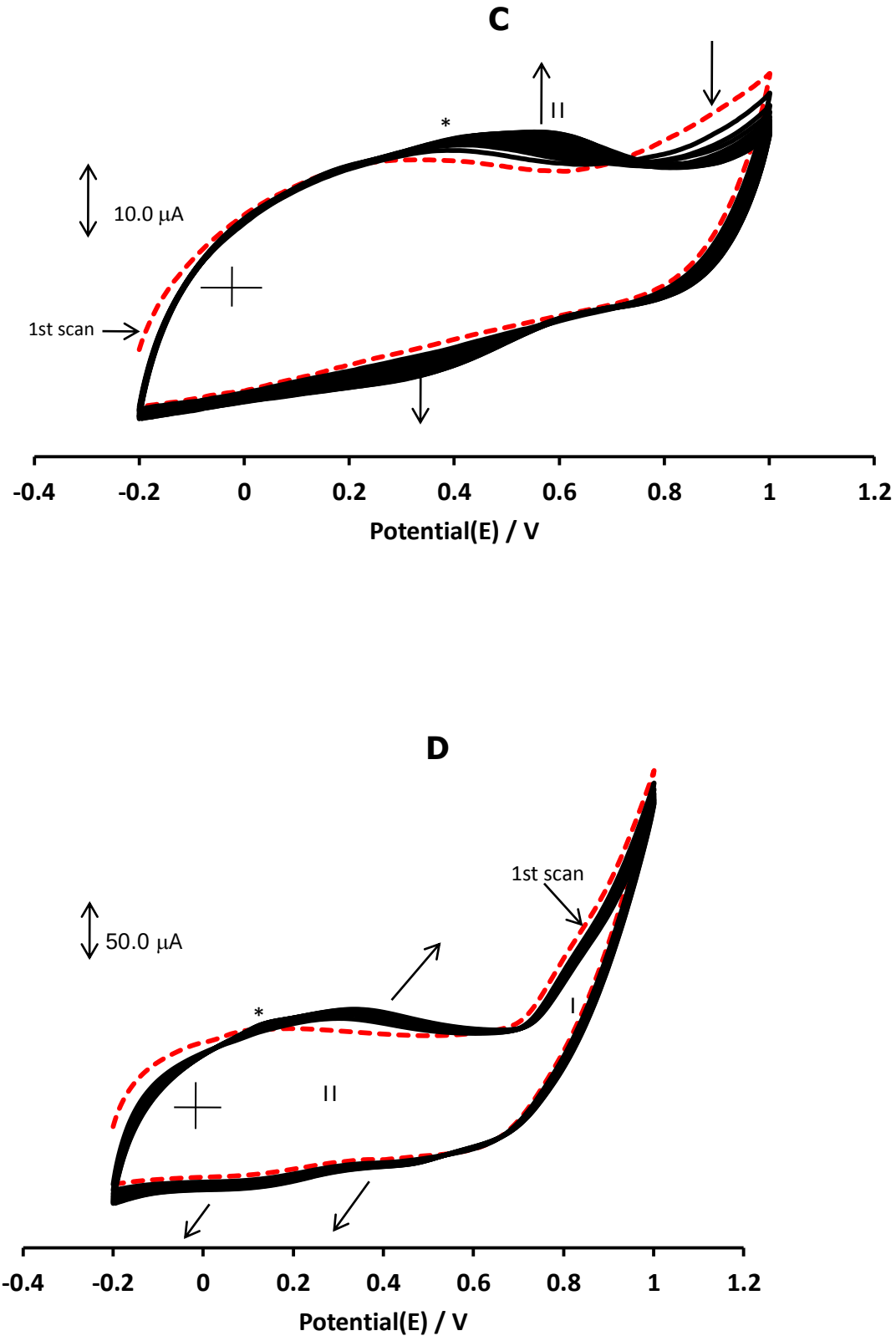

Figure 3.8: Electropolymerization of MnTAPc (A), FeTAPc (B), NiTAPc (C) and CoTAPc (D) on MWCNT-BPPGE in DMSO containing 0.1 M $TBABF_4$. Scan rate = 0.05 V/s. Reference electrode: Ag|AgCl (3M KCl).

The oxidation state of Mn in MnTAPc has been established [253] to be Mn^{III}. The processes labeled **II** and **III** observed in **Figure 3.8A** for MnTAPc are assigned to $Mn^{IV}Pc^{-2}/Mn^{III}Pc^{-2}$ metal oxidation and $Mn^{III}Pc^{-2}/Mn^{II}Pc^{-2}$ metal reduction processes, respectively, in comparison with literature [253], with expected shifts since different electrodes are employed. The processes labeled **II** and **III** in **Figure 3.8B** are due to $Fe^{III}Pc^{-2}$ /$Fe^{II}Pc^{-2}$ and $Fe^{II}Pc^{-2}/Fe^{I}Pc^{-2}$, respectively, in comparison with literature [254]. For NiTAPc polymerization (**Figure 3.8C**), the process starting at ~ 0.7 V is attributed to $Ni^{II}Pc^{-1}/Ni^{II}Pc^{-2}$ ring oxidation [255-257]. The process labelled **II** may be due to the $Ni^{III}Pc^{-2}/Ni^{II}Pc^{-2}$ oxidation process [256-259]. The peak marked (*) at ~+0.37 V (**Figure 3.8C**) was observed in the other MTAPc polymerizations as well. It appears at ~ 0.0 V in the MnTAPc and FeTAPc polymerizations, and at ~ 0.08 V in CoTAPc polymerization (**Figure 3.8D**). The peak was also observed on cycling of MWCNT in DMSO, then rinsing the electrode and recording the CV in pH 7 buffer, and has been attributed to the redox property of the oxygen-containing moieties of the MWCNT [260]. The process labeled II ($E_{1/2} \cong 0.3$ V) in **Figure 3.8D** is attributed to the $Co^{III}Pc^{-2}/Co^{II}Pc^{-2}$ metal oxidation process, in comparison with CoTAPc on GCE [161].

The oxidation of the amino groups is believed to generate free radicals which initiate the electropolymerization process in MTAPc complexes [261]. The oxidation of the amino group (labeled I in **Figures 3.8A, B, and D**) was observed at ~ 0.95 V for MnTAPc and FeTAPc polymerization, and at ~0.80 for CoTAPc polymerization.

The MTAPcs were also electropolymerized on the bare BPPGEs to establish whether the absence of the MWCNTs would have an effect on the electropolymerizations, and

to gauge the effect of co-modification with MWCNTs on electrocatalysis. **Figure 3.9** shows cyclic voltammograms representing the polymerization of the different MTAPcs on the bare BPPGE. With MnTAPc, FeTAPc and CoTAPc, scanning was done between -0.5 and +1.4 V (**Figures 3.9A, B, and D**), and between -0.2 and +1.0 V with NiTAPc (**Figure 3.9C**).

A

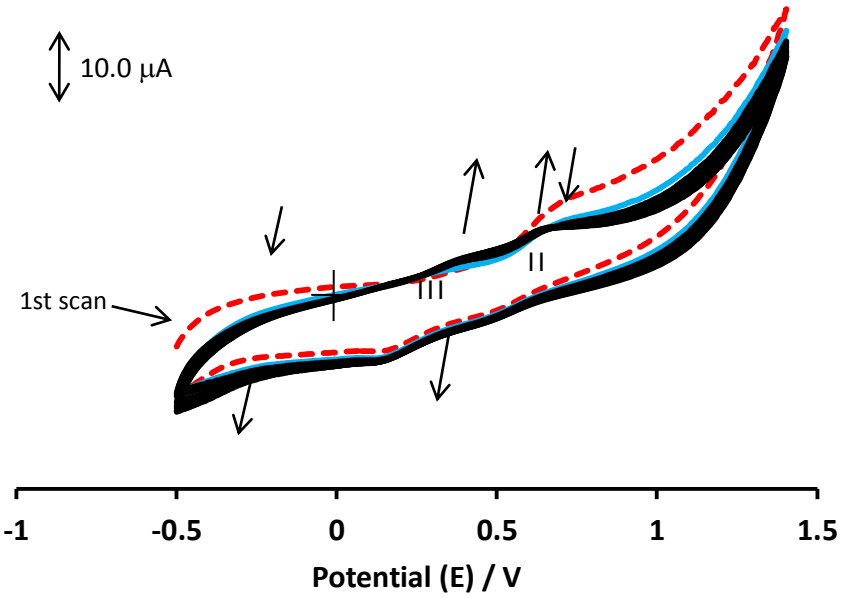
10.0 µA
1st scan
II
III
-1
-0.5
0
0.5
1
1.5
Potential (E) / V

B

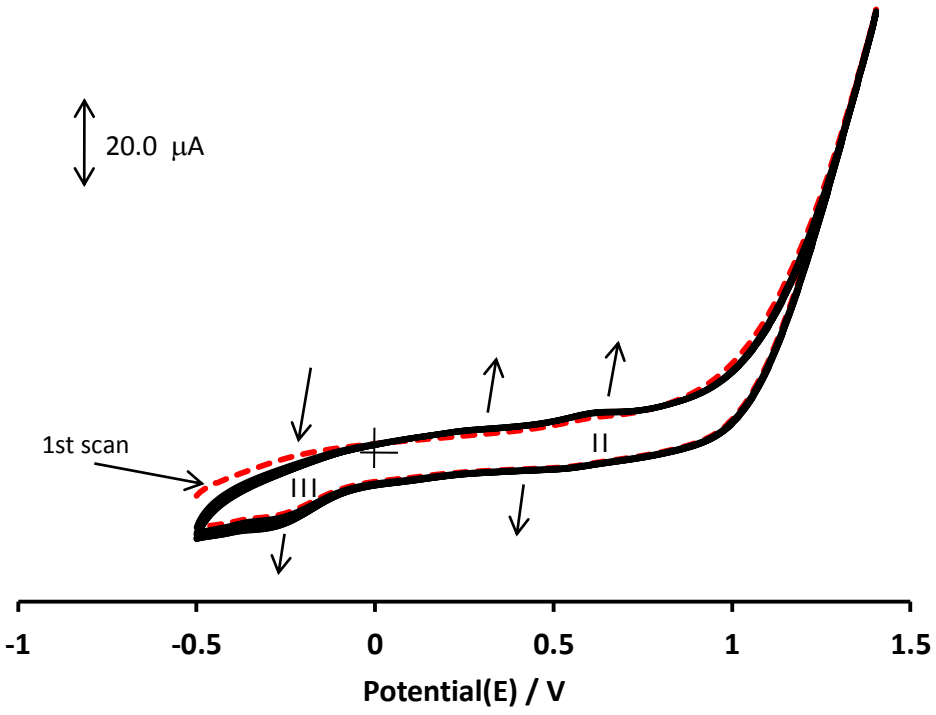
20.0 µA
1st scan
II
III
-1
-0.5
0
0.5
1
1.5
Potential(E) / V

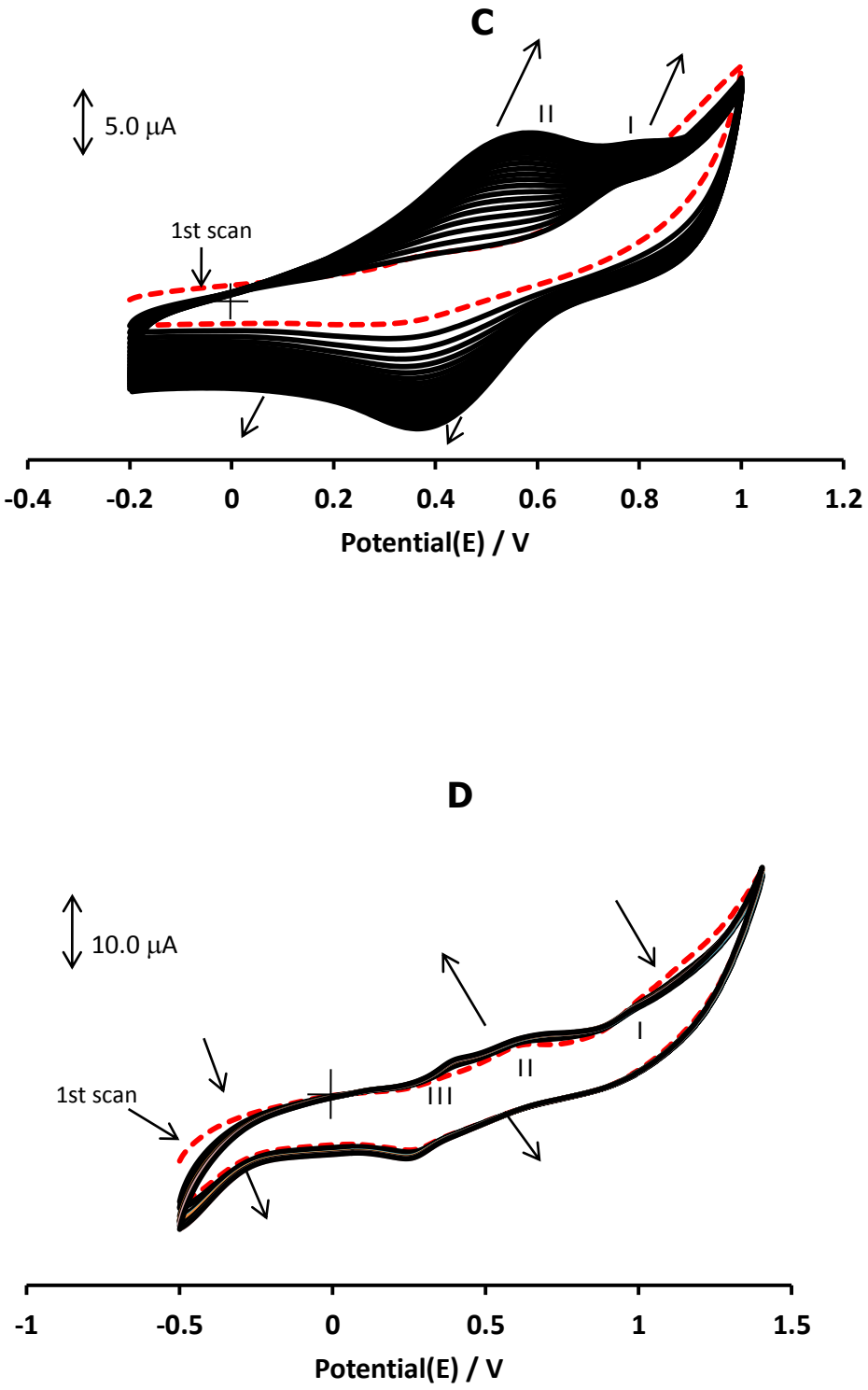

Figure 3.9: Electropolymerization of MnTAPc (A), FeTAPc (B), NiTAPc (C) and CoTAPc (D) on BPPGE in DMSO containing 0.1 M $TBABF_4$. Scan rate = 0.05 V/s. Reference electrode: Ag|AgCl 3M KCl.

As indicated earlier, the processes labelled **II** and **III** in **Figure 3.9A** are attributed to $Mn^{IV}Pc^{-2}/Mn^{III}Pc^{-2}$ metal oxidation and $Mn^{III}Pc^{-2}/Mn^{II}Pc^{-2}$ metal reduction, respectively [253]. In **Figure 3.9B**, the processes labelled **II** and **III** are due to $Fe^{III}Pc^{-2}/Fe^{II}Pc^{-2}$ metal oxidation and $Fe^{II}Pc^{-2}/Fe^{I}Pc^{-2}$ metal reduction, respectively, in comparison with literature [254]. In **Figure 3.9C**, the process labelled **I** is due to $Ni^{II}Pc^{-1}/Ni^{II}Pc^{-2}$ ring oxidation [255-256]. The process labelled **II** may be due to the $Ni^{III}Pc^{-2}/Ni^{II}\ Pc^{-2}$ oxidation process [256-259]. The process labelled **I** in **Figure 3.9D** is due to NH_2 oxidation and the process labelled **II** may be due to ring-based oxidation processes. The process labelled **III** is attributed to $Co^{III}Pc^{-2}/Co^{II}Pc^{-2}$ metal oxidation [161].

3.4 Characterization of Modified Electrodes

3.4.1 Electrochemical characterization of MPcNP/MWCNT-BPPGE

3.4.1.1 Electrochemical characterization in buffer solution

The NiPcNP/MWCNT-BPPGE and FePcNP/MWCNT-BPPGE were studied in this section since they were the only electrodes of this type that were used in electrocatalysis.

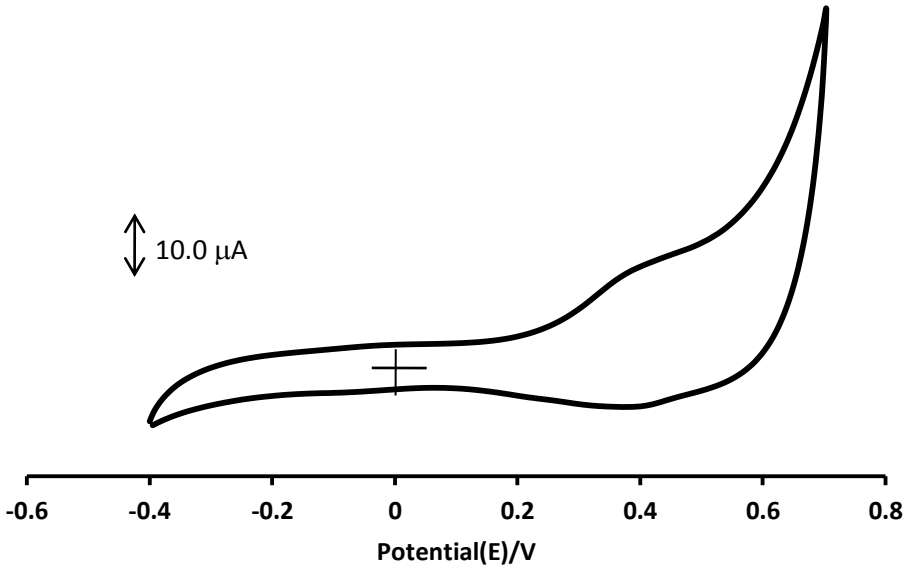

Figure 3.10: Cyclic voltammogram of NiPcNP/MWCNT-BPPGE in 0.1 M phosphate buffer at pH 7. Scan rate = 0.05 V/s. Reference electrode: Ag|AgCl (3 M KCl).

Figure 3.10 shows the $Ni^{III}Pc^{-2}/Ni^{II}Pc^{-2}$ couple typical of adsorbed NiPc at ~0.38 V [256-259]. For FePcNP/MWCNT-BPPGE, the $Fe^{III}Pc^{-2}/Fe^{II}Pc^{-2}$ redox process was observed at $E_P \cong 0.5$ V, in comparison with literature [254]. The $Ni^{III}Pc^{-2}/Ni^{II}Pc^{-2}$ and $Fe^{III}Pc^{-2}/Fe^{II}Pc^{-2}$ processes are involved in catalysis, hence they are the only ones discussed in this section.

The surface coverage ($\Gamma_{MPcNP/MWCNT}$) for MPcNP/MWCNT–BPPGE (M = Ni, Fe) in aqueous conditions was evaluated by integrating the charge under the anodic peaks of $M^{III}Pc^{-2}/M^{II}Pc^{-2}$. Using **Figure 3.10** and equation 3.3 [2]:

$$\Gamma_{MPcNP/MWCNT} = \frac{Q}{nFA} \qquad \textbf{3.3}$$

where 'Q' is the electric charge obtained from the anodic and cathodic peaks mentioned above at 0.050 V/s ($Q_{NiPcNP/MWCNT} = 3.47 \times 10^{-6}$ C, and $Q_{FePcNP/MWCNT} = 1.265 \times 10^{-5}$ C), 'n', the number of electrons (≈1), 'F', the Faraday constant (96,485

C mol^{-1}) and 'A' is the effective surface area (0.192 cm^2). The surface coverages were found to be 1.87 $\times$ 10^{-10} and 6.83 $\times$ 10^{-10} mol cm^{-2} for the NiPcNP/MWCNT-BPPGE and FePcNP/MWCNT-BPPGE, respectively, **Table 3.1.** The difference in thickness of the surface coverages may be due to the size of the nanoparticles that were mixed with the MWCNTs. From XRD measurements the apparent grain sizes of the NiPcNPs and FePcNPs were 7.67 and 31.6 nm, respectively.

Table 3.1: Parameters obtained from electrochemical characterization of the different electrodes, recorded in 0.1 M phosphate buffer at pH 7 and in 1.0 mM $[Fe(CN)_6]^{3-}/[Fe(CN)_6]^{4-}$ at 0.084 V. The values in brackets were obtained with the corresponding electrode employed without including MWCNTs as modifier.

Electrode	**Surface Coverage (Γ)/10^{-8} mol cm^{-2}**	**ΔE/V**	**EIS Parameters**		
			R_{et}/ kΩ	**n**	**$K_{et}/10^{-5}$ cm s^{-1}**
BPPGE	----------	0.640	1.831	0.66	0.08
MWCNT-BPPGE	----------	0.088	0.113	0.76	1.23
NiPcNP/MWCNT-BPPGE	0.0187 (---)[a]	0.073 (0.078)	0.093(0.104)	0.68(0.64)	1.5
FePcNP/MWCNT-BPPGE	0.0683 (0.071)	0.098 (0.117)	0.875(1.077)	0.73(0.81)	0.16
poly-MnTAPc-MWCNT-BPPGE	1.2 (0.062)	0.088 (0.390)	0.113(0.214)	0.70(0.69)	1.23
poly-FeTAPc-MWCNT-BPPGE	1.7 (0.1)	0.088 (0.312)	0.116(0.125)	0.69(0.91)	1.19
poly-NiTAPc-MWCNT-BPPGE	1.5 (0.060)	0.093 (0.405)	0.128(0.217)	0.68(0.74)	1.08
poly-CoTAPc-MWCNT-BPPGE	0.3 (0.1)	0.080 (0.264)	0.083(0.211)	0.75(0.95)	1.67

[a]Very weak peak; amount of charge cannot be determined from the peak.

3.4.1.2 Electrochemical characterization in $K_3[Fe(CN)_6]/K_4[Fe(CN)_6]$ solution

The two electrodes were then scanned in pH 7 phosphate buffer solution containing 1 mM $K_3[Fe(CN)_6]/K_4[Fe(CN)_6]$ (1:1 molar ratio), and the cyclic voltammograms obtained are shown in **Figure 3.11**. **Figure 3.11A** shows comparative cyclic voltammograms of MWCNT-BPPGE, NiPcNP/MWCNT-BPPGE, NiPcNP-BPPGE and BPPGE. From the figure, the peak potential differences (ΔE_P) of the different electrodes follow the trend: NiPcNP/MWCNT-BPPGE (~73 mV) < NiPcNP-BPPGE (~78 mV) < MWCNT-BPPGE (~88 mV) < BPPGE (~640 mV). The decrease in the ΔE_p values of the NiPcNP-based electrodes in comparison to the MWCNT-BPPGE and the BPPGE shows that modification with NiPcNPs results in faster electron-transfer kinetics at the electrode surface, with the NiPcNP/MWCNT-BPPGE showing slightly faster electron-transfer kinetics than the NiPcNP-BPPGE. This shows that the MWCNTs have a positive effect on the NiPcNP-BPPGE, improving the electronic communication between the electrode surface and the $K_3[Fe(CN)_6]/K_4[Fe(CN)_6]$ redox probe.

In **Figure 3.11B** the peak potential differences of the different electrodes follow the trend: MWCNT-BPPGE (~88 mV) < FePcNP/MWCNT-BPPGE (~98 mV) < FePcNP-BPPGE (~117 mV) < BPPGE (~640 mV). The FePcNP-based electrodes show improved electron-transfer kinetics in comparison with the BPPGE only. When the FePcNPs are mixed with the MWCNTs, ΔE increases from ~88 mV with the MWCNT-BPPGE to ~98 mV with the FePcNP/MWCNT-BPPGE. Thus, the FePcNPs have a negative effect on the MWCNT-BPPGE, slowing the electron-transfer kinetics at the

electrode surface. From the discussion above, the NiPcNP/MWCNT-BPPGE seems to show better electron-transfer kinetics than the FePcNP/MWCNT-BPPGE. This will be probed further using electrochemical impedance spectroscopy, since this technique provides a more detailed description of an electrochemical system than cyclic voltammetry [187,251].

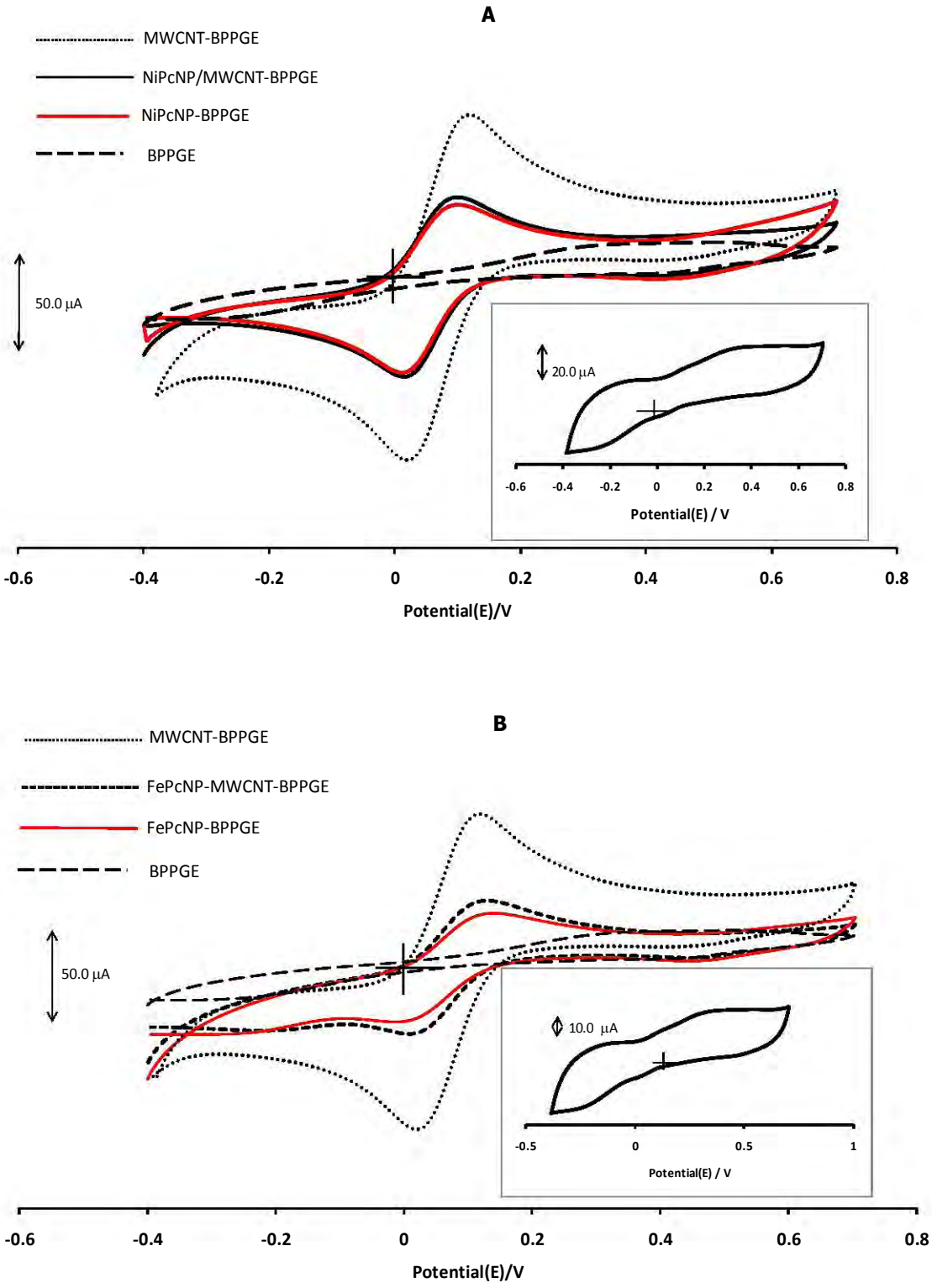

Figure 3.11: Cyclic voltammograms of NiPcNP/MWCNT-BPPGE and NiPcNP-BPPGE (A), and FePcNP/MWCNT-BPPGE and FePcNP-BPPGE (B) together with CVs of BPPGE and MWCNT-BPPGE, in pH 7 phosphate buffer containing 1 mM $[Fe(CN)_6]^{3-}/[Fe(CN)_6]^{-4}$. Inset: CV of BPPGE in 1 mM $[Fe(CN)_6]^{3-}/[Fe(CN)_6]^{-4}$. Scan rate = 0.050 V/s. Reference Electrode: Ag|AgCl (3 M KCl).

The EIS measurements were performed at the formal potential ($E_{1/2}$≈0.084 V) of the $[Fe(CN)6]^{4-}/[Fe(CN)6]^{3-}$ as recorded in the CVs (Figure 3.10). **Figure 3.12** shows examples of the Nyquist plots obtained for the NiPcNP/MWCNT-BPPGE and FePcNP/MWCNT-BPPGE in the 1 mM $[Fe(CN)_6]^{3-}/[Fe(CN)_6]^{4-}$ solution, and the Randles circuit (**Figure 3.12C**) that was employed to produce the plots. In the Randles circuit, the symbols R_s, R_{et}, Z_w, and CPE_{dl} represent the solution resistance, the electron transfer resistance, the Warburg impedance, and the constant phase element, respectively. Nyquist plots for MWCNT-BPPGE, MPcNP-BPPGE (M = Ni or Fe) and BPPGE are also included for comparison. The values of the pertinent parameters are shown in **Table 3.1**.

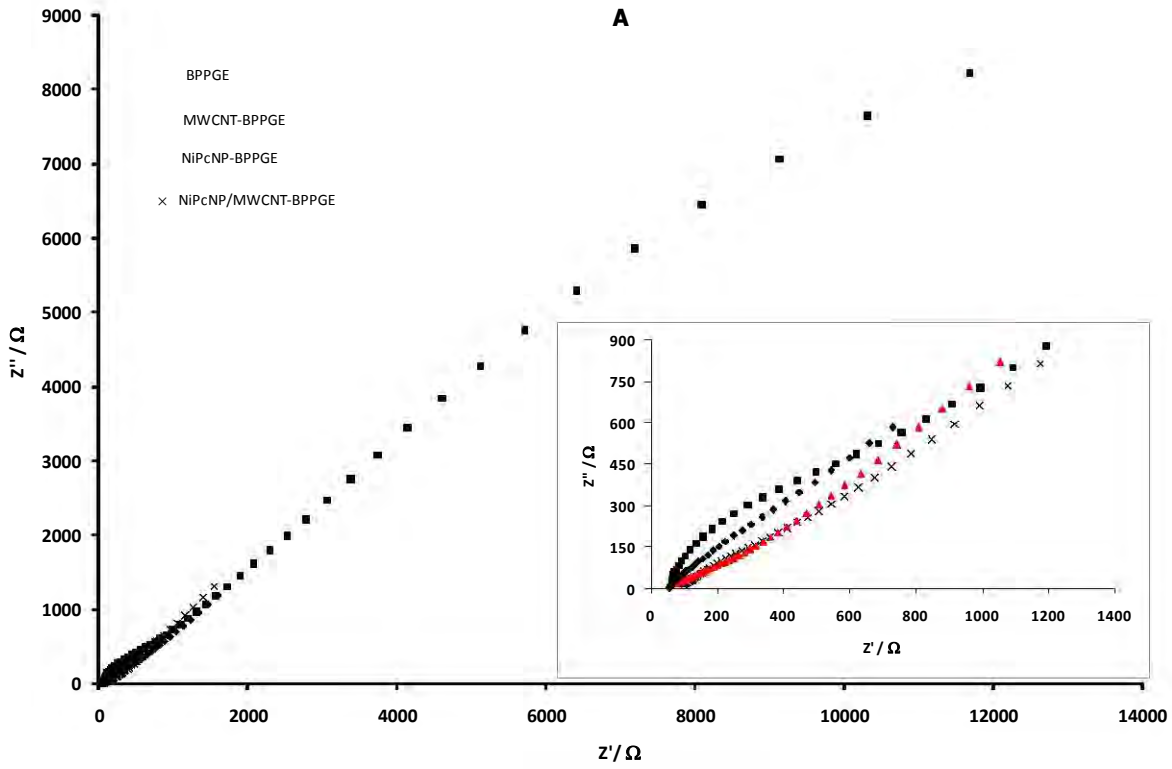
A
BPPGE
MWCNT-BPPGE
NiPcNP-BPPGE
× NiPcNP/MWCNT-BPPGE
Z'' / Ω
Z' / Ω
0
1000
2000
3000
4000
5000
6000
7000
8000
9000
0
2000
4000
6000
8000
10000
12000
14000
Z'' / Ω
Z' / Ω
0
150
300
450
600
750
900
0
200
400
600
800
1000
1200
1400

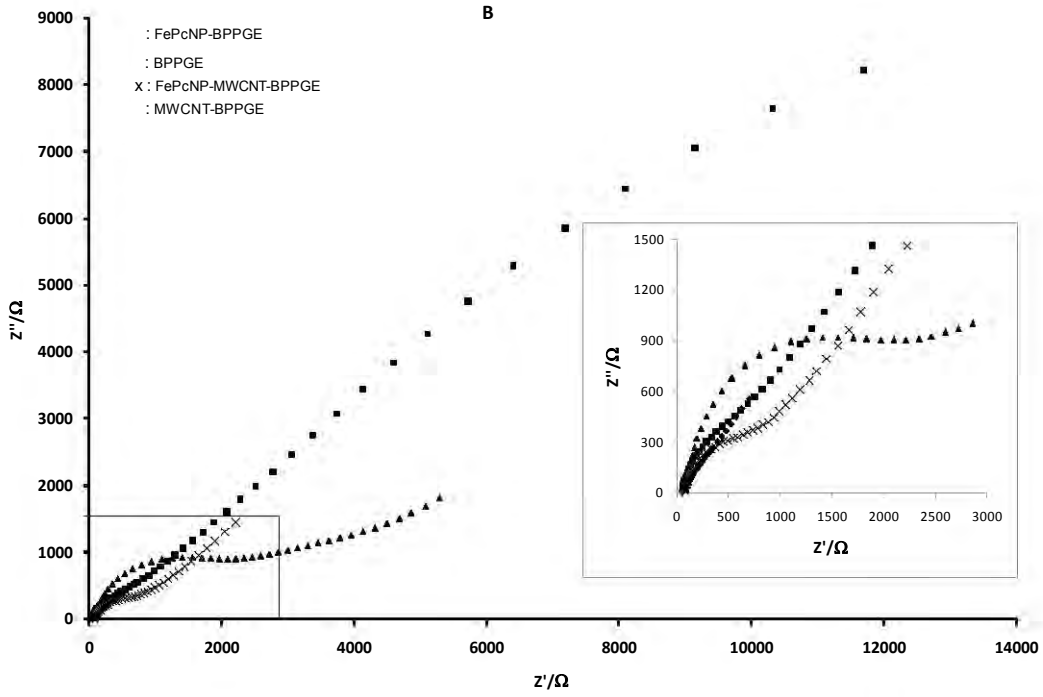
B
: FePcNP-BPPGE
: BPPGE
x : FePcNP-MWCNT-BPPGE
: MWCNT-BPPGE
Z''/Ω
Z'/Ω
0
1000
2000
3000
4000
5000
6000
7000
8000
9000
0
2000
4000
6000
8000
10000
12000
14000
Z''/Ω
Z'/Ω
0
300
600
900
1200
1500
0
500
1000
1500
2000
2500
3000

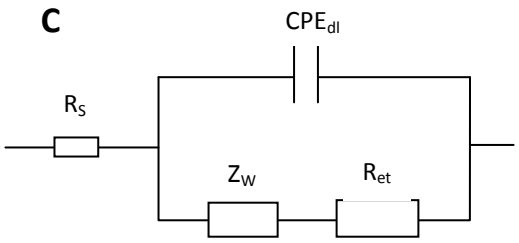

Figure 3.12: Comparative Nyquist (Z″ vs Z) plot for NiPcNP-BPPGE and NiPcNP/MWCNT-BPPGE (A), and FePcNP-BPPGE and FePcNP/MWCNT-BPPGE (B) in 0.1 M, pH 7 phosphate buffer containing 1 mM $K_3[Fe(CN)_6]/K_4[Fe(CN)_6]$ (1:1) and 0.05 M KCl (supporting electrolyte) at a fixed potential (E) = 0.084 V. The equivalent circuit (C) was used to fit the EIS data of (A) and (B).

From **Table 3.1**, it is seen that the R_{et} values of the MPcNP/MWCNT-BPPGEs (M = Ni or Fe), together with those of BPPGE and MWCNT-BPPGE follow the trend: NiPcNP/MWCNT-BPPGE < NiPcNP-BPPGE < MWCNT-BPPGE < FePcNP/MWCNT-BPPGE < FePcNP-BPPGE < BPPGE, which essentially corroborates the ΔE_P data obtained from cyclic voltammetry. This shows that, when the BPPGE is modified with MPcNP/MWCNT composite or MPcNPs alone or MWCNTs alone, the fastest electron-transfer kinetics in the $[Fe(CN)_6]^{3-}/[Fe(CN)_6]^{4-}$ solution are displayed by the NiPcNP/MWCNT-BPPGE, with the NiPcNP-BPPGE following close behind. Although modification of the BPPGE with FePcNP/MWCNT or FePcNPs alone improves reversibility, faster electron-transfer kinetics are realized with use of the MWCNTs without the FePcNPs.

The enhanced electron transport exhibited by the two NiPcNP-based electrodes in the $[Fe(CN)_6]^{3-}/[Fe(CN)_6]^{4-}$ solution may be due to the following two processes: The $[Fe(CN)_6]^{3-}/[Fe(CN)_6]^{4-}$ redox process is in the region of the $Ni^{III}Pc^{-2}/Ni^{II}Pc^{-2}$ metal oxidation process shown in **Figure 3.9**, and may be catalysed by it. Also, the

MWCNT/NiPcNP enhance electron transport in a synergistic fashion, with MWCNTs acting as electron conducting nanowires while the NiPcNPs act as the electrocatalyst. Although there is no significant difference in the electron transfer behavior of the NiPcNP and MWCNT/NiPcNP, the catalytic activity of the latter is best observed in the electrocatalytic detection of asulam (discussed later). With the FePcNP-based electrodes, the $Fe^{III}Pc^{-2}/Fe^{II}Pc^{-2}$ redox process which is observed at $E_P \approx 0.5$ V occurs much later than the $[Fe(CN)_6]^{3-}/[Fe(CN)_6]^{4-}$ redox process (at $E_{½} \cong 0.1$ V). The FePcNPs are therefore electro-inactive at this low potential at pH 7 and may negatively affect the activity of the more electro-active MWCNTs by occupying potentially active sites.

The values of n in **Table 3.1** are all close to 1, therefore all the electrodes display pseudo-capacitive behaviour at their electrode-solution interfaces. From **Figure 3.13**, it is observed that the phase angles for the different electrodes are less than the 90° associated with pure capacitive behaviour, confirming that all the electrodes display pseudo-capacitive behaviour.

The electron transfer rate constant (k_{et}) at the electrode surfaces of the different electrodes can also be determined from the listed electron transfer resistances (R_{et}). R_{et} is related to the exchange current density (I_0) and k_{et} through the equations 3.4 and 3.5:

$$R_{et} = \frac{RT}{nFI_0} \qquad \textbf{3.4}$$

$$I_0 = nFAK_{et}[S] \qquad \textbf{3.5}$$

where R is the gas constant, T is the temperature, A is the effective electrode area (= 0.192 cm^2), [S] corresponds to the bulk molar concentration (M) of the redox probe, and n is the number of transferred electrons per molecule of the redox probe [4]. The electron transfer rate constants for the modified MWCNT-BPPGEs are also listed in **Table 3.1**. The R_{et} values are higher for NiPcNP/MWCNT-BPPGE than for FePcNP/MWCNT-BPPGE, confirming the slow electron transfer for the latter.

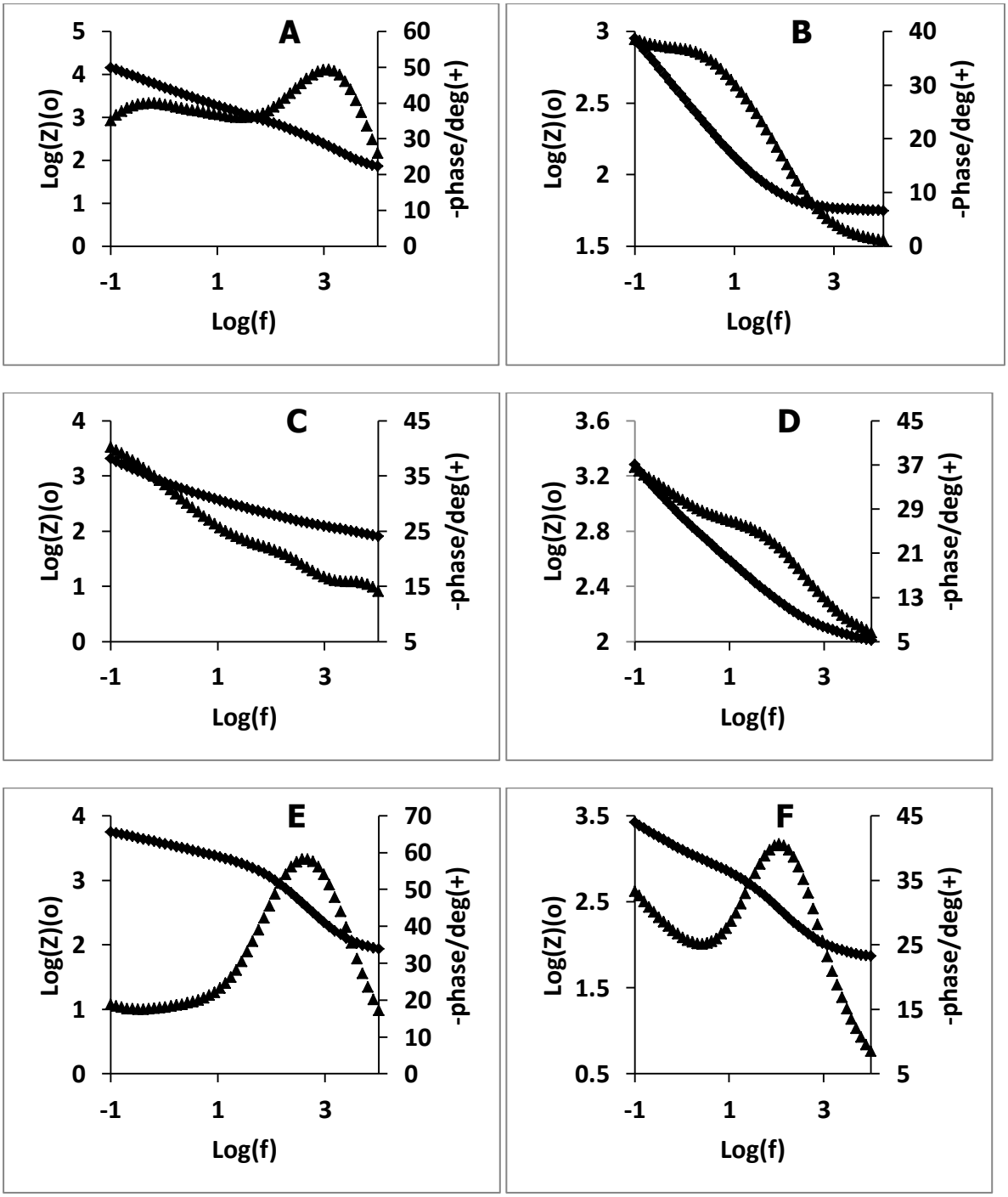

Figure 3.13: Bode plots for BPPGE(A), MWCNT-BPPGE(B), NiPcNP-BPPGE(C), NiPcNP/MWCNT-BPPGE(D), FePcNP-BPPGE(E), and FePcNP/MWCNT-BPPGE(F) in 0.1 M phosphate buffer solution (pH 7) containing 10^{-3} M $K_3[Fe(CN)_6]/K_4[Fe(CN)_6]$ (1:1), obtained at a fixed potential (E) = 0.084 V.

3.4.2 Characterization of *poly*-MTAPc-MWCNT-BPPGEs and *poly*-MTAPc-BPPGEs.

3.4.2.1 SEM characterization of *poly*-MTAPc-MWCNT-BPPGEs

The surface topography of the bare and modified BPPGE surface was investigated by scanning electron microscopy (SEM). Only CoTAPc-MWCNT-BPPGEs is considered, as an example (**Figure 3.14**).

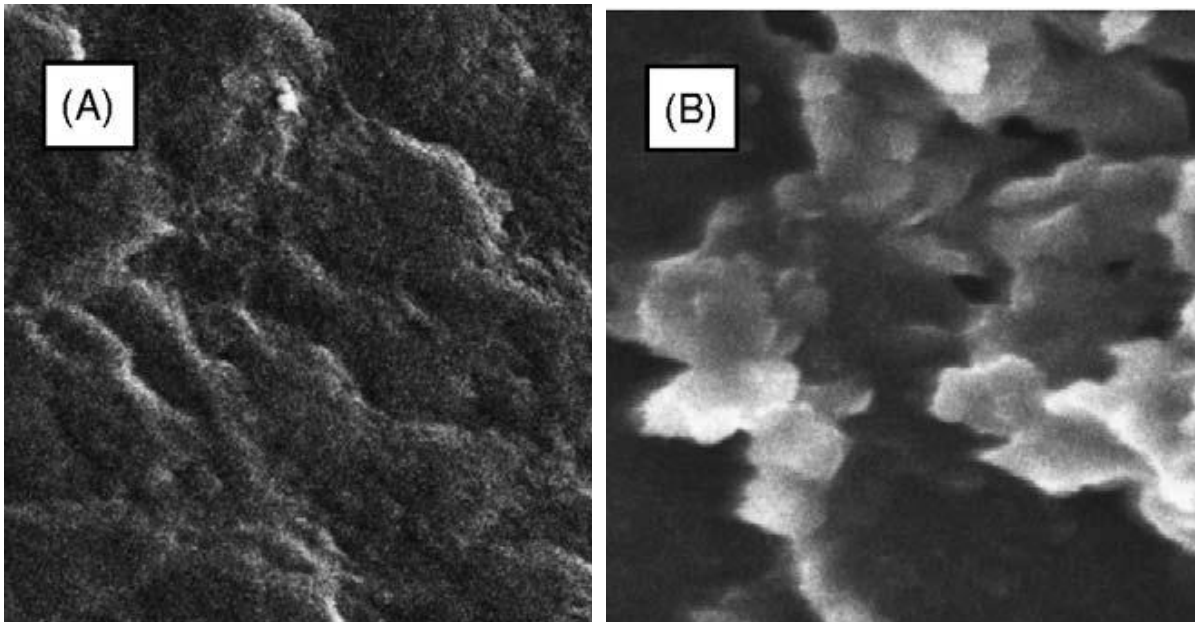

Figure 3.14: SEM images of (A) MWCNT–BPPGE and (B) *poly*-CoTAPc–MWCNT–BPPGE at 1000× magnification.

A clear difference in the textures of the two electrodes was revealed, confirming the deposition of the MTAPc onto the surface of the MWCNT–BPPGE. The white cloudy clusters in the micrograph in **Figure 3.14B** can be attributed to the grown CoTAPc particles on the MWCNTs.

3.4.2.2 Electrochemical characterization of *poly*-MTAPc-MWCNT-BPPGEs

3.4.2.2.1 Electrochemical characterization in a buffer solution.

After the electropolymerization process, the modified electrodes (*poly*-MTAPc–MWCNT–BPPGE) were rinsed in DMSO and CV scans of a blank (pH 7 buffer) recorded. **Figure 3.15** shows the first and tenth CV scans of *poly*-MnTAPc-MWCNT-BPPGE, *poly*-FeTAPc-MWCNT-BPPGE, *poly*-NiTAPc-MWCNT-BPPGE, and *poly*-CoTAPc-MWCNT-BPPGE in pH 7 phosphate buffer solution.

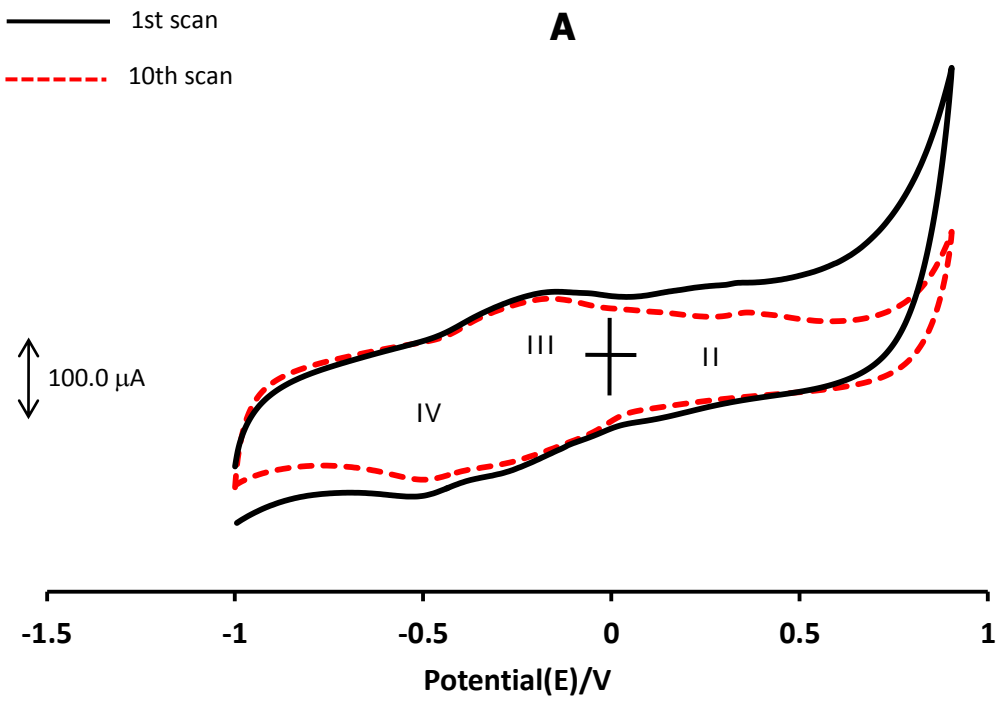
A
1st scan
10th scan
100.0 µA
III
II
IV
-1.5
-1
-0.5
0
0.5
1
Potential(E)/V

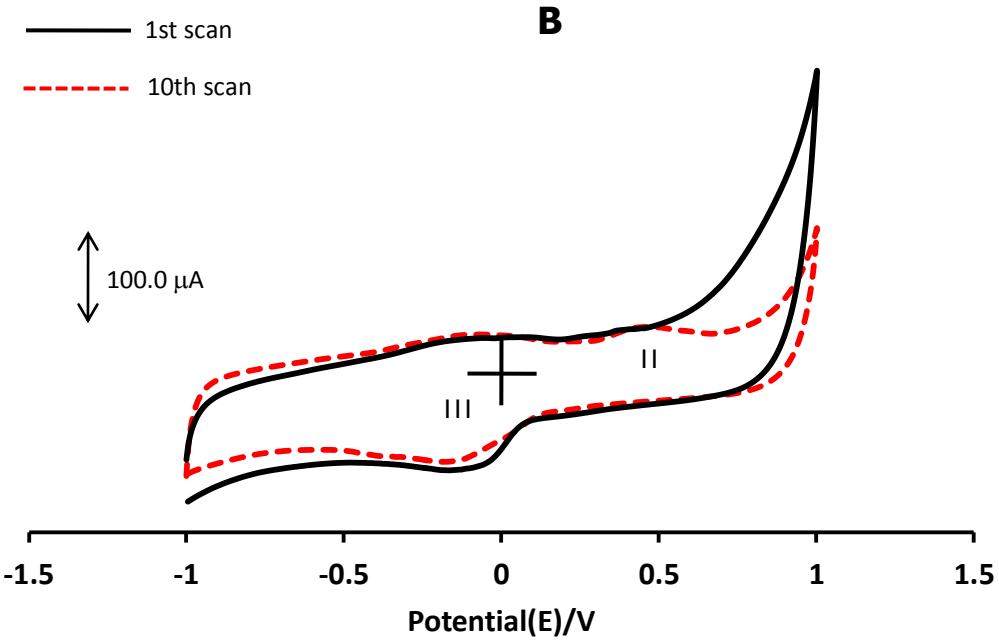
B
1st scan
10th scan
100.0 µA
II
III
-1.5
-1
-0.5
0
0.5
1
1.5
Potential(E)/V

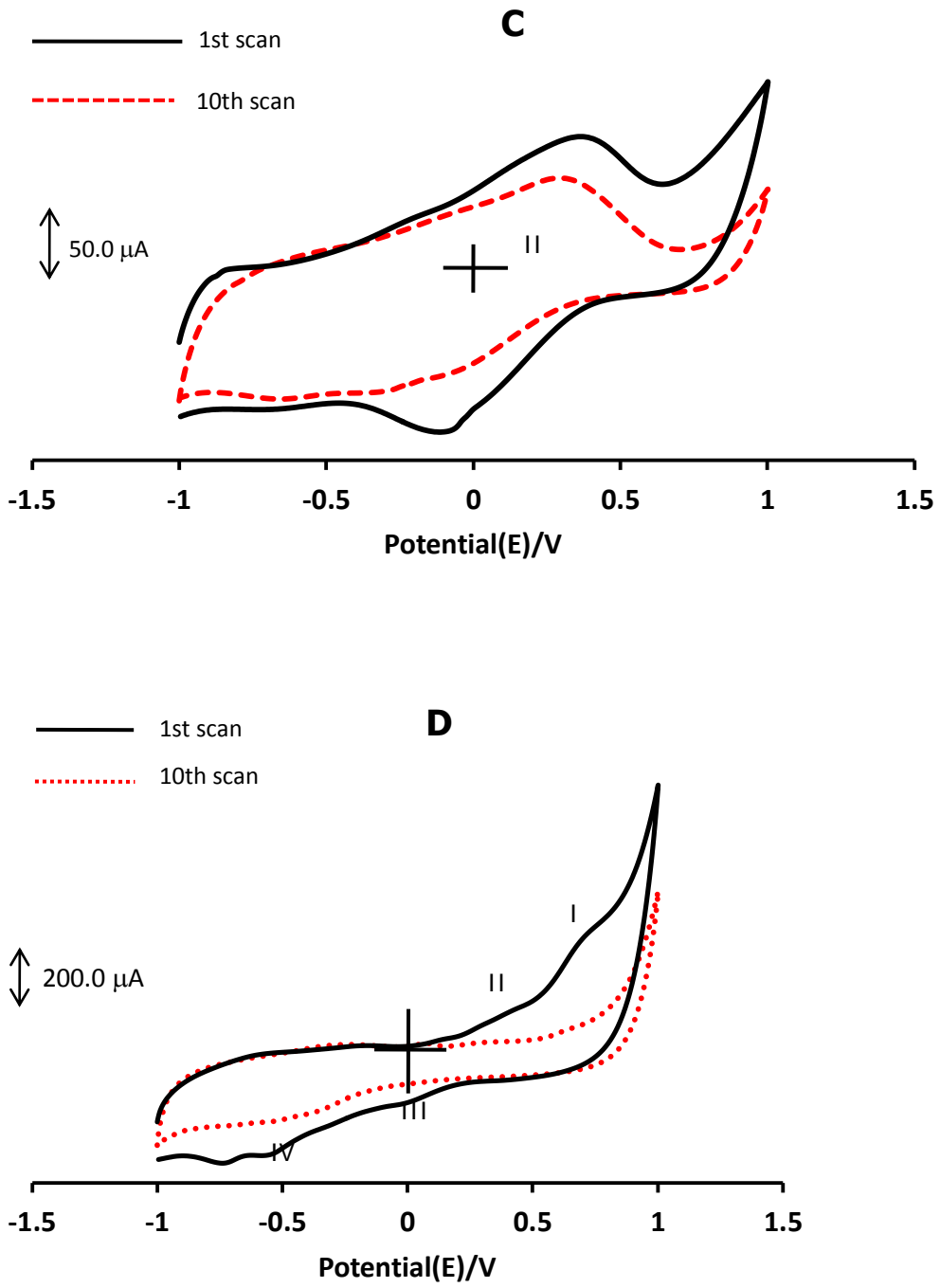

Figure 3.15: Cyclic voltammograms of a *poly*-MnTAPc–MWCNT–BPPGE (A), *poly*-FeTAPc-MWCNT-BPPGE (B), *poly*-NiTAPc-MWCNT-BPPGE (C), and *poly*-CoTAPc-MWCNT-BPPGE (D) in 0.1M phosphate buffer, pH 7, showing the 1st(—) and 10th (·····)scans. Scan rate = 0.050 V/s. Reference electrode: Ag|AgCl (3 M KCl).

When the *poly*-MnTAPc-MWCNT-BPPGE is scanned in pH 7 buffer solution (**Figure 3.15A**), the redox processes can be clearly seen and are assigned as follows: peak **II** (at $E_P \approx 0.41$ V) is due to the $Mn^{IV}Pc^{-2}/Mn^{III}Pc^{-2}$ oxidation process , couple **III** ($E_{½}$

≈ -0.17 V) is due to $Mn^{III}Pc^{-2}/Mn^{II}Pc^{-2}$ reduction (**Table 3.2**), and peak **IV** (E_P ≈ -0.40 V) is due to $Mn^{II}Pc^{-2}/Mn^{II}Pc^{-3}$ ring-reduction [253]. Only processes involved in electrocatalysis (to be discussed later) are shown in **Table 3.2**. The redox processes with the *poly*-FeTAPc-MWCNT-BPPGE (**Figure 3.15B**) are assigned as follows: peak **II** (at $E_P \cong 0.41$ V) is due to $Fe^{III}Pc^{-2}/Fe^{II}Pc^{-2}$ process, and couple **III** (at $E_{1/2} \cong -0.20$ V) is due to $Fe^{II}Pc^{-2}/Fe^{I}Pc^{-2}$ redox process [254]. Upon multiple scanning in the pH 7 phosphate buffer solution, the cathodic peak of process **II** in **Figure 3.15C** gradually decreases in height until only the anodic peak remains at ~0.23 V. Couple **II** is attributed to the $Ni^{III}Pc^{-2}/ Ni^{II}Pc^{-2}$ metal oxidation process discussed earlier for NiPcNP/MWCNT-BPPGE. With the *poly*-CoTAPc-MWCNT-BPPGE (**Figure 3.15D**), up to five redox processes were observed during the first scan. Process **II** (at ~ 0.39 V) is assigned to the $Co^{III}Pc^{-2}/Co^{II}Pc^{-2}$ redox process [161]. Process **I** (at 0.73 V) is most likely due to ring-based processes. The peak at ~ 0.1V is due to the redox property of the oxygen-containing moieties of the MWCNT [260]. The $Co^{III}Pc^{-2}/Co^{II}Pc^{-2}$ process is known to be irreversible and notoriously difficult to observe for adsorbed CoPc complexes [32]. With cycling, the processes decreased in intensity, until only **IV** remains. The attached MTAPcs gave reproducible voltammograms in aqueous solutions (pH 4.0 and 7.0), indicating excellent electrochemical stability.

Table 3.2: Oxidation potentials (E_P/V vs Ag|AgCl (3 M KCl)) of redox processes occurring at the surfaces of different electrodes in pH 12 phosphate buffer solutions. The values in brackets were obtained in pH 7 solutions.

Electrode	$M^{III}Pc^{-2}/M^{II}Pc^{-2}$	$M^{IV}Pc^{-2}/M^{III}Pc^{-2}$	Ring oxidation
FePcNP/MWCNT-BPPGE	0.25 (0.5)	----------	----------
NiPcNP/MWCNT-BPPGE	-----(0.38)	----------	-----(0.71)
Poly-MnTAPc-MWCNT-BPPGE	-0.29(-0.17)	0.23(0.41)	----------
Poly-FeTAPc-MWCNT-BPPGE	0.23(0.41)	----------	----------
Poly-NiTAPc-MWCNT-BPPGE	0.42(0.23)	----------	0.88(0.73)
Poly-CoTAPc-MWCNT-BPPGE	0.53(0.39)	----------	-----(0.73)
Poly-MnTAPc-BPPGE	-----(-0.59)	0.32(-----)	(----)(0.73)
Poly-FeTAPc-BPPGE	0.38(-----)	----------	----------
Poly-NiTAPc-BPPGE	0.53(-0.26)	----------	1.02(0.72)
Poly-CoTAPc-BPPGE	0.56(-----)	----------	----------
MnPcNP-CPE	0.07(----)	0.42(-----)	0.79(0.71)
FePcNP-CPE	0.53(0.4)	----------	------(0.8)
NiPcNP-CPE	0.06(0.13)	----------	-----(0.71)
CoPcNP-CPE	0.58(0.55)	----------	----------

The dotted lines (------) indicate that the oxidation potential could not be estimated because there was either no peak or the peak was very weak.

Cyclic voltammograms of the *poly*-MTAPc-MWCNT-BPPGEs were also obtained in pH 12 phosphate buffer solution and the peak potentials for the various redox processes are listed in **Table 3.2**. These processes have been assigned as they have been in the pH 7 phosphate buffer, except that the peaks tend to shift to lower potentials because of stabilization of the oxidized form of the phthalocyanine metal centres by the anions of the buffer solution [262]. Only the cyclic voltammogram for poly-

NiTAPc-MWCNT-BPPGE in pH 12 buffer solution is shown in **Figure 3.16**, to show the formation of O-Ni-O oxo-briges. In **Figure 3.16**, peak **I** (~0.88 V) (**Table 3.2**) is attributed to $Ni^{II}Pc^{-1}/Ni^{II}Pc^{-2}$ ring oxidation. Upon cycling of the *poly*-NiTAPc-MWCNT-BPPGE in pH 12 phosphate buffer solution, and from the second scan onwards, there was a formation of anodic and cathodic waves between +0.2 V and +0.5V (process **II**). These waves are known to correspond to the $Ni^{III}Pc^{-2}/Ni^{II}Pc^{-2}$ redox process [250,263] and are an indication of the transformation of the NiTAPc polymer into the O–Ni–O oxo-bridged form. The process **III** is attributed to $Ni^{II}Pc^{-2}$ ring reduction.

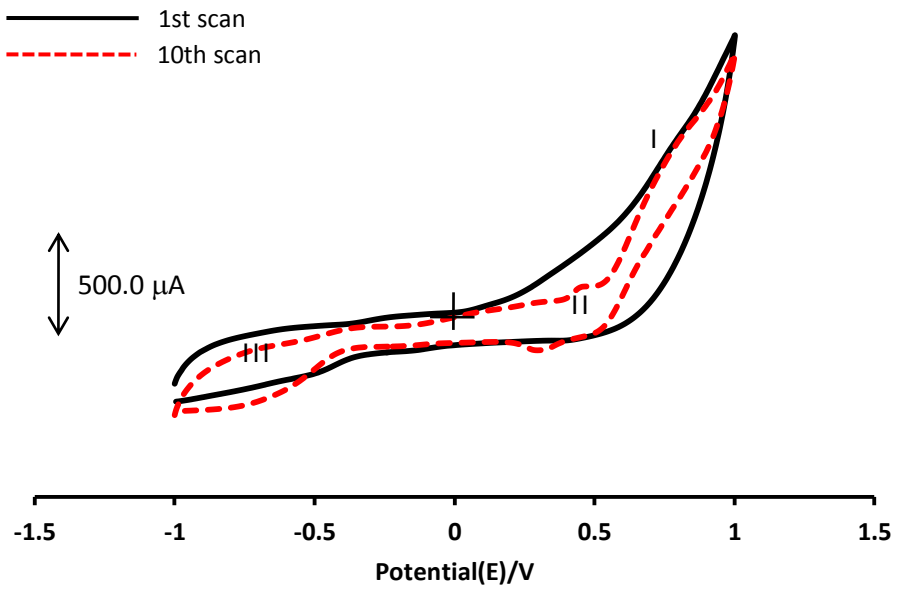

Figure 3.16: A cyclic voltammogram of *poly*-NiTAPc-MWCNT-BPPGE in 0.1 M phosphate buffer, pH 12, showing the 1st(—) and 10th (·····) scans. Scan rate = 0.050 V/s. Reference electrode: Ag|AgCl (3 M KCl).

The surface coverages ($\Gamma_{MTAPc\text{-}MWCNT}$) for *poly*-MTAPc–MWCNT–BPPGE in aqueous conditions were estimated by integrating the charge under the anodic peak of couple **III** ($Mn^{III}Pc^{-2}/Mn^{II}Pc^{-2}$) in **Figure 3.15A**, cathodic peak of couple **III** ($Fe^{II}Pc^{-2}/Fe^{I}Pc^{-2}$) in **Figure 3.15B**, anodic peak **II** ($Ni^{III}Pc^{-2}/Ni^{II}Pc^{-2}$) in **Figure 3.15C**, and the cathodic peak of the $Co^{II}Pc^{-2}/Co^{I}Pc^{-2}$ couple (**III**) in **Figure 3.15D**, and then employing equation 3.3 as has been done previously. The surface coverages were estimated to be ~ 1.2×10^{-8} mol cm^{-2} for *poly*-MnTAPc-MWCNT-BPPGE, ~ 1.5×10^{-8} mol cm^{-2} for *poly*-NiTAPc-MWCNT-BPPGE, ~ 1.7×10^{-8} mol cm^{-2} for *poly*-FeTAPc-MWCNT-BPPGE, and 0.3×10^{-8} mol cm^{-2} for *poly*-CoTAPc-MWCNT-BPPGE. These values are also listed in **Table 3.1**. These surface coverages are thicker than those reported for similar polymer films on electrode surfaces (which lie in the 10^{-9} mol cm^{-2} range) [264] probably because of the underlying carbon nanotubes.

The *poly*-MTAPc-BPPGEs (that is, the BPPGEs modified with *poly*-MTAPcs, but without co-modification with MWCNTs) were also repeatedly scanned in pH 7 and pH 12 phosphate buffer solutions, and the peak potentials of the processes displayed in the cyclic voltammograms are listed in **Table 3.2**.

By utilizing the CVs obtained in pH 7 phosphate buffer solution with the *poly*-MTAPc-BPPGEs and equation 3.3, the surface coverages of these electrodes were obtained. The surfaces coverages were estimated to be ~0.62 $\times$ 10^{-9} for *poly*-MnTAPc-BPPGE, ~1.0 $\times$ 10^{-9} mol/cm^{-2} for *poly*-FeTAPc-BPPGE, ~0.6 $\times$ 10^{-9} for *poly*-NiTAPc-BPPGE, and ~1.0 $\times$ 10^{-9} for *poly*-CoTAPc-BPPGE. These surface coverages are comparable to those reported for similar polymer films on electrode surfaces [264].

3.4.2.2.2 Electrochemical characterization in $K_3[Fe(CN)_6]/K_4[Fe(CN)_6]$ solution

The electrochemical behaviour of the different electrodes was also interrogated using the 1.0 mM $K_3[Fe(CN)_6]/K_4[Fe(CN)_6]$ (1:1) solution containing 0.05 M KCl as a redox probe. **Figure 3.17** shows CVs of the MWCNT–BPPGE, *poly*-MTAPc–MWCNT–BPPGE, *poly*-MTAPc–BPPGE (M = Mn, Fe, Ni, and Co) and bare BPPGE recorded in this solution.

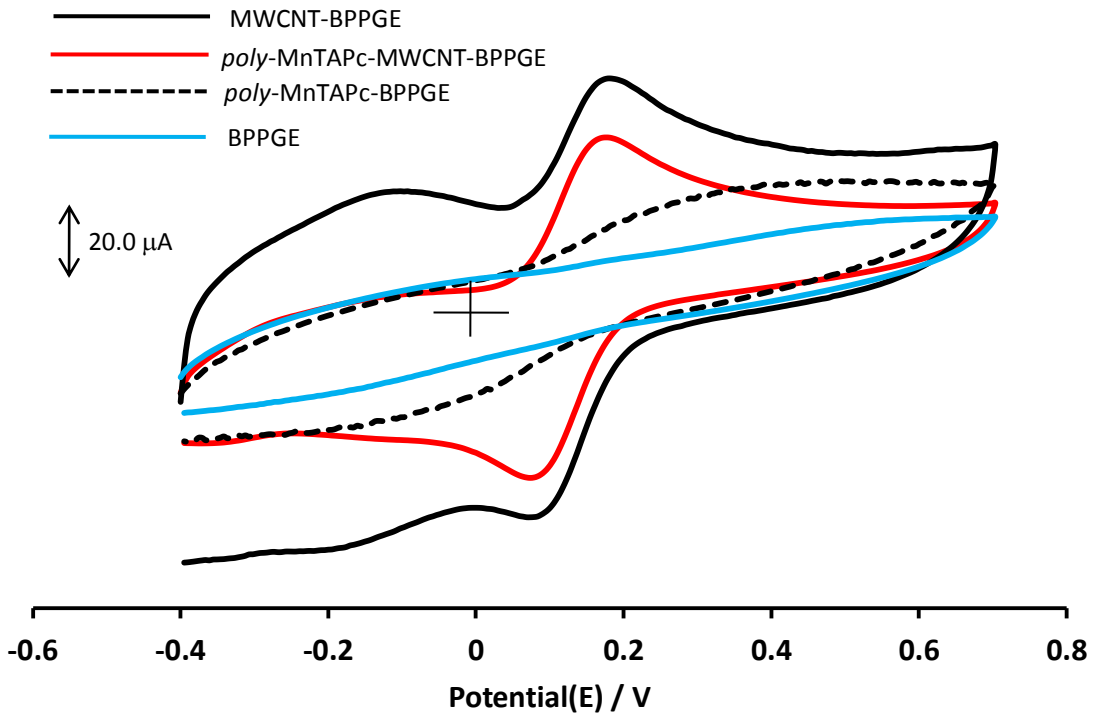
MWCNT-BPPGE
poly-MnTAPc-MWCNT-BPPGE
poly-MnTAPc-BPPGE
BPPGE
20.0 µA
-0.6
-0.4
-0.2
0
0.2
0.4
0.6
0.8
Potential(E) / V

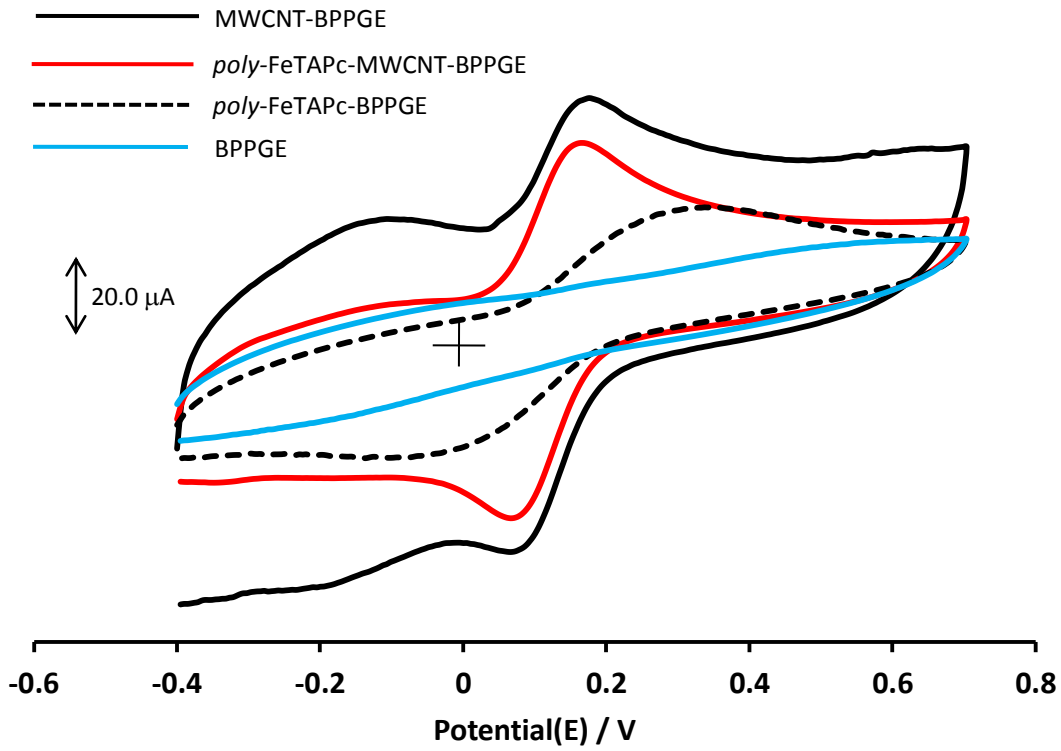
MWCNT-BPPGE
poly-FeTAPc-MWCNT-BPPGE
poly-FeTAPc-BPPGE
BPPGE
20.0 µA
-0.6
-0.4
-0.2
0
0.2
0.4
0.6
0.8
Potential(E) / V

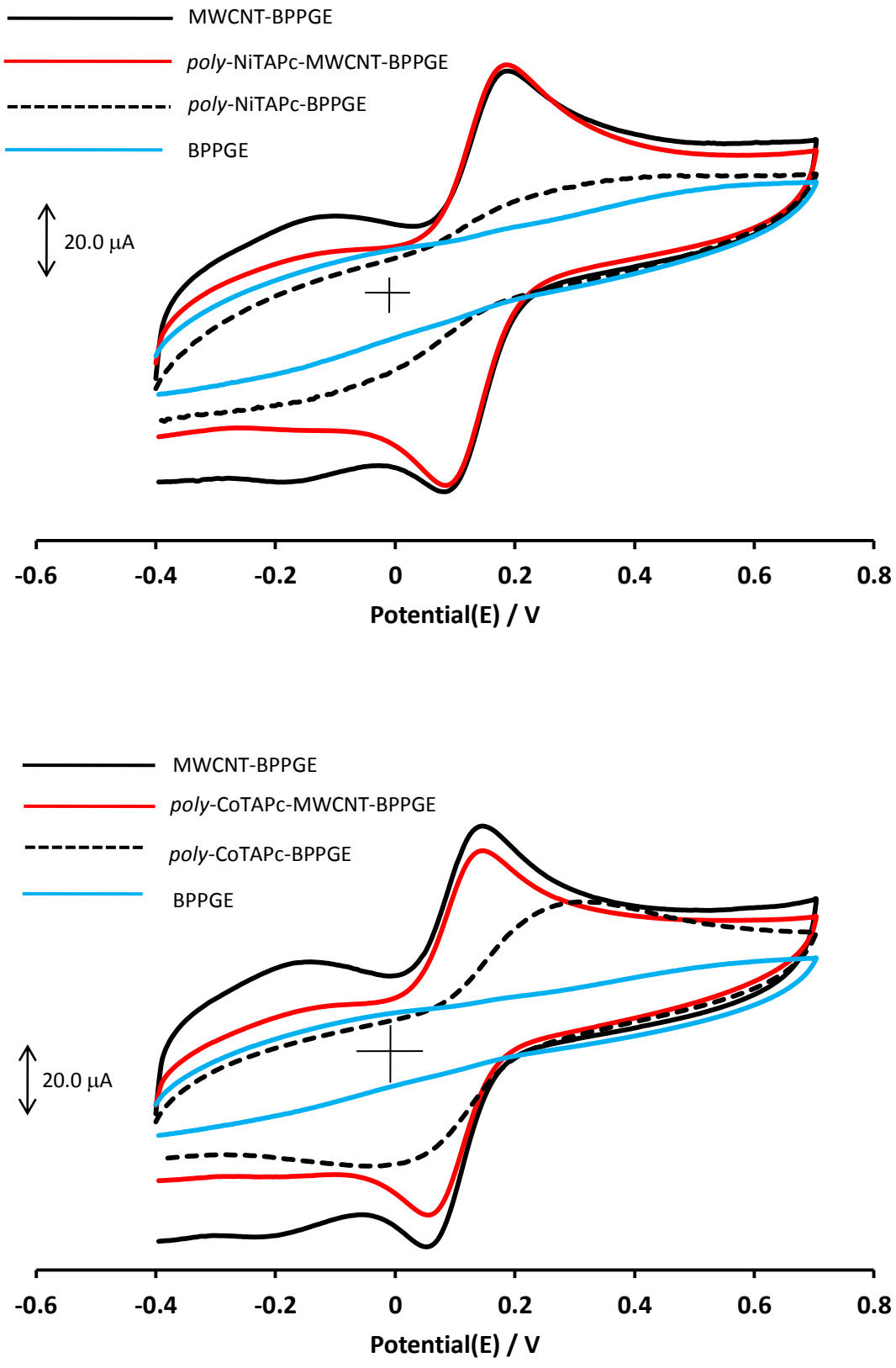

Figure 3.17: Cyclic voltammograms of *poly*-MTAPc-MWCNT-BPPGE (M = Mn, Fe, Ni, and Co), *poly*-MTAPc-BPPGE, MWCNT-BPPGE, and BPPGE in 10^{-3}M $[Fe(CN)_6]^{-3}/[Fe(CN)_6]^{4-}$ containing 0.05 M KCl. Scan rate = 25 mV/s. Reference Electrode: Ag|AgCl (3 M KCl).

The MWCNT–BPPGE and *poly*-MTAPc–MWCNT–BPPGE showed approximately similar current responses. This result confirms that the attachment of the MTAPc onto the MWCNT does not adversely affect the electronic properties of the MWCNT, in agreement with previous literature observation [265]. The peak separation (ΔE) of the $[Fe(CN)_6]^{3-}/[Fe(CN)_6]^{4-}$ solution with the different electrodes follows the trend: BPPGE > *poly*-MTAPc-BPPGE > MWCNT-BPPGE ≥ *poly*-MTAPc-MWCNT-BPPGE. Values of peak separations (ΔE) for the different electrodes are given in **Table 3.1**. The rate of electron transfer at the electrode surface is therefore improved with the attachment of MWCNTs and MTAPcs to the BPPGE surface. For the differrent *poly*-MTAPc-MWCNT-BPPGEs, the peak separations follow the following trend: *poly*-NiTAPc-MWCNT-BPPGE (~93 mV) > *poly*-MnTAPc-MWCNT-BPPGE (~88 mV) = *poly*-FeTAPc-MWCNT-BPPGE (~88 mV) > *poly*-CoTAPc-MWCNT-BPPGE (~80 mV). The small ΔE value obtained for *poly*-CoTAPc-MWCNT-BPPGE indicates that this electrode exhibits faster electron-transfer kinetics at the electrode surface than the other MTAPc-MWCNT-BPPGEs, when the potassium ferricyanide/ferrocyanide solution is used as the probe. The reactivity of the different electrodes will be investigated further, using amitrole and asulam as the test solutions.

The electrodes were also characterized using electrochemical impedance spectroscopy. **Figure 3.18** shows the Nyquist (Z″ vs Z') plots for *poly*-FeTAPc-MWCNT-BPPGE, *poly*-MnTAPc-MWCNT-BPPGE, *poly*-NiTAPc-MWCNT-BPPGE, *poly*-CoTAPc-MWCNT-BPPGE and MWCNT-BPPGE in the 1 mM $[Fe(CN)_6]^{3-}/[Fe(CN)_6]^{4-}$ solution.

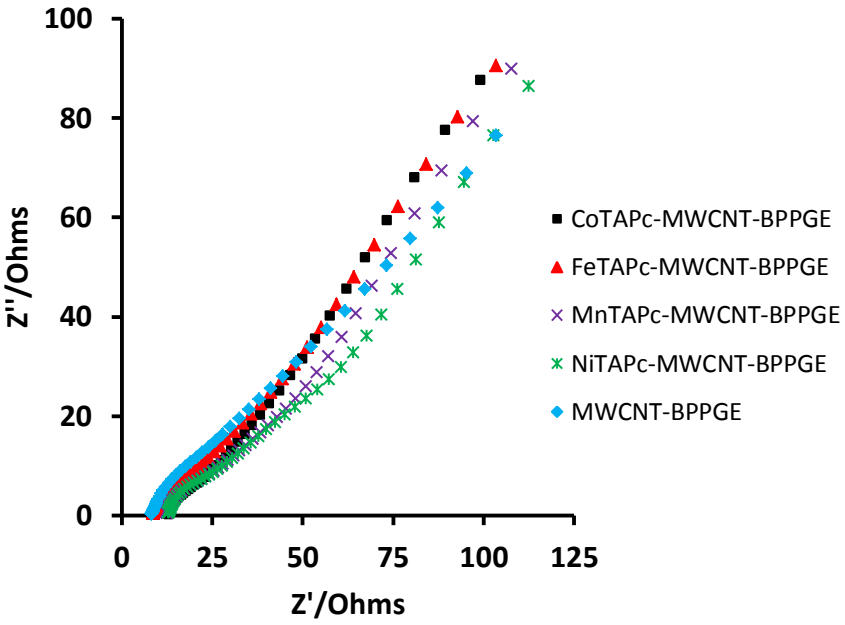

Figure 3.18: Nyquist (Z″ vs Z′) plot of different electrodes in 1 mM $[Fe(CN)_6]^{-3}/[Fe(CN)_6]^{4-}$ solution containing 0.05 M KCl. $E_{1/2}$ = 0.124 V.

The pertinent data from the plots is shown in **Table 3.1** together with the electron transfer rate constants (k_{et}). For the *poly*-MTAPc-MWCNT-BPPGEs, the electron-transfer resistance, R_{et}, follows the trend: *poly*-NiTAPc-MWCNT-BPPGE (0.128 kΩ) > *poly*-FeTAPc-MWCNT-BPPGE (0.116 kΩ) ≅ *poly*-MnTAPc-MWCNT-BPPGE (0.113 kΩ) > *poly*-CoTAPc-MWCNT-BPPGE (0.083 kΩ). Correspondingly, the electron-transfer rate constant follows the trend: *poly*-CoTAPc-MWCNT-BPPGE (1.67×10^{-5} cm s^{-1}) > *poly*-MnTAPc-MWCNT-BPPGE (1.23×10^{-5} cm s^{-1}) > *poly*-FeTAPc-MWCNT (1.19×10^{-5} cm s^{-1}) > *poly*-NiTAPc-MWCNT-BPPGE (1.08×10^{-5} cm s^{-1}), again showing the superiority of the *poly*-CoTAPc-MWCNT-BPPGE. The values of n for all electrodes are close but not equal to 1, the value associated with pure capacitive behavior. Therefore, pseudo-capacitive behavior is displayed by all the electrodes at the electrode-solution interface.

From the –phase angle vs log (f) plots (**Figure 3.19**), the phase angles for the different electrodes are less than the 90° expected for an ideal capacitor. This confirms the pseudo-capacitive behaviour of all the electrodes.

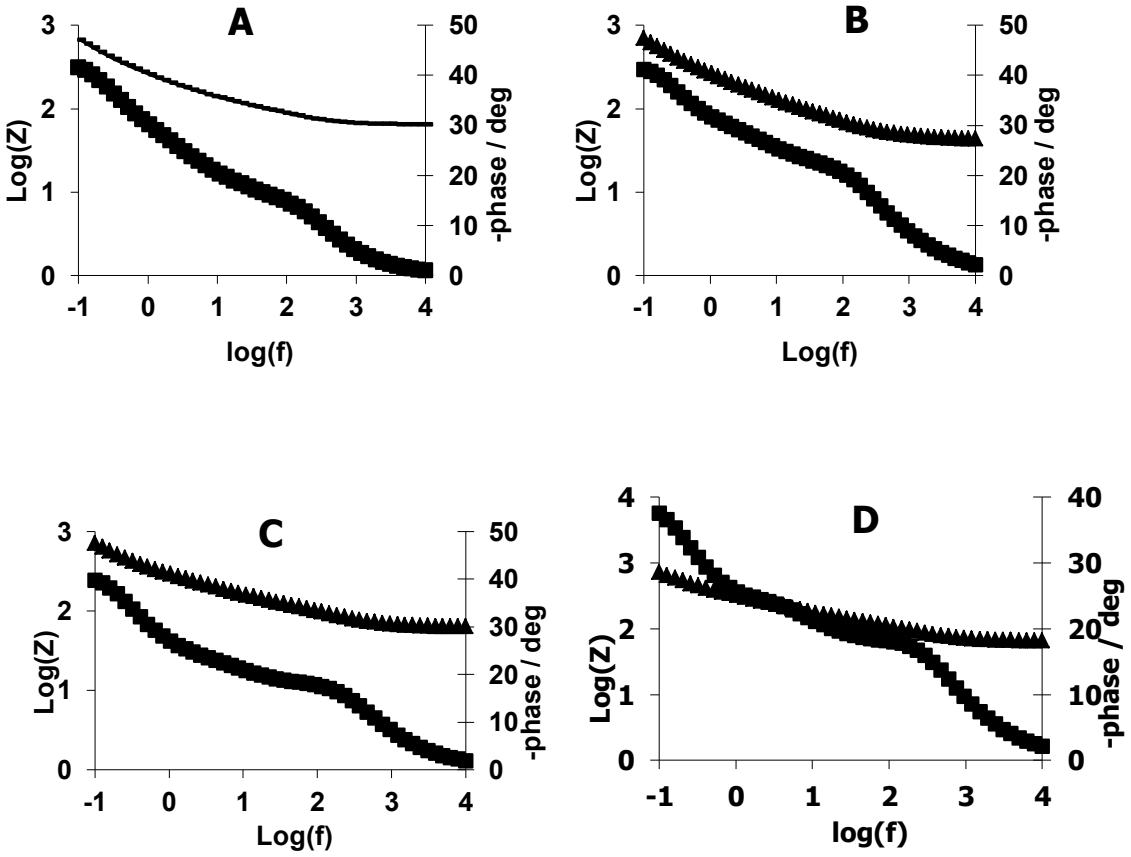

Figure 3.19: Bode plots for *poly*-CoTAPc-MWCNT-BPPGE (A), *poly*-FeTAPc-MWCNT-BPPGE (B), *poly*-MnTAPc-MWCNT-BPPGE (C), *poly*-NiTAPc-MWCNT-BPPGE (D) in a (1:1)mixture of 1.0 mM $[Fe(CN_6)]^{3-}$ /$[Fe(CN)_6]^{4-}$ solution containing 0.05 M KCl.

3.5 Electrochemical Characterization of MPcNP-CPEs

Figure 3.20 shows the cyclic voltammograms of the MPc nanoparticles-modified carbon paste electrodes (MPcNP-CPE) in 0.1 M phosphate buffer solution at pH 7.

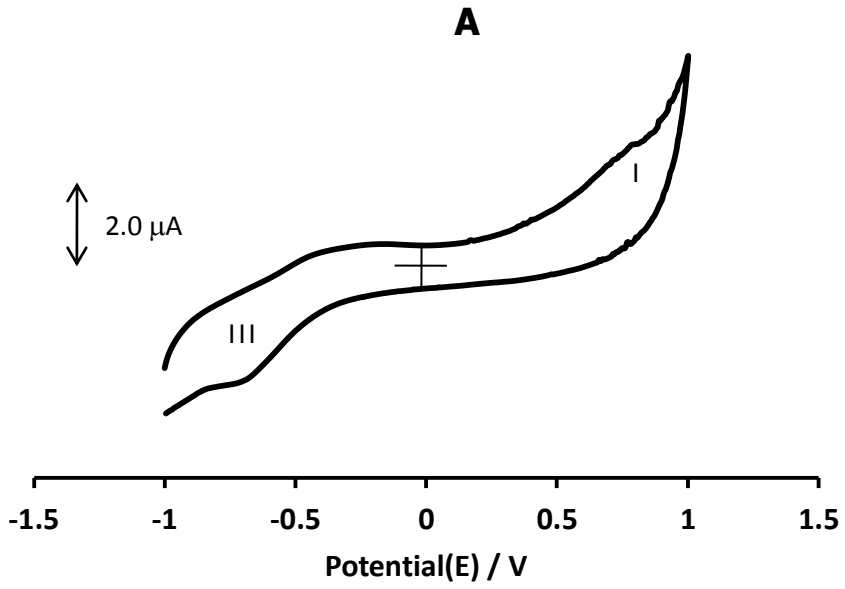
A
2.0 μA
I
III
-1.5
-1
-0.5
0
0.5
1
1.5
Potential(E) / V

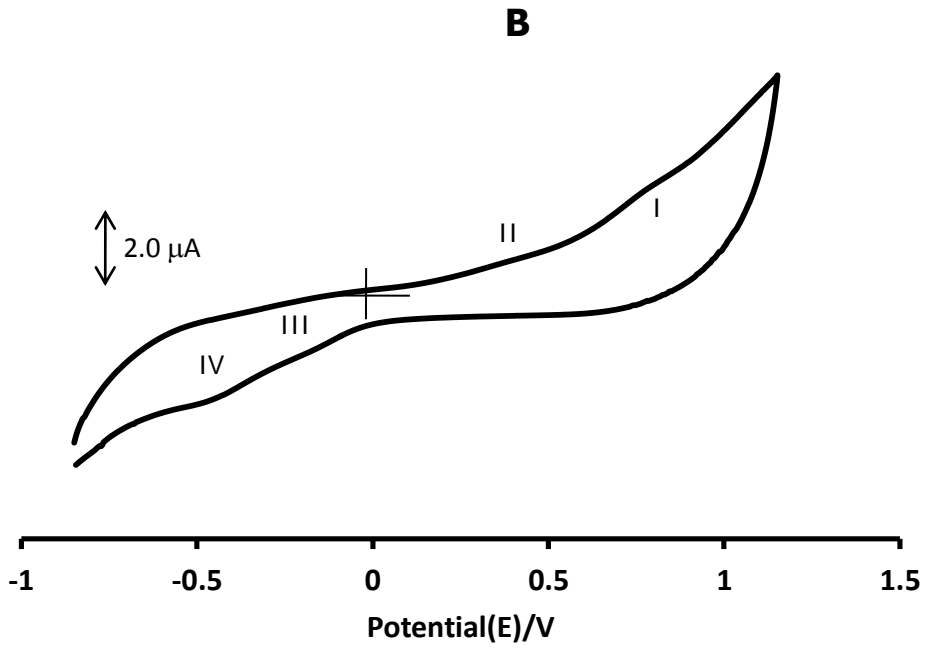
B
2.0 μA
I
II
III
IV
-1
-0.5
0
0.5
1
1.5
Potential(E)/V

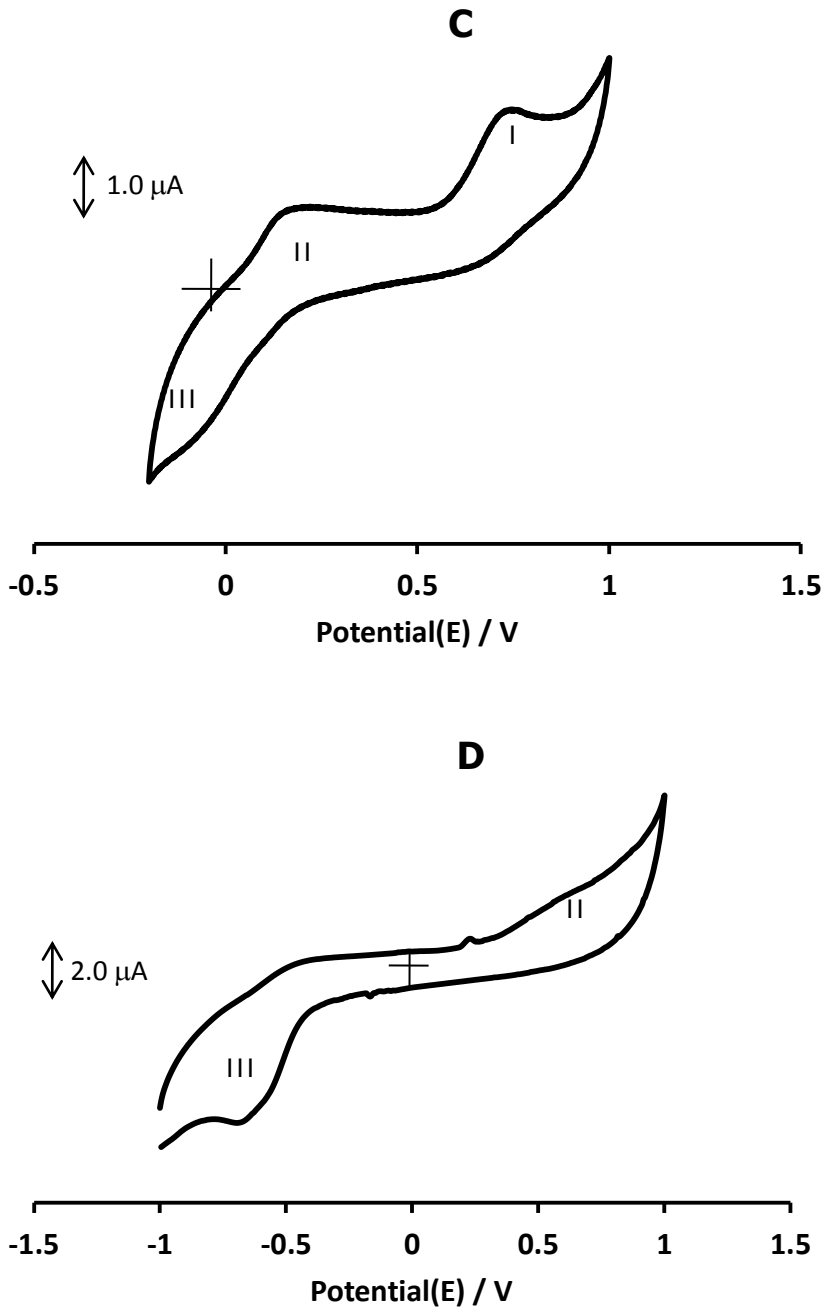

Figure 3.20: Cyclic voltammograms of MnPcNP-CPE (A), FePcNP-CPE (B), NiPcNP-CPE (C), CoPcNP-CPE in 0.1 M phosphate buffer solution at pH 7. Scan rate = 0.05 V/s. Reference electrode: Ag|AgCl (3.0 M KCl).

In **Figure 3.20A**, peak **I** which appears at $E_P \cong 0.71$ V is attributed to ring oxidation and peak **III** which appears at $E_P \cong -0.5$ V is attributed to $Mn^{III}Pc^{-2}/Mn^{II}Pc^{-2}$ metal reduction, in accordance with literature [253] (**Table 3.2**). In **Figure 3.20B**, the broad peak **I** ($E_P \cong 0.8$ V) is attributed to ring oxidation, peak **II** ($E_P \cong 0.4$) is

attributed to $Fe^{III}Pc^{-2}/Fe^{II}Pc^{-2}$ metal oxidation and peak **III** ($E_P \cong$ -0.2 V) and peak **IV** ($E_P \cong$ -0.4 V) are attributed to metal and ring reduction, respectively, in accordance with literature [254] (**Table 3.2**). In **Figure 3.20C**, peak **I** ($E_P \cong$ 0.71 V) (**Table 3.2**) is attributed to $Ni^{II}Pc^{-1}/Ni^{II}Pc^{-2}$ ring oxidation [255-256] and peak **II** ($E_P \cong$ 0.13 V) is assigned to the $Ni^{III}Pc^{-2}/Ni^{II}Pc^{-2}$ metal oxidation process (with anodic peak potential slightly shifted to lower potential because of the use of different electrodes and solutions), in accordance with previous literature assignments [256-259]. In **Figure 3.20D**, peak **II** ($E_P \cong$ 0.6 V) is assigned to $Co^{III}Pc^{-2}/Co^{II}Pc^{-2}$ metal oxidation [161] and peak **III** ($E_P \cong$ -0.58 V) is assigned to $Co^{II}Pc^{-2}/Co^{I}Pc^{-2}$ metal reduction [32, 261].

The different MPcNP-CPEs were also scanned in 0.1 M phosphate buffer at pH 12, and the peak potentials corresponding to the different processes are listed in **Table 3.2**.

3.6 Conclusions

TEM and XRD were used to show that the sizes of the NiPc particles synthesized were less than 100 nm, therefore NiPcNPs were successfully synthesized from NiPc. TEM was also employed to show that the NiPcNPs, in particular, were attached to the walls of the MWCNTs. Electrochemical experiments have shown that MWCNTs and MPcNP/MWCNT composites improve reversibility at the BPPGE surface. Also, a NiPcNP/MWCNT-BPPGE displayed faster electron transfer kinetics than a MWCNT-BPPGE, whilst the latter displayed faster electron transfer kinetics than an FePcNP/MWCNT-BPPGE.

The difference in surface topography of the MWCNT-BPPGE and CoTAPc-MWCNT-BPPGE, observed using SEM, showed that CoTAPc had been deposited on the MWCNT-BPPGE surface. Electrochemical experiments showed that CoTAPc was actually electropolymerized on the MWCNT-BPPGE surface to form a *poly*-CoTAPc-MWCNT-BPPGE. Electrochemical experiments also showed that the poly-CoTAPc-MWCNT-BPPGE displayed the fastest electron transfer kinetics at the electrode surface, of all the *poly*-MTAPc-MWCNT-BPPGEs investigated.

Chapter 4

Electroanalysis with Carbon Paste Electrodes Modified with Nanoparticles of MPcs.

In this chapter, carbon paste electrodes modified with MPcNPs are employed in the electroanalytical detection of amitrole and asulam.

4.1 Electroanalytical Detection of Amitrole

Amitrole experimental conditions were optimized using the FePcNP-CPE as the representative electrode. For the optimization of asulam experimental conditions, the NiPcNP-CPE was used for the same purpose.

4.1.1 Optimization of parameters using FePcNP-CPE

The effect of varying pH on the current response of FePcNP- CPE at constant amitrole concentration (1×10^{-3} M) was determined (**Figure 4.1**).

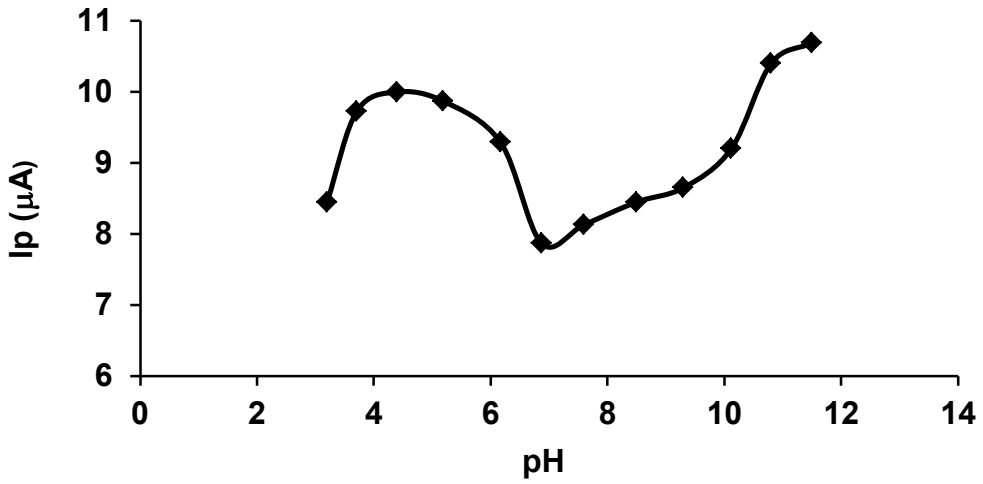

Figure 4.1: Effect of pH on current response of FePcNP-CPE in phosphate buffer containing 1 x 10^{-3} M amitrole.

There is a maximum at pH 4.4. The current response decreased from pH 4.4, but then increased from pH 7.0 and began to stabilize at pH 11.5. These observations are in agreement with the known pK_a values of 4.2 and 10.7 for amitrole [266], indicating the presence of different forms of amitrole ions in acidic and basic media. Since a larger current response was obtained at ≥pH 11.5 than at pH 4.4, it is

expected that in alkaline conditions, all the amitrole species will be completely ionized at pH 12.0, thus all subsequent experiments were performed in pH 12.0 phosphate buffer solution. From the known solution chemistry of the triazoles [267], the possible routes for the formation of the amitrole ions in acidic and basic media may be depicted as shown in **Scheme 4.1**.

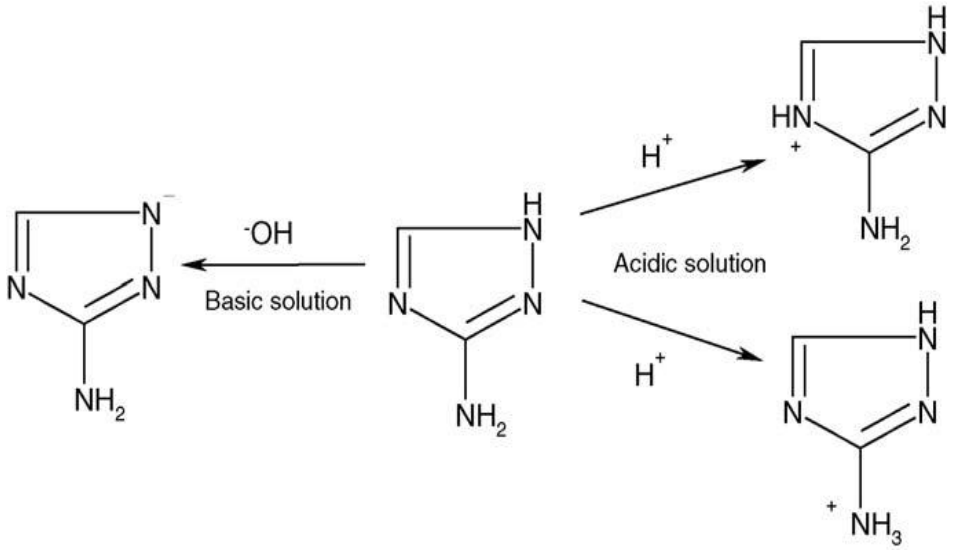

Scheme 4.1. Proposed mechanism for formation of amitrole ions in acidic and basic media.

Also, the plot of peak potential (E_p) against pH (**Figure 4.2**) shows two linear relations in acidic (pH < 7) and basic (pH > 8) media. These two linear relations would then correspond to the different forms of amitrole that exist in acidic and basic media. The magnitudes of the slopes of the lines in Figure 4.2 (ca. 53 and 60 mV/pH) indicate that one-electron (accompanied by one-proton) oxidation processes take place on the electrode surface.

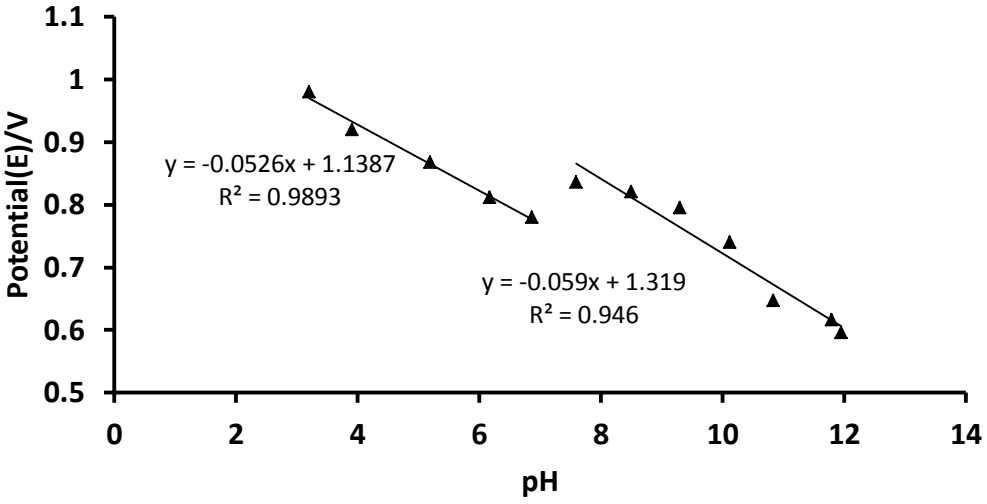

Figure 4.2: Effect of pH on peak potential for FePcNP-CPE in phosphate buffer containing 1×10^{-3} M amitrole. Supporting electrolyte is 0.05 M Na_2SO_4. Reference electrode: Ag|AgCl (3 M KCl).

The FePcNP loading on the CPE was set at 3%, because the highest amitrole current response was obtained with this fraction. (**Figure 4.3)**.

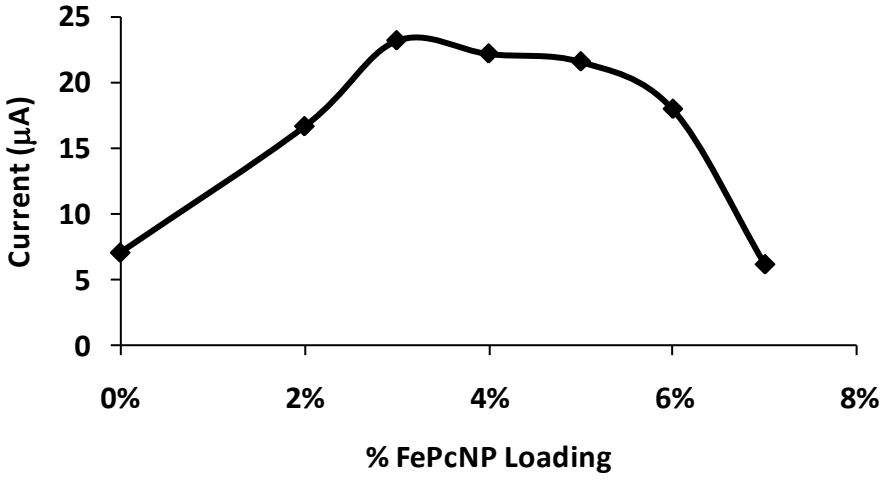

Figure 4.3: Effect of FePcNP loading of an FePcNP-CPE on the current of phosphate buffer at pH 12 containing 1×10^{-3} M amitrole.

Supporting electrolytes have been known [262] to enhance the electrocatalytic response of MPc modified electrodes towards the detection of certain analytes by increasing either the catalytic current response and/or lowering the detection

potential. The dependence of current response on the nature of anion used was thus examined. **Table 4.1** presents the electrochemical response characteristics of the FePcNP-CPE in phosphate buffer at pH 12.0, using different sodium salts as supporting electrolytes.

Table 4.1: Effect of different supporting electrolytes (0.05 M) on the current and potential response of the FePcNP-CPE at fixed amitrole concentration (1 mM) at pH 12.0 phosphate buffer solution (PBS, 0.1 M); scan rate = 25 mV/s

Electrolyte	**Current density, J, (10^4 A/cm^2)**	**Peak Potential, E_P/V (vs Ag|AgCl, 3 M KCl)**
PBS alone	3.5	0.71
CH_3COONa	5.7	0.56
$NaNO_3$	7.1	0.56
Na_2SO_4	9.2	0.55
NaCl	2.8	0.61
$NaClO_4$	4.6	0.58

From **Table 4.1** it can be seen that the highest current response and lowest peak potential were obtained with 0.05M sodium sulphate as the supporting electrolyte. This behaviour indicates that anions should be responsible for neutralizing the electrode surface, allowing the redox activity to occur. The anions should interact with the metal at the center of the FePc complex on the electrode, stabilizing the oxidized form according to the electron donor capacity [262]. Hence, all subsequent electrocatalytic experiments on amitrole were carried out using 0.05 M Na_2SO_4 as the supporting electrolyte.

4.1.2 Comparative electrocatalysis of amitrole with different MPcNP-CPEs

The optimum operating conditions established with the FePcNP-CPE (that is, 3% MPcNP loading on CPE, and 0.05 M Na_2SO_4 in pH 12 buffer solution) were employed in the investigation of the electrocatalytic behaviour of all the MPcNP-CPEs (M = Mn, Fe, Ni, Co) used in this work. **Figure 4.4** shows the cyclic voltammograms of the different MPcNP-CPEs in 1×10^{-3} M amitrole, together with those of the corresponding MPc-CPEs and bare CPEs. The data is presented in **Table 4.2**.

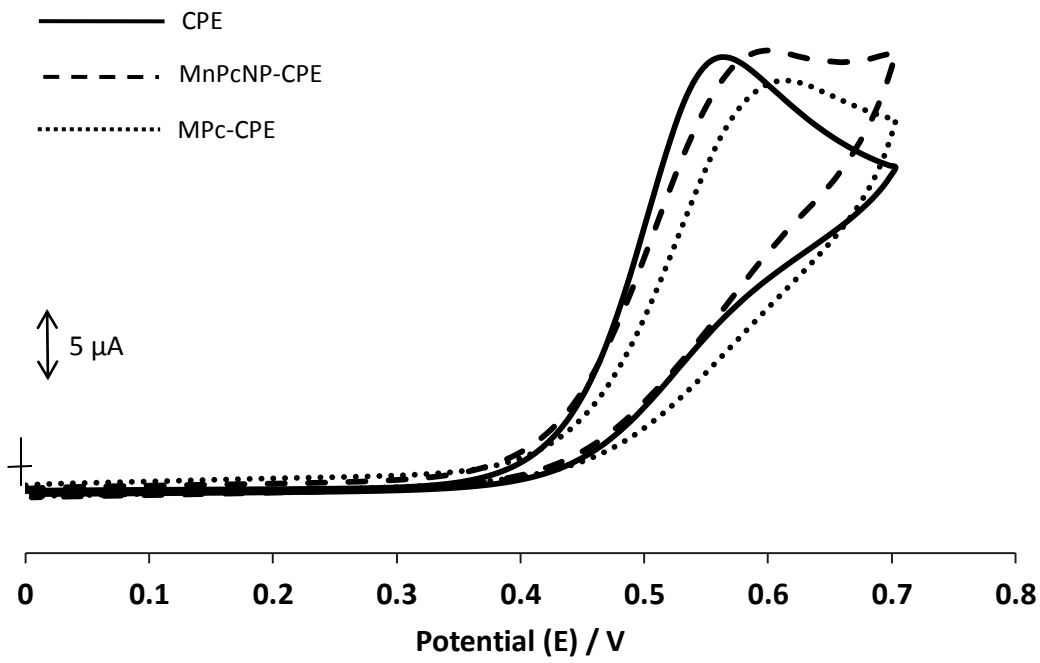
CPE
MnPcNP-CPE
MPc-CPE
5 µA
0
0.1
0.2
0.3
0.4
0.5
0.6
0.7
0.8
Potential (E) / V

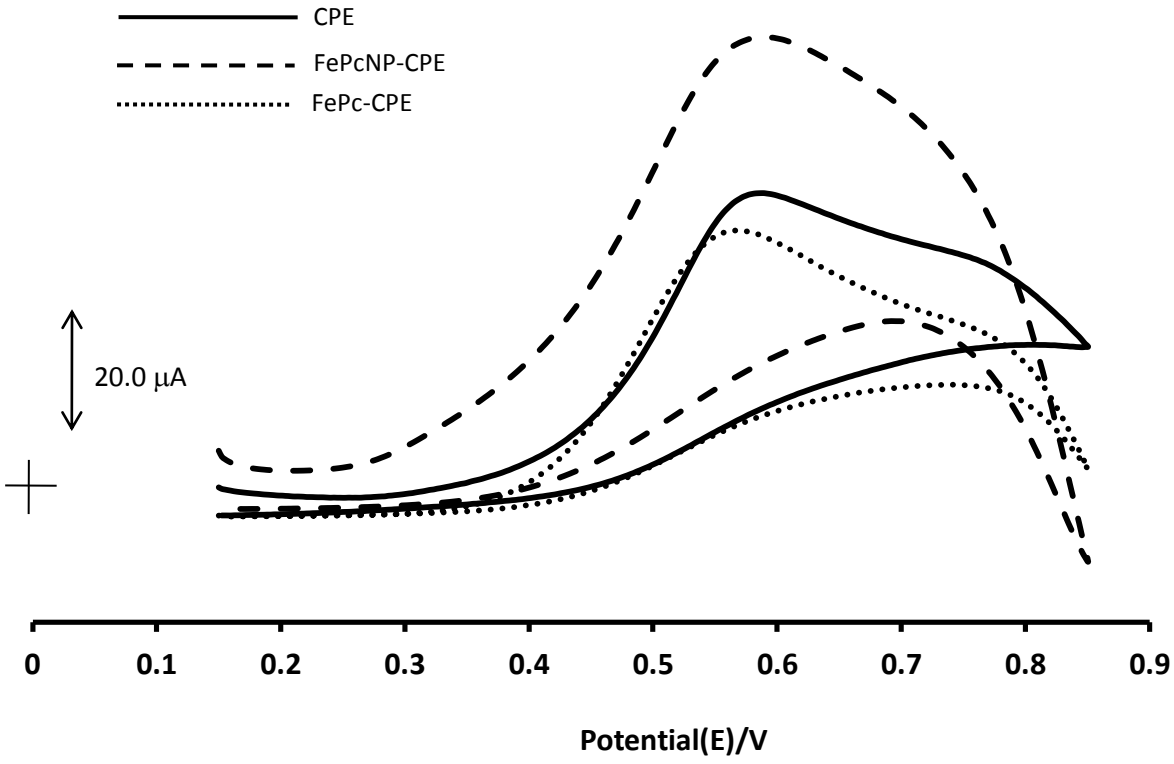
CPE
FePcNP-CPE
FePc-CPE
20.0 µA
0
0.1
0.2
0.3
0.4
0.5
0.6
0.7
0.8
0.9
Potential(E)/V

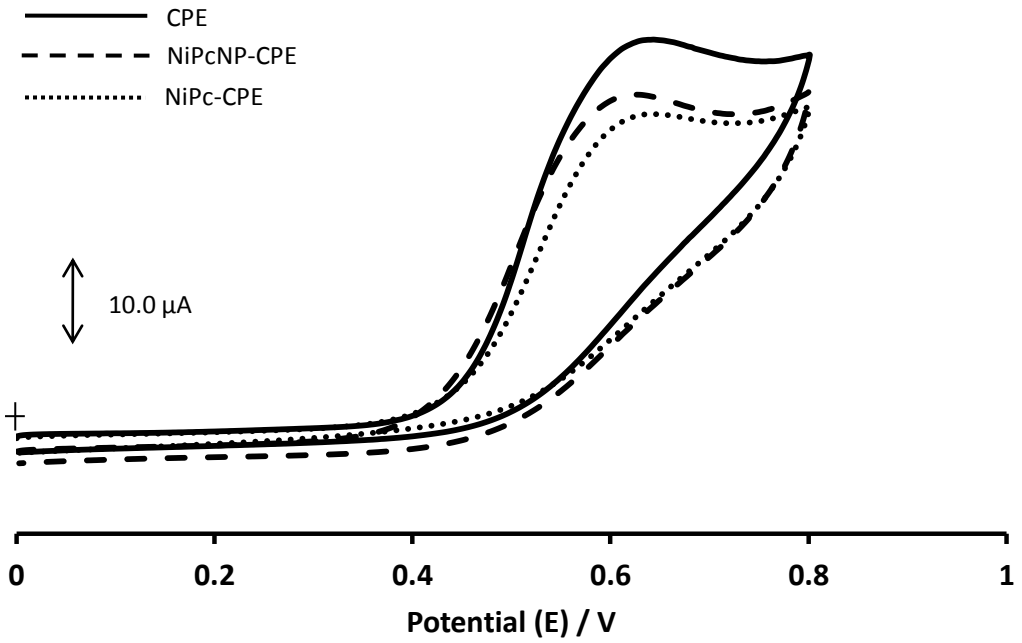

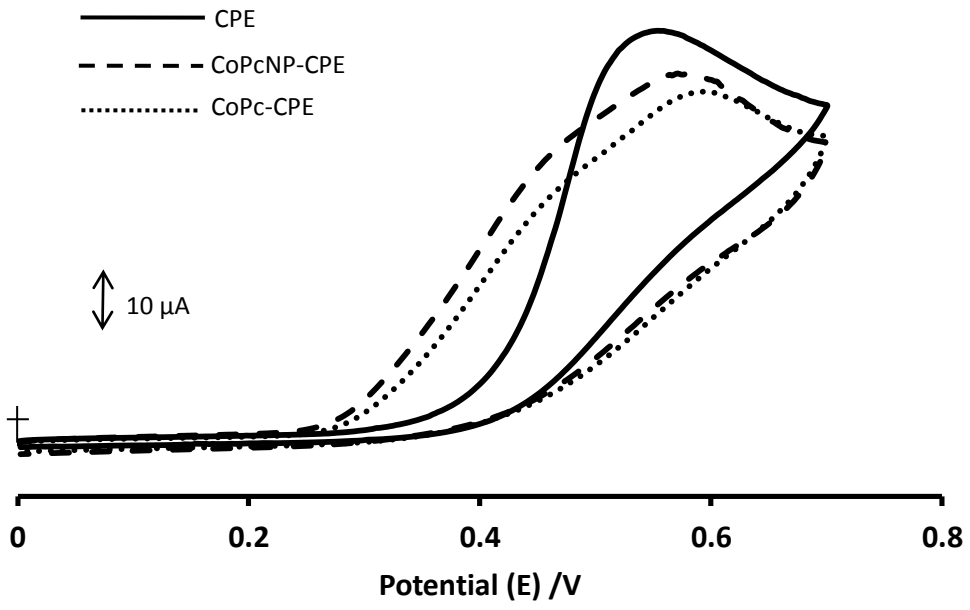

Figure 4.4: Cyclic voltammogramms obtained with MnPcNP-CPE, FePcNP-CPE (background corrected), NiPcNP-CPE, CoPcNP-CPE in pH 12 phosphate buffer solution containing 1×10^{-3} M amitrole. The CVs of the CPE and corresponding MPc-CPE are included for comparison. Reference electrode: Ag|AgCl (3 M KCl). Supporting electrolyte: 0.05 M Na_2SO_4. Scan rate = 0.025 V/s

Table 4.2: Oxidation potentials (E/V vs Ag|AgCl, 3 M KCl) of 10^{-3} M amitrole and 10^{-3} M asulam with different MPcNP-CPEs, and redox potentials of MPc in pHs 7 and 12 phosphate buffer solutions (PBS).

Electrode	Oxidation potential of 10^{-3} M amitrole	Oxidation potential of 10^{-3} M asulam	Redox process of MPc	Potential of MPc redox process in pH 12 PBS.	Potential of MPc redox process in pH 7 PBS.
CPE	0.55 V	[a]0.90 V	----------	----------	----------
MnPc-CPE MnPcNP-CPE	0.59 V 0.58 V	0.92 V 0.91 V	$Mn^{IV}Pc^{-1}/Mn^{IV}Pc^{-2}$ $Mn^{IV}Pc^{-2}/Mn^{III}Pc^{-2}$	0.42 V 0.07 V	0.71 V
FePc-CPE FePcNP-CPE	0.55 V 0.55 V	0.91 V 0.91 V	$Fe^{III}Pc^{-2}/Fe^{II}Pc^{-2}$	0.53 V	0.41 V
NiPc-CPE NiPcNP-CPE	0.58 V 0.58 V	0.93 V 0.93 V	$Ni^{III}Pc^{-2}/Ni^{II}Pc^{-2}$ $Ni^{II}Pc^{-1}/Ni^{II}Pc^{-2}$	0.06 V	0.13 V 0.71 V
CoPc-CPE CoPcNP-CPE	0.45 V 0.45 V	0.91 V 0.90 V	$Co^{III}Pc^{-2}/Co^{II}Pc^{-2}$	0.58 V	0.6 V

[a]In the CVs of NiPc-CPE, NiPcNP-CPE and CPE in 10^{-3}M asulam, $E_{CPE} \cong 0.94$ V.

Figure 4.4 shows that the oxidation potential of amitrole at the NiPc-CPE and NiPcNP-CPE (~0.58 V) is higher than at the CPE (0.55 V), while the current response

at this potential is higher with the bare CPE. The oxidation potentials at the MnPc- and MnPcNP-CPE (~0.59 V and 0.58V, respectively) are higher than that of the CPE at ~0.55 V. It may therefore be deduced that the NiPcNP-CPE and MnPcNP-CPE do not catalyse amitrole oxidation under the stated optimum conditions. The amitrole oxidation peaks with the FePcNP-CPE and FePc-CPE and CPE appear at the same potential (~ 0.55 V), but enhanced current response is displayed by the FePcNP-CPE, clearly showing that this electrode is electrocatalytic towards amitrole oxidation (**Figure 4.4**). There is clear catalysis with the CoPc-CPE and CoPcNP-CPE, with the oxidation potentials of both electrodes appearing at ~0.45 V, compared to the 0.55 V of the CPE. The peaks displayed by the CoPcNP-CPE and CoPc-CPE are very broad though, due to their overlap with the $Co^{III}Pc^{-2}/Co^{II}Pc^{-2}$ redox couple [152,268]. The CPE showed larger currents than CoPc-CPE and CoPcNP-CPE. Thus, of all the electrodes, FePcNP-CPE showed clear catalytic activity in terms of current enhancement and relative low potential. The detection potential of 0.55 V versus Ag|AgCl, 3 M KCl (0.40 V vs Ag|AgCl pseudo-reference electrode) is similar to the literature report [269] of 0.55V versus Ag|AgCl (sat'd KCl) for the detection of amitrole in alkaline conditions with CoPc-based electrode using chronoamperometric technique coupled to flow injection analysis (FIA-Amp).

4.1.3 Mechanism for the oxidation of amitrole using the FePcNP-CPE

When the anodic peak current (I_{pa}) was plotted against the square root of the scan rate ($\nu^{1/2}$) (**Figure 4.5)**, a straight line was observed, indicating a diffusion-controlled oxidation of amitrole. Also, a plot of $I_{pa}/\nu^{1/2}$ versus ν resulted in the characteristic shape that is typical for a catalytic process [270] (**Figure 4.6**).

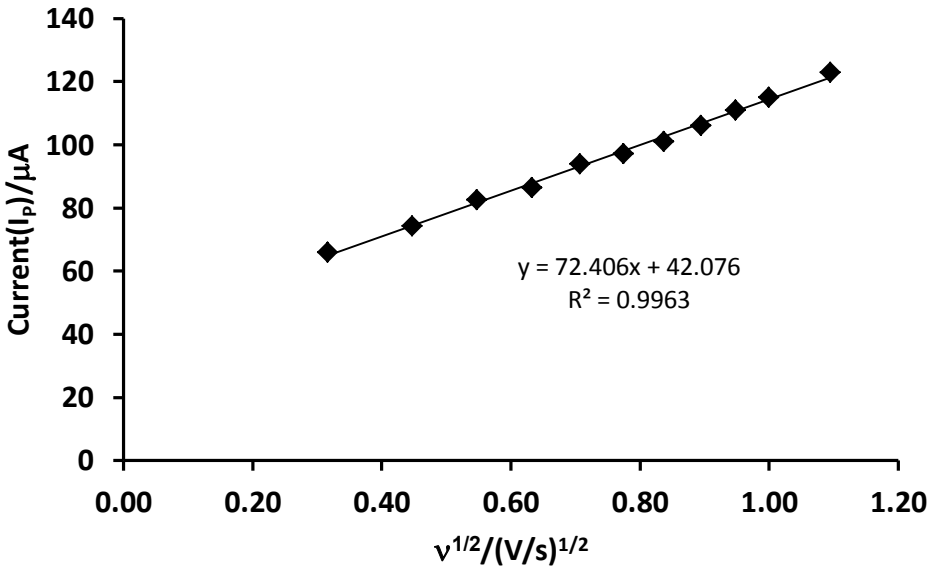

Figure 4.5: A plot of current response (I_P) vs $\nu^{1/2}$ for FePcNP-CPE in pH 12 phosphate buffer solution containing 1×10^{-3} M amitrole. Supporting electrolyte is 0.05 M Na_2SO_4.

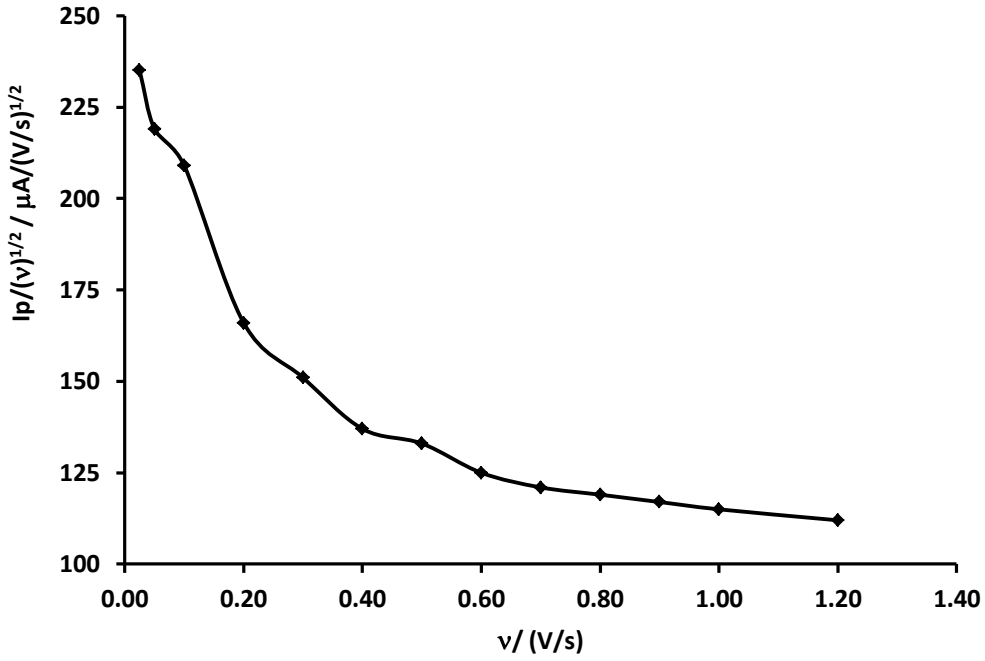

Figure 4.6: Plot of $I_P/(\nu)^{1/2}$ vs ν for FePcNP-CPE in pH 12 phosphate buffer containing 1 x 10^{-3} M amitrole. Supporting electrolyte is 0.05 M Na_2SO_4.

For a totally irreversible, diffusion controlled process such as amitrole oxidation [271–273], equation 4.1 applies:

$$E_P = \frac{b}{2}\log\nu + \text{constant} \qquad \textbf{4.1}$$

The plot of E_p versus ½ log ν gave a linear relationship, with a Tafel slope (b = 2.303$RT/\alpha nF$) of approximately 235 mV/decade, suggesting that the rate-determining step for the electrocatalysis is a one-electron transfer process assuming a transfer coefficient of α < 0.5 at 298 K (**Figure 4.7**).

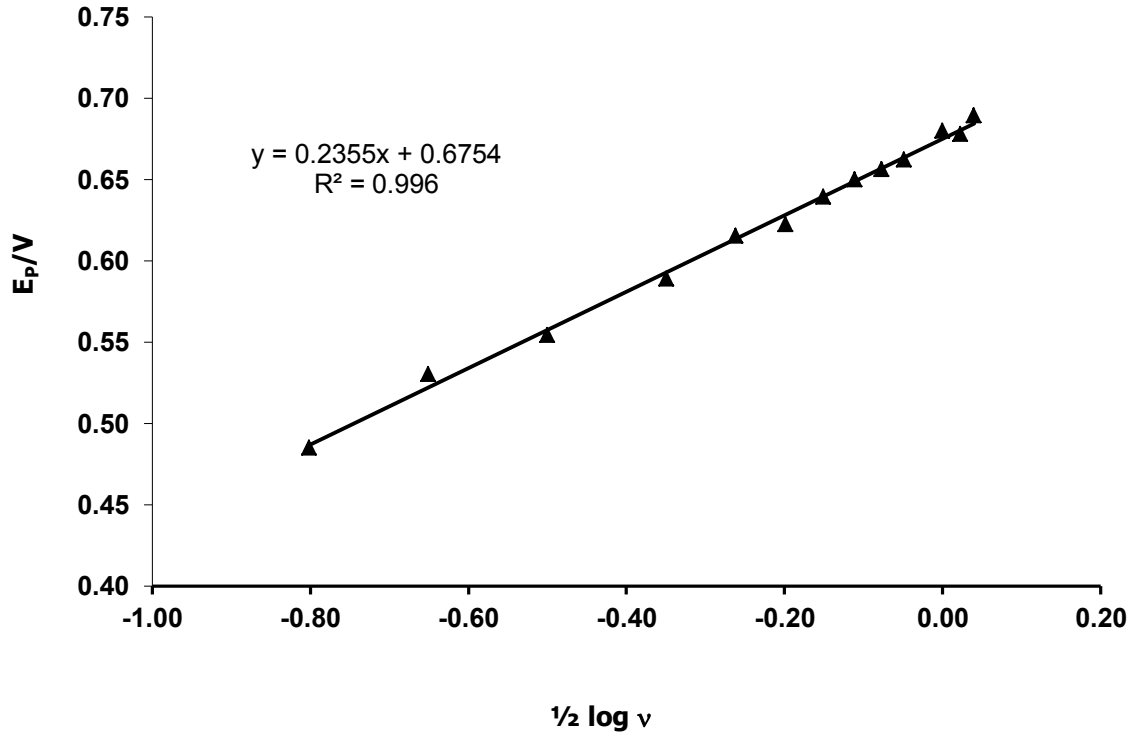

Figure 4.7: Plot of E_P against ½ log ν for FePcNP-CPE in pH 12 phosphate buffer containing 1×10^{-3} M amitrole. Supporting electrolyte is 0.05 M Na_2SO_4. Reference electrode: Ag|AgCl (3 M KCl).

The Tafel slope obtained in this work is comparable (within the limits of experimental errors) to the 239 mV/decade reported by Zen et al. [274] for amitrole oxidation using a Nafion/lead–ruthenium oxide pyrochlore chemically modified electrode. Tafel slopes greater than the normal 30–120 mV/decade are known [274-276] to be due to the substrate–catalyst interactions, where the substrate binds very strongly to the catalyst during the interaction as the reaction intermediate step. The Tafel slope obtained in this work may also be rationalised as strong binding of the amitrole–FePcNP in the intermediate step.

A previous report on the interaction of CoPc with amitrole [269] proposed the involvement of the $Co^{III}Pc^{-2}/Co^{II}Pc^{-2}$ redox processes. $Fe^{III}Pc^{-2}/Fe^{II}Pc^{-2}$ redox

processes may similarly be involved in the oxidation of amitrole since the $Fe^{III}Pc^{-2}/Fe^{II}Pc^{-2}$ redox potential is very close to the oxidation potential of the amitrole (see **Table 4.2**). Thus, the mechanism through which electrocatalytic oxidation of amitrole operates at the FePcNP-CPE may be represented (for basic media where amitrole is an anion) as shown by Eqs. (4.2)–(4.4):

$$Fe^{II}Pc^{-2} \rightarrow Fe^{III}Pc^{-2} + e^{-} \qquad \textbf{4.2}$$

$$Fe^{III}Pc^{-2} + \text{amitrole}^{-} \rightarrow [Fe^{III}Pc^{-2}(\text{amitrole}^{-})] \qquad \textbf{4.3}$$

$$[Fe^{III}Pc^{-2}(\text{amitrole}^{-})] \rightarrow Fe^{II}Pc^{-2} + \text{amitrole}_{\text{(oxidized)}} \qquad \textbf{4.4}$$

That is, initial oxidation of the $Fe^{II}Pc^{-2}$ to $Fe^{III}Pc^{-2}$ is followed by the oxidation of the amitrole anion to its products via $Fe^{III}Pc^{-2}$ and subsequent regeneration of the $Fe^{II}Pc^{-2}$ complex.

4.1.4 Chronoamperometry with the FePcNP-CPE

Chronoamperometry can be used to evaluate the catalytic rate constant [156, 277]. To obtain the catalytic rate constant, chronoamperograms were obtained at a fixed potential of 0.60 V (versus Ag|AgCl) over 40 s for the FePcNP-CPE in the absence and presence of 1×10^{-9} M amitrole. At the intermediate times (t = 0.8 – 2.2 s) used in this study, the catalytic current (I_{cat}) is dominated by the rate of the electrocatalysed oxidation of amitrole, and the rate constant for the chemical reaction between amitrole and redox sites of the surface-confined FePcNP-CPE can be determined according to the method described in the literature [156,277]:

$$\frac{I_{cat}}{I_L} = \gamma^{1/2}\left[\left(\pi^{1/2}\text{erf}\left(\gamma^{1/2}\right) + \exp(-\gamma)\right)/\gamma^{1/2}\right] \qquad \textbf{4.5}$$

where I_{cat} and I_L are the currents of the FePcNP-CPE in the presence and absence of amitrole, respectively, and $\gamma = kC_0t$ (C_0 is the bulk concentration of amitrole) and erf

is the error function. In the cases where γ exceeds 2, the error function is almost equal to 1 and the above equation can be reduced to:

$$\frac{I_{cat}}{I_L} = \gamma^{1/2}\pi^{1/2} = \pi^{1/2}(kC_0t)^{1/2} \qquad \textbf{4.6}$$

where k, C_0 and t are the catalytic rate constant (M^{-1} s^{-1}), catalyst concentration (M), and time elapsed (s). From the slope of a plot of I_{cat}/I_L versus $t^{1/2}$, the value of k for a given concentration of amitrole can be calculated. **Figure 4.8** shows one such plot, constructed from the chronoamperograms for the FePcNP-CPE in the absence and presence of 1×10^{-9} M amitrole, and the value of k was found to be 50.4 x 10^6 M^{-1} s^{-1} (**Table 4.3**).

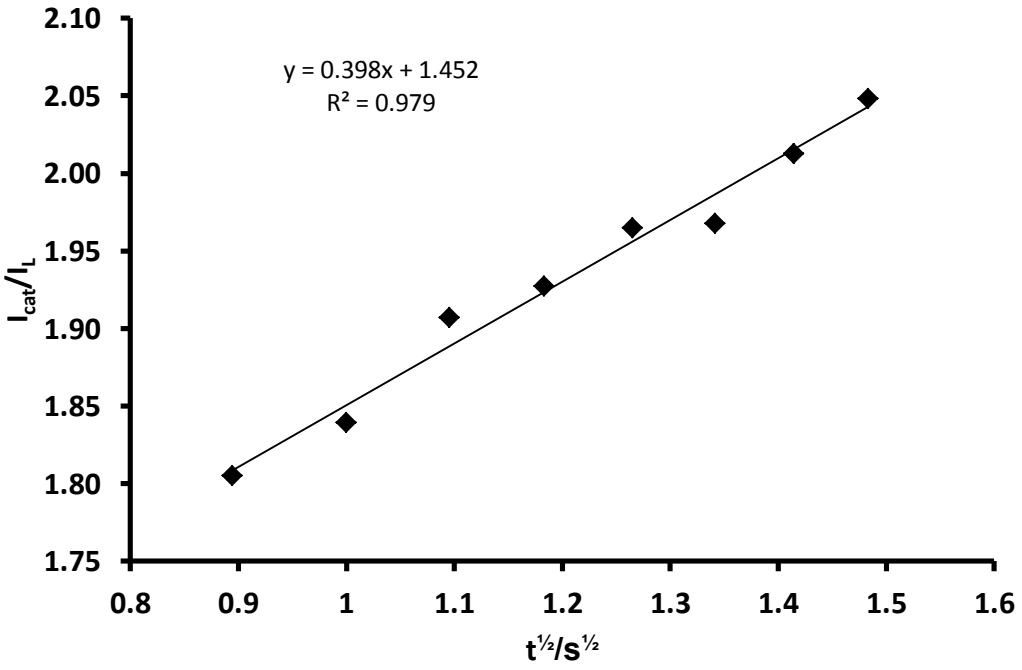

Figure 4.8: A plot of I_{cat}/I_L vs $t^{½}$ for the catalytic oxidation of amitrole with the FePcNP-CPE. Electrolyte is pH 12 phosphate buffer. Supporting electrolyte: 0.05 M Na_2SO_4.

Chronoamperometry was also employed in the electroanalytical detection of amitrole because of the sensitivity of this technique. There was a steady increase in current response of the FePcNP-CPE following addition of increasing concentrations of

amitrole in pH 12.0 phosphate buffer solution. The electrode surface had to be renewed and a new chronoamperogram recorded after each addition of an amitrole aliquot, because of fouling of the electrode surface by amitrole and/or its oxidation products. A plot of amperometric response (I_p) versus amitrole concentration was linear from 1 to 7 nM, stabilising at concentrations >7 nM due to a possible decrease in the conductive area of the catalyst (**Figure 4.9**).

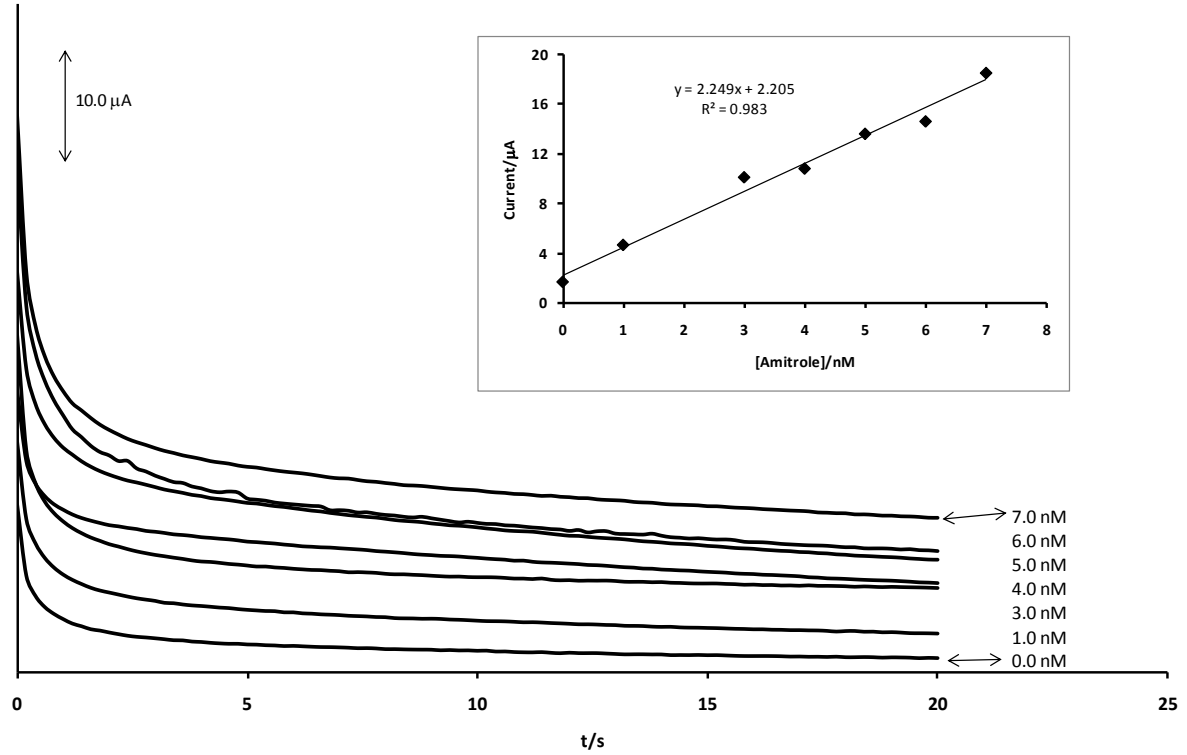

Figure 4.9: Chronoamperogramms obtained with the FePcNP-CPE in different concentrations of amitrole. Inset: Plot of current response (represented by chronamperogram) against concentration of amitrole. Reference electrode: Ag| AgCl (3 M KCl).

The sensitivity of the electrode was obtained from the slope of the calibration curve (see inset, **Figure 4.9**), and the limit of detection was calculated using the $Y_B + 3_{\sigma B}$ criterion [278] (i.e., the intercept plus three times the standard deviation of the blank). The data obtained is summarized in **Table 4.3**.

Table 4.3: Electrochemical parameters associated with FePcNP-CPE and NiPcNP-CPE. Reference electrode: Ag|AgCl (3 M KCl).

Parameter	**FePcNP-CPE**	**NiPcNP-CPE**
Analyte	Amitrole (in pH 12 PBS with 0.05 M Na_2SO_4)	Asulam (in pH 7 PBS)
Detection Potential	~0.55 V	~0.93 V
Limit of Detection	2.48 nM (1.07 μM[a], 0.38 μM[b])	61.9 nM (1.74 μM[c], 7.1 μM[d])
Catalytic rate constant	50.4×10^6 M^{-1} s^{-1} (18.95×10^{-2} s^{-1})[b]	1.26×10^3 M^{-1} s^{-1} (1.108×10^3 M^{-1} s^{-1})[e]
Sensitivity	2.00 μA/nM (4.41 pA/nM[a], 0.073 nA/nM[b])	1.98 μA/μM (0.91 μA/μM[c])
Linear Measuring Range	1 – 7 nM (23.0 – 230 nM[a], 0 – 260 μM[b])	0.4 – 2 μM (4 – 109 μM[c],10 – 90 μM[d])
Stability of electrode	~92 % of initial current recovered upon renewal of CPE surface	~90 % of initial current recovered upon renewal of CPE surface

[a] ref 269, [b] ref 274, [c] ref 225, [d] ref 231, and [e] ref 282.

Detection limits ranging from 0.3 – ~1.0 μM with sensitivities in the order of μA/μM have been obtained previously using carbon paste modified with cobalt phthalocyanine complex [269] or with lead–ruthenium oxide pyrochlore chemically modified electrode [274]. The sensitivity and detection limit shown by the FePcNP-CPE (**Table 4.3**) are approximately three orders of magnitude better than these previous reports [269,274] (**Table 4.3**) for the electrocatalytic detection of amitrole. This shows that the FePcNP-CPE is far more electrocatalytic towards amitrole

oxidation (in terms of current enhancement) than the electrodes in these reports [269,274], and this is confirmed by the much higher catalytic rate constant exhibited by the FePcNP-CPE (**Table 4.3**). These results further indicate that the FePcNP-CPE would improve the sensitivity and limit of detection of amitrole if a more sensitive analytical technique such as the FIA-Amp is employed.

4.1.5 Selectivity of the FePcNP-CPE

The selectivity of the electrode was investigated using the mixed solution method [279]. The concentration of the interfering species and amitrole were 10^{-6} and 10^{-7} M, respectively. The selectivity was checked against NH_4SCN (a common component of many amitrole-based herbicide formulations) and asulam. The values of K_{amp} (where K_{amp} = the amperometric selectivity coefficient) were determined from Equation 4.7 [279] for analysis in the presence of NH_4SCN (a similar equation will apply for analysis in the presence of other interfering ions):

$$K_{amp} = \left(\frac{\Delta I_{mixture}}{\Delta I_{amitrole}} - 1\right)\frac{[amitrole]}{[NH_4SCN]} \qquad \textbf{4.7}$$

where $\Delta I_{mixture}$ and $\Delta I_{amitrole}$ are respectively, the changes in current for the mixture containing amitrole and the interfering ion, and amitrole alone. The K_{amp} values are $(7.41 \pm 0.14) \times 10^{-4}$ for NH_4SCN but $(3.16 \pm 0.10) \times 10^{-3}$ for asulam. According to Stefan et al. [279], a K_{amp} value less than 10^{-3} (as obtained for NH_4SCN) clearly indicates non-interference. On the other hand, if the K_{amp} value falls within the order of 10^{-3} (as obtained for asulam), that suggests that the species is an interferent but not a strong one. Thus, the proposed electrode can be reliably used in the detection of amitrole in the presence of these species, particularly the NH_4SCN, under the conditions employed in this work.

4.1.6 Application of FePcNP-CPE to real sample analysis

To assess the applicability of the developed electrode for the proposed direct amperometric procedure, a commercially available amitrole herbicide Illico®, was analysed by the standard addition method. A fresh, unbuffered, tap water sample containing 1.9 nM of commercial amitrole (in Illico®) was spiked with 3.0 nM aliquots of amitrole. Six replicate determinations showed recovery of 99.61 ± 0.12% of the spike. When the experiment was performed using pH 12.0 phosphate buffer instead of unbuffered tap water, a 98.46 ± 0.24% recovery of amitrole was realized, which is about the same value as the manufacturer's cited values. These results thus demonstrate the suitability of the proposed FePcNP-CPE for real sample analysis.

4.1.7 Stability and reproducibility of the FePcNP-CPE

The effect of continuous scanning (20 scans) on the catalytic peak currents using cyclic voltammetry (at 25 mVs^{-1}) was investigated at a fixed concentration of amitrole (1×10^{-5} M). A dramatic decrease in peak currents (>70%) was observed after the first scan, which is an indication of a poisoned electrode possibly due to strong co-ordination of the oxidation product(s) of amitrole with the FePcNP catalyst. However, upon renewal of the electrode by simply polishing on an alumina paper or pushing and cutting the paste to obtain a new surface, 90% of the initial catalytic current was recovered (**Table 4.3**). Electrode fouling is less significant at low (nanomolar) range than at much higher amitrole concentration, meaning less polishing during the analysis of amitrole at low concentrations. The FePcNPs used in the fabrication of this electrode have been repeatedly used for the CPE for up to 8 months for the fabrication of this carbon paste electrode without detectable change in its response towards the detection of amitrole.

4.2 The Electroanalytical detection of asulam.

4.2.1 Optimisation of parameters

Electrolyte ions are the only ions in the buffer solutions used, since anion optimization was not done in this study. The effect of changes in pH of 1.0 mM asulam on current response was first investigated. The NiPcNP-CPE was chosen as an example for these studies. Effect of pH on the detection of asulam is shown in **Figure 4.10**.

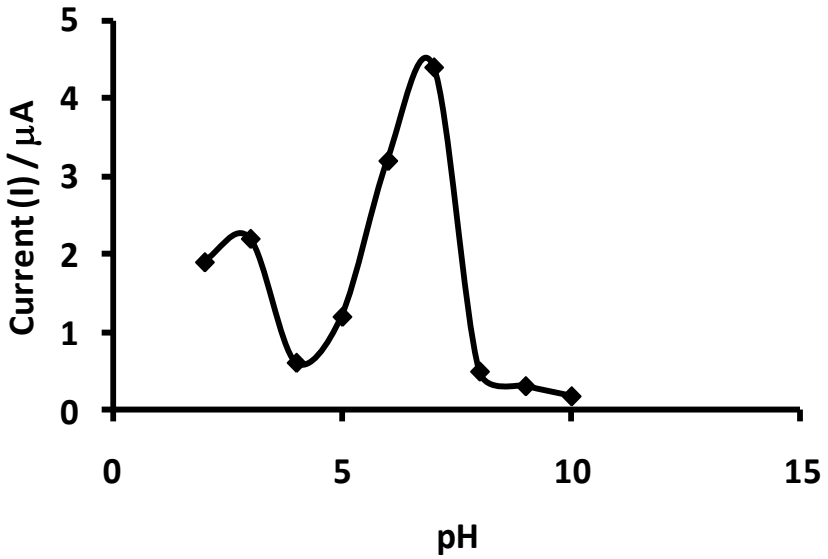

Figure 4.10: The effect of changes in pH of 1×10^{-3} M asulam at a NiPcNP-CPE.

Two maxima, one at pH 3 and a higher one at pH 7, can be observed. These peaks are in close agreement with the current peaks observed at about pH 2 and pH 6 by other workers [231]. Since the higher peak current occurred at pH 7, and to achieve similarity with biological pH conditions, asulam solutions were prepared at pH 7. It was also established that a 3% NiPcNP loading in the carbon paste gave the best current response (**Figure 4.11**). The NiPcNP-CPE and the other MPcNP-CPEs were prepared using this fraction of MPcNPs for further studies.

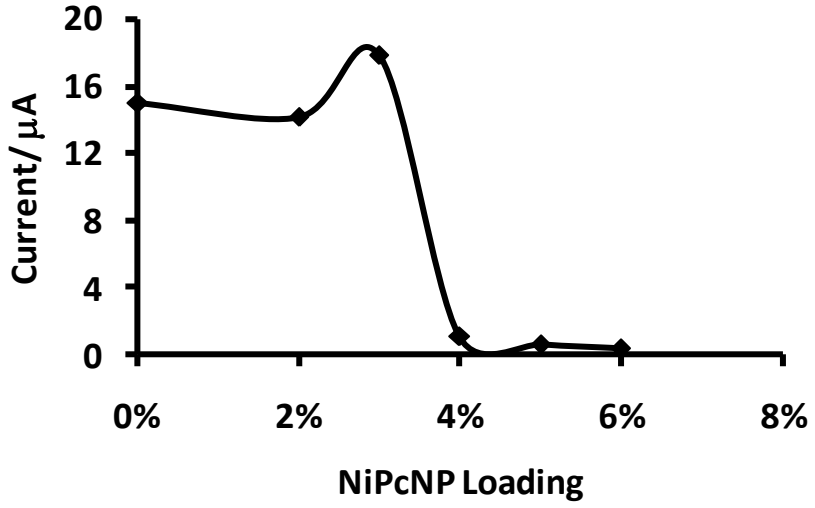

Figure 4.11: Effect of NiPcNP loading of NiPcNP-CPE on current response of pH 7 phosphate buffer containing 1×10^{-3} M asulam.

4.2.2 Electrocatalytic behavior of the MPc- and MPcNP-CPEs in asulam

The electrocatalytic behavior of the MPc- and MPcNP-CPEs was then investigated using these conditions: asulam dissolved in pH 7 phosphate buffer solution, and 3% MPc and MPcNP loading on CPE. Cyclic voltammograms of the bare CPE, the MPc-CPE, and the MPcNP-CPE in 10^{-3} M asulam are shown in **Figure 4.12**.

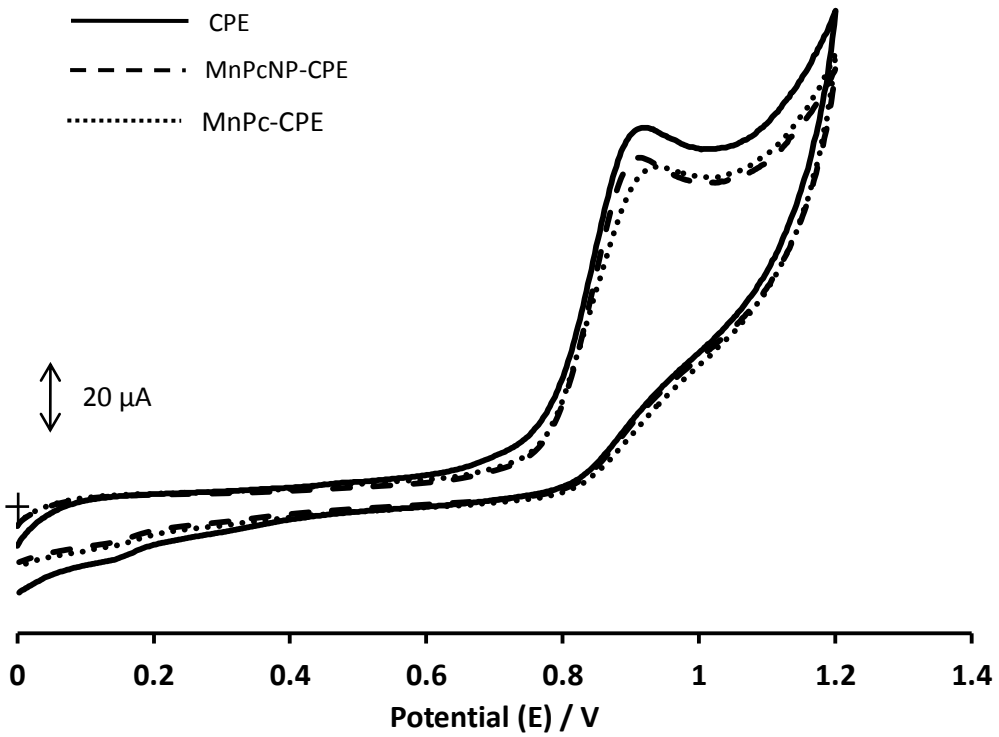
CPE
MnPcNP-CPE
MnPc-CPE
20 µA
0
0.2
0.4
0.6
0.8
1
1.2
1.4
Potential (E) / V

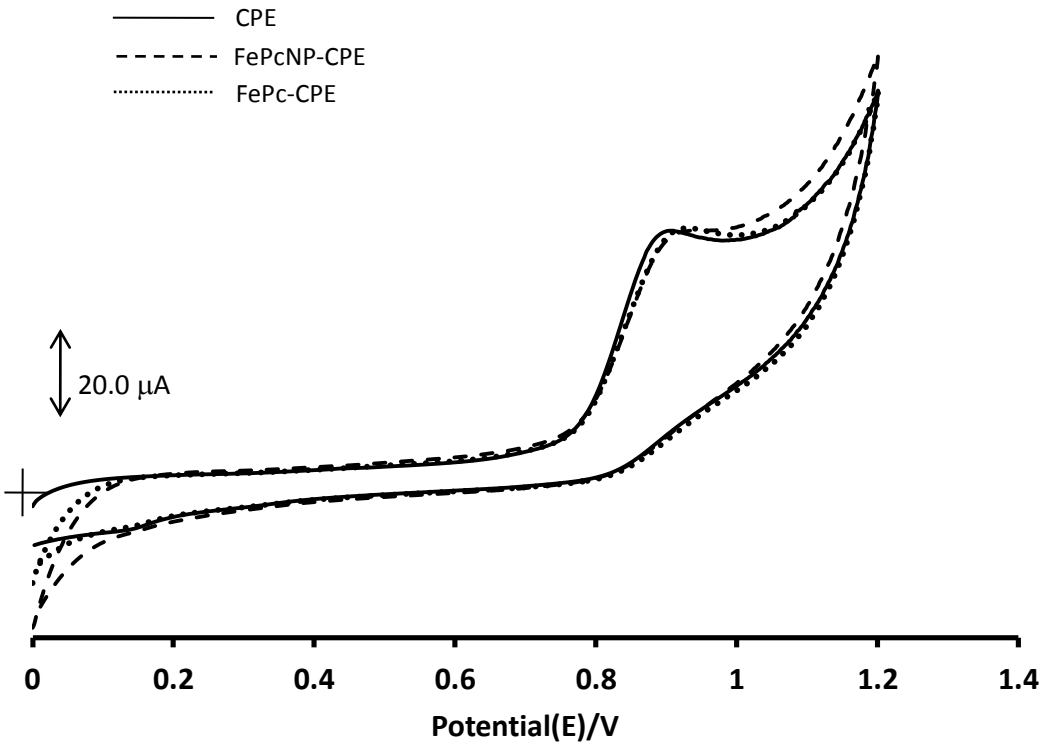
CPE
FePcNP-CPE
FePc-CPE
20.0 µA
0
0.2
0.4
0.6
0.8
1
1.2
1.4
Potential(E)/V

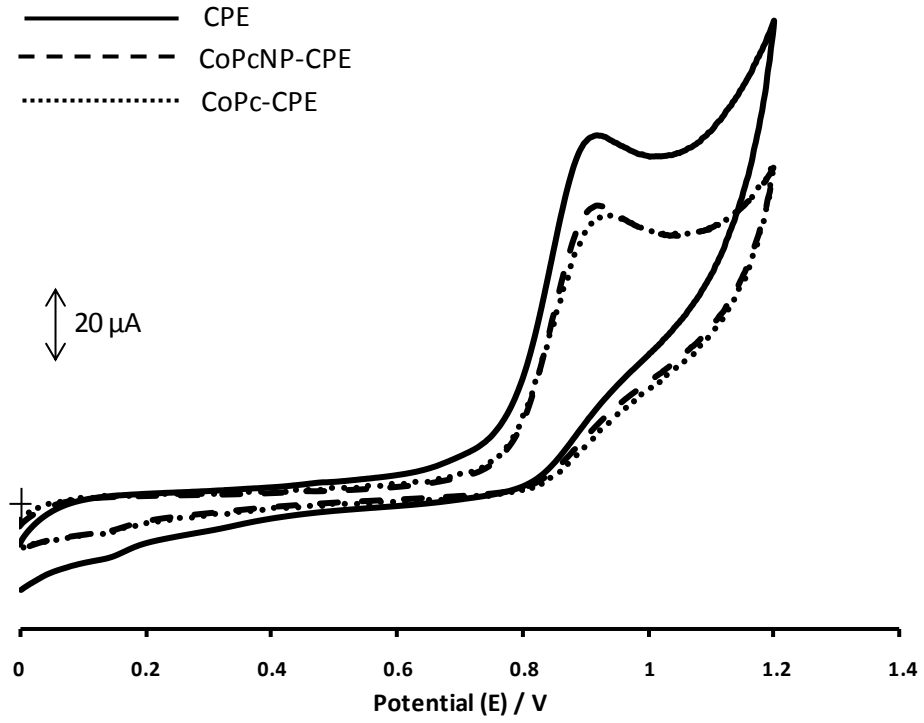

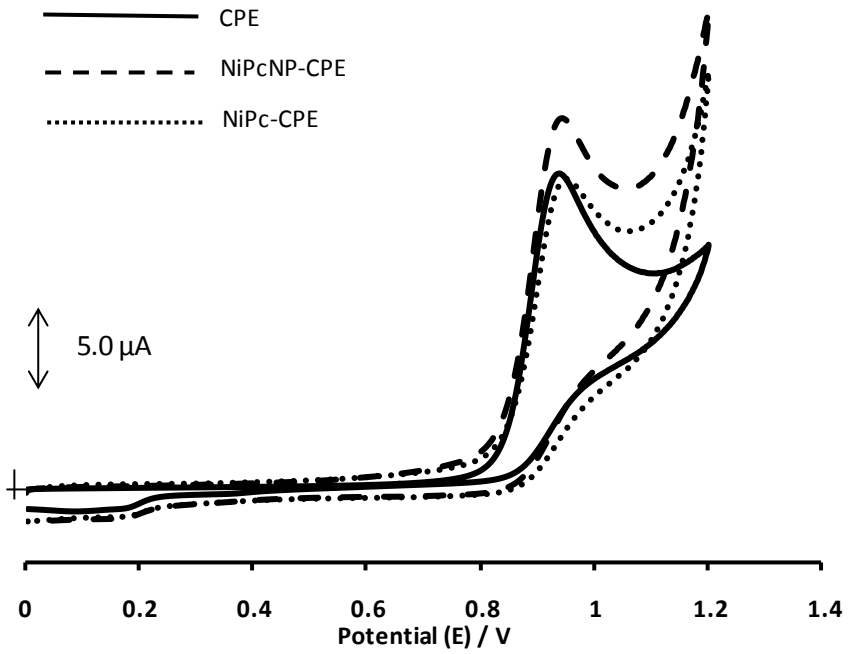

Figure 4.12: Cyclic voltammograms of pH 7 phosphate buffer containing 1×10^{-3} M asulam, obtained with different MPc-CPEs and MPcNP-CPEs (M = Mn, Ni, Co, Fe). Scan rate = 0.025 V/s. Reference electrode: Ag|AgCl (3 M KCl).

From the cyclic voltammograms in **Figure 4.12**, it is observed that only the NiPcNP-CPE shows electrocatalytic behavior towards asulam (**Figure 4.12**). The current response increases from about 14.4 μA with the CPE to about 18 μA with the NiPcNP. This enhancement of current shows that the NiPcNP-CPE is electrocalalytic towards the oxidation of asulam. Therefore further investigations were conducted with the NiPcNP-CPE. The rest of the MPcNPs showed no catalytic activity towards asulam oxidation (**Figure 4.12**)

4.2.3 Mechanism of asulam oxidation with the NiPcNP-CPE

The number of electrons involved in asulam oxidation at the NiPcNP-CPE surface was obtained from a plot of oxidation potential against pH of asulam solution (**Figure 4.13**).

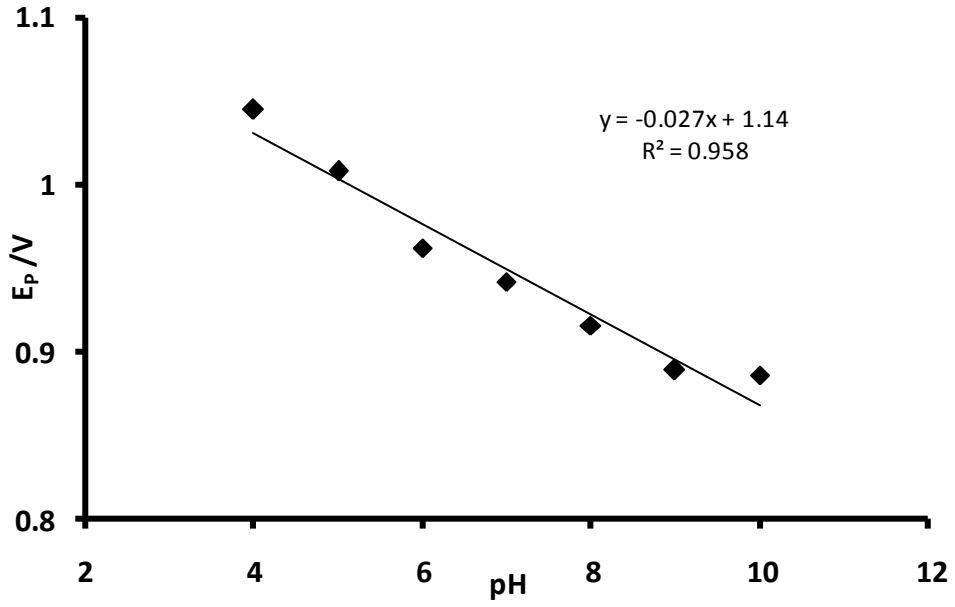

Figure 4.13: Plot of peak potential (E_P) vs pH for NiPcNP-CPE in phosphate buffer containing 1 x 10^{-3} M asulam. Reference electrode: Ag|AgCl (3 M KCl).

From the plot above, it is observed that the peak potential decreases gradually with increasing pH values, with a slope of ~ 27 mV/pH. This slope is in close agreement with the theoretical value of 30 mV/pH at 25°C for a two-electron transfer process.

A two-electron transfer oxidation process for asulam was reported by other workers as well [232]. Also, a plot of $I_{pa}/\nu^{½}$ versus ν resulted in the characteristic shape that is typical of a catalytic process (**Figure 4.14**).

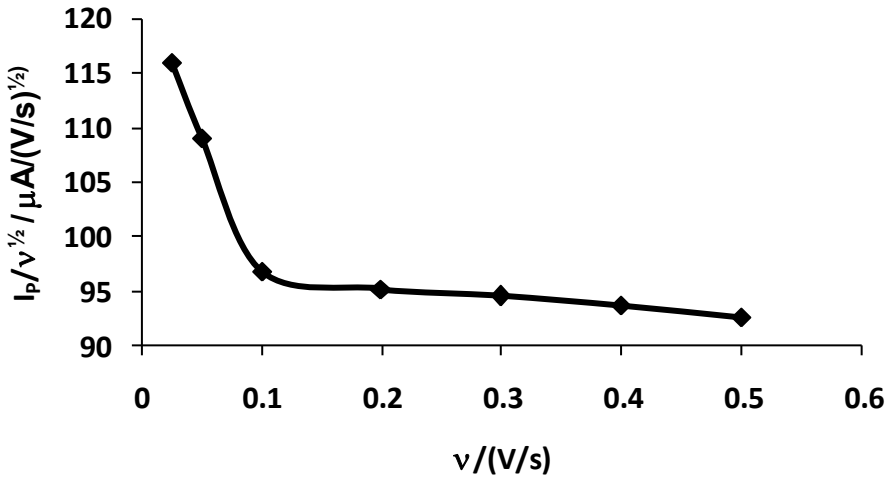

Figure 4.14: A plot of $I_P/\nu^{½}$ vs ν for NiPcNP-CPE in pH 7 phosphate buffer containing 1×10^{-3} M asulam.

A plot of anodic peak current (I_P) against the square root of scan rate ($\nu^{1/2}$) (**Figure 4.15**) resulted in a straight line, indicating that the oxidation of asulam at the electrode surface is diffusion-controlled.

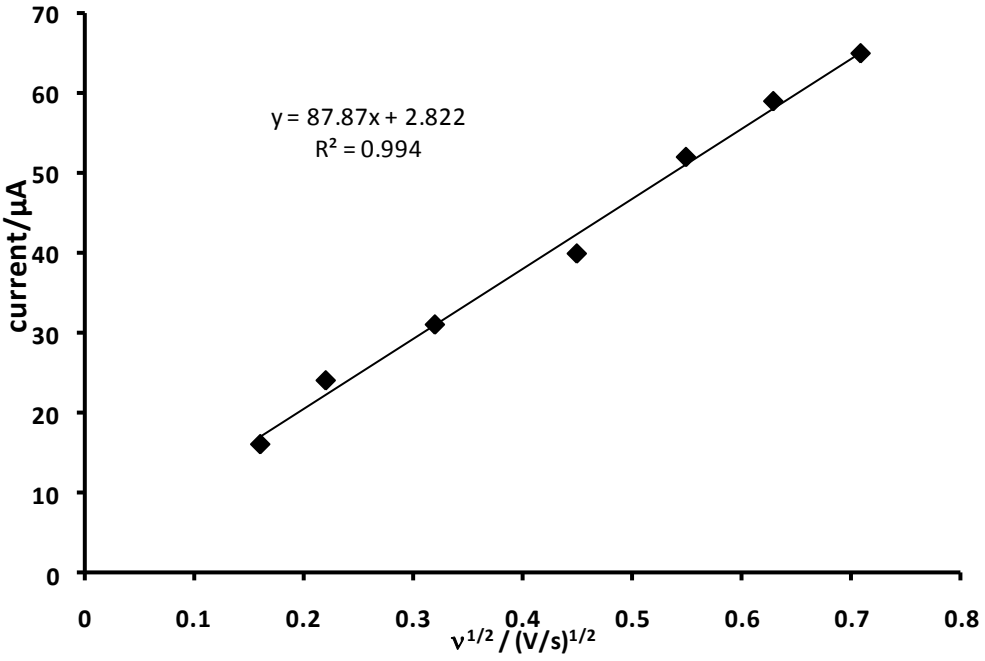

Figure 4.15: Plot of I_P vs $\nu^{½}$ for NiPcNP-CPE in pH 7 phosphate buffer containing 1×10^{-3} M asulam.

A plot of E_P versus ½ log ν (**Figure 4.16**) gave a linear relationship, with a Tafel slope of approximately 65 mV/decade, suggesting that the electrocatalysed oxidation of asulam is a two-electron transfer process, assuming a transfer coefficient, $\alpha \cong 0.5$ at 298 K. This is to be expected since the oxidation of carbamates (and asulam belongs to this group of compounds) consists of two, one-electron transfer steps [280,281].

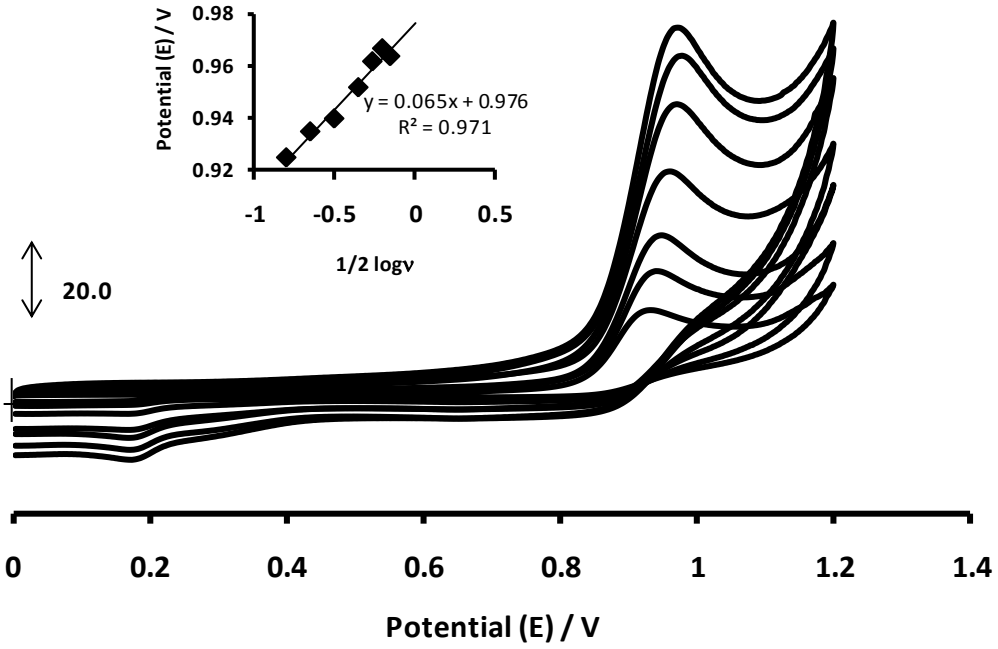

Figure 4.16: Cyclic voltammograms obtained at different scanrates with the NiPcNP-CPE in pH 7 phosphate buffer containing 10^{-3} M asulam. Inset: plot of potential (E) vs ½ log ν. Reference electrode: Ag|AgCl (3 M KCl).

Asulam oxidation occurs in the same region as NiPc ring oxidation (**Table 4.2**). Thus, the mechanism through which electrocatalytic oxidation of asulam may occur at the NiPcNP-CPE may be represented as shown in the following mechanism, which is based on the general mechanism for the oxidation of carbamates [280,281]:

$$Ni^{II}Pc^{-2} \rightarrow [Ni^{III}Pc^{-2}]^{+} + e^{-} \qquad \textbf{4.8}$$

$$[Ni^{III}Pc^{-2}] \rightarrow [N^{III}Pc^{-1}] + e^{-} \qquad \textbf{4.9}$$

$$[Ni^{III}Pc^{-1}]^{+} + \text{asulam} \rightarrow Ni^{II}Pc^{-2} + \text{asulam oxidation products} \qquad \textbf{4.10}$$

That is, ring oxidation of the $Ni^{II}Pc^{-2}$ occurs which facilitates electron-transfer from the nitrogen lone pair of the asulam [280,281].

4.2.4 Chronoamperometry with the NiPcNP-CPE

The catalytic rate constant for asulam on the NiPcNP-CPE was determined using chronoamperometry. Chronoamperograms were obtained at a fixed potential of 1.0 V (versus Ag|AgCl, 3 M KCl) over 500 s for the NiPcNP-CPE in the absence and presence of 1×10^{-6} M asulam, within the intermediate time interval: t = 30 s $\rightarrow$ t = 36 s. A plot of I_{cat}/I_L against $t^{½}$ (**Figure 4.17**) gave a catalytic rate constant of 1.26 $\times 10^3$ M^{-1} s^{-1}. No value could be found in the literature for the catalytic rate constant for the oxidation of asulam, but the rate constant obtained is quite comparable to that obtained for the oxidation of carbofuran (a carbamate pesticide) by ozone [282] (**Table 4.3**). This shows that the electrochemical oxidation of asulam at the NiPcNP-CPE is fairly fast, considering that ozone is a highly reactive compound.

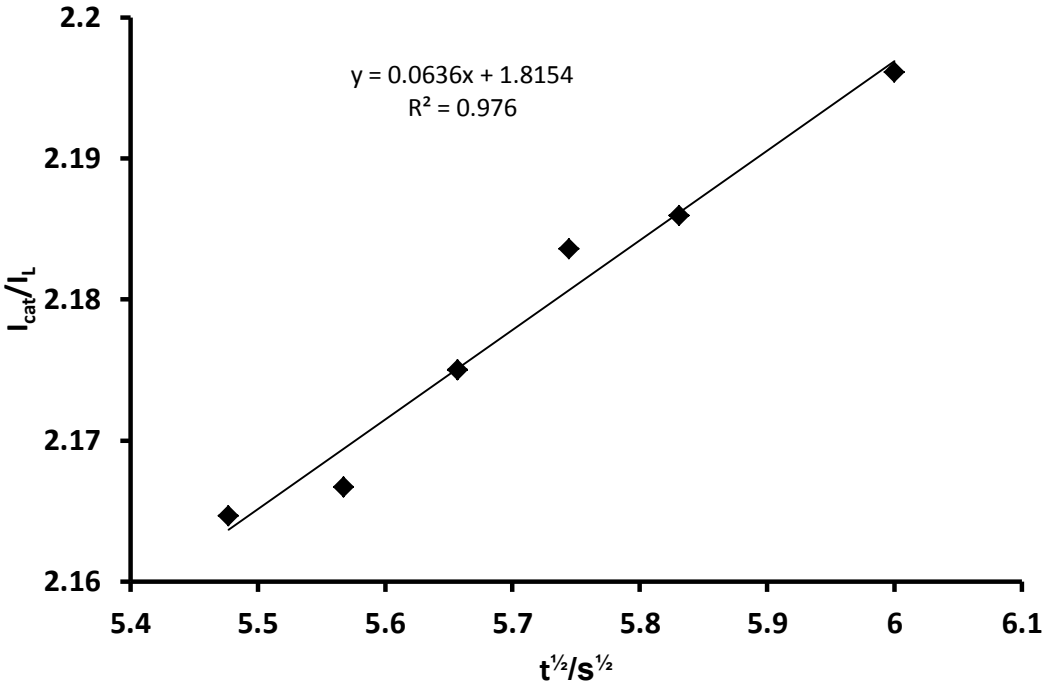

Figure 4.17: A plot of I_{cat}/I_L vs $t^{½}$ for the catalytic oxidation of asulam with the FePcNP-CPE.

Electrochemical detection of asulam was performed using chronoamperometry because of the sensitivity of the technique. There was a steady increase in current response following addition of increasing concentrations of asulam in pH 7 phosphate buffer solution. Again, the electrode surface had to be renewed and a new chronoamperogram recorded after each and every addition of an asulam aliquot, because of fouling by the products of asulam oxidation which adsorb easily on the CPE surface, thus reducing the current considerably. A plot of amperometric response versus asulam concentration was linear from 0.4 to about 2 μM (**Figure 4.18,** inset).

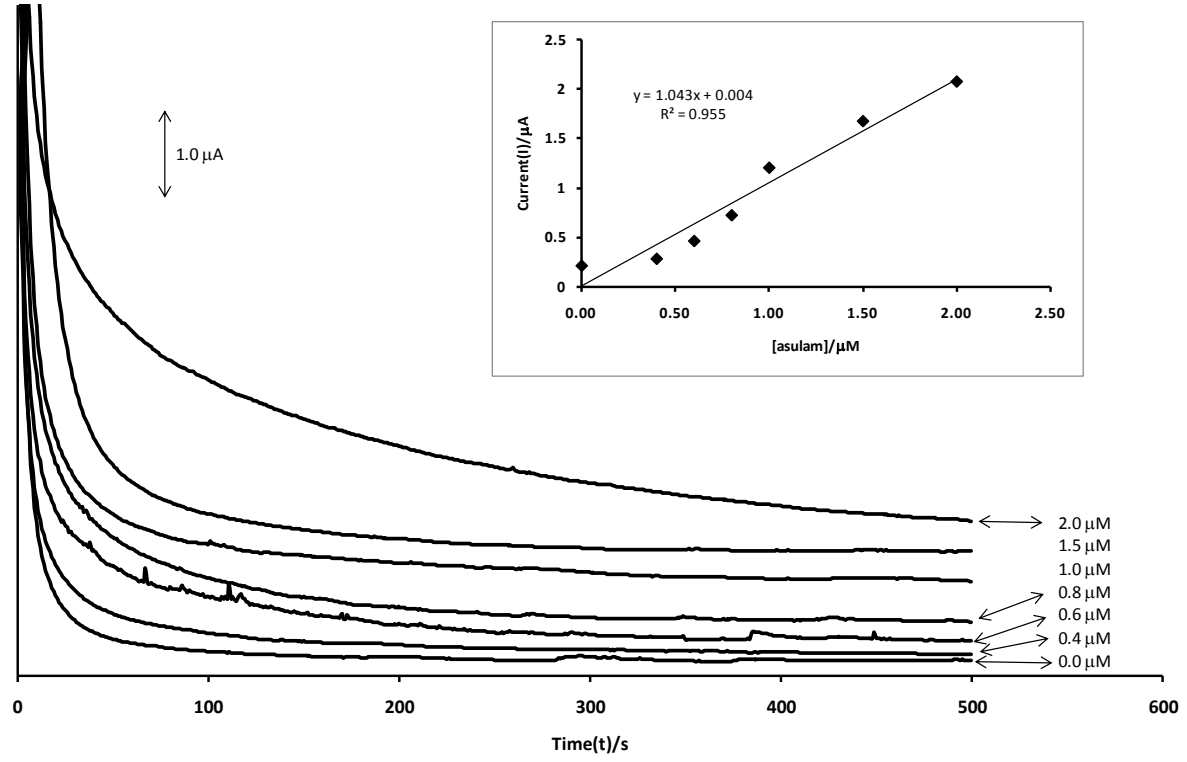

Figure 4.18: Chronoamperograms obtained with the NiPcNP-CPE in different concentrations of asulam. Inset: Plot of current (I_P) against concentration of asulam. Reference electrode: Ag|AgCl (3 M KCl).

The sensitivity of the NiPcNP-CPE was determined from the slope of the calibration curve, and the limit of detection was calculated using the $Y_B + 3\sigma$ criterion. The analytical data is summarized in **Table 4.3**. The limit of detection and sensitivity obtained with the NiPcNP-CPE are better than those reported for asulam at a glassy carbon electrode [231] and a glassy carbon electrode coupled to a capillary electrophoresis instrument [225] (**Table 4.3**).

4.2.5 Stability of the NiPcNP-CPE

The effect of continuous scanning (17 scans) on the catalytic peak currents was investigated at a fixed concentration of asulam (1×10^{-4} M) using cyclic voltammetry. A significant decrease in peak current ((~ 43 % at the last scan) was observed with an increase in number of scans when the electrode was left unrenewed, which is an indication of a poisoned electrode. However, upon renewal of the electrode by polishing on alumina paper, the decrease was more gradual (**Figure 4.19**). An initial sample of NiPcNPs was used repeatedly for about 7 months to prepare the NiPcNP-CPE without any detectable change in its response towards the detection of asulam.

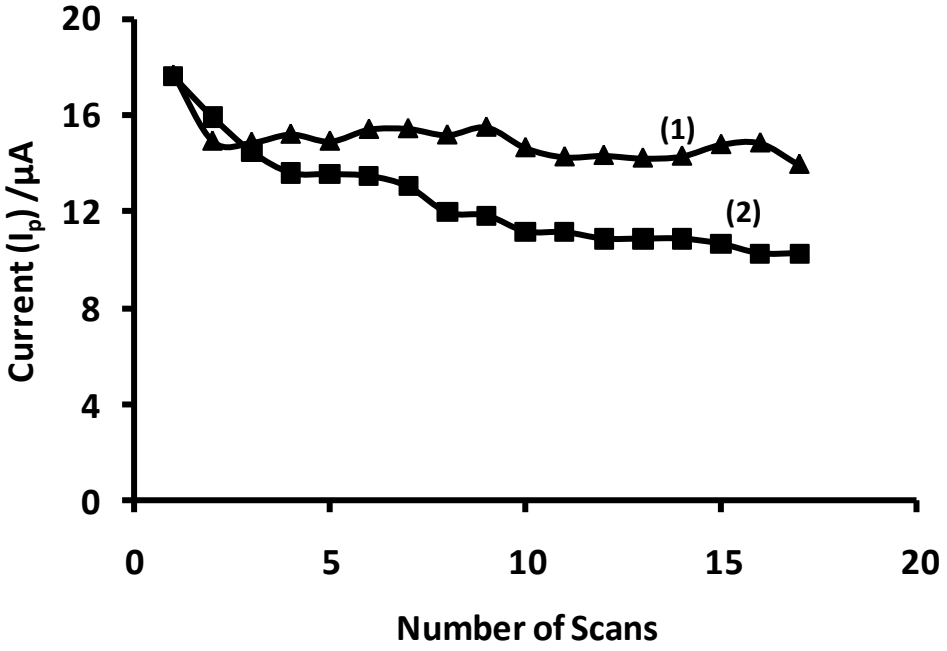

Figure 4.19: : I_P vs Number of Scans for the NiPcNP-CPE in 1×10^{-3} M asulam when the electrode surface is renewed (1) and not renewed (2). Scan rate = 0.025 V/s.

4.3 Conclusions

Four carbon paste electrodes (MnPcNP-CPE, FePcNP-CPE, NiPcNP-CPE, and CoPcNP-CPE) were constructed and their electrocatalytic behaviour towards amitrole and asulam oxidation was investigated. Further investigations were conducted on the electrodes that displayed the most electrocatalytic behaviour to establish the associated electrochemical parameters. Based on these investigations, the following conclusions can be made:

1. The FePcNP-CPE displayed the best electrocatalytic behaviour towards oxidation of amitrole. Furthermore, the electrode exhibited a very high catalytic rate constant (50.4×10^6 M^{-1} s^{-1}), high sensitivity (2.00 µA/nM), low LOD (2.48 nM), but a rather narrow linear concentration range (1 – 7 nM), in comparison with reported literature values.

2. The NiPcNP-CPE showed the best electrocatalytic behaviour towards asulam oxidation. The electrode displayed a high catalytic rate constant (1.26×10^3 M^{-1} s^{-1}) (no literature values were found for asulam oxidation, to compare with), high sensitivity(1.98 μA/μM), a low LOD (61.9 nM), but a narrow linear concentration range (0.4 – 2.0 μM), in comparison with reported literature values.
3. Both electrodes can be used repeatedly if the surface is renewed.

Since the FePcNP-CPE and NiPcNP-CPE were the best performing electrodes in amitrole and asulam solutions, respectively, the FePc and NiPc nanoparticles were mixed with multiwalled carbon nanotubes (MWCNTs) and the behaviours of the resulting electrodes in the corresponding analytes were investigated. This is discussed in the next chapter.

Chapter 5

Electroanalysis with Basal Plane Pyrolytic Graphite Electrode Modified with NiPcNP/MWCNT and FePcNP/MWCNT Composites.

In this chapter, basal plane pyrolytic graphite electrodes modified with NiPcNP/MWCNT and FePcNP/MWCNT are employed in the electroanalytical detection of amitrole and asulam.

5.1 Electroanalytical Detection of Amitrole

5.1.1 Electrocatalysis of amitrole

These studies were done with the FePcNP/MWCNT-BPPGE since a CPE modified with FePcNPs displayed the best electrocatalytic behavior towards amitrole detection. Comparative cyclic voltammograms of the BPPGE, MWCNT-BPPGE, FePcNP-BPPGE, and FePcNP/MWCNT-BPPGE recorded in 0.1 M PBS (pH 12.0) containing 1×10^{-3} M amitrole are shown in **Figure 5.1**.

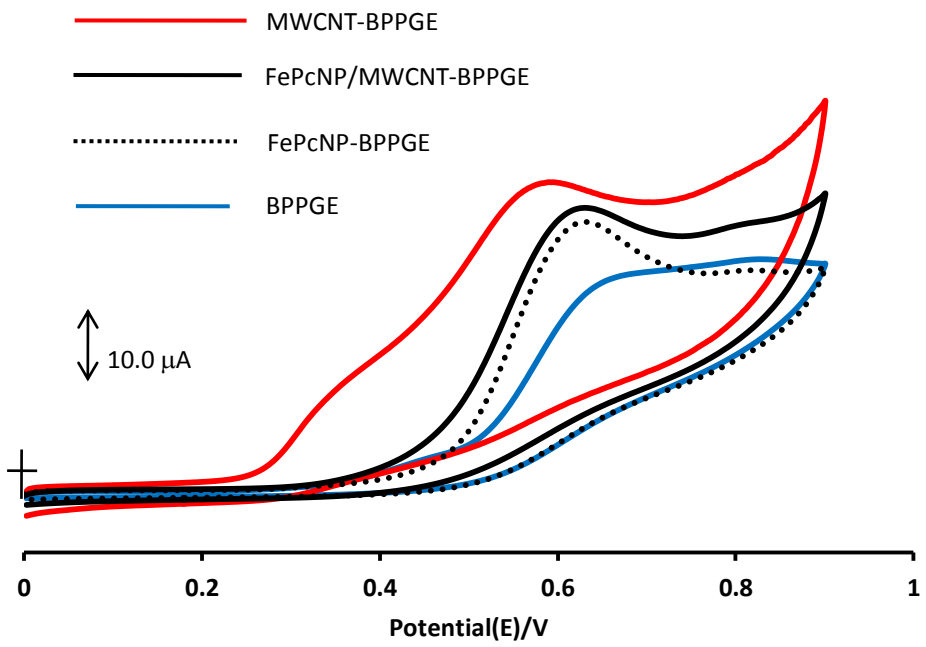

Figure 5.1: Cyclic voltammograms of different electrodes in 1 x 10^{-3} M amitrole in 0.1 M phosphate buffer solution at pH 12. Supporting electrode is 0.05 M Na_2SO_4. Scan rate = 0.025 V/s. Reference electrode: Ag|AgCl (3 M KCl).

All the modified electrodes, that is, the MWCNT-BPPGE, FePcNP/MWCNT-BPPGE and FePcNP-BPPGE display electrocatalytic behaviour towards amitrole oxidation when attached to the BPPGE surface , in terms of lowering of potential and increase in current. The cyclic voltammogram of amitrole on the MWCNT–BPPGE shows two

peaks, one broad peak at ~ 0.33 V, and the other, the amitrole oxidation peak at about 0.57 V. Such double oxidation peaks have been observed before for CNT-based electrodes during electrocatalysed detection [260]. Two peaks for the oxidation of thiols on MWCNT were attributed [26] to oxidation at different parts of the MWCNT. Based on these reports, the first peak (at ~ +0.33 V) is attributed to amitrole oxidation at the quinone-like functional groups at the tube ends of the MWCNT, while the second peak (i.e., at ~ +0.57 V) is attributed to amitrole oxidation at the edge plane-like carbon at the MWCNT [26] (**Table 5.1**). This explanation is consistent with the work done by Gong et al. [260], where two of such peaks were observed for thiols with SWCNT-based electrodes.

The amitrole oxidation potentials (E_P) with the different electrodes follow the trend: BPPGE > FePcNP-BPPGE ≈ FePcNP/MWCNT-BPPGE > MWCNT-BPPGE (**Table 5.1**).

Table 5.1: The oxidation potentials (E/V vs Ag|AgCl, 3 M KCl) of 10^{-3} M amitrole and 10^{-3} M asulam with MPcNP/MWCNT-BPPGEs (M = Fe, Ni).

Electrode	Oxidation potential (E) of 10^{-3} M amitrole	Oxidation potential (E) of 10^{-3} M asulam	Redox process of MPc	Redox potential of MPc process at pH 12	Redox potential of MPc process at pH 7
BPPGE	0.65 V	0.96 V	----------	---------	----------
MWCNT-BPPGE	0.57 V	0.93 V	----------	----------	----------
FePcNP/MWCNT-BPPGE	0.61 V	--------	$Fe^{III}Pc^{-2}$ /$Fe^{II}Pc^{-2}$	0.4 V	---------
FePcNP-BPPGE	0.61 V	--------	$Fe^{III}Pc^{-2}$ /$Fe^{II}Pc^{-2}$	0.4 V	---------
NiPcNP-BPPGE	----------	0.94 V	$Ni^{II}Pc^{-1}$ /$Ni^{II}Pc^{-2}$	-------	0.89 V
NiPcNP/MWCNT-BPPGE	----------	0.90 V	$Ni^{II}Pc^{-1}$ /$Ni^{II}Pc^{-2}$	-------	0.71 V

The relatively low oxidation potential (hence faster electrode kinetics) displayed by the MWCNT-BPPGE for amitrole oxidation were also predicted by electrochemical impedance spectroscopy and cyclic voltammetry characterizations. However, the two broad, overlapping current peaks displayed by the MWCNT-BPPGE may result in inaccurate amitrole current responses being measured since one contributes to the current response of the other. Therefore, the FePcNP/MWCNT-BPPGE, which

displayed the next best catalytic behaviour in terms of both current and potential, was chosen for further investigation because of these factors.

5.1.2 Mechanism of amitrole oxidation using the FePcNP/MWCNT-BPPGE

A plot of I_{pa} against $\nu^{½}$ (**Figure 5.2**) resulted in a straight line, showing that for this electrode, amitrole oxidation is diffusion-controlled. A plot of $I_{pa}/\nu^{½}$ against ν (**Figure 5.3**) resulted in the characteristic shape that is typical of a catalytic process [270].

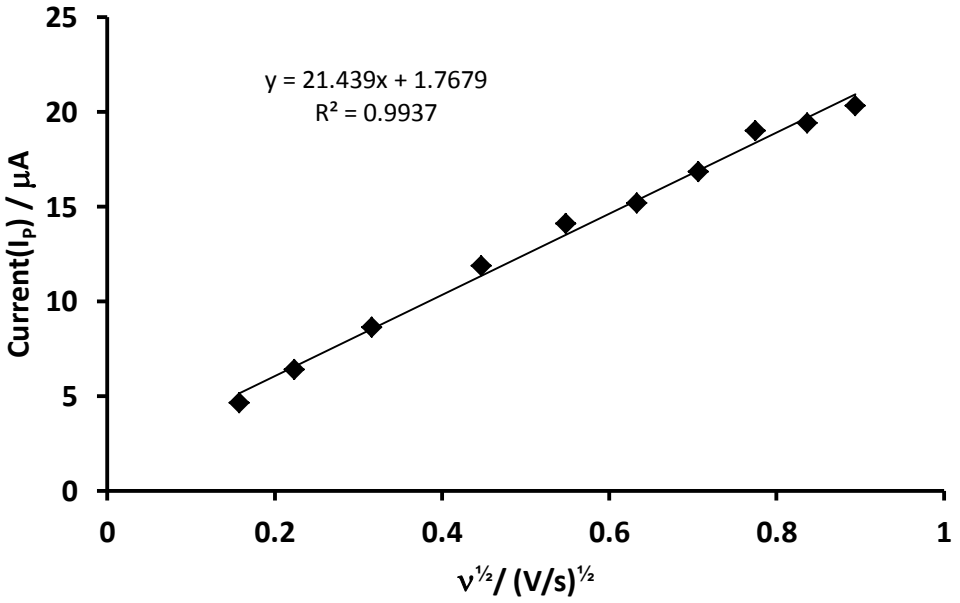

Figure 5.2: Plot of current (I_P) vs $\nu^{½}$ for FePcNP/MWCNT-BPPGE in pH 12 phosphate buffer containing 1×10^{-3} M amitrole. Supporting electrolyte is 0.05 M Na_2SO_4.

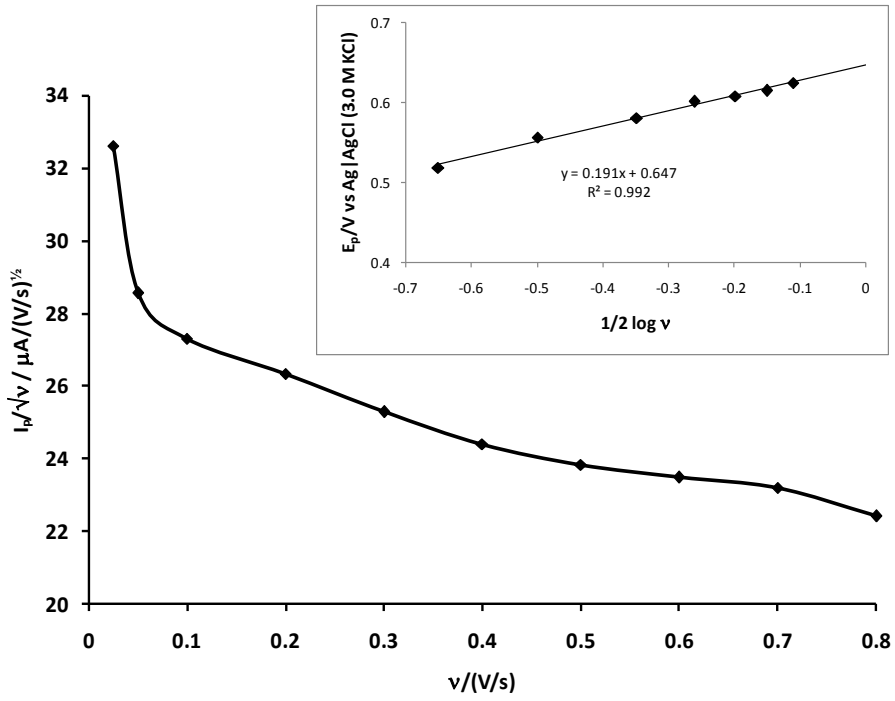

Figure 5.3: Plot of $I_P/\nu^{½}$ vs ν for FePcNP/MWCNT-BPPGE in pH 12 phosphate buffer containing 1×10^{-3} M amitrole. Supporting electrolyte is 0.05 M Na_2SO_4.

From a plot of oxidation peak potential (E_p) against ½ log ν (**Figure 5.3**, inset), a Tafel slope of 191 mV/decade was obtained. It has been established that amitrole oxidation is a one-electron transfer process, therefore the Tafel slope (from equation 4.1) was expected to be ~120 mV/decade (assuming α = ½). The steeper slope of 191 mV/decade means that there is adsorption as well on the electrode surface, as has been mentioned earlier (amitrole and/or its products bind to the catalyst on the electrode surface) [274]. Also, amitrole oxidation occurs in the same region as the $Fe^{III}Pc^{-2}/Fe^{II}Pc^{-2}$ redox process (**Table 5.1**). From this discussion, it is suggested that the oxidation of amitrole at the FePcNP/MWCNT-BPPGE surface should follow a mechanism similar to that proposed earlier for amitrole detection with an FePcNP-CPE (equations 4.2 – 4.4).

5.1.3 Chronoamperometry with the FePcNP/MWCNT-BPPGE

Chronoamperometry was used to evaluate the catalytic rate constant [156, 280]. To obtain the catalytic rate constant, chronoamperograms were obtained at a fixed potential of 0.65 V (versus Ag|AgCl) over 40 s for the FePcNP/MWCNT–BPPGE in the absence and presence of 1×10^{-4} M amitrole, at the intermediate times, t = 1.0 – 2.2 s. From the slope of a plot of I_{cat}/I_L versus $t^{1/2}$ (**Figure 5.4**) (see equation 4.6), the value of k was found to be 18.05 $M^{-1}\,s^{-1}$ (**Table 5.2**). The value of K is lower than that obtained with the FePcNP-CPE, but it is still 100 times higher than that obtained with a Nafion/lead–ruthenium oxide pyrochlore chemically modified electrode [274] (**Table 5.2**).

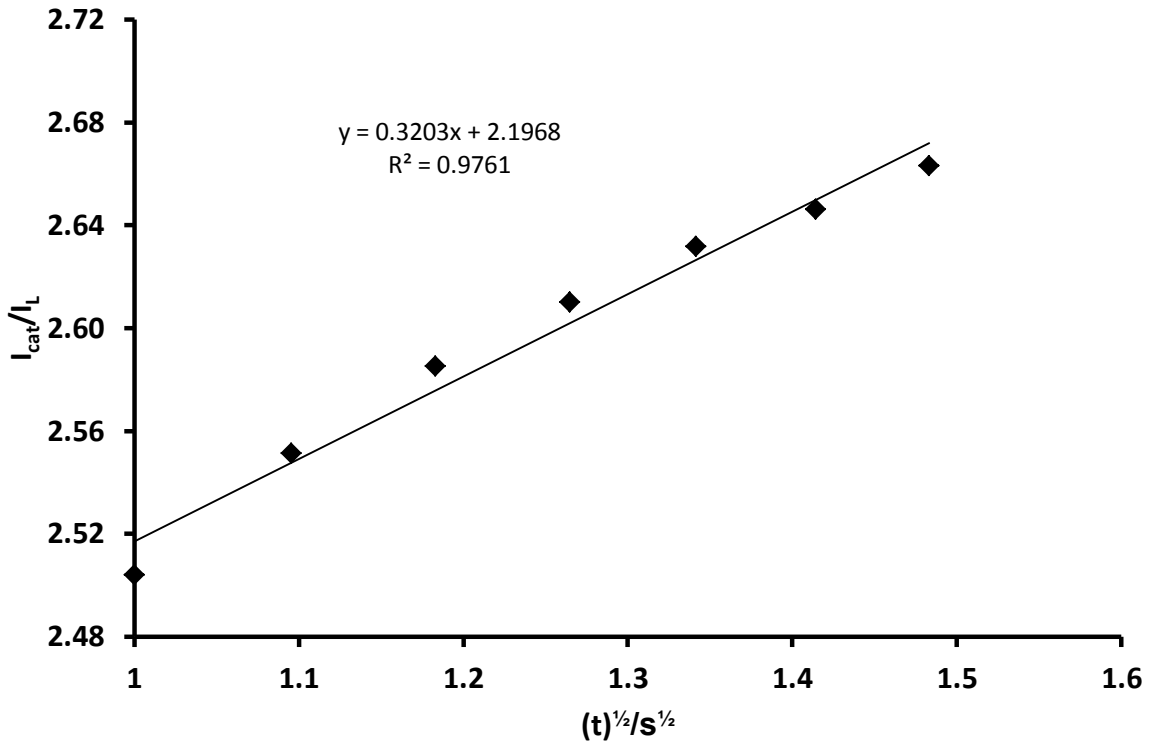

Figure 5.4: A plot of I_{cat}/I_L vs $t^{½}$ for the catalytic oxidation of amitrole with the FePcNP/MWCNT-BPPGE. Supporting electrolyte is 0.05 M Na_2SO_4.

The chronoamperometric response with the FePcNP/MWCNT-BPPGE did not show any detectable variation with increase in amitrole concentration at very low concentrations ($\leq 1 \times 10^{-5}$ M). High concentrations of amitrole had to be used in this experiment (10^{-4} M range), and SWV was chosen for current-concentration studies of amitrole because of the sharp current peaks obtained with the technique which afforded greater accuracy of measurement (**Figure 5.5**). The amperometric response showed a linear relationship with concentration of amitrole within the range 1×10^{-4} M $\rightarrow 9 \times 10^{-4}$ M. The linear measuring range is wider than the one obtained with the FePcNP-CPE but narrower than the ones reported in the literature (**Table 5.2**).

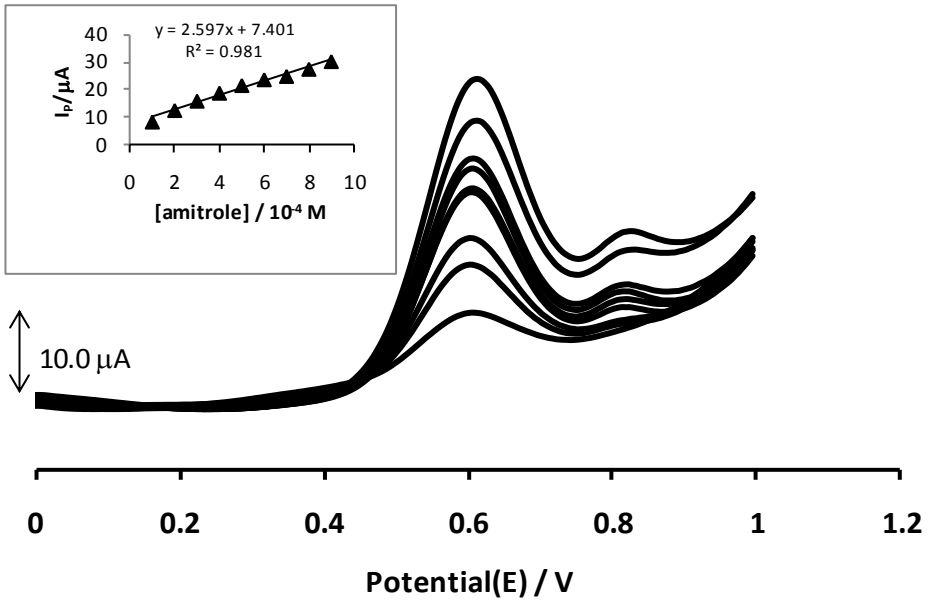

Figure 5.5: Square wave voltammograms for FePcNP/MWCNT-BPPGE in amitrole solutions of increasing concentration ($1.0 \rightarrow 9.0 \times 10^{-4}$ M) prepared with 0.1 M phosphate buffer solution at pH 12. Supporting electrolyte is 0.05 M Na_2SO_4. Reference electrode: Ag|AgCl, 3 M KCl.

From the calibration curve the sensitivity of the electrode was determined to be 25.97 μA/mM and the limit of detection was estimated to be ~5.2 μM (**Table 5.2**),

using the $y = y_B + 3\sigma$ criterion. The LOD value is less favourable than those reported in literature or that obtained on FePcNP-CPE (**Table 5.2**).

Table 5.2: Electrochemical parameters associated with FePcNP/MWCNT-BPPGE and NiPcNP/MWCNT-BPPGE (vs Ag|AgCl, 3 M KCl). The values in round brackets were obtained with the corresponding MPcNP-CPE.

Parameter	**FePcNP/MWCNT-BPPGE**	**NiPcNP/MWCNT-BPPGE**
Analyte	Amitrole (in pH 12 PBS)	Asulam (in pH 7 PBS)
Detection Potential	0.61 V (0.55 V)	0.9 V (0.9 V)
Limit of Detection	5.2 μM (2.48 nM) [1.07 μM[a], 0.38 μM[b]]	0.285 μM (61.9 nM) [1.74 μM[c], 7.1 μM[d]]
Sensitivity	25.97 pA/nM (2.00 μA/nM) [4.41 pA/nM[a], 0.073 nA/nM[b]]	44.6 nA/μM (1.98 μA/μM) [0.91 μA/μM[c]]
Linear Measuring Range	$1 \rightarrow 9 \times 10^{-4}$ M ($1 \rightarrow 7$ nM) [23.0 – 230 nM[a], 0 – 260 μM[b]]	$91 \rightarrow 412$ μM ($0.4 \rightarrow 2$ μM) [4 – 109 μM[c], 10 – 90 μM[d]]
Catalytic Rate constant	18.05 M^{-1} s^{-1} (50.4×10^6 M^{-1} s^{-1}) [18.95×10^{-2} s^{-1}][b]	13.04 M^{-1} s^{-1} (1.26×10^3 M^{-1} s^{-1}) [1.108×10^3 M^{-1} s^{-1}][e]
Stability	~90% of initial current recovered upon rinsing in pH 7 phosphate buffer after measurement. (92% with FePcNP-CPE)	~86 % of initial current recovered upon rinsing in pH 7 phosphate buffer after measurement. (90% with NiPcNP-CPE)

[a] ref 269, [b] ref 274, [c] ref 225, [d] ref 231, and [e] ref 282.

The sensitivity is lower than that displayed by the FePcNP-CPE but higher than the reported literature values, and the catalytic rate constant is lower than that obtained with the FePcNP-CPE but higher than the reported literature value (**Table 5.2**). The detection potential with the FePcNP/MWCNT-BPPGE is slightly higher (at 0.61 V) than that obtained with the FePcNP-CPE (0.55 V), and the percentage recovery of current response after rinsing with buffer (~90%) is almost the same as that obtained with the FePcNP-CPE upon renewal of electrode surface (~92%).

5.2 Electroanalytical Detection of Asulam

5.2.1 Electrocatalysis of asulam with NiPcNP/MWCNT-BPPGE

In chapter 4, a carbon paste electrode modified with NiPcNPs displayed the best electrocatalytic behaviour towards asulam oxidation, therefore the NiPcNP/MWCNT-BPPGE was employed in asulam studies in this chapter. **Figure 5.6** shows the comparative background-corrected cyclic voltammograms of the BPPGE, NiPcNP-BPPGE, and NiPcNP/MWCNT-BPPGE recorded in 0.1 M PBS (pH 7.0) containing 1×10^{-3} M asulam.

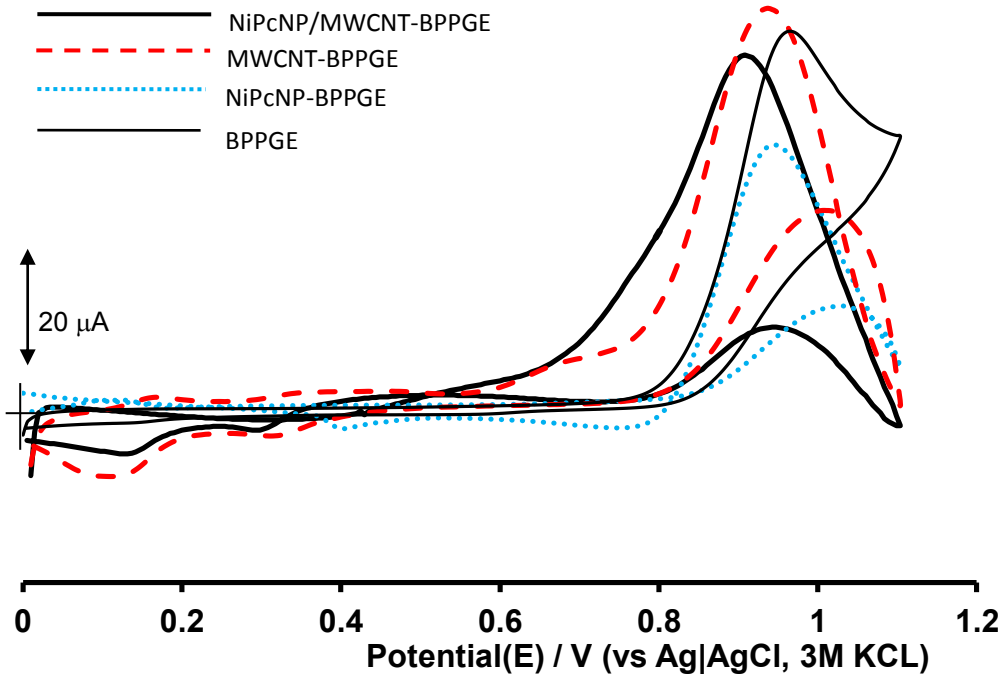

Figure 5.6: Background-corrected cyclic voltammograms for BPPGE, MWCNT-BPPGE, NiPcNP-BPPGE, and NiPcNP/MWCNT-BPPGE in 10^{-3} M asulam. Supporting electrolyte is 0.1 M phosphate buffer at pH 7. Reference electrode: Ag|AgCl, 3 M KCl.

It is clearly seen that NiPcNP/MWCNT-BPPGE gave the best electrocatalytic behavior as its onset potential (~0.65 V) is about 100 mV lower than that of the MWCNT-BPPGE which occurs at ~0.75 V, and ~150 mV lower than that of the other electrodes that occurs at approximately 0.8 V (see **Table 5.2** for values of oxidation

peak potentials of the different electrodes). The enhanced catalysis observed at the NiPcNP/MWCNT-BPPGE is attributed to the nanocomposite nature of the NiPc/MWCNTs as already explained in the discussion on electron transport.

5.2.2 Mechanism of electrocatalytic oxidation of asulam

A plot of I_{pa} against $\nu^{1/2}$ (**Figure 5.7**) resulted in a straight line, showing that for this electrode, asulam oxidation is diffusion-controlled. A plot of $I_{pa}/\nu^{1/2}$ against ν (**Figure 5.8**) resulted in the characteristic shape that is typical of a catalytic process [268].

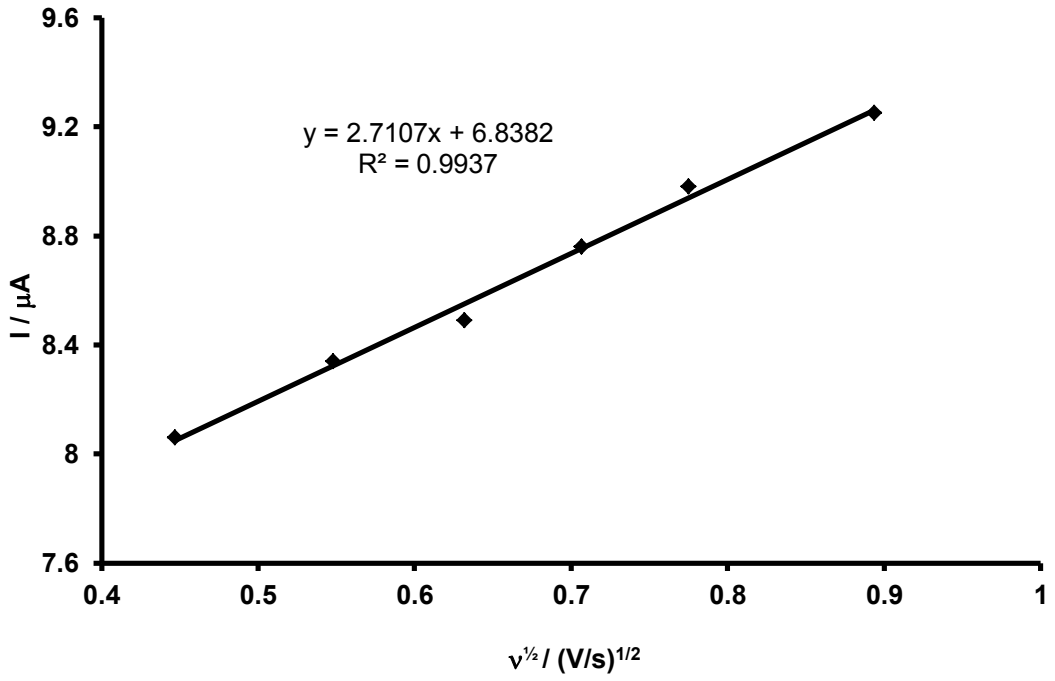

Figure 5.7: Plot of Peak current (I_P) vs $\nu^{1/2}$, for NiPcNP/MWCNT-BPPGE in phosphate buffer at pH 7 containing 1×10^{-3} M asulam.

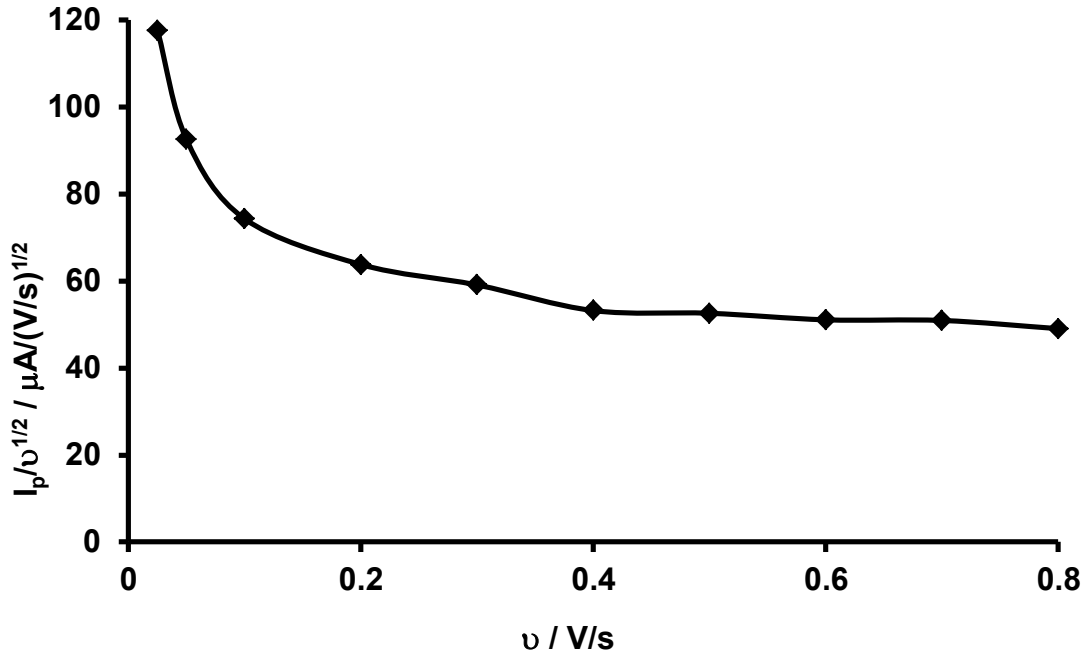

Figure 5.8: Plot of $I_P/\nu^{½}$ vs ν for NiPcNP/MWCNT-BPPGE in phosphate buffer at pH 7 containing 1 x 10^{-3} M asulam.

The oxidation of asulam occurs in the same region as the ring oxidation of the NiPc [255- 256] (**Table 5.1**) and the mechanism proposed in chapter 4 (equations 4.8 – 4.10) applies.

5.2.3 Chronoamperometry with the NiPcNP/MWCNT-BPPGE

Chronoamperometry was used to evaluate the catalytic rate constant as explained in section 5.1.3. To obtain the catalytic rate constant (k), chronoamperograms were obtained at a fixed potential of 0.92 V (versus Ag|AgCl, 3M KCl) over 60 s with the NiPcNP/MWCNT–BPPGE in the absence and presence of 1×10^{-4} M asulam. From the slope of a plot of I_{cat}/I_L versus $t^{1/2}$ (**Figure 5.9)**, the value of k was calculated using equation 4.6 and found to be 13.04 M^{-1} s^{-1}. This value of k is about 100 times less than the value obtained with the NiPcNP-CPE and the literature value for the oxidation of carbofuran by ozone (**Table 5.2**).

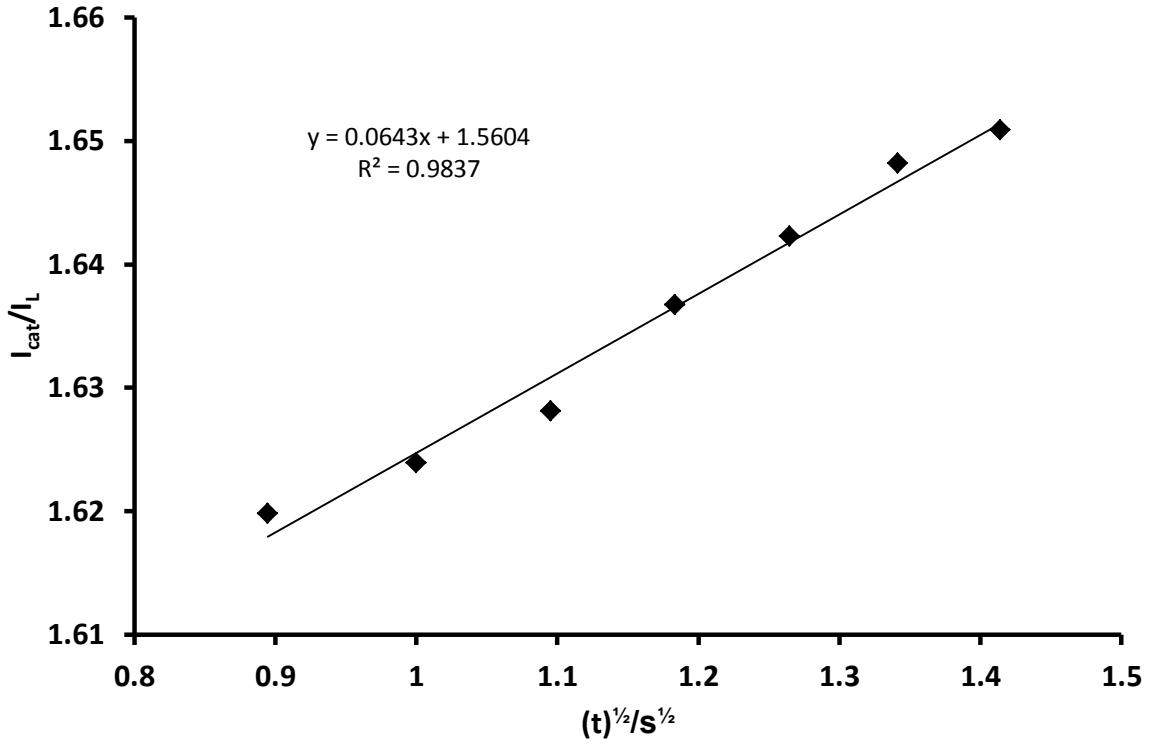

Figure 5.9: A plot of I_{cat}/I_L vs $t^{½}$ for the catalytic oxidation of asulam with the NiPcNP/MWCNT-BPPGE.

The analytical performance of the NiPcNP/MWCNT-BPPGE was tested by employing it in the chronoamperometric detection of asulam under pH 7.0 conditions (**Figure 5.10**) at a fixed potential of 0.92 V (vs Ag|AgCl, 3 M KCl). The plot showed linearity over the concentration range of 91– 412 µM with a sensitivity of 44.6 µA.mM^{-1} and a detection limit of 0.285 µM using the Y_B+3σ criterion (**Table 5.2**).

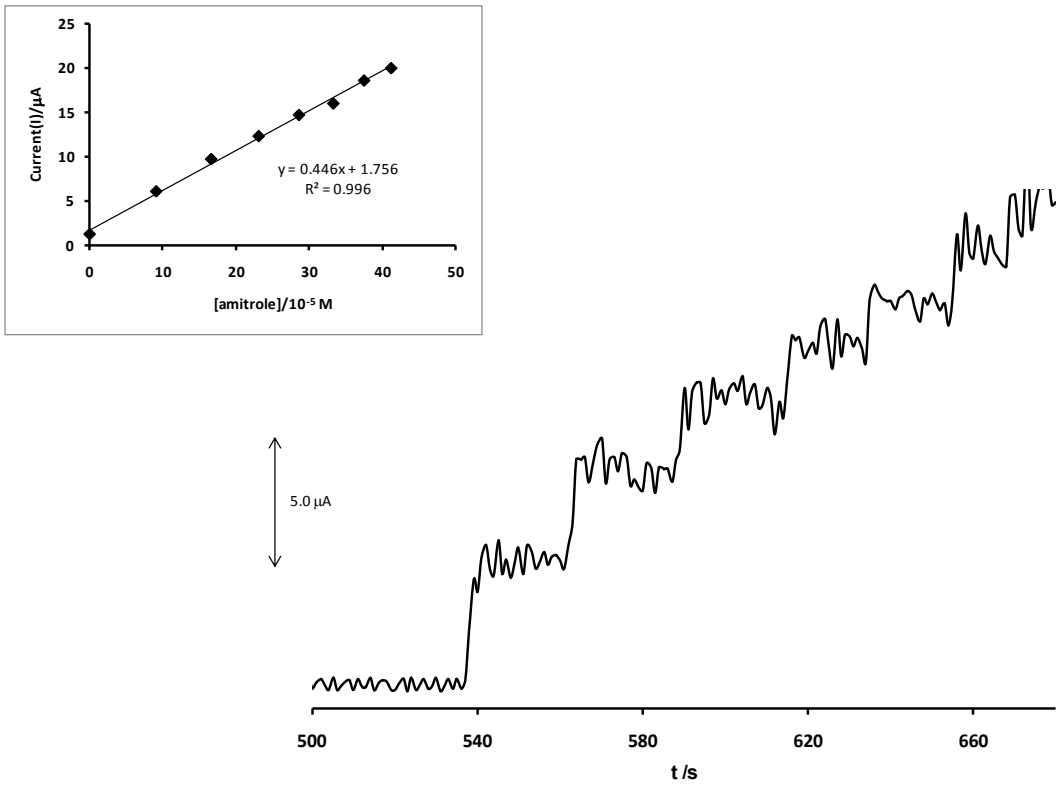

Figure 5.10: Chronoamperograms recorded on sequential injection of aliquots of asulam (1 ml of 1×10^{-3}M) to pH 7 buffer using NiPcNP/MWCNT-BPPGE.

It is noteworthy that NiPcNP/MWCNT-BPPGE displayed a comparable or even better analytical data than reported works such as the limits of detection of 7 and 1.7 µM recorded for asulam at a glassy carbon electrode [231] and a glassy carbon electrode coupled to a capillary electrophoresis instrument [225], respectively. A comparison of the electrochemical parameters listed in **Table 5.2** shows that (i) the detection potential remains the same for both the NiPcNP-CPE and the NiPcNP/MWCNT-BPPGE (~0.9 V), (ii) the limit of detection and sensitivity are better with the NiPcNP-CPE than the NiPcNP/MWCNT-BPPGE (iii) the linear measuring range is improved with the NiPcNP/MWCNT-BPPGE. A low limit of detection, high sensitivity, a wide linear measuring range, and a stable electrode with repeatable

measurements are amongst the desirable attributes of a good electrode. However, the relative importance of the factors mentioned above also depends on the intended use of the electrode. The NiPcNP-CPE, with its lower limit of detection and higher sensitivity, may be a better electrode to use than the NiPcNP/MWCNT-BPPGE if the concentration range is to be strictly monitored and adhered to, assumimg that the other factors are the same for both electrodes. Any concentration outside this range becomes unimportant. However, if the concentration is unknown and/or so high that it lies outside the NiPcNP-CPE measuring range, then this electrode will not be very useful, and the NiPcNP/MWCNT-BPPGE may be the better electrode to use because of its wide linear measuring range.

5.2.4 Stability of the NiPcNP/MWCNT-BPPGE

The stability of the electrode was examined by studying the impact of scan number on the current response (**Figure 5.11**).

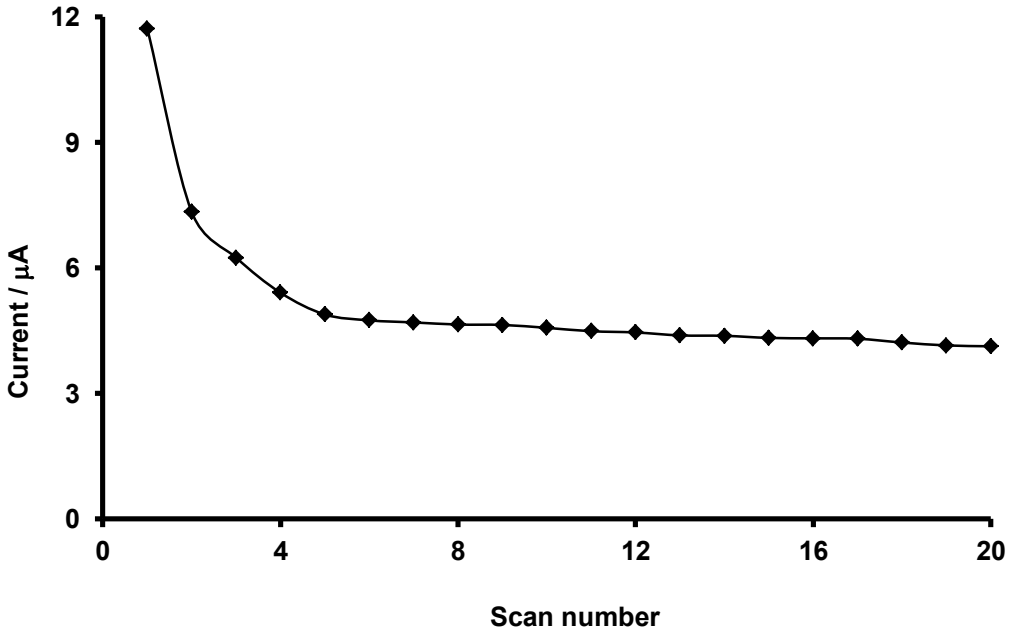

Figure 5.11: Plot of current response (I_P) vs scan number for the NiPcNP/MWCNT-BPPGE in phosphate buffer at pH 7 containing 10^{-3} M asulam.

The plot shows that the current response decreases to 42% of its initial value after about the fourth scan and then stabilizes. Also, 86% of the initial current response is recovered upon rinsing of the electrode in phosphate buffer at pH 7. Furthermore, if the electrode is rinsed and then left in the refrigerator for 2 weeks, 91% of the initial current response is displayed.

5.3 Conclusions

An FePcNP/MWCNT-BPPGE and NiPcNP/MWCNT-BPPGE were constructed and their ability to catalyse amitrole and asulam oxidation, respectively, were investigated. The electrode parameters associated with the electrocatalytic detection of amitrole and asulam were also established. The following conclusions can be made:

1. Although the FePcNP/MWCNT-BPPGE showed electrocatalytic behaviour towards amitrole oxidation, its detection potential of 0.61 V is higher than that of the FePcNP-CPE (0.55 V). Its catalytic rate constant of 18.05 M^{-1} s^{-1} is far lower than that of the FePcNP-CPE (50.4×10^6 M^{-1} s^{-1}), and its sensitivity (25.97 pA/nM) is far lower than the 2.00 μA/nM displayed by the FePcNP-CPE. Its LOD is very high (5.2 μM), in comparison to the 2.48 nM obtained with the FePcNP-CPE, and the linear concentration range ($1 - 9 \times 10^{-4}$ M) displayed by the FePcNP/MWCNT-BPPGE is actually obtained only at high concentrations of amitrole, making it imposible to measure very low amitrole concentrations such as those in the micro- or nanomolar range.
2. The NiPcNP/MWCNT-BPPGE showed electrocatalytic behaviour towards asulam, and its detection potential of 0.9 V is similar to that of the NiPcNP-CPE in the same analyte. A catalytic rate constant of 13.04 M^{-1} s^{-1} was obtained at the NiPcNP/MWCNT-BPPGE. This rate constant is much lower

than the 1.26×10^3 M^{-1} s^{-1} obtained at the NiPcNP-CPE, and the sensitivity of the NiPcNP/MWCNT is expectedly lower, at 44.6 nA/μM, than the 1.98 μA/μM obtained with the NiPcNP-CPE. The electrode displayed a LOD of 0.285 μM, which is higher than the 61.9 nM obtained with the NiPcNP-CPE. However, this electrode displayed a much wider linear concentration range of 91 – 412 μM than the 0.4 → 2 μM concentration range displayed by the NiPcNP-CPE.

3. Both electrodes could be used repeatedly if rinsed in buffer after each measurement, with the FePcNP/MWCNT-BPPGE showing a percentage recovery of 92% of the initial current after rinsing, and the NiPcNP/MWCNT-BPPGE, a percentage recovery of 91%.

In the next chapter, metal tetra-amino phthalocyanines (MTAPcs, M = Fe, Co, Mn, Ni) will be electropolymerized on the MWCNTs (instead of mixing the MPcs with the MWCNTs), and an investigation of the electrocatalytic behaviour of such electrodes will be done, using amitrole and asulam as test analytes.

Chapter 6

Electroanalysis with Basal Plane Pyrolytic Graphite Electrode Modified with MWCNTs and Electropolymerized Metal tetra-amino phthalocyanines (MTAPcs).

In this chapter, basal plane pyrolytic graphite electrodes modified with MWCNTs and electropolymerized MTAPcs are employed in the electroanalytical detection of amitrole and asulam.

6.1 Electroanalytical Detection of Amitrole

6.1.1 Electrocatalysis of amitrole

Figure 6.1 shows the cyclic voltammograms of BPPGE, MWCNT-BPPGE, *poly*-CoTAPc-MWCNT-BPPGE, *poly*- FeTAPc-MWCNT-BPPGE, *poly*- MnTAPc-MWCNT-BPPGE, and *poly*- NiTAPc-MWCNT-BPPGE obtained from 1×10^{-3} M amitrole dissolved in a phosphate buffer solution at pH 12 with 0.05 M Na_2SO_4 as the supporting electrolyte.

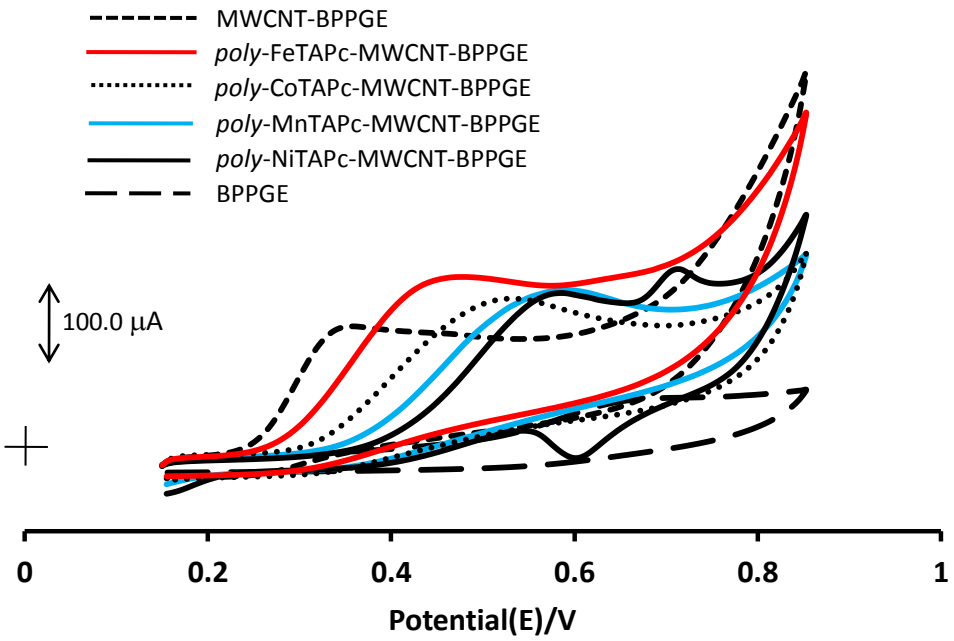

Figure 6.1: Cyclic voltammograms of different electrodes in pH 12 phosphate buffer containing 1×10^{-3} M amitrole. Supporting electrolyte is 0.05 M Na_2SO_4. Scan rate = 0.025 V/s. Reference electrode: Ag|AgCl (3 M KCl).

All the modified electrodes show catalytic behaviour when attached to the BPPGE surface, with the MWCNT-BPPGE displaying the best behaviour in terms of the detection potential. Amongst the MTAPc-MWCNT-BPPGEs, the *poly*-FeTAPc-MWCNT-BPPGE showed the best electrocatalytic behaviour in terms of reduction of potential and current enhancement (**Figure 6.1**). A comparison of the current

response of the *poly*-FeTAPc-MWCNT-BPPGE with that of the *poly*-FeTAPc-BPPGE shows the effect of co-modification of the BPPGE surface with both MWCNTs and electropolymerized FeTAPc (**Figure 6.2**). The current enhancement and negative potential shift is far more pronounced with the poly-FeTAPc-MWCNT-BPPGE than with the poly-FeTAPc-BPPGE.

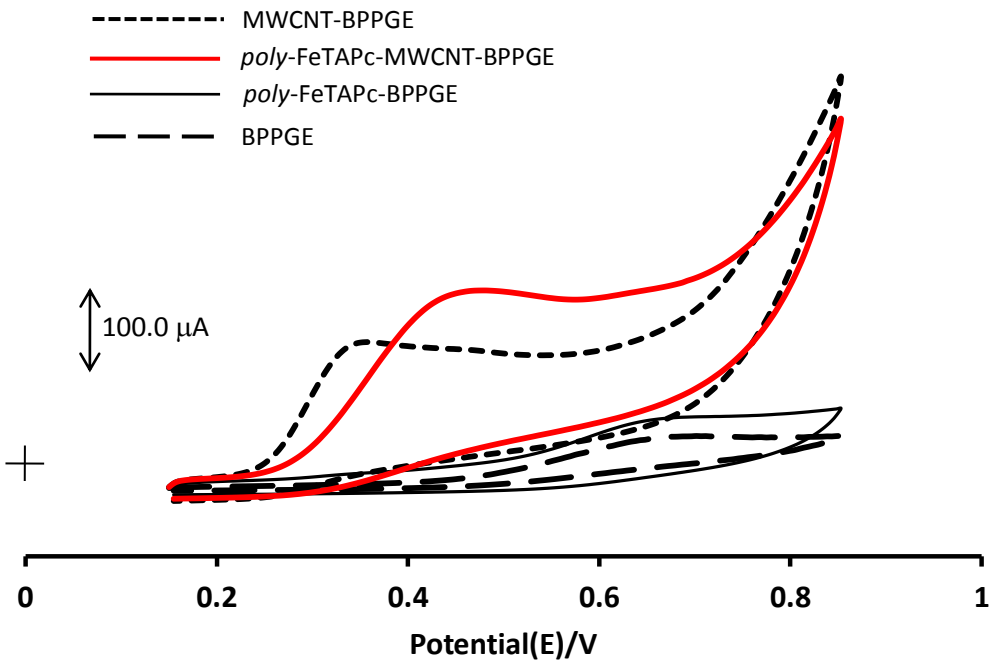

Figure 6.2: Cyclic voltammograms of *poly*-FeTAPc-MWCNT-BPPGE, *poly*-FeTAPc-BPPGE, MWCNT-BPPGE and BPPGE in 1×10^{-3} M amitrole. Supporting electrolyte is Na_2SO_4. Scan rate = 0.05 V. Reference electrode: Ag|AgCl (3 M KCl)

The pronounced electrocatalytic behaviour displayed by the *poly*-FeTAPc-MWCNT-BPPGE relative to the *poly*-FeTAPc-BPPGE indicates that (i) modification of MWCNT with FeTAPc improves electronic communication between the amitrole and the BPPGE and (ii) electrocatalytic oxidation and detection of amitrole is improved further by electrodeposition of FeTAPc on the MWCNT surface. The oxidation potentials of the different electrodes in the presence of MWCNTs (**Table 6.1**) follow the trend: BPPGE > *poly*-NiTAPc-MWCNT-BPPGE > *poly*-MnTAPc-MWCNT-BPPGE >

poly-CoTAPc-MWCNT-BPPGE > *poly*-FeTAPc-MWCNT-BPPGE > MWCNT-BPPGE. Although the lowest amitrole detection potential (of all the electrodes) was obtained with the MWCNT-BPPGE, the *poly*-FeTAPc-MWCNT-BPPGE was chosen for further investigation because of the expected high sensitivity (due to the high current response) and better stability (less amitrole adsorption on this electrode surface than at the MWCNT-BPPGE surface) of the electrode (to be discussed later).

The NiTAPc-MWCNT-BPPGE displayed the poorest electrocatalysis of the MTAPc-MWCNT-BPPGEs, in terms of current enhancement and detection potential. The redox couple that appears at ~0.5 V at the NiTAPc-MWCNT-BPPGE is due to the $Ni^{III}Pc^{-2}/Ni^{II}Pc^{-2}$ redox process mentioned earlier [255-258]. An interesting observation from **Table 6.1** is that, although *poly*-NiTAPc-MWCNT-BPPGE displayed the highest amitrole oxidation potential in comparison to the other *poly*-MTAPc-MWCNT-BPPGEs, the corresponding *poly*-NiTAPc-BPPGE (without MWCNTs) displayed the lowest amitrole oxidation potential when compared to the other *poly*-MTAPc-BPPGEs. The reason may be that, with the *poly*-NiTAPc-BPPGE, amitrole oxidation may be catalysed by the $Ni^{III}Pc^{-2}/Ni^{II}Pc^{-2}$ redox process whereas this is not the case with the *poly*-NiTAPc-MWCNT-BPPGE, where amitrole oxidation occurs at a potential which is lower than the half-wave potential of the $Ni^{III}Pc^{-2}/Ni^{II}Pc^{-2}$ couple and is thus unaffected by it.

Table 6.1: Oxidation potentials (E_P/V vs Ag|AgCl (3 M KCl) of different electrodes in 1×10^{-3} M amitrole at pH 12 and in 1×10^{-3} M asulam at pH 7.

Electrode	Oxidation potential of 10^{-3} M amitrol	Oxidation potential of 10^{-3} M asulam	Redox process of MPc	Potential of redox process of MPc in pH 12	Potential of redox process of MPc in pH 7
BPPGE	0.66 V	0.96 V	----------	----------	----------
MWCNT-BPPGE	0.34 V	0.89 V	----------	----------	----------
Poly-MnTAPc-MWCNT-BPPGE	0.56 V	0.86 V	$Mn^{IV}Pc^{-2}/Mn^{III}Pc^{-2}$	0.36 V	0.56 V
Poly-FeTAPc-MWCNT-BPPGE	0.44 V	0.88 V	$Fe^{III}Pc^{-2}/Fe^{II}Pc^{-2}$	0.38 V	0.56 V
Poly-NiTAPc-MWCNT-BPPGE	0.58 V	0.94 V	$Ni^{III}Pc^{-2}/Ni^{II}Pc^{-2}$ $Ni^{II}Pc^{-1}/Ni^{II}Pc^{-2}$	0.6 V 0.88 V	0.38 V *-------
Poly-CoTAPc-MWCNT-BPPGE	0.51 V	0.87 V	$Co^{II}Pc^{-1}/Co^{II}Pc^{-2}$ $Co^{III}Pc^{-2}/Co^{II}Pc^{-2}$	*-------- 0.66 V	(0.73 V) 0.54 V

Poly-MnTAPc -BPPGE	0.68 V	0.97 V	$Mn^{IV}Pc^{-1}/Mn^{IV}Pc^{-2}$	0.45 V	0.86 V
Poly-FeTAPc-BPPGE	0.66 V	0.91 V	$Fe^{III}Pc^{-2}/Fe^{II}Pc^{-2}$	0.51 V	*--------
Poly-NiTAPc-BPPGE	0.63 V	0.93 V	$Ni^{II}Pc^{-1}/Ni^{II}Pc^{-2}$ $Ni^{III}Pc^{-2}/Ni^{II}Pc^{-2}$	1.15 V 0.66 V	0.85 V -0.12 V
Poly-CoTAPc-BPPGE	0.68 V	0.93 V	$Co^{III}Pc^{-2}/Co^{II}Pc^{-2}$	0.69 V	*-------

*peak was not detected.

6.1.2 Mechanism of electrocatalytic oxidation of amitrole

A plot of I_P vs $\nu^{½}$ (**Figure 6.3**), from scan rate (ν) = 10 mV/s to ν = 240 mV/s, produced a straight line, indicating that oxidation of amitrole with the *poly*-FeTAPc-MWCNT-BPPGE at these scan rates is diffusion-controlled. From ν = 300 mV/s to ν = 900 mV/s the current response stabilized, indicating electrode fouling.

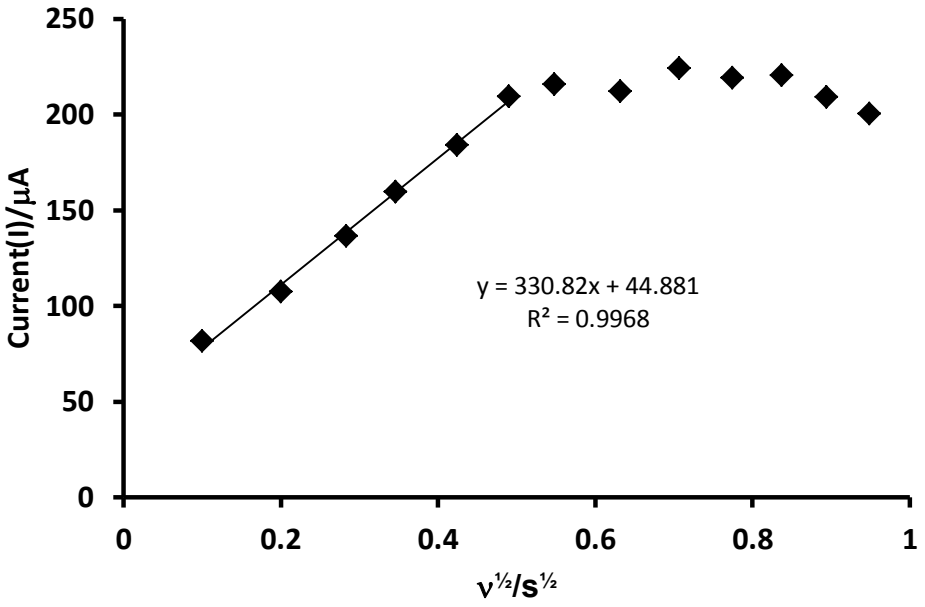

Figure 6.3: Plot of I_P vs $\nu^{½}$ for the FeTAPc-MWCNT-BPPGE in pH 12 phosphate buffer containing 10^{-3} M amitrole. Supporting electrolyte is 0.05 M Na_2SO_4.

A plot of $I_P/\nu^{1/2}$ vs ν (**Figure 6.4**) produced the characteristic shape of a coupled chemical reaction (EC_{cat}) for the amitrole, clearly confirming catalytic activity.

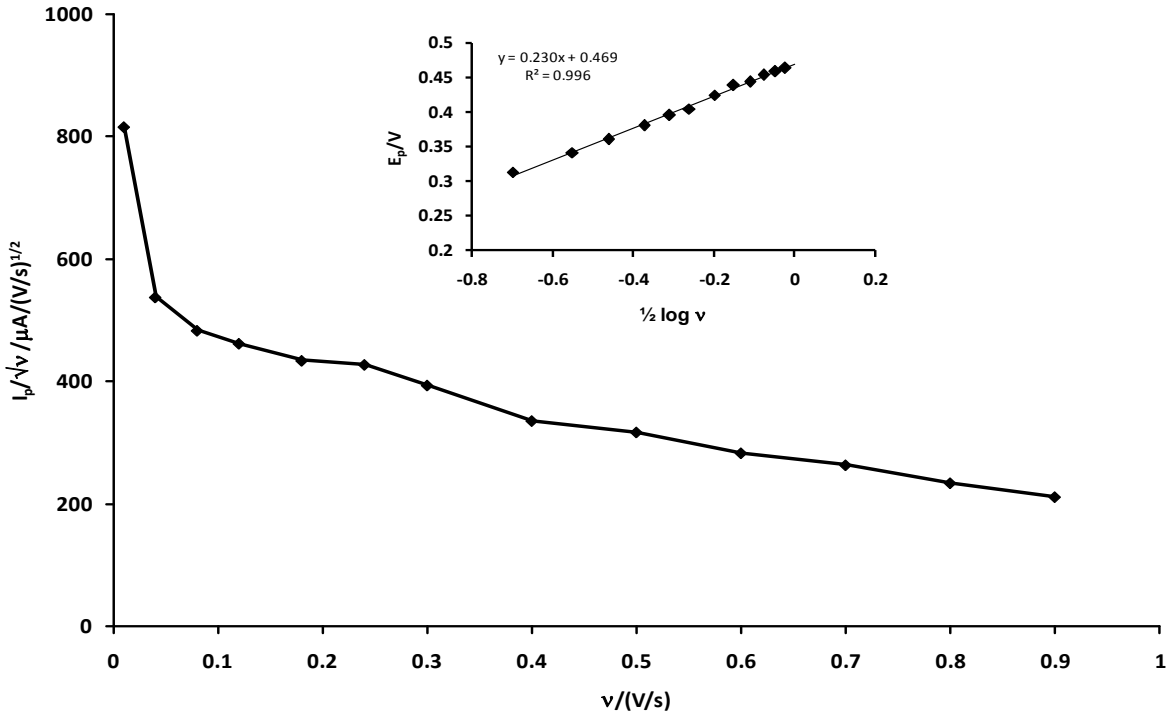

Figure 6.4: Plot of $I_P/\nu^{½}$ vs ν for FeTAPc-MWCNT-BPPGE in 10^{-3} M amitrole in phosphate buffer at pH 12. Supporting electrolyte is 0.05 M Na_2SO_4. Inset: Plot of E_P vs ½ log ν.

From a plot of E_P vs ½ log ν (Figure 6.4, inset), a Tafel slope of 230 mV/decade was obtained, indicating that the rate-determining step for the electrocatalysis is a one-electron transfer process. The Tafel slope $\left(b = \frac{2.303RT}{\alpha nF}\right)$ is greater than the 120 mV that is expected for a one-electron process, due to binding of amitrole or its oxidation products to the surface. On the basis of the information extracted from the plots above, the mechanism proposed in chapter 4 (equations 4.2 – 4.4) for the oxidation of amitrole is suggested.

6.1.3 Chronoamperometry with the *poly*-FeTAPc-MWCNT-BPPGE

To obtain the catalytic rate constant, chronoamperograms were obtained at a fixed potential of 0.4 V (versus Ag|AgCl pseudo-reference electrode) over 40 s for the *poly*-FeTAPc–MWCNT–BPPGE in the absence and presence of 1×10^{-6} M amitrole. From the slope of a plot of I_{cat}/I_L versus $t^{1/2}$ (**Figure 6.5**) the value of k (equation 4.6) was found to be 3.85×10^4 M^{-1} s^{-1} (**Table 6.2**).

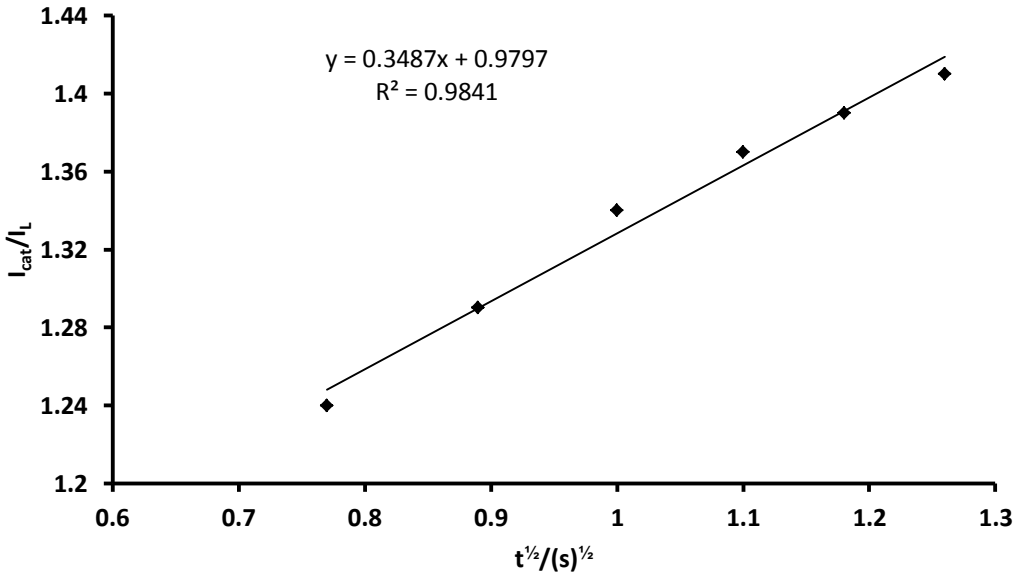

Figure 6.5: Plot of I_{cat}/I_L vs. $t^{½}$ for the catalytic oxidation of amitrole in pH 12 phosphate buffer, on *poly*-FeTAPc–MWCNT–BPPGE. Supporting electrolyte is 0.05 M Na_2SO_4.

This value of k is far higher than the value reported in the literature (**Table 6.2**), and also about 200 times higher than the value obtained with the FePcNP/MWCNT-BPPGE (**Table 5.2**). However, it is still about 10^3 times lower than value of k obtained with the FePcNP-CPE (**Table 5.2**).

Figure 6.6 shows chronoamperomegrams recorded at different concentrations of amitrole at a fixed potential E = 0.5 V vs Ag|AgCl (3 M KCl). The electrode had to be taken out of the solution and rinsed in pH 12 phosphate buffer between chronoamperometric measurements because of fouling of the electrode surface by amitrole or its products or intermediates.

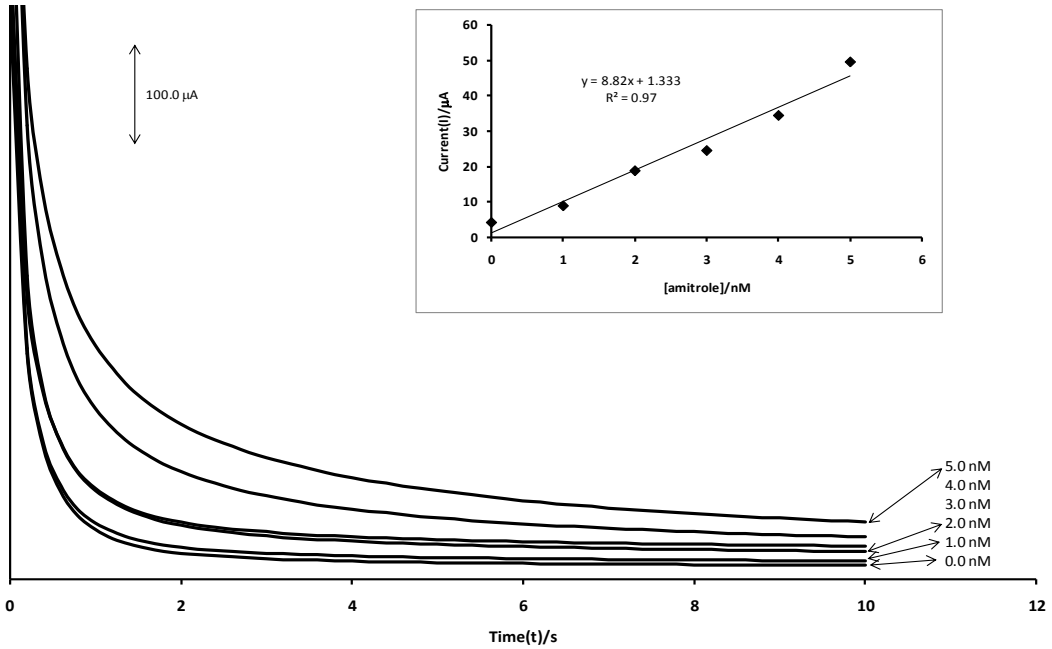

Figure 6.6: Chronoamperograms of FeTAPc-MWCNT-BPPGE, obtained at a fixed potential of 0.4 V vs Ag|AgCl (3 M KCl), in pH 12 phosphate buffer containing different concentrations of amitrole. Supporting electrolyte is 0.05 M Na_2SO_4. Scan rate = 0.05 V/s. Inset: Plot of Current (I) vs [Amitrole].

More than 90% of the original current recorded at each amitrole concentration was regenerated after rinsing with the buffer, thus establishing the viability of continuous use of the electrode once fabricated. A linear relationship, within a concentration range of 1.0 to 5.0 nM, was obtained when the current response was plotted against amitrole concentration (**Figure 6.6**, inset). The sensitivity of the electrode was obtained from the slope of the straight line, and the limit of detection was calculated using the $y=y_B + 3\sigma$ criterion. The limit of detection obtained with the poly-FeTAPc-MWCNT-BPPGE is far lower than those reported in the literature, and its sensitivity is far higher than the reported literature values (**Table 6.2**). However, its linear measuring range is much narrower than those reported in the literature (**Table 6.2**). The three electrodes that have been constructed will be compared in Section 6.3.

Table 6.2: Electrochemical parameters associated with electrodes investigated. Reference electrode: Ag|AgCl (3 M KCl).

Parameter	***Poly*-FeTAPc-MWCNT-BPPGE**	***Poly*-CoTAPc-MWCNT-BPPGE**
Analyte	Amitrole (at pH 12)	Asulam (at pH 7)
Detection Potential	0.44 V	0.87 V
Limit of Detection	0.325 nM (1.07 μM[a], 0.38 μM[b])	1.15 μM (1.74 μM[c], 7.1 μM[d])
Sensitivity	8.82 μA/nM (4.41 pA/nM[a], 0.073 nA/nM[b])	241x10^{-3} μA/μM (0.91 μA/μM[c])
Linear Measuring Range	1.0 → 5.0 nM (23.0 – 230 nM[a], 0 – 260 μM[b])	4.5 → 20.6 μ M (4 – 109 μM[c], 10 – 90 μM[d])
Catalytic Rate constant	3.85×10^4 $M^{-1} s^{-1}$ (18.95×10^{-2} s^{-1})[b]	1.60×10^2 $M^{-1} s^{-1}$ (1.108×10^3 $M^{-1} s^{-1}$)[e]
Stability	90 % of initial current recovered after rinsing in phosphate buffer.	96 % of initial current recovered after rinsing in phosphate buffer.

[a] ref 269, [b] ref 274, [c] ref 225, [d] ref 231, and [e] ref 282.

6.1.4 Selectivity Studies

The selectivity of the FeTAPc-modified BPPGE-MWCNT was investigated using the mixed solution method [279]. The concentration of the interfering species and amitrole were 10^{-6} and 10^{-7} M, respectively. The selectivity was checked against the pesticides atrazine, simazine, 3,6-dichloro-2-methoxybenzoic acid (dicamba) and

ammonium thiocyanate (component of many herbicide formulations). The values of K_{amp} (where K_{amp} is the amperometric selectivity coefficient) were determined from equation 4.7 (now equation 6.1) for analysis in the presence of interfering ions:

$$K_{amp} = \left(\frac{\Delta I_{mixture}}{\Delta I_{amitrole}} - 1 \right) \frac{[amitrole]}{[\text{int}\, erferent]} \qquad \textbf{6.1}$$

where $\Delta I_{mixture}$ and $\Delta I_{amitrole}$ are respectively, the changes in current for the mixture containing amitrole and the interfering ion, and amitrole alone. The K_{amp} values are graphically represented in **Figure 6.7**.

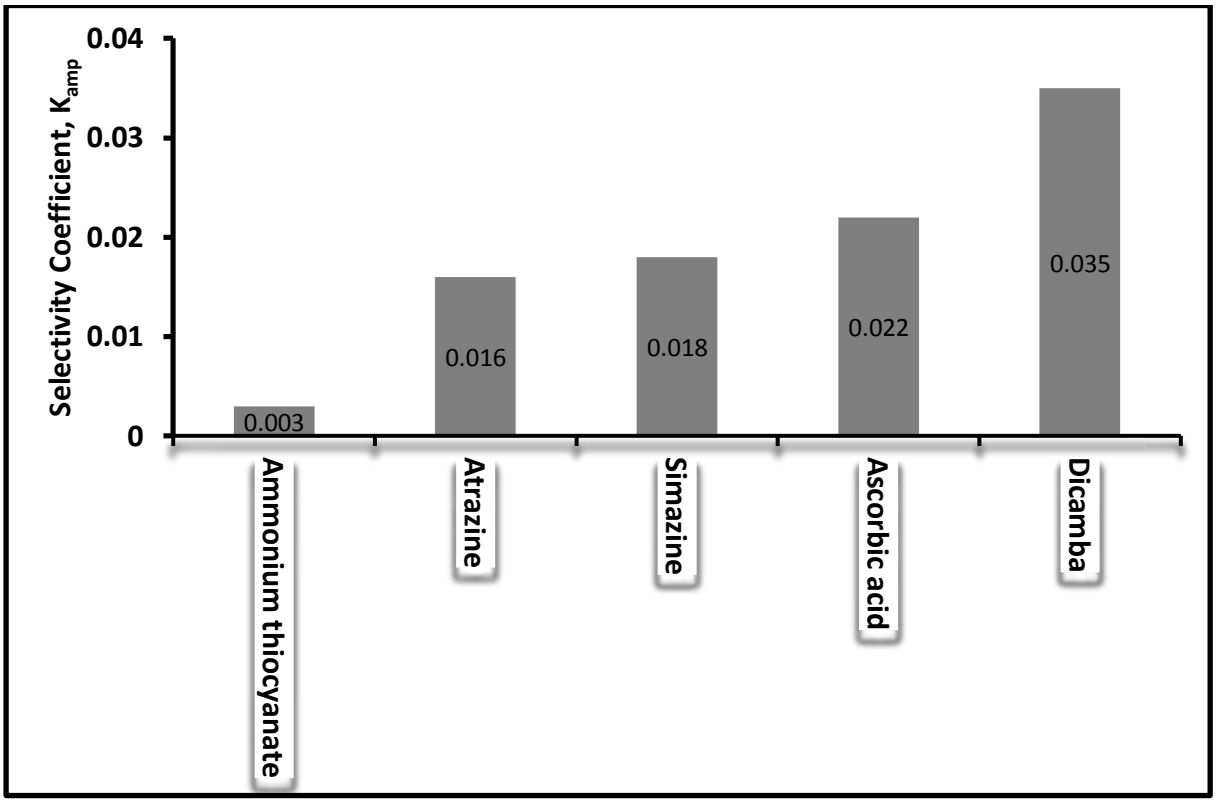

Figure 6.7: Amperometric selectivity coefficient of *poly*-FeTAPc-MWCNT-BPPGE for different potentially interfering species in the presence of amitrole.

As stated in chapter 4, a K_{amp} value of less than 10^{-3} indicates non-interference, while one which falls within the order of 10^{-3} suggests that the species is an interferent, but not a strong one. Of all the possible interferents studied, dicamba

interfered most strongly, while ammonium thiocyanate is the least interferent. Thus, the electrode could be most conveniently used for the detection of amitrole in solution where ammonium thiocyanate is present.

6.2. Electroanalytical Detection of Asulam

6.2.1 Electrocatalysis of asulam

The electrocatalytic behaviour of the different electrodes was investigated using an asulam as the test analyte. **Figure 6.8** shows the cyclic voltammograms of a 1×10^{-3} M asulam solution, obtained with the different *poly*-MTAPc-MWCNT-BPPGEs and the bare BPPGE. Clearly, the *poly*-MTAPc-MWCNT-BPPGEs show electrocatalytic behaviour towards oxidation of asulam, as indicated by the negative shift of the amitrole oxidation potential with all of them, in comparison with that obtained with the BPPGE. The *poly*-CoTAPc-MWCNT-BPPGE exhibits the most electrocatalytic behaviour of all the electrodes (**Figure 6.8**(top)), displaying a negative potential shift of ~100 mV in comparison to that obtained with the BPPGE (**Table 6.1**). The amitrole oxidation potentials obtained with the different electrodes (containing MWCNTs) follow the sequence: BPPGE (~0.96 V) > *poly*-NiTAPc-MWCNT-BPPGE (0.94 V) > *poly*-FeTAPc-MWCNT-BPPGE (~0.88 V) > *poly*-MnTAPc-MWCNT-BPPGE (~0.86 V) > *poly*-CoTAPc-MWCNT-BPPGE (~0.87 V). The *poly*-NiTAPc-MWCNT-BPPGE displayed the highest current response though (~25.2 μA), followed by the *poly*-CoTAPc-MWCNT-BPPGE (~22.5 μA). If we consider the lowest detection potential exhibited by the different electrodes, *poly*-CoTAPc-MWCNT-BPPGE is therefore the most catalytic towards amitrole oxidation. In **Figure 6.8** (bottom), cyclic voltammograms of the *poly*-CoTAPc-MWCNT-BPPGE, MWCNT-BPPGE, *poly*-CoTAPc-BPPGE and BPPGE are displayed. Although amitrole oxidation with the

MWCNT-BPPGE occurs at about the same potential as with the poly-CoTAPc-MWCNT-BPPGE, the anodic peak obtained is very broad.

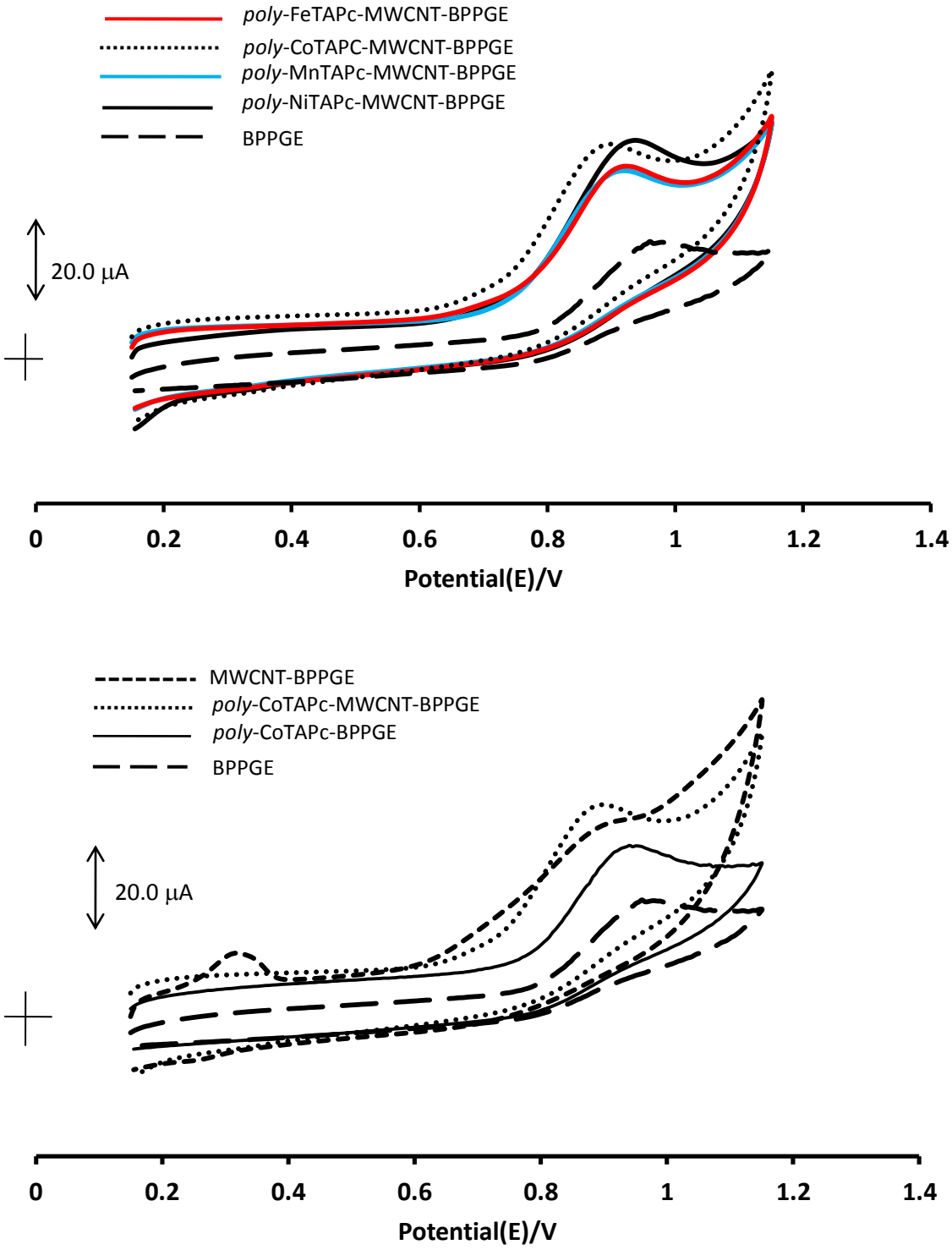

Figure 6.8: Cyclic voltammograms of *poly*-MTAPc-MWCNT-BPPGE and BPPGE (top), and cyclic voltammograms of *poly*-CoTAPc-MWCNT-BPPGE, *poly*-CoTAPc-BPPGE, MWCNT-BPPGE, and BPPGE (bottom) in 1×10^{-3} M asulam in phosphate buffer, pH 7. Scan rate = 0.025 V/s. Reference electrode: Ag|AgCl (3 M KCl).

The observations of a sharp peak with enhanced current and lower potential with the *poly*-CoTAPc-MWCNT-BPPGE are an indication of the improved electronic communication between the asulam and the BPPGE, and improved electrocatalytic oxidation and detection of asulam, as explained before. The CoTAPc-MWCNT-BPPGE was thus employed in all subsequent investigations. The peak due to the oxidation of asulam at ~0.87 V is in the range of the peak due to ring oxidation of CoTAPc and the formation of a Pc^{-1} species (**Table 6.1**), thus suggesting that ring-based processes are involved in the catalytic oxidation. This also confirms a two-electron oxidation process for asulam catalysed by $Co^{III}Pc^{-1}$.

6.2.2 Mechanism for the electrocatalytic oxidation of asulam

A plot of anodic peak current (I_{pa}) against the square root of scan rate ($\nu^{1/2}$) (**Figure 6.9**) (for scan rates less than 300 mV/s) resulted in a straight line, an indication of a diffusion controlled asulam oxidation. However, at higher scan rates (300–1200 mV/s) the I_p versus $\nu^{1/2}$ plot was non-linear, most likely due to the adsorption of asulam on the surface of the carbon nanotubes [40,238,283].

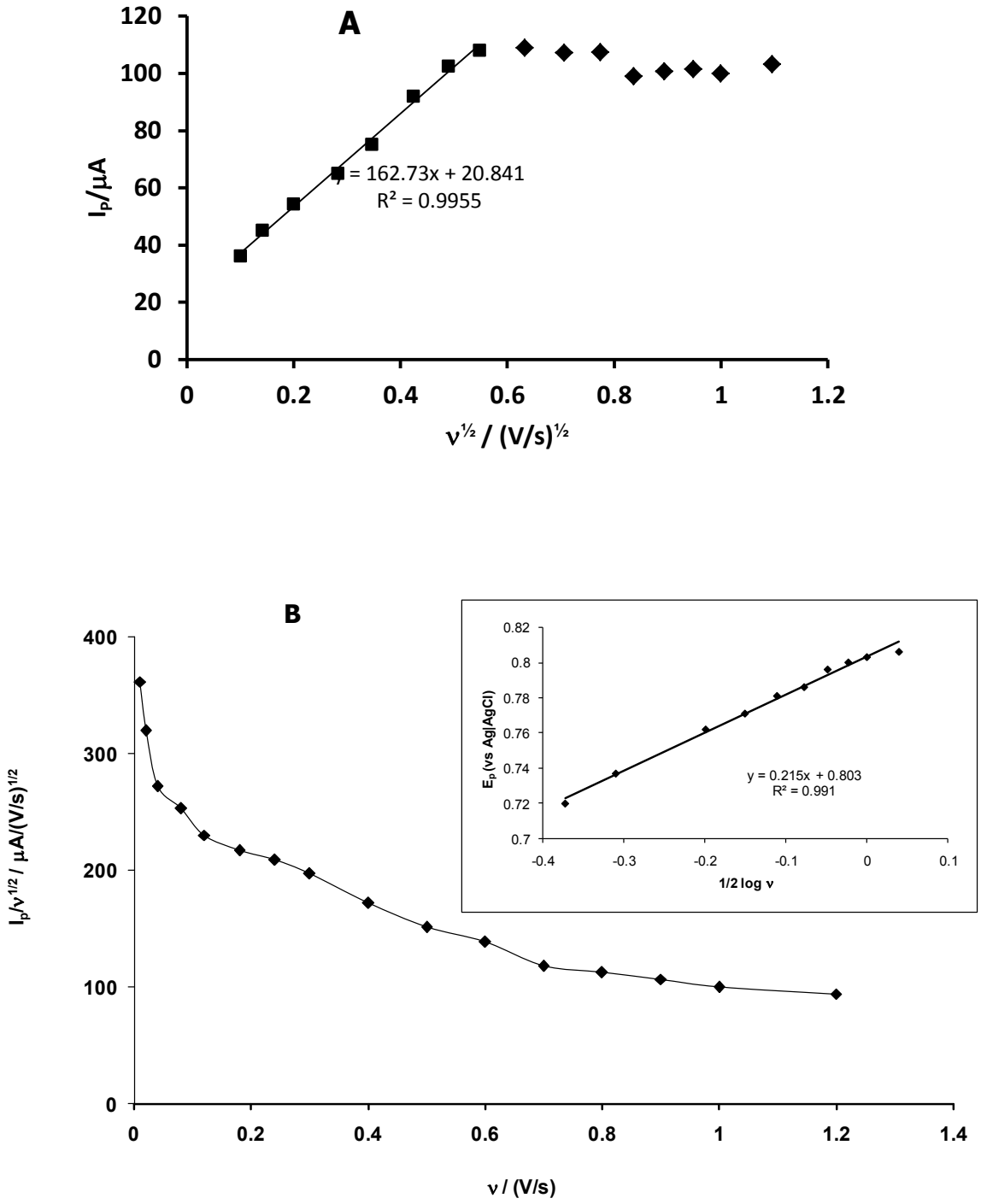

Figure 6.9 : Plots of I_P vs $\nu^{1/2}$ (**A**) and $I_P/\nu^{1/2}$ vs ν (**B**) for CoTAPc-MWCNT-BPPGE in 1×10^{-3} M asulam. Inset: Plot of E_P vs ½ log ν.

A plot of $I_{pa}/\nu^{1/2}$ against ν (**Figure 6.9B**) resulted in the characteristic shape that is typical of a catalytic process of electrochemical reaction preceding a chemical reaction (EC_{cat}) [270]. A plot of E_p versus ½ log ν (**Figure 6.9B**, inset) gave a linear

relationship, with a Tafel slope (b = 2.303RT/αnF) of approximately 215 mV/decade, indicating that the rate determining step for the catalysis is a one-electron transfer process. The Tafel slope obtained in this work is greater than the normal 30–120 mV/decade, and this may be due to stronger binding of the CoTAPc with the asulam during the intermediate reaction step, as reported by others for such occurrence [274-276].

From the discussion above the following conclusion can be made about the oxidation process: a total of two electrons are involved during the electro-oxidation process, in separate one electron oxidation steps (Tafel plot, **Figure 6.9B**, inset). A two-electron, two-proton oxidation process has also been proposed for the oxidation of carbamates [281]. Also cyclic voltammetry shows that oxidation of asulam occurs at the potentials of $Co^{III}Pc^{-1}$ species, hence confirming a two electron catalytic oxidation process. The following mechanism may be proposed for the CoTAPc-catalysed oxidation of asulam:

$$Co^{II}TAPc^{2-} \rightarrow [Co^{III}TAPc^{2-}]^{+} + e^{-} \qquad \textbf{6.2}$$

$$[Co^{III}TAPc^{2-}]^{+} \rightarrow [Co^{III}TAPc^{1-}]^{2+} + e^{-} \qquad \textbf{6.3}$$

$$[Co^{III}TAPc^{1-}]^{2+} + \text{asulam} \rightarrow [Co^{II}TAPc] + \text{asulam oxidation products} \qquad \textbf{6.4}$$

The possibility of coordination of asulam to $Co^{III}TAPc$ was studied by spectrophotometric experiments of immobilized CoTAPc on a glass slide surface. **Figure 6.10** shows the UV/Vis spectra for the $Co^{II}TAPc$ (**curve 1**) when immobilized onto a glass surface, $Co^{III}TAPc$ (**curve 2**) which was generated by

exposing the Co^{II}TAPc to bromine vapour, dipping the formed Co^{III}TAPc into a 1×10^{-2} M solution of asulam, followed by drying (**curve 3**).

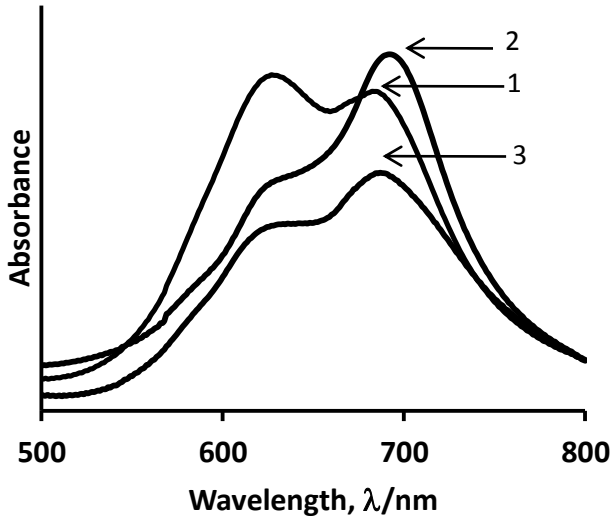

Figure 6.10: UV/Vis spectra of Co^{II}TAPc (curve 1), Co^{III}TAPc (curve 2), Co^{III}TAPc in the presence of asulam (curve 3). Spectra recorded in DMF.

Two peaks (at 623 and 682 nm) were observed (**curve 1**) for Co^{II}TAPc.

The presence of two peaks in the visible region is typical [120] of aggregation in MPc complexes with the low energy peak being due to the aggregate. On oxidation of Co^{II}TAPc to Co^{III}TAPc with bromine, Co^{III}TAPc was formed with a main absorption band at 690 nm, which shifted to 683 nm on exposure of Co^{III}TAPc to asulam, and is very close 682 nm of the low energy peak of Co^{II}TAPc, suggesting reduction back to the latter species. No changes in spectra were observed on addition of asulam to Co^{II}TAPc. Normally small shifts in Q band are typical of axial ligation in MPc complexes [120], however a shift of just 1 nm between Co^{II}TAPc in the absence of asulam and Co^{II}TAPc formed by addition of asulam to Co^{III}TAPc is not adequate to suggest coordination, but Tafel slopes do suggest coordination, maybe to Co^{III}TAPc.

It is however important to note that changes represented in **Figure 6.10** are due to adsorbed monomer, and could be different for adsorbed polymer. The difference in the relative magnitudes of the low and high energy peaks in **curve 1** and **curve 3** is a result of different extents of aggregation.

6.2.3 Chronoamperometry with the *poly*-CoTAPc-MWCNT-BPPGE

Chronoamperometry was used to evaluate the catalytic rate constant. To obtain such data, chronoamperograms were obtained at a fixed potential of 0.73 V (versus Ag|AgCl) over 60 s for the *poly*-CoTAPc–MWCNT–BPPGE in the absence and presence of 1×10^{-4} M asulam. Using equation 4.6, the value of k was determined graphically from the slope of a plot of I_{cat}/I_L versus $t^{1/2}$ (**Figure 6.11**), between t = 0.8 and t = 2.2 s. The value of k was found to be 1.60×10^2 $M^{-1}s^{-1}$ (**Table 6.2**)

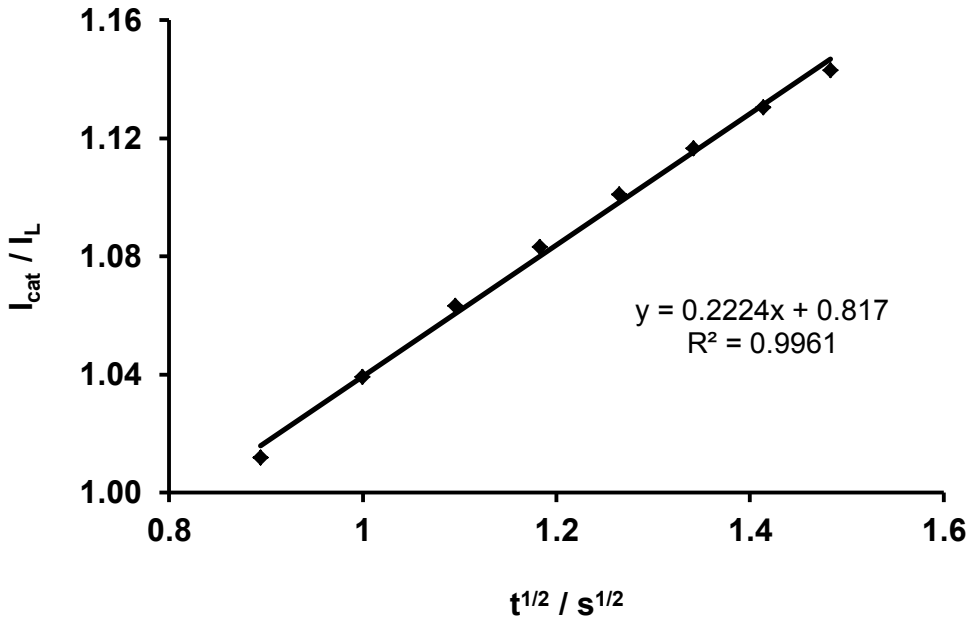

Figure 6.11: Plot of I_{cat}/I_L vs. $t^{½}$ for the catalytic oxidation of asulam in pH 7 phosphate buffer, on *poly*-CoTAPc–MWCNT–BPPGE.

The rate constant obtained here is less than, but comparable to, the rate constant of 11.08×10^2 M^{-1} s^{-1}, calculated for the oxidation of carbofuran (a carbamate

pesticide) by ozone [282]. This shows that the electrochemical oxidation of asulam at CoTAPc is fairly fast, considering that ozone is a highly reactive compound.

Figure 6.12 shows typical current response of asulam when the potential of the *poly*-CoTAPc–MWCNT–BPPGE was kept at 0.90V versus Ag|AgCl. Upon successive addition of 1ml of 1×10^{-4} M asulam, a well-defined response was observed.

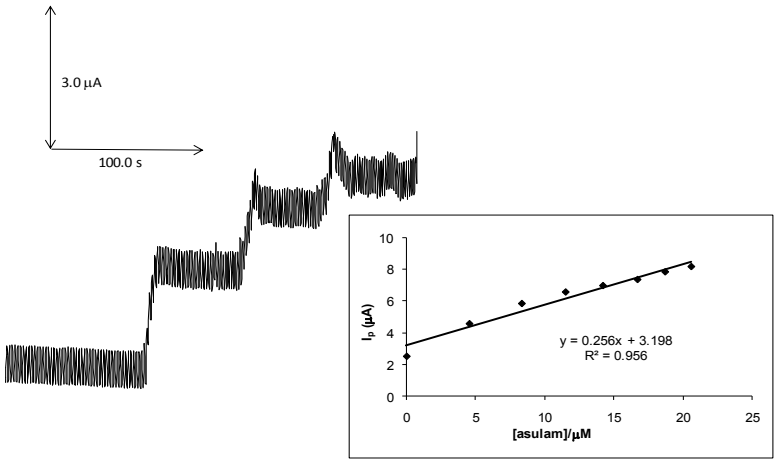

Figure 6.12: Chronoamperomegrams (recorded at 0.90 V) observed on addition of aliquots of asulam (1 ml of 1×10^{-4} M) to pH 7 buffer. Inset: plot of I_p vs [asulam], using *poly*-CoTAPc–MWCNT–BPPGE. Reference electrode: Ag|AgCl (3 M KCl)

A plot of current versus asulam concentration (inset) gave a linear relationship over a concentration range of 4.5–20.6 μM with a sensitivity of 241×10^{-3} μA/μM (r^2 = 0.9904), and a detection limit of 1.15 μM (using the $Y_B + 3\sigma$ criterion). The limit of detection obtained with this electrode is better than the 1.74 μM and 7.1 μM obtained for asulam at glassy carbon electrodes (**Table 6.2**), and the sensitivity is slightly lower than the one reported in the literature (**Table 6.2**). A comparison of the various electrodes constructed follows in Section 6.3.

The suitability of the developed electrode for electrochemical detection of asulam in a real sample was tested by confirming a known concentration of this herbicide in tap water, using the standard addition method. Five replicate determinations showed recovery of 105±0.10% of the spike, thus demonstrating the suitability of the developed CoTAPc–MWCNTs -modified BPPGE for real sample analysis.

6.3 Conclusions

Table 6.3 lists the values of the electrochemical parameters obtained in the electrocatalytic detection of amitrole and asulam with the different fabricated electrodes.

Table 6.3: Electrochemical parameters of fabricated electrodes, and the corresponding test analytes. Reference electrode: Ag|AgCl (3 M KCl)

Analyte	Electrode	Electrochemical Parameters				
Amitrole (pH 12)		Detection Potential/ V	Limit of Detection /μM	Sensitivity / μA/μM	Linear Range / M	Catalytic Rate Constant $/M^{-1}\ s^{-1}$
	FePcNP-CPE	0.55	2.48 $\times 10^{-3}$	2.0 x 10^{3}	1-7 $\times 10^{-9}$	50.4 $\times 10^{6}$
	FePcNP/ MWCNT-BPPGE	0.61	5.20	0.026	1-9 $\times 10^{-4}$	18.05
	poly-FeTAPc-MWCNT-BPPGE	0.45	0.33 $\times 10^{-3}$	8.82 x 10^{3}	1-5 $\times 10^{-9}$	3.85 $\times 10^{4}$
Asulam (pH 7)	NiPcNP-CPE	0.90	6.19 $\times 10^{-2}$	1.98	0.4-2 $\times 10^{-6}$	1.26 $\times 10^{3}$
	NiPcNP/MWCNT-BPPGE	0.90	0.29	0.045	91- 412 $\times 10^{-6}$	13.04
	poly-CoTAPc-MWCNT-BPPGE	0.87	1.15	0.241	4.5-20.6 $\times\ 10^{-6}$	1.60 $\times 10^{2}$

A close inspection of **Table 6.3** shows that, for amitrole detection, the lowest detection potential (0.44 V), the lowest limit of detection (0.33 $\times 10^{-3}$ μM), and the

highest sensitivity (8.82×10^3 μA/μM) are obtained with the *poly*-FeTAPc-MWCNT-BPPGE, followed closely by the FePcNP-CPE. However, the catalytic rate constant for poly-FeTAPc-MWCNT-BPPGE (3.85×10^4 M^{-1} s^{-1}) is lower than that of the FePcNP-CPE (50.4×10^6 M^{-1} s^{-1}). This is not expected since a higher rate constant should correspond with a higher sensitivity and lower detection potential (better electrocatalysis). The reasons for this discrepancy are not clear. The linear measuring range of the *poly*-FeTAPc-MWCNT-BPPGE ($1\text{-}5 \times 10^{-9}$ M) is almost equal to that of the FePcNP-CPE ($1\text{-}7 \times 10^{-9}$ M). It has been shown that 90% of the initial current of the poly-FeTAPc-MWCNT-BPPGE is recovered after rinsing with buffer. This is comparable to the 92% obtained with the FePcNP-CPE after renewal of its surface. Ammonium thiocyanate (NH_4SCN) is usually present in most pesticide formulations. K_{amp} values of 0.003 and 0.000741 were obtained with the *poly*-FeTAPc-MWCNT-BPPGE and FePcNP-CPE, respectively, for NH_4SCN. These values show that there is minimal NH_4SCN interference with the amitrole measurement when the *poly*-FeTAPc-MWCNT-BPPGE is used for detection, whilst there is no NH_4SCN interference at all when the FePcNP-CPE is employed. The very little NH_4SCN interference displayed by the *poly*-FeTAPc-MWCNT-BPPGE and FePcNP-CPE re-affirms their viability as amitrole detecting instruments. Therefore, considering all the factors mentioned above (especially the detection potential, limit of detection, sensitivity and stability of electrode), the most viable electrode, from the three that were investigated for amitrole detection, is the *poly*-FeTAPc-MWCNT-BPPGE.

In the detection of asulam, the detection potential is almost the same at ~ 0.9 V for all three electrodes investigated, with the *poly*-CoTAPc-MWCNT-BPPGE showing a

slightly lower detection potential of 0.87 V. The lowest limit of detection (6.19×10^{-2} μM) and the highest sensitivity (1.98 μA/μM) were obtained with the NiPcNP-CPE, although this electrode has the narrowest measuring range (0.4 -2 $\times 10^{-6}$ M) of all the electrodes investigated for detection of asulam. The highest catalytic rate constant for asulam oxidation (1.26×10^{3} M^{-1} s^{-1}) is obtained at the NiPcNP-CPE, which corresponds well with its high sensitivity. The narrow measuring range renders it a little difficult to use for investigative detection of unknown asulam concentrations since any concentration lying outside this range cannot be detected. It can be employed, though, to confirm measurements that should be lying within this range. The NiPcNP/MWCNT-BPPGE has the second lowest limit of detection for asulam (0.29 μM) and the lowest sensitivity (0.045 μA/μM), and the *poly*-CoTAPc-MWCNT-BPPGE displayed the highest limit of detection (1.15 μM) and the second highest sensitivity (0.241 μA/μM). The higher catalytic rate constant for asulam oxidation (1.60×10^{2} M^{-1} s^{-1}) at the *poly*-CoTAPc-MWCNT-BPPGE, relative to that of the NiPcNP/MWCNT-BPPGE (13.04 M^{-1} s^{-1}), corresponds well with the sensitivities of these two electrodes, with the former displaying a higher sensitivity than the latter. However, the NiPcNP/MWCNT-BPPGE displayed the widest linear measuring range (91- 412 $\times 10^{-6}$ M) of the electrodes investigated for asulam oxidation, followed by the *poly*-CoTAPc-MWCNT-BPPGE (4.5-20.6 $\times$ 10^{-6} M). The detection potential of the NiPcNP/MWCNT-BPPGE (0.9 V) is almost equal to that of the *poly*-CoTAPc-MWCNT-BPPGE (0.87 V). With regard to the stability of the two electrodes, the percentage recoveries of the initial current after rinsing with pH 7 phosphate buffer are 96% and 86% with the *poly*-CoTAPc-MWCNT-BPPGE and NiPcNP/MWCNT-BPPGE, respectively. With the NiPcNP-CPE the percentage recovery is 90%. The *poly*-

CoTAPc-MWCNT-BPPGE has a fairly wide linear measuring range as well, in addition to a higher sensitivity. Therefore, the NiPcNP/MWCNT-BPPGE would be suitable for detection of unknown quantities of asulam, because of the wide measuring range and the low limit of detection.The *poly*-CoTAPc-MWCNT-BPPGE would be best suited to repeated monitoring of known asulam concentration levels, because of the stability of the electrode, its sensitivity, and the fairly wide concentration range. The NiPcNP-CPE would be suitable for this purpose, too, as explained earlier.

General Conclusions

In this project, nanoparticles of metallophthalocyanines (CoPcNP, FePcNP, MnPcNP, and NiPcNP) have been used, alone or in combination with multi-walled carbon nanotubes, to construct electrodes for employment in the electrocatalytic detection of the pesticides amitrole and asulam. Furthermore, the corresponding tetra-aminophthalocyanines (CoTAPc, FeTAPc, MnTAPc, and NiTAPc) have been electropolymerized on the multi-walled carbon nanotubes and the resulting electrodes employed for the same purpose. Six electrodes in all were constructed. The following conclusions can be made about this exercise:

(i) In terms of the electrochemical parameters listed, the best performing electrodes were those based on NiPc, FePC, and CoPc.

(ii) Nanoparticles of phthalocyanines can be used effectively as electrocatalysts, alone (for example, in the carbon paste electrodes) or in combination with multiwalled carbon nanotubes, to produce viable electrodes which can be used continuously for the detection of amitrole and asulam.

(iii) The electrodes modified with NiPc nanoparticles (alone or in combination with MWCNTs) displayed good electrocatalytic behaviour towards asulam oxidation. However, *poly*-CoTAPc displayed the best electrocatalytic behavior towards asulam amongst the *poly*-MTAPcs.

(iv) The FePc-based electrodes displayed good electrocatalytic behavior towards amitrole oxidation, and the best analytical parameters were obtained with the *poly*-FeTAPc-MWCNT.

It has been shown that the electrodes can be used continuously without too much effect on the current response if the electrode surface is renewed by rinsing in buffer or preparing a new surface (with carbon paste electrodes).

Future work could involve the following activities:

(i) Investigation of the effect of the nature of the supporting electrolyte on the detection potential and current response of amitrole at the CoPcNP-CPE. It would be interesting to see whether the nature of anions present in solution could significantly enhance the amitrole oxidation current response at this electrode surface (see **Figure 4.4**).

(ii) Similar investigations will also be undertaken with the NiPcNP-CPE in asulam, to enrich those studies.

(iii) Investigation of the electrocatalytic behavior of a CoPcNP/MWCNT-BPPGE towards the detection of asulam. Since a poly-CoTAPc-MWCNT-BPPGE displayed good electrocatalytic behavior towards asulam oxidation, it would be interesting to investigate the electrocatalytic behavior of CoPcNP/MWCNT-BPPGE towards the same analyte.

(iv) The MTAPcs will also be covalently attached to the MWCNTs and such electrodes will be used in pesticide analyses.

References

[1] J. Manriquez, J.L. Bravo, S. Gutierrez-Granados, S. Sucar Succar, C. Bied-Charreton, A. Alatorre Ordaz, F. Bedoui, Anal. Chim. Acta, 1999, 378, 159

[2] J. Wang, Analytical Electrochemistry, VCH Publishers Inc., New York, 1994.

[3] I. Švancara, M. Galik, K. Vytřas, Talanta, 2007, 72, 512.

[4] C.M.A. Brett, A.M.O. Brett, Electrochemistry, Principles, Methods and Applications, Oxford University Press, Oxford, 1993.

[5] X. Cui, G. Liu, Y. Lin, Nanomedicine: Nanotech. Biol. Med., 2005, 1, 130.

[6] T. Thomas, R.J. Mascarenhas, C. Nethravathi, M. Rajamathi, B.E.K. Swamy, J. Electroanal. Chem., 2011, 659, 113.

[7] I.E. Mülazimoğlu, E. Yilmaz, Desalination, 2010, 256, 64.

[8] C. Hu, S. Hu, Electrochim. Acta, 2004, 49, 405.

[9] P. Nigam, S. Mohan, S. Kundu, R. Prakesh, Talanta, 2009, 77, 1426.

[10] R.N. Adams, Anal. Chem., 1958, 30, 1576.

[11] I. Švancara, M. Galík, K. Vytřas, Talanta, 2007, 51

[12] P. Mailley, E. Cummings, S. Mailley, S. Cosnier, B.R. Eggins, E. McAdams, Bioelectrochem., 2007, 70, 408.

[13] S.B. Hočevar, I. Švancara, K. Vytřas, B. Ogorevc, Electrochim. Acta, 2005, 51, 706.

[14] J. Wang, L. Chen, M.-P. Chatrathi, Anal. Chim. Acta, 2000, 411, 187.

[15] I. Švancara, K. Vytřas, J. Barek, J. Zima, Crit. Rev. Anal. Chem., 2001, 31, 311.

[16] J. Wang, Ü.A. Kirgoz, J.-W. Mo, J. Lu, A.N. Kawde, A. Muck, Electrochem. Commun., 2001, 3, 203.

[17] E. Nossol, A.J.G. Zarbin, Electrochim. Acta, 2008, 54, 582

[18] M.E. Spahr, D. Goers, W. Märkle, J. Dentzer, A. Würsig, H. Buqa, C. Vix-Guterl, P. Novák, Electrochim. Acta, 2010, 55, 8937.

[19] W. Märkle, J.-F. Colin, D. Goers, M.E. Spahr, , P. Novák, Electrochim. Acta, 2010, 55, 4964.

[20] J. Oni, P. Westbroek, T. Nyokong, Electrochem. Commun., 2001, 3, 524.

[21] I. Švancara, K. Kalcher, A. Walcarius, K. Vytřas, Electroanalysis with Carbon Paste Electrodes, CRC Press, 2012.

[22] R.L. McCreery, Electroanalytical Chemistry, ed. A.J. Bard, Marcel Dekker, New York, 1990, 17.

[23] A.W. Moore, Chemistry and Physics of Carbon, eds. P.L. Walker, P.A. Thrower, Marcel Dekker, New York, 1973, 11, 69.

[24] H. Fredriksson, D. Chakarov, B. Kasemo, Carbon, 2009, 47, 1335

[25] R.L. McCreery, Chem. Rev., 2008, 108, 2646

[26] C.E. Banks, T.J. Davies, G.G. Wildgoose, R.G. Compton, Chem. Commun., 2005, 829.

[27] M. Ligaj, J. Jasnowska, W.G. Musial, M. Filipiak, Electrochim. Acta, 2006, 51, 5193.

[28] T. Thomas, R.J. Mascarenhas, C. Nethravathi, M. Rajamathi, B.E.K. Swamy, J. Electroanal. Chem., 2011, 659, 113.

[29] R.P. da Silva, S.H.P. Serrano, J. Pharm. Biomed. Anal., 2003, 33, 735.

[30] C.R. Martin, C.A. Foss Jr., Laboratory Techniques in Electroanalytical Chemistry, 2nd ed., Eds. P.T. Kissinger, W.R. Heinemann, Marcel Dekker Inc., New York, 1996.

[31] Y. Li, L. Shi, W. Ma, D.-W. Li, H.-B. Kraatz, Y.-T. Long, Biochem., 2011, 80, 128.

[32] S. Griveau, J. Pavez, J.H. Zagal, F. Bedoui, J. Electroanal. Chem., 2001, 497, 75.

[33] J. Zhang, X. Li, W. Guo, T. Hreid, J. Hou, H. Su, Z. Yuan, Electrochim. Acta, 2011, 56, 3147.

[34] G. Alarcón-Ángeles, M. Guix, W.C. Silva, M.T. Ramirex-Silva, M. Palomar-Pardavé, M. Romero-Romo, A. Merkoçi, Biosens. Bioelectron., 2010, 26, 1768.

[35] M. H. Pournaghi-Azar, B. Habibi, Electrochim. Acta, 2007, 52, 4222.

[36] S.B. Revin, S.A. John, Electrochim. Acta, 2011, 56, 8934.

[37] A.J. Bard, L.R. Faulkner, Electrochemical Methods: Fundamentals and Application, John Wiley and Sons, New York, 1980.

[38] K.V. Gobi, T. Okajima, K. Tokuda, T. Ohsaka, Langmuir, 1998, 14, 1108.

[39] Z. Wang, A.-M. Nygard, M.J. Cook, D.A. Russell, Langmuir, 2004, 20, 5850.

[40] J.-S. Ye, Y. Wen, W.D. Zhang, H.F. Cui, G.Q. Xu, F.-S. Sheu, Electroanalysis, 2005, 17, 89.

[41] G.I. Goldstein, D.E. Newbury, P. Echlin, D.C. Joy, C. Fiori, E. Lifshin, Scanning Electron Microscopy and x-ray microanalysis, Plenum Press, New York, 1981.

[42] K.R. Patil, S.D. Sathaye, R. Hawaldar, B.R. Sathe, A.B. Mandale, A. Mitra, J. Coll. Int. Sc., 2007, 312(2), 747.

[43] C. van Gulijk, K.M. Lathouder, R. Haswell, Carbon, 2006, 44, 2956.

[44] S. Reddy, B.E. Kumara Swamy, H. Jayadevappa, Electrochim. Acta, 2012, 61, 78.

[45] G. Perego, Catalysis Today, 1998, 41, 251.

[46] P. Scherrer, Nachr. Ges. Wiss. Göttingen, Math.-Phys. Klasse, 1918, 26, 98.

[47] F.W. Jones, J. Sci. Instrum., 1941, 18, 157.

[48] R.P. Janek, W.R. Fawcett, Langmuir, 1998, 14, 3011

[49] A.S. Bondarenko, Anal. Chim. Acta, 2012, 743.

[50] F. Patolsky, M. Zayats, E. Katz, I. Willner, Anal. Chem. 1999, 71, 3171.

[51] M.E. Orazem, B. Tribollet, Electrochemical Impedance Spectroscopy, Wiley, Hoboken, 2008.

[52] B.-W. Park, R. Zheng, K.-A. Ko, B.D. Cameron, D.Y. Yoon, D.-S. Kim, Biosens. Bioelec., 2012, 38, 295.

[53] V. Horvat-Radošević, K. Kvastek, M. Kraljić-Roković, Electrochim. Acta, 2006, 51, 3417.

[54] P. Mashazi, C. Togo, J. Limson, T. Nyokong, J. Porphyrins Phthalocyanines, 2010, 14, 252.

[55] A.F. Carley, Encyclopedia of Materials: Science and Technology (2nd Ed.), 2001, 8991.

[56] S. Tougaard, Encyclopedia of Analytical Science (2nd Ed.), 2005, 446.

[57] P.N. Mashazi, P. Westbroek, K.I. Ozoemena, T. Nyokong, Electrochim Acta, 2007, 53, 1858.

[58] C.V. Raman, K.S. Krishnan, Nature, 1928, 501, 3048.

[59] T. Vankeirsbilck, A. Vercauteren, W. Baeyens, G. van der Weken, F. Verpoort, G. Vergote, J.P. Remon, Trends in Anal. Chem., 2002, 21, 869.

[60] G. Gouedec, P. Colomban, Progress in Crystal Growth and Characterization of Materials, 2007, 53, 1.

[61] P. Colomban (Ed.), Proton Conductors. Solids, Membranes and Gels-Materials and devices, Cambridge University Press, Cambridge, U.K., 1992, p329.

[62] K.S. Lokesh, Bioelectrochemistry, In Press, Accepted Manuscript, Available online 20 December, 2012.

[63] A. Orbelin, M. Endo, J. Cryst. Growth, 1976, 32, 335.

[64] P.G. Wiles, J. Abrahamson, Carbon, 1978, 16, 341

[65] S. Iijima, Nature, 1991, 354, 56.

[66] H.J. Wang, H. Yu, F. Peng, P. Lv, Electrochem. Commun., 2006, 8, 499.

[67] F. Xu, W.Q. Zhu, L. Yan, H. Xu, L.H. Xiong, J.H. Li, Org. Electron., 2012, 13, 302.

[68] R.A. Croce Jr, S. Vaddiraju, P.-Y. Chan, R. Seyta, F.C. Jain, Sensors and Actuators B: Chemical, 2011, 160, 154.

[69] T. Rueckes, K. Kim, E. Joselevich, Science, 2000, 289, 94.

[70] C. Li, T.-W. Chou, Int. J. Sol. Struc., 2003, 40, 2487.

[71] R.M. Reilly, J. Nuclear Medicine, 2007, 48, 1039.

[72] M.S. Dresselhaus, G. Dresselhaus, P.C. Eklund, Physics World, 1998 (January issue), 33.

[73] M.S. Strano, C.A. Dyke, M.L. Usrey, P.W. Barone, M.J. Allen, H. Shan, C. Kittrell, R.H. Hauge, J.M. Tour, R.E. Smalley, Science, 2003, 301, 1519.

[74] J. Li, R. Stevens, L. Delzeit, H.T. Ng, A. Cassel, J. Han, M. Meyyappan, Appl. Phys. Lett., 2002, 81, 910.

[75] G.K. Vertelov, A.Y. Olenin, G.V. Lisichkin, J. Anal. Chem., 2007, 62, 903

[76] G.-L. Wang, X.-Y. Zhu, H.-J. Jiao, Y.-M. Dong, Z.-J. Li, Biosens. Bioelectron., 2012, 31, 337.

[77] A. Ganguly, P. Trinh, K.V. Ramanujachary, T. Ahmad, A. Mugweru, A.K. Ganguli, J. Coll. Int. Science, 2011, 353, 137.

[78] E. Kockrick, C. Schrage, A. Grigas, D. Geiger, S. Kaskel, J. Sol. State Chem., 2008, 181, 1614.

[79] X. Phung, J. Groza, E.A. Stach, L.N. Williams, S.B. Ritchey, 2003, 359, 261.

[80] E. Katz, I. Wilner, J. Wang, Electroanalysis, 2004, 16, 19.

[81] A.O. Simm, S. Ward-Jones, C.E. Banks, R.G. Compton, Anal. Sci., 2005, 21, 667.

[82] C.R. Raj, T. Okajima, T Ohsaka, J. Electroanal. Chem., 2003, 543, 127.

[83] S.A. Miscoria, G.D. Barrera, G.A. Rivas, Electroanalysis, 2005, 17, 1578.

[84] Y. Wang, K. Deng, L. Gui, Y. Tang, J. Zhou, L. Cai, J. Qiu, D. Ren, Y. Wang, J. Coll. Int. Science, 1999, 213, 270.

[85] A. Abbaspour, F. Norouz-sarvestani, E. Mirahmadi, Electrochim. Acta, 2012, 76, 404.

[86] K. Wang, J.-J. Xu, K.-S. Tang, H.-Y. Chen, Talanta, 2005, 67, 798.

[87] K. Wang, J.-J. Xu, H.-Y. Chen, Biosens. Bioelectron., 2005, 20, 1388.

[88] L. Cui, L. Chen, M. Xu, H. Su, S. Li, Anal. Chim. Acta, 2012, 712, 64.

[89] Y. Tamaki, T. Tsuyoshi, H. Masuhara, J. Phys. Chem. A, 2002, 106, 2135

[90] S. Barcikowski, A. Hahn, A.V. Kabashin, B.N. Chichkov, Appl. Phys. A, 2007, 87, 47.

[91] A.V. Kabashin, M. Meunier, C. Kingston, J.H.T. Luong, J. Phys. Chem. B, 2003, 107, 4527.

[92] N. Touka, H. Benelmadjat, B. Boudine, O. Halimi, M. Sebais, J. Assoc. Arab Univ. for Basic and Appl. Sciences, Article in Press.

[93] S. Karan, D. Basak, B. Mallik, Chemical Physics letters, 2007, 434, 265.

[94] J. Pillay, K.I. Ozoemena, Electrochim. Acta, 2009, 54, 5053.

[95] P. Gregory, J. Porphyrins and Phthalocyanines, 1999, 3, 468

[96] N.B. McKeown, Chem. Ind., 1999, 92.

[97] J.M. Robertson, J. Chem. Soc., 1936, 1195

[98] Phthalocyanines: Properties and Applications, eds. C.C. Leznoff and A.B.P. Lever, VCH publishers, New York, 1989, 1993, 1993, 1996, Vol 1-4.

[99] A. Erdoğumuş, T. Nyokong, Polyhedron, 2009, 28, 2855.

[100] C. Kantar, F. Mert, S. Şaşmaz, J. Organometallic Chem., 2011, 696, 3006.

[101] M.P. Somashekarapha, K.R.V. Reddy, M.N.K. Harish, J. Kashavayya, J. Mol. Structure, 2005, 753, 190.

[102] T.V. Basova, A.G. Gürek, D. Atilla, A.K. Hassan, V. Ahsen, Polyhedron, 2007, 26, 5045.

[103] G. de la Torre, M. Nicolau, T. Torres in Supramolecular Photosensitive and Electroactive Materials, Ed. Hari Singh Nalwa, Academic Press, New York, 2001, p1-111.

[104] C.C. Leznoff in Phthalocyanines: Properties and Applications, eds. C.C. Leznoff and A.P.B. Lever, VCH publishers, New York, 1989, Vol. 1.

[105] T. Rawling, A. McDonagh, Coordination Chemistry Reviews, 2007, 251, 1128.

[106] A. Shabaani, J. Chem. Res. (S), 1998, 672.

[107] D.M. Maree, T. Nyokong, J. Chem. Res. (S), 2001, 68.

[108] Z. Zhang, X. Sun, Y. Niu, R. Xu, G. Wang, Z. Jiang, Polymer, 2006, 47, 1569.

[109] Z. Huang, J. Huang, N. Chen, J. Huang, Dyes and Pigments, 2008, 77, 584.

[110] A. Erdoğmus, T. Nyokong, Dyes and Pigments, 2010, 86, 174.

[111] T. Rawling, A.M. McDonagh, S.B. Colbran, Inorg. Chim. Acta, 2008, 361, 49.

[112] A. Günsel, M. Kandaz, A. Koca, B. Salih, Polyhedron, 2011, 30, 1446.

[113] M. Canlica, I.N. Boosen, T. Nyokong, Polyhedron, 2011, 30, 508.

[114] M. Kandaz, M.N.U. Yasasir, A. Koca, D. Bekaroğlu, Polyhedron, 2002, 21, 255.

[115] F. Durmoulin, M. Durmuş, V. Ahsen, T. Nyokong, Coord. Chem. Rev., 2010, 254, 2792.

[116] B. Çoşut, S. Yeşilot, M. Durmuş, A. Kiliç, V. Ahsen, Polyhedron, 2010, 29, 675.

[117] C. Barker, K.S. Findlay, S. Bettingtton, A.S. Batsanov, I.F. Perepichka, M.R. Bryce, A. Beeby, Tetrahedron, 2006, 62, 9433.

[118] L. Boucher, Coordination Chemistry of Macrocyclic Compounds, ed. G.A. Melson, Plenium Press, 1979, 461.

[119] A.B.P. Lever, Adv. Inorg. Radiochem., 1965, 7, 28.

[120] T. Nyokong, M.J. Stillman in Phthalocyanines: Properties and Applications, eds. C.C. Leznoff and A.B.P. Lever, VCH Publishers, New York, 1989, Vol.1.

[121] M. Goutermann, in Porphyrins, Vol. III, part A, Physical Chemistry, ed. D. Dolphin, Academic Press, New York, 1978.

[122] A.B.P. Lever, S.R. Picekens, P.C. Minor, L. Licoccia, B.S. Ramswamy, K. Magnell, J. Am. Chem. Soc., 1981, 103, 6800.

[123] J.J. Gou, S.-R. Wang, X.-G. Li, M.-Y. Yuan, Dyes and Pigments, 2012, 93, 1463.

[124] J.R. Platt, H.C. Longuett-Higgins, C.W. Rector, J. Chem. Phys., 1950, 18, 1174.

[125] T.V. Dubinina, A.V. Ivanov, N.E. Brisova, S.A. Traskin, S.I. Gurskiy, L.G. Tomilova, N.S. Zefirov, Inorg. Chim. Acta, 2010, 363, 1869.

[126] R.A. Binstead, J.R. Reimers, N.S. Hush, Chem. Phys. Lett., 2003, 378, 654.

[127] V.E. Pushkarev, E.V. Shulishov, Y.V. Tomilov, L.G. Tomilova, Tetrahedron lett., 2007, 48, 5269.

[128] P. Zhu, Y. Wang, M. Ren, X. Zhao, X. Zhang, Inorg. Chim. Acta, 2012, In Press.

[129] J. Sleven, C. Görller-Walrand, K. Binnemans, Materials Science and Engineering C, 2001, 18, 229.

[130] A. B. P. Lever, J. Porphyrins Phthalocyanines, 1999, 3, 488.

[131] H. Zhan, W. Chen, M. Wang, Materials letters, 2003, 57, 1108.

[132] K. Palewska, J. Sworakowski, J. Lipiński, Optical Materials, 2012, 34, 1717.

[133] M. Kostka, P. Zinicik, M. Miletin, P. Klemera, K. Kopecky, Z. Musil, J. Photochem. Photobiol. A: Chemistry, 2006, 178, 16.

[134] B. Brożek-Płuska, I. Szymczyk, H. Abramczyk, J. Mol. Structure, 2005, 744, 481.

[135] J. Cerný, M. Karásková, J. Rakušan, S. Nešpurek, J. Photochem. Photobiol. A: Chemistry, 2010, 210, 82.

[136] Z. Hongbing, C. Wenzhe, L. Guanghui, W. Minquan, Materials Science and Engineering B, 2003, 100, 82.

[137] Z. Odabas, E.B. Orman, M. Durmus, F. Dumludağ, A.R. Özkaya, M. Bulut, Dyes and Pigments, 2012, 540.

[138] M. Kandaz, M.N. Yasir, A. Koca, Polyhedron, 2009, 257.

[139] M.K Şener, A. Koca, A. Gül, M.B. Koçak, Polyhedron, 2007, 26, 1070.

[140] N.B. McKeown, Comprehensive Coordination Chemistry II, 2003, 1, 507

[141] Y. Liu, D. Zhu, Handbook of Surfaces and Interfaces of materials, 2001, 4, 405.

[142] O.A. Osmanbaş, A. Koca, I. Özçeşmeci, A.İ. Okur, A. Gül, Electrochim. Acta, 2008, 53, 4969.

[143] A.L. Uğur, A. Erdoğmus, A. Koca, U. Avciata, Polyhedron, 29, 3310.

[144] G.K. Karaoğlan, G. Gümrükçü, A. Koca, A. Gül, U. Avciata, Dyes and Pigments, 2011, 90, 11.

[145] Ş. Özçelik, A. Koca, A. Gül, Polyhedron, 2012, 42, 227.

[146] G. Kwag, C. Bae, S. Kim, J.-J. Lee, M.E. Kenney, Inorg. Chim. Acta, 2008, 362, 2027.

[147] V. Chauke, T. Nyokong, Inorg. Chim. Acta, 2010, 363, 3662.

[148] Y. Arslanoğlu, A. Koca, E. Hamuryudan, Polyhedron, 2007, 26, 891.

[149] A.R. Özkaya, E. Hamuryudan, Z.A. Bayir, Ö. Bekaroğlu, J. Porphyrins Phthalocyanines, 2000, 4, 689.

[150] G. Gümrükcü, M.Ü. Özgür, A. Altindal, A.R. Özkaya, B. Salih, Ö. Bekaroğlu, Synthetic Metals, 2011, 161, 112.

[151] Z. Biyikhoğlu, A. Koca, H. Kantekin, Polyhedron, 2009, 28, 2171.

[152] A.B.P. Lever, E.R. Malieva, G. Speier, Phthalocyanines: Properties and Applications, eds. A.B.P. Lever and C.C. Leznoff, VCH Publishers, New York, 1993, Vol.3.

[153] J. Obirai, T. Nyokong, Electrochim. Acta, 2005, 50, 5427

[154] N. Sehlotho, T. Nyokong, Electrochim. Acta, 2006, 51, 4463.

[155] T. Nyokong, Z. Gaysna, M. Stillman, ACS, Symp. Ser., 1986, 321, 309.

[156] M.N. Pournaghi-Azar, R. Sabzi, J. Electroanal. Chem., 2003, 543, 115.

[157] T. Nyokong in N_4-Macrocyclic Metal Complexes, eds. J.H. Zagal, F. Bedioui, J.-P. Dodelet, Springer, New York, 2006.

[158] B.O. Agboola, K.I. Ozoemena, T. Nyokong, Electrochim. Acta, 2006, 51, 6470.

[159] D.A. Geraldo, C.A. Togo, J. Limson, T. Nyokong, Electrochim. Acta, 2008, 53, 8051.

[160] N. Grootboom, T. Nyokong, Anal. Chim. Acta, 2001, 432, 49.

[161] S. Maree, T. Nyokong, J. Electroanal. Chem., 2000, 492, 120.

[162] N. Pereira-Rodriguez, R. Cofré, J.H. Zagal, F. Bedioui, Bioelectrochem., 2007, 70, 147.

[163] P. Tau, T. Nyokong, J. Electroanal. Chem., 2007, 611, 10.

[164] A. Abbaspour, M.A. Mehrgardi, R. Kia, J. Electroanal. Chem., 2004, 568, 261.

[165] K. De Wael, A. Adriaens, Talanta, 2008, 74, 1562.

[166] T. Mugadza, T. Nyokong, J. Coll. Int. Science, 2011, 354, 437.

[167] V.P. Chauke, E. Entunes, T. Nyokong, J. Electroanal. Chem., 2011, 661, 1.

[168] T. Mugadza, T. Nyokong, Polyhedron, 2011, 30, 1820.

[169] J.F. Silva, S. Griveau, C. Richard, J.H. Zagal, F. Bedoui, Electrochem. Commun., 2007, 9, 1629.

[170] T. Mugadza, T. Nyokong, Electrochim. Acta, 2010, 55, 6049.

[171] T. Mugadza, T. Nyokong, Electrochim. Acta, 2009, 54, 6347.

[172] T.B. Ogunbayo, T. Nyokong, J. Mol. Catalysis A: Chemical, 2011, 337, 68.

[173] T. Mugadza, Y. Arslanoğlu, T. Nyokong, Electrochim. Acta, 2012, 68, 44.

[174] D.A. Geraldo, C.A. Togo, J. Limson, T. Nyokong, Electrochim. Acta, 2008, 53, 8051.

[175] P. Mashazi, T. Mugadza, N. Sosibo, P. Mdluli, S. Vilakazi, T. Nyokong, Talanta, 2011, 85, 2202.

[176] B. Wang, X. Zhou, Y. Wu, Z. Chen, Sensors and Actuators B, 2012, 171, 398.

[177] D. Nkosi, K.I. Ozoemena, Electrochim. Acta, 2008, 53, 2782.

[178] D. Nkosi, K.I. Ozoemena, J. Electroanal. Chem., 2008, 621, 304.

[179] K.I. Ozoemena, T. Nyokong, D. Nkosi, I. Chambrier, M.J. Cook, Electrochim. Acta, 2007, 52, 4132.

[180] K.I. Ozoemena, D. Nkosi, J. Pillay, Electrochim. Acta, 2008, 53, 2844.

[181] T. Mugadza, T. Nyokong, Electrochim. Acta, 2011, 56, 1995.

[182] T. Mugadza, T. Nyokong, Electrochim. Acta, 2010, 55, 2606.

[183] E. Jubete, K. Zelechowska, O.A. Loaiza, P.J. Lamas, E. Ochoteko, K.D. Farmer, K.B. Roberts, J.F. Biernat, Electrochim. Acta, 2011, 56, 3988.

[184] J. Pillay, K.I. Ozoemena, Electrochim. Acta, 2007, 52, 3630.

[185] T. Mugadza, T. Nyokong, Synthetic Materials, 2010, 160, 2089.

[186] B.O. Agboola, K.I. Ozoemena, T. Nyokong, T. Fukuda, N. Kobayashi, Carbon, 2010, 48, 763.

[187] J. Pillay, K.I. Ozoemena, Electrochim. Acta, 2009, 54, 5053

[188] W. Lu, N. Li, S. Bao, W. Chen, Carbon, 2011, 49, 1699

[189] H. Yin, Y. Zhou, J. Xu, S. Ai, L. Cui, L. Zhu, Anal. Chim. Acta, 2010, 659, 144.

[190] X. Zuo, H. Zhang, N. Li, Sensors and Actuators B: Chemical, 2012, 161, 1074.

[191] F.C. Moraes, D.L.C. Golinelli, C.H. Mascaro, S.A.S. Machado, Sensors and Actuators B: Chemical, 2010, 148, 492.

[192] O.O. Fashedemi, K.I. Ozoemena, Sensors and Actuators B: Chemical, 2011, 160, 7.

[193] A.L. Verma, S. Soxena, G.S.S. Sani, V. Gaur, V.K. Jaim, Thin Solid Films, 2011, 519, 8144.

[194] F.C. Moraes, L.H. Mascaro, S.A.S. Machado, C.M.A. Brett, Talanta, 2009, 79, 1406.

[195] Z. Xu, H. Li, G. Cao, Q. Zhang, K. Li, X. Zhao, J. Mol. Catal. A: Chemical, 2011, 335, 89.

[196] Y. Yuan, B. Zhao, Y. Jeon, S. Zhong, S. Zhou, S. Kim, Bioresource Tech., 2011, 102, 5849.

[197] I. Balan, L.G. David, V. David, A.-L. Stoica, C. Mihailciuc, I. Stamatin, A.A. Ciucu, J. Electroanal. Chem., 2011, 654, 8.

[198] X. Zhu, S. Ai, Q. Chen, H. Yin, J. Xu, Electrochem. Commun., 2009, 11, 1543.

[199] S.A. Mamuru, K.I. Ozoemena, T. Fukuda, N. Kobayashi, T. Nyokong, Electrochim. Acta, 2010, 55, 6367.

[200] I. Cesarino, F.C. Moraes, T.C.R. Ferreira, M.R.V. Lanza, S.A.S. Machado, J. Electroanal. Chem., 2012, 672, 34.

[201] C.-Y. Lin, A. Balamuguran, Y.-H. Lai, K.-C. Ho, Talanta, 2010, 82, 1905.

[202] D. Patrascu, L. David, V. David, C.M. Mihailcuic, L. Stamatin, J. Ciurea, L. Naggy, G. Naggy, A.A. Ciucu, Sensors and Actuators B: Chemical, 2011, 156, 731.

[203] A. Morozan, S. Campidelli, A. Filoramo, B. Jousselme, S. Palacin, Carbon, 2011, 4839.

[204] B. Qiu, Z. Lin, J. Wang, Z. Chen, G. Chen, Talanta, 2009, 76, 195.

[205] S.A. Mamuru, K.I. Ozoemena, Electrochem. Commun., 2010, 12, 1539.

[206] M. Fielding, D. Barcelo, A. Helweg, S. Galassi, L. Tortenson, P. Van Zoonen, R. Wolter, G. Ageletti, in Pesticides in Ground and Drinking Water, Water Pollution Research Report 27, Commission of the European Communities, Directorate for Science, Research and Development, 1991.

[207] J.M. van der Poll, M. Vink, J.K. Quirijns, Chromatographia, 1998, 25, 511.

[208] T. Desterreich, U. Klaus, M. Volk, B. Neidhart, M. Spiteller, Chemosphere, 1999, 38, 379.

[209] R. Barkission, D. Murray, V. Hoffstein, Chest, 1992, 101, 1174.

[210] F. Mattioli, L. Robbiano, P. Barachhini, Fundam. Appl. Toxicol., 1994, 23, 101.

[211] Extension Toxicology Network (EXTOXNET), Pesticide Information Profiles (http://extoxnet.orst.edu/pips/amitrole.htm).

[212] I. Bobeldijk, K. Broess, P. Speksnijder, T. van Leerdam, J. Chromatogr. A, 2001, 938, 15.

[213] F. Sánchez-Bayo, R.V. Hyne, K.L. Desseille, Anal. Chim. Acta, 2010, 675, 125.

[214] J. Dugay, M.-C. Hennion, Trend Anal. Chem., 1995, 14, 8.

[215] M.-C. Hennion, P. Subra, V. Coquart, R. Rosset, Fresenius J. Anal. Chem., 1991, 339, 488.

[216] E.A. Hogendoorn, R. Hoogerbrugge, R.A. Baumann, H.D. Meiring, A.P.J.M. de Jong, P. van Zoonen, J. Chromatogr. A, 1996, 754, 49.

[217] K.A. Osman, A.M. Al-Humaid, S.M. Al-Rehiayani, K.N. Al-Redhaiman, Ecotoxicology and Environmental Safety, 2010, 73, 1433.

[218] M. Hunsche, K. Bürling, G. Noga, Pesticide Biochem. Physiol., 2011, 101, 39.

[219] F.O. Green, R.N. Feinstein, Anal. Chem., 1957, 29, 1658.

[220] R. Grover, A.E. Smith, H.C. Korven, Can. J. Plant Sci., 1980, 60, 185.

[221] D. Moreno-González, L. Gámiz-Garcia, J.M. Bosque-Sendra, A.M. García-Campaña, J. Chromatogr. A, 2012, 1247, 26.

[222] M. Chicharro, A.S. Arribas, M. Moreno, E. Bermejo, A. Zapardiel, Talanta, 2007, 74, 376.

[223] A. Chivulescu, M. Catalá-Icardo, J.V. García Mateo, J. Martinez-Catalavud, Anal. Chim. Acta, 2004, 519, 113.

[224] F. García-Sánchez, A.N. Díaz, C.D. Téllez, M. Algarra, Talanta, 2008, 77, 294.

[225] M. Chicharro, A. Zapardiel, E. Bermejo, A. Sanchez, Anal. Chim. Acta, 2002, 469, 243.

[226] M. Hutta, D. Kaniasky, E. Kovalcikova, J. Marak, M. Chalanyova, V. Madajova, E. Simunicova, J. Chromatogr., 1995, 689, 123.

[227] M. Moder, P. Popp, R. Eisert, J. Pawliszyn, Fresenius J. Anal. Chem., 1999, 363, 680.

[228] M.C. Gennaro, C. Abrigo, D. Giacosa, L. Rigotti, A. Liberatori, J. Chromatogr. A, 1995, 718, 81.

[229] F. García-Sanchez, A. Navas-Díaz, A. García-Pareja, V. Bracho, J. Liq. Chromatogr. Relat. Technol., 1997, 20, 603.

[230] H. Tsui, N. Henmi, Y. Kaneda, Jpn. J. Toxicol. Environ. Health, 1995, 41, 292.

[231] H.P.A. Nouws, C. Delerue-Matos, J.L.F.C. Lima, E.M. Garrido, P. Vincke, N.A. Maes, Intern. J. Environ. Anal. Chem., 2002, 82, 69.

[232] Q.G. von Nehring, J.W. Hightower, J.L. Anderson, Anal. Chem., 1986, 58, 2777.

[233] S.W. Oliver, T.D. Thomas, Heterocycles, 1984, 22, 2047.

[234] B.N. Achar, G.M. Fohlen, J.A. Parker, J. Polym. Sci., 1982, 20, 2773.

[235] B.N. Achar, G.M. Fohlen, J.A. Parker, J. Keshayava, Polyhedron, 1987, 6, 1463.

[236] G.-J. Yang, K. Wang, J.-J. Xu, H.-Y. Chen, Anal. Lett., 2004, 37, 629.

[237] J. Liu, G. Rinzler, H. Dai, J.H. Hafner, R.K. Bradley, P.J. Boul, A. Lu, T. Iverson, K. Shelimov, C.B. Huffman, F. Rodrigues-Macias, Y.-S. Shon, T.R. Lee, D.T. Colbert, R.E. Smalley, Science, 1998, 280, 1253.

[238] A. Salimi, R.G. Compton, R. Hallaj, Anal. Chem., 2004, 333, 49.

[239] R.R. Moore, C.E. Banks, R.G. Compton, Anal. Chem., 2004, 76, 26.

[240] M. Yang, Y. Yang, F. Qu, Y. Lu, R. Yu, 2006, 571, 211.

[241] B.D. Cullity, Elements of X-Ray Diffraction, Addison-Wesley Publishing Company, Inc., Massachusetts, 1967, Chapter 3.

[242] W. Chao, X. Zhang, C. Xiao, D. Liang, Y. Wang, J. Coll. Int. Science, 2008, 325, 198.

[243] R.J. Nemanich, S.A. Solin, Phys. Rev. B, 1994, 20, 392.

[244] M.S. Dresselhaus, A. Jorio, R. Saito, Annu. Rev. Condens. Matter. Phys., 2010, 1, 89.

[245] H. Sharma, A.K. Shukla, V.D. Vankar, Thin Solid Films, 2012, 520, 1902.

[246] S. Lee, J.-W. Peng, J. Phys. and Chem. of Solids, 2011, 72, 1133.

[247] T.V. Basova, B.A. Kolesov, A.G. Gürek, V. Ahsen, Thin Solid Films, 2001, 385, 246.

[248] M. Yudasaka, R. Kikuchi, Y. Ohki, S. Yomishura, Carbon, 1997, 35, 195.

[249] M. Brumbach, P.A. Veneman, F.S. Marrikar, T. Schulmeyer, A. Simmonds, W. Xia, P. Lee, N.R. Armstrong, Langmuir, 2007, 23, 11089.

[250] M.S. Ureta-Zañartu, C. Berrios, J. Pavez, J. Zagal, C. Gutiérrez, J.F. Marco, J. Electroanal. Chem., 2003, 553, 147.

[251] A.C. Dillon, T. Genett, K.M. Jones, J.L. Alleman, P.A. Parrila, M.J. Heben, Adv. Mater., 1999, 11, 1354.

[252] H.S. Sharma, S.-M. Park, J. Electrochem. Soc., 2004, 151, 61.

[253] J. Obirai, T. Nyokong, Electrochim Acta, 2004, 49, 1417.

[254] A.B.P. Lever, J.P. Wilshire, Can. J. Chem., 1976, 54, 2514.

[255] H. Li, T.H. Guarr, J. Chem. Soc. Chem. Commun., 1989, 832.

[256] H. Li, T.H. Guarr, J. Electroanal. Chem. ,1991, 317, 189

[257] T.-F. Kang, G.-L. Shen, R.-Q. Yu, Anal. Chim. Acta, 1997, 356, 245.

[258] M.A. Ruiz, M.G. Blazquezs, J.M. Pingarron, Anal. Chim. Acta, 1995, 305, 49.

[259] A. Wolberg, J. Manassen, J. Am. Chem. Soc., 1970, 92, 2982.

[260] K. Gong, X. Zhu, R. Zhao, S. Xiong, L. Mao, C. Cheng, Anal. Chem., 2005, 77, 8158.

[261] Y.-H. Tse, P. Janda, H. Lam, J.J. Zhang, W.J. Pietro, A.B.P. Lever, J. Porphyrins Phthalocyanines, 1997, 1, 3.

[262] E.F. Perez, L.T. Kubota, A.A. Tanaka, G. De Oliveira Neto, Electrochim. Acta 43 (1998) 1665.

[263] T. Malinski, A. Ciszewski, J. Bennett, J.R. Fish, L. Czuchajowski, J. Electrochem. Soc., 1991, 138, 2008.

[264] F. Bedioui, S. Trevin, V. Albin, M. Guadalupe, G. Villegas, J. Devynck, Anal. Chim. Acta 341 (1997) 177.

[265] X. Wang, Y. Liu, W. Qiu, D. Zhu, J. Mater. Chem., 2002, 12, 1636.

[266] C.D.S. Tomlin (Ed.), The Pesticide Manual, 11th ed., British Crop Protection Council, Farnham, Surrey, UK, 1997.

[267] T. Eicher, S. Hauptmann, The Chemistry of Heterocycles: Structure, Reactions, Syntheses and Applications (translated by H. Suschitzky, J.Suschitzky), Georg Thieme Verlag, Stuttgart, New York, 1995 (Chapter 5).

[268] C.A. Caro, F. Bedioui, J.H. Zagal, Electrochim. Acta, 2002, 47, 1489.

[269] M. Chicharro, A. Zapardiel, E. Bermejo, M. Moreno, E. Madrid, Anal. Bioanal. Chem. 373 (2002) 277.

[270] S.M. Golabi, H.R. Zare, J. Electroanal. Chem., 1999, 465, 168.

[271] J. Zhang, Y.-H. Tse, W.J. Pietro, A.B.P. Lever, J. Electroanal. Chem. 1996, 406, 203.

[272] J.H. Zagal, M.A. Paez, Electrochim. Acta, 1997, 42, 3477.

[273] L. Niu, T. You, J.Y. Gui, E. Wang, S. Dong, J. Electroanal. Chem., 1998, 448, 79.

[274] J.-M. Zen, A. S. Kumar, M.-R. Chang, Electrochim. Acta, 2000, 45, 1691.

[275] M.E.G. Lyons, C.A. Fitzgerald, M.R. Smyth, Analyst, 1994, 119, 855.

[276] B. Wermeckers, F. Beck, Electrochim. Acta 30 (1985) 1491.

[277] R.D. Rocklin, R.W. Murray, J. Phys. Chem., 1981, 85, 2104.

[278] J.C. Miller, J.N. Miller, P.J. Worsfold, Statistics for Analytical Chemists, Horwood, Chichester, 1984.

[279] R.I. Stefan, J.F. van Staden, H.Y. Aboul-Enein, Electrochemical Sensors in Bioanalysis, Marcel Dekker, New York, 2001.

[280] O. Hammerich, H. Lund (Eds.), Organic Electrochemistry, 4th Ed. Marcel Dekker, Inc., New York (2001), p.570.

[281] T. Shono, H. Hamaguchi, Y. Matsumura, J. Am. Chem. Soc. 97 issue15 (1975) 4264.

[282] F.J. Benitez, J.L. Acero, F.J. Real, J. Hazard. Mater. B, 2002, 89, 51.

[283] A. Salimi, C.E. Banks, R.G. Compton, Analyst 129 (2004) 225.